AN ABSTRACT OF THE DISSERTATION OF

Hyoungsu Park for the degree of Doctor of Philosophy in Civil Engineering presented on March 10, 2016.

Title: Probabilistic Tsunami Hazard and Damage Assessment of the Built Environment Applied at Seaside, Oregon

Abstract approved:

_____

Daniel T. Cox

Damage estimates to the built environment from tsunamis are important for disaster mitigation, including planning emergency response and recovery. This dissertation evaluates the damage states of buildings in a small urban coastal city, Seaside, Oregon, from tsunami hazards generated by a Cascadia Subduction Zone (CSZ) event. This study is separated into two parts: (1) tsunami hazard assessment, and (2) tsunami damage assessment of buildings.

For the tsunami hazard assessment, a new method is presented to characterize the randomness of the fault slip in terms of the moment magnitude, peak slip location, and a fault slip shape distribution parameterized as a Gaussian distribution. For the tsunami inundation resulting from the seismic event, five tsunami intensity measures (IMs) are estimated: (1) the maximum inundation depth, h_{Max}, (2) the maximum velocity, V_{Max}, (3) the maximum momentum flux, M_{Max}, (4) the initial arrival time exceeding a 1 m inundation depth, T_A, and (5) the duration exceeding a 1 m inundation depth, T_h, and presented in the form of annual exceedance probabilities conditioned on a full-rupture CSZ event. The IMs are generally observed to increase as the moment magnitude increases, as the proximity of the peak slip becomes closer to the study area, and as the distribution of fault shape narrows. Among the IMs, the arrival time (T_A) shows a relatively weak sensitivity to the aleatory uncertainty while the other IMs show significant sensitivity, especially M_{Max}. It is observed at the shoreline that M_{Max} increases by an order of magnitude from the 500-year to the 1,000-year event, while h_{Max} increases by a factor of 3, and T_A decreases by only

factor of 0.05. The intensity of IMs generally decreases inland, but there are also varying dependencies on bathymetry. For example, a shorter inundation duration, T_h (< 10 min) is observed at the higher ground level (z > 3 m) while a longer T_h (~100 min) is observed near the river and creek.

For the tsunami damage assessment, the annual exceedance of the IMs, h_{Max} and M_{Max} are used to estimate building damage using a fragility curve analysis. Tax lot data, Google Street View, and field reconnaissance surveys are used to classify the buildings at a community scale and match with existing fragility curves according to construction material, floor level and build year. The fragility analysis is used to estimate the damage probability of buildings for a 1,000-year event conditioned on a full-rupture CSZ event. The sensitivity of building damage to the both the aleatory and epistemic uncertainty involved in the process of damage estimation are presented. Fragility curves based on depth and based on momentum flux both generally show higher damage probability for structures that are wooden and closer to the shoreline than those that are reinforced concreted (RC) and landward of the shoreline. However, a relatively high damage probability was found at the river and creek region from the fragility curve analysis using h_{Max}. Within 500 m from the shoreline, wood structure damage shows a significant sensitivity to the aleatory uncertainty of the tsunami generation from the CSZ event. On the other hand, RC structure damage showed equal sensitivity to the aleatory uncertainty of the tsunami generation as well as the epistemic uncertainties due to the numerical modelling of the tsunami inundation (friction), the building classification (material and build year), and the type of fragility curves (depth or momentum type curves). Further from the shoreline, the wood structures showed similar uncertainties to the aleatory and epistemic uncertainties.

©Copyright by Hyoungsu Park
March 10, 2016
All Rights Reserved

Probabilistic Tsunami Hazard and Damage Assessments of the Built Environment: Applied at Seaside, Oregon

by
Hyoungsu Park

A DISSERTATION

submitted to

Oregon State University

in partial fulfillment of
the requirements for the
degree of

Doctor of Philosophy

Presented March 10, 2016
Commencement June 2016

Doctor of Philosophy dissertation of Hyoungsu Park presented on March 10, 2016

APPROVED:

Major Professor, representing Civil Engineering

Head of the School of Civil and Construction Engineering

Dean of the Graduate School

I understand that my dissertation will become part of the permanent collection of Oregon State University libraries. My signature below authorizes release of my dissertation to any reader upon request.

Hyoungsu Park, Author

ACKNOWLEDGEMENTS

I would like to express my sincere gratitude to my advisor Dr. Daniel Cox for his continuous support of my Ph.D. study and related research, patience, motivation, and immense knowledge. I could not have imagined having a better advisor and mentor for my Ph.D. study.

Besides my advisor, I would like to thank the rest of my thesis committee: Dr. Andre Barbosa, Dr. David Hill, Dr. Michael Scott, and Dr. Anne Trehu for their insightful comments and encouragement, and also for their insightful questions which have widen my understanding from various perspectives.

I am also grateful with the professors in the School of Civil and Construction and in the College of Earth, Ocean and Atmospheric Sciences: Dr. Merrick Haller, Dr. Tuba Ozkan-Haller, Dr. Peter Ruggiero, Dr. Harry Yeh, and Dr. Solomon Yim, for their enthusiastic lectures and guidance during my course work.

Last but not least, I would like to thank my family: my parents, for giving birth to me and supporting me throughout my life, my wife, Eunyi Jeong, for her love, devotion, and trust and my daughter, Leia Park.

CONTRIBUTION OF AUTHORS

Chapter 2: Dan Cox provided constructive comments to improve the manuscript.

Chapter 3: Dan Cox and Andre Barbosa provided constructive comments to improve the manuscript.

TABLE OF CONTENTS

Page

1. Introduction 1

2. Probabilistic Assessment of Near-field Tsunami Hazards: Arrival Time, Inundation Depth, Velocity, Momentum Flux, and Duration Applied to Seaside, Oregon. 5

2.1 Abstract 5

2.2 Introduction 6

2.2.1 Near-field tsunami hazards at the CSZ 6

2.2.2 Previous tsunami studies at CSZ 9

2.2.3 Objectives of this study. 9

2.3 Tsunami generation model 10

2.3.1 Inversion model and Gaussian distribution 10

2.3.2 Relation between earthquake intensity and rupture area 15

2.3.3 Development of a new fault slip method 17

2.3.4 Tsunami scenarios at the CSZ 18

2.4 Numerical model setup for tsunami generation, propagation, and inundation 20

2.4.1 Numerical models 20

2.4.2 Model setup 21

2.4.3 Example of model output time series at Points A and B. 24

2.5 Probabilistic near-field tsunami hazard assessment (PNTHA) 29

2.5.1 Methodology of PNTHA 29

2.5.2 PNTHA results at observation points 32

TABLE OF CONTENTS (Continued)

Page

2.5.3 Spatial distributions of IMs for Seaside, OR 37

2.6 Discussion 41

2.6.1 Uncertainties on the input slip conditions 41

2.6.2 Uncertainties on the weighting factors 42

2.6.3 Uncertainties on the initial conditions of numerical models 42

2.7 Conclusions 43

2.8 Appendix 44

2.9 References 46

2.10 Nomenclature 51

3. Probabilistic Tsunami Damage Estimation on Built Environments and Sensitivity Applied at Seaside, Oregon. 52

3.1 Abstract 52

3.2 Introduction 52

3.3 Study Area and Methodology 55

3.3.1 Study area 55

3.3.2 Methodology 57

3.3.3 Review of probabilistic tsunami hazards assessment at Seaside, OR. 58

3.4 Fragility curves analysis 61

3.4.1 Tsunami fragility curves with the maximum inundation depth 63

3.4.2 Tsunami fragility curves with the maximum momentum flux 64

3.4.3 Comparison of two types of fragility curves 65

TABLE OF CONTENTS (Continued)

Page

3.5 Building Classification (Typology) 70

3.6 Probabilistic damage estimation. 74

3.7 Sensitivity tests 75

3.7.1 Tsunami intensity (Tsunami generation) 76

3.7.2 Frictions (Manning, n=0.04, 0.03, and 0.02) 78

3.7.3 Floor levels (Low, Mid, and High-Rise) 79

3.7.4 Seismic Design Categories (Pre, Moderate, and High) 80

3.7.5 Fragility curve types 82

3.7.6 Summary of sensitivity tests 83

3.8 Discussions 84

3.8.1 Limits of the fragility curves used in this study 84

3.8.2 Limits of intensity measures from numerical modelling 85

3.8.3 Limited building information for the fragility analysis. 85

3.8.4 Multi-hazard (Earthquake) and other factor beyond current fragility curves… 85

3.9 Conclusions 85

3.10 Reference 87

3.11 Nomenclature 91

4. General conclusions 92

5. Appendix 101

5.1 Appendix A 101

TABLE OF CONTENTS (Continued)

Page

5.2 Appendix B 128

LIST OF FIGURES

Figure Page

Fig. 1.1 Flow chart of the probabilistic tsunami damage estimation process. 3

Fig. 2.1 Regional map of Cascadia Subduction Zone (CSZ) and study area, Seaside, Oregon. 7

Fig. 2.2 The left panels show fault slip distributions of inversion models for 2011 Tohoku tsunami from (a) Shao et al., 2013 and (c) Hayes, 2011, and (e) for 2010 Chile tsunami inversion model from Fujii and Satake, 2013. The right panels show the cross-profiles of fault slip distribution from each inversion model. Each blue dashed lines in panel b, d, and f presents the cross-profile of normalized fault slip (D') along the strike direction (Y'/dL), and thick black dash line the fault slip distribution at the peak slip transect. The solid line presents and the fitting curve for cross-profiles with a Gaussian distribution form (Eq. 1)..... 12

Fig. 2.3 (a) Gaussian distribution curves fitted for the tsunami inversion models along the strike direction and (b) the decay rate of slips along the dip slip direction. Numbered lines correspond to events listed in Table 2.1. Solid thick line in (b) presents the average of all decay rates of slips excluding (7). 14

Fig. 2.4 Scaling relationship of rupture area with respect to the moment magnitude. Solid line is the fitting curve (Eq. 4) and dotted line is updated fitting curve in this study (Eq. 5). Blue dashed lines show upper and lower bounds by multiplying Eq. 4 by 2.0 and 0.5, respectively. Red dots present the data from Murotani et al. (2008), and cross symbols are data from Murotani et al. (2013). Asterisk symbols present the data by authors from Table 2.2, and black solid circle indicates the maximum rupture area at the CSZ (1,000 km × 120 km)..... 16

Fig. 2.5 Logic tree of the CSZ event at Seaside, OR 18

Fig. 2.6. Examples of the slip shapes at peak slip transect for (a) M_W 8.8, (b) M_W 9.0, and (c) M_W 9.2 with α'=0.35. Solid line presents the smallest β' among three β' per each M_W scenarios. Blue dash and red dot line presents the middle and largest β', respectively..... 20

Fig. 2.8 (a) Satellite image of Seaside, OR with representative observation points and (b) detail bathymetry applied in COULWAVE. Dotted lines in Fig. 2.8b present 3 m contours above the MHW..... 23

Fig. 2.9 Time series of (a) free surface elevation, η, at point A, (b) inundation depth, h, (c) velocity, V, and (d) momentum flux, M each at Point B. Scenarios are for β' = 0.81 (black solid), 1.73 (blue dash) and 3.46 (red dash-dot) with M_W 9.0 and α'=0.35. 24

LIST OF FIGURES (Continued)

Figure Page

Fig. 2.10 Initial tsunami wave conditions at the COULWAVE model boundary (Point A, in Fig. 2.7) for the CSZ tsunami scenarios against the latitude positions of peak slip. Panel a, b, and c shows the maximum surface elevation (η_{Max}), representative period of tsunami (T_R), and Iribarren number (ξ) of 72 scenarios. Panel d shows the regional map of Seaside, OR. Top x-axis of panel d shows the eight peak slip location in terms of α'. Symbols represents a different β' as triangle (smallest β'), square, and circle (largest), and color presents a different M_W 8.8 (white), 9.0 (yellow), and 9.2 (black)..... 26

Fig. 2.11 Tsunami IMs at the shoreline of Seaside, OR (Point B) for all scenarios against the latitude positions of peak slip for (a) inundation depth (h_{Max}), (b) velocity (V_{Max}), (c) momentum flux (M_{Max}), (d) arrival time exceeding 1 m inundation depth (T_A), and (e) total duration exceeding 1 m inundation depth (T_h). Symbols are the same as Fig 2.10. 28

Fig. 2.12 Non-exceedance probability of the maximum inundation depth at Point B with the given three moment magnitudes. Each symbol presents the scenarios with M_W 8.8 (green circle), 9.0 (blue square), and 9.2 (red triangle). 30

Fig. 2.13 Total mean occurrence rate of the max inundation depth at Point B (thick solid line). Three thin lines present the mean occurrence rate of the scenarios with M_W 8.8 (green dash-dot), 9.0 (blue dash), and 9.2 (red dot). 31

Fig. 2.14 Annual exceedance probability of the maximum inundation depth at Point B. . 32

Fig. 2.15 Annual exceedance probability of (a) h_{Max}, (b) V_{Max} , (c) M_{Max}, (d) T_h , (e) T_A , (f) Froude number, F at Points 1 (black solid), 2 (red dash), and 3 (blue dash-dot)..... 33

Fig. 2.16 Annual exceedance probability of the h_{Max} (panel a), V_{Max} (panel b), M_{Max} (panel c), T_h (panel d), T_A (panel e) and Froude number, F (panel f) at Points 2 (black solid line), 5(red dash line), and 8(blue dash-dot line)..... 36

Fig. 2.17 Spatial distributions of h_{Max} for (a) P = 0.002 and (b) P = 0.0001. 38

Fig. 2.18 Spatial distribution of V_{Max} for (a) P = 0.002 and (b) P = 0.001..... 39

Fig. 2.19 Spatial distribution of M_{Max} for (a) P = 0.002 and (b) P = 0.001..... 40

Fig. 2.20 Spatial distribution of T_h for (a) P = 0.002 and (b) P = 0.001. 41

LIST OF FIGURES (Continued)

Figure Page

Fig. 3.1 (a) Regional map of Cascadia Subduction Zone with numerical model grids and (b) C-Grid bathymetry. Dotted and dashed lines in are 3 m and 5 m elevation contours from the MHW. 56

Fig. 3.2 Aerial photos of Seaside, Oregon (images modified from Google Earth). 57

Fig. 3.3 Flow chart of the probabilistic tsunami damage estimation process. 57

Fig. 3.4 Example of the annual exceedance of the maximum inundation depth and momentum flux at Point 1. 59

Fig. 3.5 Spatial distributions of h_{Max} (top panels), and M_{Max} (bottom panels) from 1,000-year event at CSZ over the tax lot shapefile format at Seaside, OR. 60

Fig. 3.6 Examples and comparisons of two types of tsunami fragility curves using h_{Max} or M_{Max} as IMs. (a) fragility curve for 1 story wood structure (thin solid), 2 stories wood (thin dash line), 2 stories RC structure (thick solid), and RC structure more than 3 stories (thick dash) from S2013 model. (b) wood structure fragility curves developed with momentum flux. Thin solid line presents the wood structure fragility curve from Koshimura et al. (2009) which is converted to momentum flux, and each thin dash and think solid line presents the wood structure less than 5,000 ft^2 and greater than 5,000 ft^2 from FEMA model. (c) the fragility curve of the RC building with a moment frame and 1 – 3 floors level. Thin solid line present the both 'Moderate' and 'Extensive' damage state fragility curves, and the thick solid line presents the 'Complete' damage state fragility curve of FEMA model. (d) the fragility curve of RC building with a moment frame, 'Complete' damage state and 4 – 6 stories, but having four different Seismic Design Categories, Pre (solid, light), Low (dash, light), Moderate (solid, heavy), and High (dash, heavy). 68

Fig. 3.7 Building classification map for (a) building type, (b) building stories, and (c) building Seismic Design Code for detail portion of Seaside..... 72

Fig. 3.8 Spatial distribution of probability of complete damage from 1,000-year event using two types of fragility curves. (a) S2013 model, (b) detail, (c) FEMA model, and (d) detail). 75

Fig. 3.9 The map of tax lot parcels applied in the sensitivity test. Each dot presents the centroid of tax lot. Box indicates the unit width (50 m)..... 76

LIST OF FIGURES (Continued)

Figure Page

Fig. 3.10 Average probability of complete damage for (a) wood and (b) RC buildings with different tsunami events, 2,000-year (red square), 1,000-year (black triangle), and 500-year event (blue circle). (c) Total number of wood (circle) and RC (triangle) buildings parcels in each bin.. 77

Fig. 3.11 Average probability of complete damage for (a) wood and (b) RC buildings with different friction terms, n=0.02 (red square), 0.03 (black triangle), and 0.04 (blue circle).. 79

Fig. 3.12 (a) Building damage sensitivity to the building floor level information such as Low-Rise (blue circle), Mid-Rise (red triangle), and High-Rise (green square). Solid line presents the results from the correct floor level information. (b) the number of tax lot cells of different floor levels used for averaging in each bin. 80

Fig. 3.13 (a) Building damage sensitivity to the building floor level information with different SDCs assumptions: Pre and Low (blue circle), Moderate (red triangle), and High code (green square). Solid line presents the results from the correct SDC information. (b) the number of parcels use for bin averaging. 81

Fig. 3.14 Building damage sensitivity to fragility curve types for (a) wood and (b) RC structures. Symbols: the 1,000-year (solid) and 500-year event (dashed); S2013 model (black) and FEMA model (red). 83

Fig. 3.15 Summary of building damage sensitivity tests with standard error for 50% confidence interval for (a) Region A with wood (black lines, star symbols) and RC (red lines, circles) and (b) Region B for wood only (black lines, star symbols). 84

LIST OF TABLES

Tables Page

Table 2.1 Inversion models information and slip distribution parameters. 14

Table 2.2 Summary of recent events to update work of Murotani et al. (2013). 16

Table 2.3 Summary of slip distribution parameters and weighting factors 18

Table 2.4. Sub-fault information for Aleutian–Alaska–Cascadia Subduction Zone (ACSZ). 44

Table 3.1 Summary of developed fragility curve since 2004 Indian Ocean tsunami 62

Table 3.2 Summary of the comparison of two types of fragility curves 65

Table 3.3 Damage state (DS) comparisons 66

Table 3.4 Detail information of fragility curves 69

Table 3.5 Applied building classification standard using the ‘stat class’ in tax lot data of Seaside, OR. 71

Table 3.6 Seismic Design Codes applied for the buildings in Oregon State 73

Table 3.7 General number of buildings by type and region in detail area of Seaside (Fig 3.7a). 73

Table 3.8 Detailed number of buildings by type and region in detail area of Seaside (Fig 3.7a).. 73

1. Introduction

Over the past two decades, megathrust earthquakes and resulting tsunamis, such as the 2004 Indian Ocean tsunami, the 2010 Chile tsunami, and the 2011 Tohoku tsunami have generated catastrophic casualties and damage to the built and natural environments. The loss of life and damage is particularly severe for a near-field (local) tsunami because (1) the preceding earthquake is felt locally and causes significant damage and disorientation to the public, (2) the tsunami arrives to the coast in only tens of minutes resulting in short evacuation times, and (3) tsunami intensity is greater for the near-field locations because the energy of tsunami cannot be dispersed over the large ocean. The US Pacific Northwest coast is facing the threat of an earthquake and near-field tsunami from the Cascadia Subduction Zone (CSZ) along the converging area between Juan de Fuca Plate and North American Plate. The Juan de Fuca Plate generally moves in a northeast direction with the mean speed of 0.004 m/year (Heaton and Hartzell, 1986). It is sinking beneath the North American Plate, causing elastic potential energy to be accumulated between the two plates as it moves. This energy is released in megathrust earthquake events, which causes ground shaking that can be last for 3 to 5 minutes. The rapid motion of the seafloor results in the generation of a tsunami in both offshore and onshore directions. The last such megathrust event at the CSZ occurred on January 26, 1700, with a full rupture event along the entire 1,000 km length of the fault. The range of the moment magnitude (M_W) of that event is estimated to be 8.7 to 9.2 (Satake et al., 2003). The probability of the next event at the CSZ with M_W 9.0 has been estimated to be 17% in the next 50 years and 25% in the next 100 years (Goldfinger et al., 2012; Kulkarni et al., 2013).

Post-disaster surveys provide records of tsunami damage to the built environment (Jaffe et al., 2006; Rosetto et al., 2007; Mikami et al., 2012). These studies highlight the need for strategies to increase the resilience of communities to prepare and minimize damages and losses from future tsunami events. For the study of tsunami resilience, it is necessary to understand the hazard, to estimate how the systems in the built environment will respond, and to predict the recovery processes of these systems. The five most critical civil infrastructure systems are buildings, transportation networks (bridges and roads, harbors, railways, and airports), water and wastewater networks, energy networks (electric power and fuel) and communication networks (radio, landlines and wireless). To mitigate or minimize the damage and to improve the resilience

against future tsunami events, it is important to evaluate both the future tsunami hazards and the corresponding damage and loss to the engineered systems.

However, both the hazard and damage estimations contain uncertainties due to the randomness of the tsunami generation and due to the modeling complexity of how the systems interact and are damaged by the tsunami hazard. Specifically, the tsunami hazard analysis comprises three steps: tsunami *generation*, the connection between the fault displacement and the resulting displacement of the water; *propagation*, how the tsunami wave travels from the source through the open ocean; and *inundation*, the overland flow of water to the maximum limit of uprush and the return flow of water back to the sea. Each the three steps have some implied uncertainties and can be classified as either *aleatory* or *epistemic* uncertainty. Aleatory uncertainty refers to the uncertainty generated from the randomness of nature, such as the magnitude of earthquake and the fault slip distribution or the condition of the tide at the time of tsunami event, which could not be predicted and minimized (Geist and Parsons, 2006). Epistemic uncertainty refers the uncertainty involved in our methodology of tsunami analysis and the limited knowledge about tsunamis, such as the way to define the initial deformation of ground motion from earthquake or the accuracy of the computation model for generation, propagation or inundation. We can minimize the epistemic uncertainty through the improvement of our analysis methods. Epistemic uncertainties of tsunami propagation are generally considered to be small relative to the uncertainties of tsunami inundation because the turbulent overland flow is more complex than the irrotational propagation of long waves through the open ocean.

A major research theme of this work is to understand the relative importance of the aleatory uncertainty in the tsunami hazard to the epistemic uncertainties in the inundation modeling and in the characterization of the built environment. These processes are important in determining the probability of building damage conditioned on a full-rupture CSZ event. In considering community resilience, life safety is more important than building damage; however, predicting tsunami evacuation and the resulting mortality rate is beyond the scope of this project. In any case, the arrival time of the tsunami is a critical parameter in tsunami evacuation dynamics, so we track this intensity measure in our analysis. The earthquake preceding the tsunami event is also important for community resilience because the local ground shaking can affect the local evacuation through unplanned network disruption and can lead to damage to the engineered systems. However, there is already a large body of knowledge related to seismic

damage, and we do not include direct earthquake damage. For this work, we performed probabilistic tsunami hazard and damage assessment of the built environment with a community scale, using the coastal city of Seaside, Oregon, as a test bed for our work. As shown in the flow chart in Fig. 1.1, we separate the work into two parts: tsunami hazard assessment (Chapter 2) and tsunami damage assessment (Chapter 3).

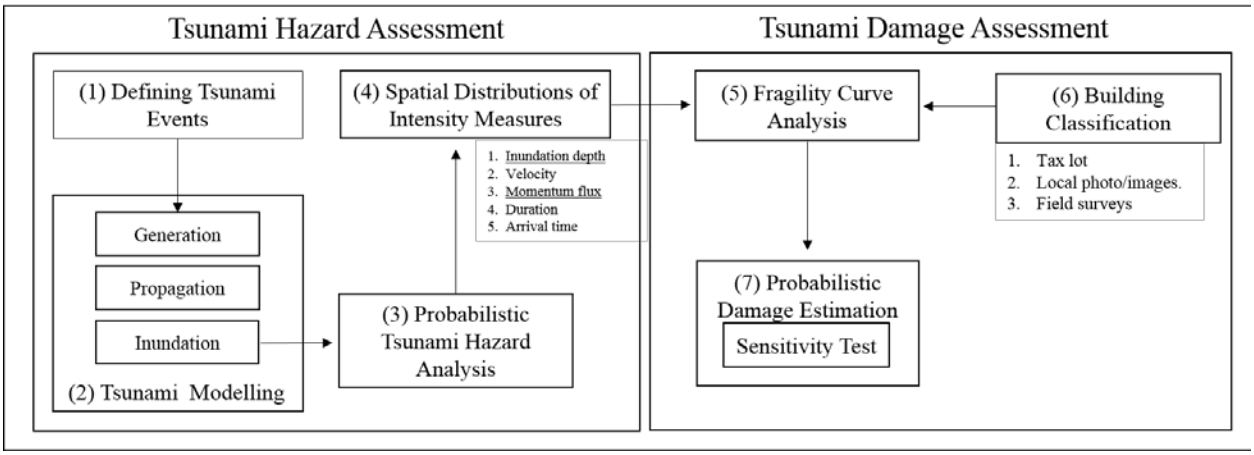

Fig. 1.1 Flow chart of the probabilistic tsunami damage estimation process.

In Chapter 2, we define the tsunami event at the CSZ by implementing a new fault slip distribution model. This model simplifies the randomness of moment magnitude, peak slip location, and the slip shape parameterized as a Gaussian distribution. We applied a total of 72 CSZ event scenarios to represent aleatory uncertainty, using a linear elastic dislocation model (Okada, 1985), and examine the resulting tsunami hazards. We model the tsunami inundation results with a Poisson arrival process to estimate the annual exceedance probability of five tsunami intensity measures (IMs): the maximum inundation depth, h_{Max}, maximum velocity, V_{Max}, maximum momentum flux, M_{Max}, the arrival time exceeding a 1 m inundation depth, T_A, and the total duration exceeding a 1 m inundation depth, T_h. The research theme of Chapter 2 is to understand how earthquake magnitude, peak slip location, and slip distribution can affect the tsunami intensity on land. A related research question concerns how to estimate the annual probability of exceedance for different intensity measures and how these intensity measures vary with the annual probability of exceedance and local bathymetric and topographic conditions.

In Chapter 3, we utilize the spatial distributions of two IMs, the maximum inundation depth and the maximum momentum flux, to estimate building damage with a fragility curve analysis at a community scale. We collect the building information with tax lot data, Google

Street View, and field reconnaissance (rapid visual screening, RVS) to classify buildings at Seaside, Oregon. This classification is used to match the building class to the existing fragility curves. The curves are developed for different damage states (from minor to complete damage), building characteristics (material, floors, or year of built) and types of IMs (inundation depth and momentum flux). The research theme of Chapter 3 is related to the tsunami intensity measures with the expected damage probability using a fragility curve analysis. There are several related research questions: How best to characterize the building classes, given that there can be several thousands of buildings of different construction type in a community? How does the spatial variation of different intensity measures affect the damage estimates? How do the uncertainties of tsunami hazard intensity, the building classification, and fragility curve affect the damage estimates? This last question, in particular, combines the work of Chapter 2 and Chapter 3 to investigate the overall research theme related to the relative importance of the aleatory and epistemic uncertainties in the modeling of tsunami damage to buildings conditioned on a full-rupture CSZ event.

Chapter 2 and 3 contain the majority of this dissertation work and are in the form of manuscripts to be submitted to *Coastal Engineering* and to *Natural Hazards*, respectively. For completeness of each manuscript, some of the literature review is repeated. Chapter 4 provides a general summary of these two works and makes suggestions for future work, particularly for combining this work with an earthquake engineering damage analysis. Chapter 5 (Appendix) provides two manuscripts related to tsunami inundation for which Hyoungsu Park is the lead author and which were published during the course of his Ph.D. dissertation. The first manuscript (Appendix A) is a comparison of laboratory data to numerical model using the COULWAVE model for the complex tsunami inundation through the built environment considering the effects of buildings. The second manuscript (Appendix B) uses COULWAVE to develop an empirical tsunami run-up model and demonstrates the applicability of this model to the 2011 Tohoku tsunami.

2. Probabilistic Assessment of Near-field Tsunami Hazards: Arrival Time, Inundation Depth, Velocity, Momentum Flux, and Duration Applied to Seaside, Oregon. [1]

2.1 Abstract

The generation, propagation and inundation for a probabilistic near-field tsunami hazards assessment (PNTHA) at the Cascadia Subduction Zone (CSZ) are analyzed numerically. For the tsunami hazard assessment, a new method is presented to characterize the randomness of the fault slip in terms of the moment magnitude, peak slip location, and a fault slip shape distribution parameterized as a Gaussian distribution. For the tsunami inundation resulting from the seismic event, five tsunami intensity measures (IMs) are estimated: (1) the maximum inundation depth, h_{Max}, (2) the maximum velocity, V_{Max}, (3) the maximum momentum flux, M_{Max}, (4) the initial arrival time exceeding a 1 m inundation depth, T_A, and (5) the duration exceeding a 1 m inundation depth, T_h, and presented in the form of annual exceedance probabilities conditioned on a full-rupture CSZ event. The IMs are generally observed to increase as the moment magnitude increases, as the proximity of the peak slip becomes closer to the study area, and as the distribution of fault shape narrows. Among the IMs, the arrival time (T_A) shows a relatively weak sensitivity to the aleatory uncertainty while the other IMs show significant sensitivity, especially M_{Max}. It is observed at the shoreline that M_{Max} increases by an order of magnitude from the 500-year to the 1,000-year event, while h_{Max} increases by a factor of 3, and T_A decreases by only factor of 0.05. The intensity of IMs generally decreases inland, but there are also varying dependencies on bathymetry. For example, a shorter inundation duration, T_h (< 10 min) is observed at the higher ground level (z > 3 m) while a longer T_h (~100 min) is observed near the river and creek.

[1] Hyoungsu Park and Daniel T. Cox. “Probabilistic Assessment of Near-field Tsunami Hazards: Arrival Time, Inundation Depth, Velocity, Momentum Flux, and Duration Applied to Seaside, Oregon,” in preparation for *Coastal Engineering*.

2.2 Introduction

2.2.1 Near-field tsunami hazards at the CSZ

Tsunamis caused by megathrust subduction zone events have a small frequency of occurrence relative to other coastal hazards such as hurricanes, but these events can result in significant loss of life and extensive damage to coastal regions. Loss and damage are particularly serious problems for near-field (local) tsunamis because the tsunami energy is concentrated in a small area and because the arrival time is only tens of minutes after the event, limiting the evacuation time. The destructive power of near-field tsunamis has been reported for recent disasters such as the 2004 Indian Ocean tsunami (e.g., Jaffe et al., 2006; Rosetto et al., 2007) and the 2011 Tohoku tsunami (e.g., Mikami et al., 2012).

The US Pacific Northwest coast is facing the similar threat of an earthquake and near-field tsunami from the Cascadia Subduction Zone (CSZ) along the converging area between Juan de Fuca Plate and North American Plate. The Juan de Fuca Plate generally moves in a northeast direction with the mean rate of 0.004 m/year (Heaton and Hartzell, 1986). It is sinking beneath the North American Plate, and as it moves, it causes elastic potential energy to be accumulated between the two plates. This energy is released in megathrust earthquake events, which cause ground shaking that can be last for 3 to 5 minutes. The rapid motion of the seafloor results in the generation of a tsunami in both offshore and onshore directions. The last such megathrust event at the CSZ occurred on January 26, 1700, with a full rupture event along the entire 1,000 km length of the fault. The range of the moment magnitude (M_W) of that event is estimated to be 8.7 to 9.2 (Satake et al., 2003). The probability of the next event at the CSZ with M_W 9.0 has been estimated to be 17% in the next 50 years and 25% in the next 100 years (Goldfinger et al., 2012; Kulkarni et al., 2013).

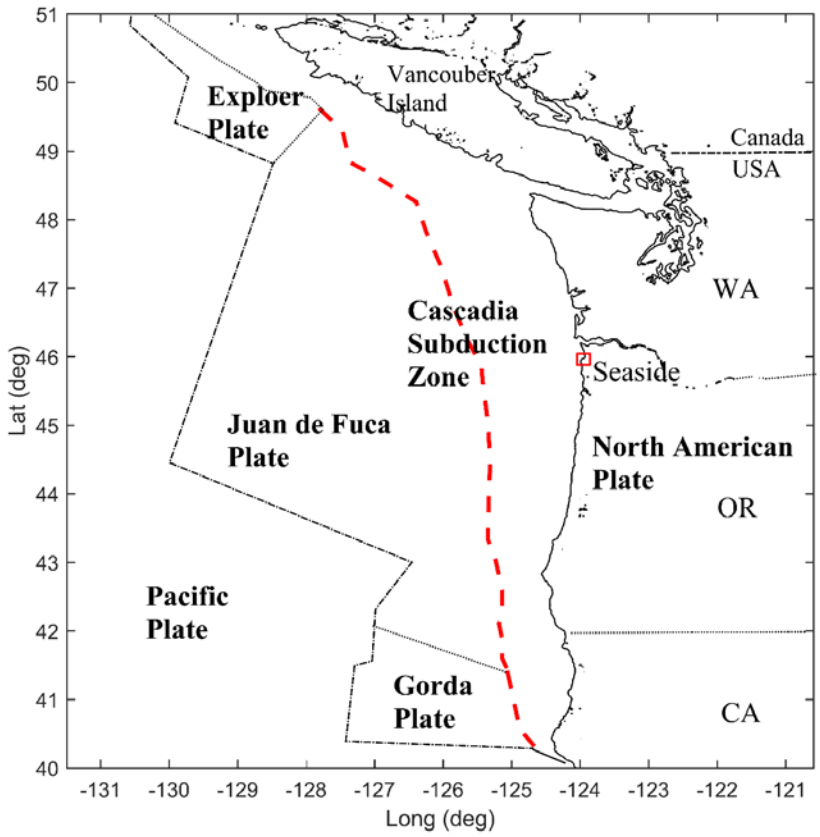

Fig. 2.1 Regional map of Cascadia Subduction Zone (CSZ) and study area, Seaside, Oregon.

Community resilience is generally defined as the ability of a community to absorb and recover from a natural hazard (e.g., Bruneau et al., 2003). Resilience involves many social, economic, political, ecological, and civil engineering infrastructure systems. In general, there are five infrastructure systems considered to be most important to community resilience: buildings, transportation networks (bridges and roads, harbors, railways, and airports), water and wastewater networks, energy networks (electric power and fuel) and communication networks (radio, landlines and wireless). Similar to the analysis for other hazards such seismic or high wind, we assume that the response of each system can be evaluated stochastically using a fragility analysis based on the intensity measures (IMs) of tsunami. The most common IMs are the tsunami arrival time, maximum tsunami inundation or run-up, and tsunami inundation depth. These IMs have been used for tsunami evacuation planning, to develop tsunami inundation maps (Tsunami Pilot Study Working Group, 2006; Gonzales et al., 2009; Priest et al., 2010), and to evaluate the building damages or economic loss (e.g., Dominey-Howes et al., 2010; Wiebe and Cox, 2014).

Although arrival time and the extent of inundation have proven useful for evacuation planning, the response of the complex built environment and the five infrastructure systems described earlier requires a more detailed understanding of the IMs within the inundation zone. In case of building damage for example, there are several types of forces on structures induced by the tsunami: hydrodynamic force (drag force imposed by quasi-steady flow), hydrostatic force, buoyant force, impulsive force (due to the transient bore or leading edge of the tsunami), debris impact force, debris damming force, and uplift force (FEMA P-646, 2012). Although these individual forces can be analyzed for structures individually, it is not currently possible to apply these methods at a community scale. Therefore, it is advantageous to apply a fragility analysis, or estimate a probable level of damage for a certain class of structure, at a community scale comprising thousands of individual buildings.

The IMs for estimating tsunami damage have limited availability compared to seismic IMs such as peak ground acceleration due to the complexity of tsunami analysis. Generally, the analysis process comprises of three steps: generation, propagation, and inundation. The propagation step can be considered a “solved problem” in that the tsunami motion in the open ocean is well-described by conventional long wave theory (Titov et al., 2005). The generation and inundation steps, however, contain uncertainties which are classified as either epistemic or aleatory uncertainty. Epistemic uncertainty refers the error involved in our modeling methodology, such as the way to define the initial deformation of the ground motion from the earthquake such as slip, strike, dip, rake, and depth (Goda et al., 2014) or in the accuracy of our computation tsunami inundation models. Thus we can minimize the epistemic uncertainties through the improvement of our modelling methodology. On the other hand, aleatory uncertainty generally arises from the randomness of nature, such as the fault slip distribution of earthquake event, the location of epicenter and hypocenter, or the condition of the tide at the time of tsunami event (Geist and Parsons, 2006). For example, the location of the peak fault slip and distribution of the slips played a significant role in determining the local intensity of the tsunami hazard along the east coast of Japan for the 2011 Tohoku event. The run-up was generally larger for the Iwate and Miyagi prefectures which were in closer proximity to the peak fault slip compared to the smaller run-up observed for Aomori, Fukushima, and Miyagi prefectures located further from the peak (Mori et al., 2011). Of course, local bathymetric and topographic effects are played a role in determining the maximum run-up elevations (e.g., Park et al., 2015; see Appendix A).

2.2.2 Previous tsunami studies at CSZ

Geist and Parsons (2006) performed a probabilistic tsunami hazard analysis (PTHA) using both far-field and near-field tsunami sources to estimate the run-up. They utilized 100 randomized slip distributions to account for the aleatory uncertainties (Geist, 2005) of the near-field tsunami conditioned on a M_W 9.0 event. Their study was intended to provide a probabilistic run-up or Peak Nearshore Tsunami Amplitude (PNTA) along the West Coast of the US. González et al. (2009; see also Tsunami Pilot Study Working Group, 2006) used a probabilistic seismic hazard assessment (PSHA) methodology to provide the maximum tsunami inundation map. This study provided inundation depths in terms of an annual probability of exceedance, such as 100 or 500-year event, at Seaside, Oregon. They utilized 14 historic tsunami events as far-field tsunami sources and one near-field tsunami source from the CSZ composed of 12 scenarios. Priest et al. (2010) conducted a PTHA for Cannon Beach, Oregon, in which they provided the confidence levels for their tsunami inundation map as inferred from expert opinion of a 10,000 year record of turbidite events along the CSZ (Goldfinger et al., 2012). They used 25 deterministic scenarios of near-field sources at the CSZ, and two far-field sources in Alaska. In a similar study, Witter et al. (2013) developed inundation maps for Bandon, Oregon, classified into five sizes (S, M, L, XL, and XXL) based on the historical turbidite data (Goldfinger et al., 2012). Both studies utilized a 3-D dislocation model (Wang et al., 2003) of the CSZ for the initial tsunami slip condition and a numerical inundation model (Zhang et al., 2008) to estimate tsunami hazards. They only reported the maximum limits of inundation and the inundation depth as the tsunami IMs for each representative scenario.

2.2.3 Objectives of this study.

In this study, we perform a probabilistic near-field tsunami hazard assessment (PNTHA) conditioned on the near-field CSZ event because the resulting tsunami hazard is more relevant to life safety and damage to the built environment compared to far-field tsunamis. We examine the impact of aleatory uncertainty on five intensity measures (inundation depth, velocity, momentum flux, arrival time, and duration of inundation). There are four major objectives of this study:

1) Provide the framework for probabilistic near-field tsunami hazard assessment (PNTHA) at CSZ including aleatory uncertainty, originated from the randomness of the event magnitude, peak slip location, and fault slip distribution.

2) Introduce a new method to determine a fault slip distribution parameterized as a Gaussian distribution.
3) Quantify tsunami hazard intensity measures (IMs): the maximum inundation depth, h_{Max}, velocity, V_{Max}, momentum flux, M_{Max}, the arrival time of exceeding 1 m inundation depth, T_A, and the total duration of exceeding 1 m inundation depth, T_h.
4) Evaluate the annual exceedance probability of each IM, and provide the spatial distribution of IMs over the inundation region.

These objectives are achieved in the following sections. Section 2.3 introduces the new method to define fault slip distributions to provide the model scenarios utilized in this study. Section 2.4 introduces the setup of the tsunami model for generation, propagation and inundation. This section also presents estimates of the five IMs at representative observation points. Section 2.5 introduces the methodology of probabilistic near-field tsunami assessment and provides the result including probabilistic tsunami hazards map of Seaside, Oregon, as a test location. Section 2.6 discusses the limitations of the current work, compares to previous studies, and discusses possible future work. Finally, Section 2.7 provides a general summary and conclusion.

2.3 Tsunami generation model

Generally, the input source condition for tsunami models is given as an initial surface water displacement. The Okada (1985) model, which is based on the linear co-seismic dislocation of fault slips, is conventionally used for many tsunami generation models. The initial surface displacement is assumed to occur simultaneously along the fault. In this section, we review the possible earthquake fault slip patterns based on inversion models of historic tsunami events, and we parameterize those complex fault slips to provide a general format for the probabilistic model.

2.3.1 Inversion model and Gaussian distribution

Inversion models provide a co-seismic fault slip distribution over the rupture area where the significant dislocations of faults have occurred due to the earthquake. This motion triggers a tsunami event. Inversion models are comprised of a finite number of sub-faults with the relevant geologic information (slip, strike, dip, rake, and depth) determined for each sub-faults, and apply

a Green's function approach to find the slip distribution that has the minimum error between observation and model (Fujji and Satake, 2007).

To evaluate the general form of the fault slip distribution triggers a tsunami event, we examine the inversion models of recent tsunami events. Fig 2.2 shows the fault slip distributions of inversion models (Fig 2.2a, c, and e) and the general slip distributions (Fig 2.2b, d, and f). Fig. 2.2a and c presents the fault slip distribution of inversion models for 2011 Tohoku tsunami from Shao et al. (2013) and Hayes (2011), respectively, and Fig. 2.2e presents the inversion model for the 2010 Chile tsunami from Fujii and Satake (2013). The length of faults along Y' is rupture length (L) and the length of fault along X' is rupture width (W). To characterize the fault slip distribution, we examine the cross-profile of fault slip distribution of each sub-fault transect along Y'. We normalized each fault slip (D) by the peak fault slip (D_P) at each transect, and plot it against the normalized Y' by the sub-fault length (dL). The blue dotted lines are the cross-profiles having relatively large fault slips, and the black dotted line is the cross-profile of the peak slip (D_P) among them.

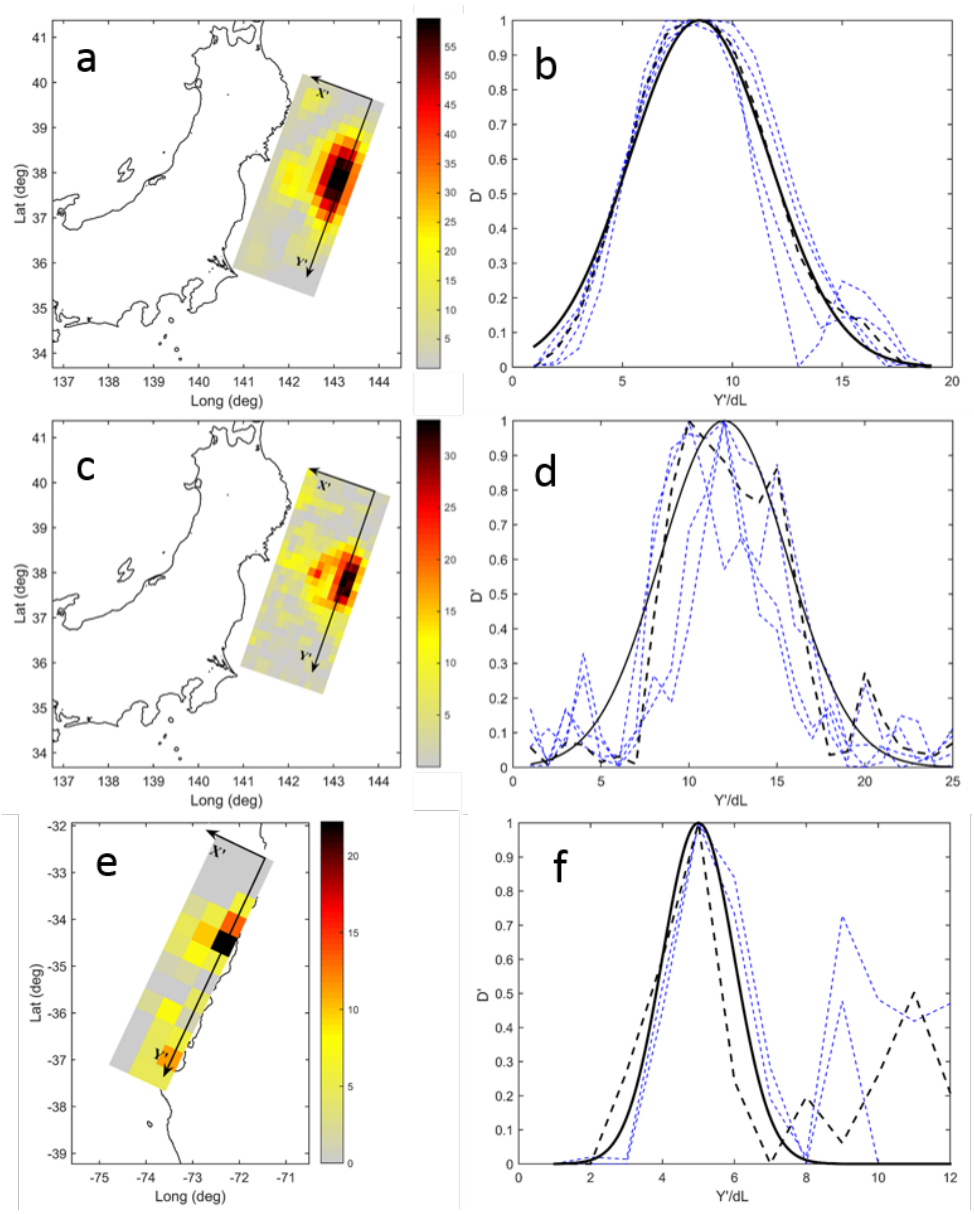

Fig. 2.2 The left panels show fault slip distributions of inversion models for 2011 Tohoku tsunami from (a) Shao et al., 2013 and (c) Hayes, 2011, and (e) for 2010 Chile tsunami inversion model from Fujii and Satake, 2013. The right panels show the cross-profiles of fault slip distribution from each inversion model. Each blue dashed lines in panel b, d, and f presents the cross-profile of normalized fault slip (D') along the strike direction (Y'/dL), and thick black dash line the fault slip distribution at the peak slip transect. The solid line presents and the fitting curve for cross-profiles with a Gaussian distribution form (Eq. 1).

The figure shows that the normalized fault slip distribution along each transect is generally symmetric at the peak slip, and allows us to parameterize the fault slip shape using a Gaussian distribution. The following probability density function is applied to find the fitted curve (solid line) in Fig. 2.2b, d, and f

$$f\left(Y'/dL \mid \alpha,\beta\right)=\frac{1}{\beta\sqrt{2\pi}}\exp\left(\frac{-\left(Y'/dL-\alpha\right)^2}{2\beta^2}\right) \quad (1)$$

where α and β are the slip distribution parameters of the fitted curve relating to the mean and standard deviation, respectively, of the slip shape along the strike direction (Y'). Parameter α controls the location of the peak slip along Y'. Since we defined Y' as the distance of the rupture length from the north boundary to the south, the distance of the peak slip from the north boundary increases as α increases. Parameter β controls the width of curve along Y'. As β increases, the shape of slip is wider and vise-versa.

Since each inversion model used by the investigators consisted of different sizes for the unit sub-fault, we normalized the distance of the rupture length (Y') by a uniform rupture length, 100 km, to compare the inversion model results at the same scale. We then replace β with β' as a slip shape parameter to indicate this change. Similarly, we introduce α' which is α normalized by the parameter L/dL such that the location parameter ranges $0 \leq \alpha' \leq 1$. When α' is 0.5, the peak slip is located at the center of the rupture area, and when α' is close to zero or unity, the peak slip is near the northern or southern boundary, respectively.

Table 2.1 summarizes seven cases of the tsunami inversion models and the corresponding slip distribution parameters, α′ and β' developed for this study. We limited our study by selecting recent tsunami events whose moment magnitudes were greater than 8.1 and for which we had sufficient access to the inversion model data published in the literature. Generally, both the rupture area ($S = LW$) and the peak slip displacement (D_P) increase as M_W increases. Interestingly, D_P shows a significant deviation for the same tsunami events (2011 Tohoku, v1, 2, 3) while the rupture area (S) shows small deviation. These differences arise from the different inversion model sources such as seismic, geodetic or tsunami data (Koketsu et al., 2011). A more detail relationship between the moment magnitude and rupture area will be examined at Subsection 2.3.2. For the Kuril, Chile and Tohoku tsunami, α' ranges from 0.4 to 0.6, and for the Indian Ocean tsunami the peak slip was located on southern boundary of rupture area ($\alpha' = 0.92$). The widest slip width was found for the 2004 Indian Ocean tsunami ($\beta' = 2$ or 6), and the three different versions of 2011 Tohoku tsunami show the similar range of β' (0.62 – 0.81). On the other hand, the two different versions of 2010 Chile tsunami show large deviation of slip width ($\beta' = 0.25$ and 0.75).

Table 2.1 Inversion models information and slip distribution parameters

Tsunami	M_W [-]	D_P [m]	L [km]	dL [km]	W [km]	dW [km]	α' [-]	β' [-]	Fig. 2.3	Reference
2004 Indian Ocean	9.3	30	1,400	100	200	100	0.92	2 or 6	(1), (2)	Fujji & Satake, 2007
2007 Kuril	8.1	20	200	8	40	5	0.46	0.13	(8)	Ji, 2015a
2010 Chile, v1	8.8	13	600	50	187	17	0.63	0.74	(5)	Shao et al., 2015
2010 Chile, v2	8.8	22	600	50	150	50	0.42	0.25	(7)	Fujji & Satake, 2013
2011 Tohoku, v1	9.0	32	600	25	260	20	0.46	0.81	(3)	Hayes, 2011
2011 Tohoku, v2	9.1	59	500	25	200	20	0.42	0.62	(6)	Shao et al., 2011
2011 Tohoku, v3	9.0	69	550	50	200	50	0.50	0.75	(4)	Satake et al., 2013

Fig. 2.3a compares the Gaussian distributions developed for the data sets summarized in Table 2.1. We set $\alpha' = 0$ for all cases, and we plot the normalized slip, D', versus the dimensional rupture length, L. The labels (1) to (8) on Fig. 2.3a indicate the ascending values of β' in Table 2.1. The estimated range of rupture length from β' in Table 2.1 shows significant variations depending on the tsunami.

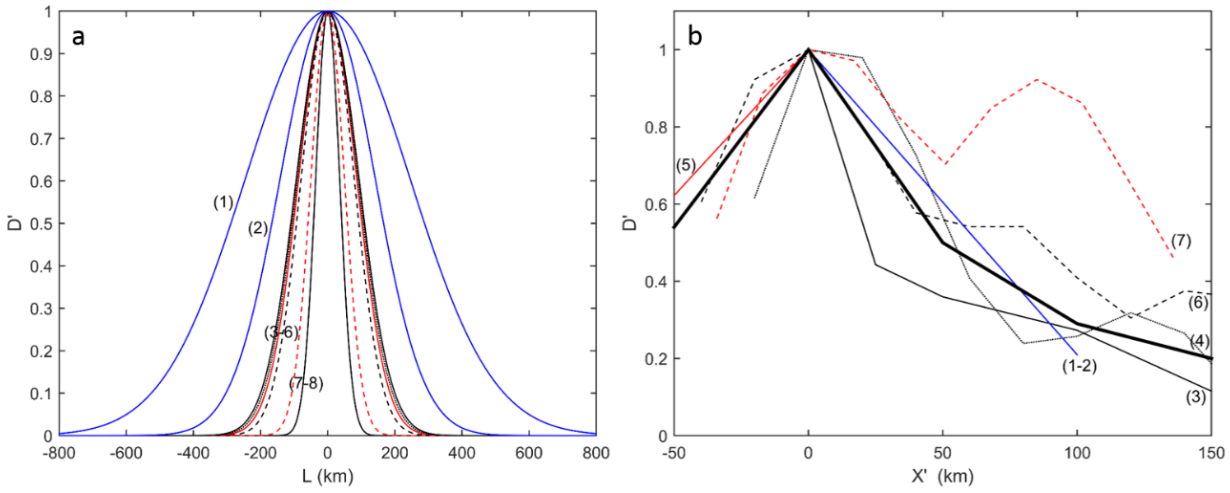

Fig. 2.3 (a) Gaussian distribution curves fitted for the tsunami inversion models along the strike direction and (b) the decay rate of slips along the dip slip direction. Numbered lines correspond to events listed in Table 2.1. Solid thick line in (b) presents the average of all decay rates of slips excluding (7).

Fig. 2.3b shows the slip decay in the dip slip direction (positive X' is directed onshore). We calculate the sum of the slip for each transect and then normalized these by the maximum sum of transect. The origin of X' is at along the maximum sum of transect. Overall, the normalized sum of each transect decays shoreward, except for the 2010 Chile v2 event (line (7) in Fig 2.3b). The thick line is the average normalized slip for all cases excluding the 2010 Chile v2. For simplicity, we assume that all normalized slip distributions along Y' have the same normalized slip distribution as the peak slip as shown in Fig. 2.2b. We can then extend the peak slip distribution to the other transects by multiplying the average slip decay ratio, thereby

generating a 3-D slip distribution. Application of this method will be discussed in the context of the CSZ event in Subsection 2.3.3.

2.3.2 Relation between earthquake intensity and rupture area

The seismic moment (M_0) and moment magnitude (M_W) are representative scale factors to parameterize the intensity of an earthquake. M_0 is defined as

$$M_0 = \mu S \bar{D} \tag{2}$$

where μ is the shear modulus of the rock adjacent to the fault plane and S and $\bar{D}$ are the rupture area and mean slip over the rupture area, respectively. The increase of both rupture area and slip displacement varies linearly with the seismic moment. The moment magnitude M_W is related to the seismic moment M_0 by the following relationship (e.g., Hanks and Kanamori, 1979).

$$M_W = \frac{2}{3}(\log_{10} M_0) - 10.7 \tag{3}$$

Murotani et al. (2008) found a positive correlation between rupture area and seismic moments from past tsunami events in Japan, suggesting a logarithmic fit between seismic moments and rupture area. However, the data for the fitting curve originated for relatively small magnitude earthquakes (M_W < 8.5). Recently, Murotani et al. (2013) modified their previous work by including larger events (M_W > 8.5), and their modified fitting curve is

$$S = 1.34 \times 10^{-10} M_0^{2/3} \tag{4}$$

Fig. 2.4 shows the relation between the rupture area and the moment magnitude. The solid line presents the fitted curve of Murotani et al. (2013) given by Eq. 4. The dots and crosses show the data from Murotani et al. (2008) and Murotani et al. (2013), respectively. Since the work of Murotani mostly focused on earthquakes in Japan, we add an additional 11 inversion model results from the studies listed in Table 2.2 (asterisk) using a constant shear modulus (μ = 4×10^{10} N/m^2). We find a similar fitting curve (dotted line) using the same format of Murotani et al. (2013) which can be given by

$$S = 1.20 \times 10^{-10} M_0^{2/3} \tag{5}$$

Both Eq. 4 and 5 indicate that there is a positive correlation between rupture area and seismic moment. We plot two additional curves as a possible upper and lower limits by multiplying factors 2.0 and 0.5, respectively, to Eq. 4. We find that most inversion model results are located between these lower and upper limits (dashed lines in Fig. 2.4). If we assume that the next

earthquake on the CSZ has a specific rupture area, we can estimate a reasonable range of the intensity of the earthquake on the CSZ from Fig. 2.4. It is reported that the maximum full rupture length of the CSZ is approximately 1,000 km from Vancouver Island to northern California, with a rupture width of approximately120 km (Wang et al., 2003, Witter, et al., 2013). With the given rupture area at the CSZ (filled circle at Fig. 4), the corresponding M_W is nearly 9.0. If we consider the both upper and low limits of rupture area (dashed lines), the range of M_W for the CSZ full-rupture event is approximately $8.6 < M_W < 9.3$. This range is similar to that estimated by Satake et al. (2003) for the most recent CSZ event of 1700 and for the range of values reported by Witter et al. (2013).

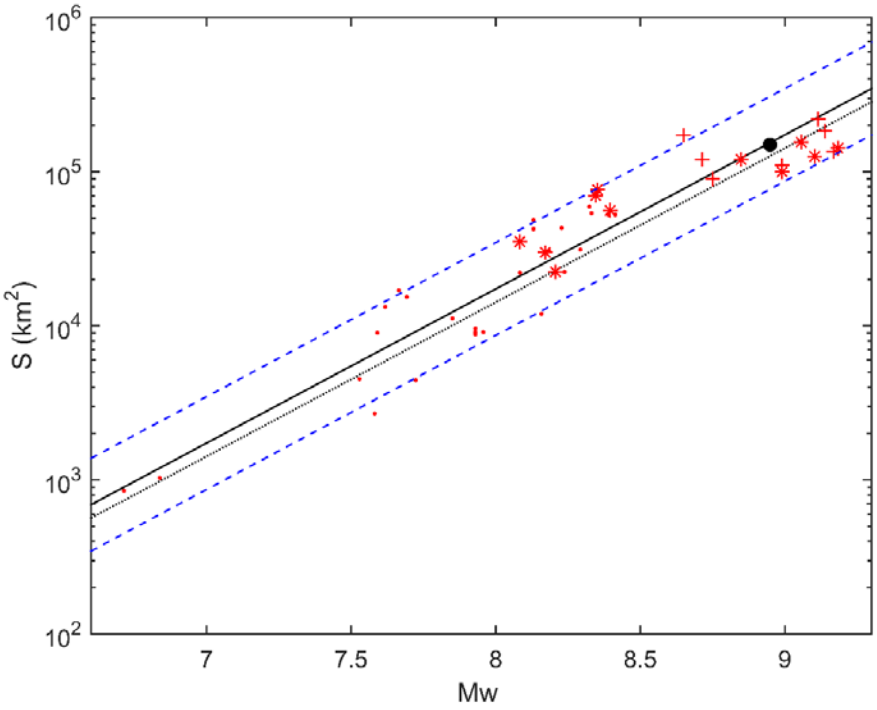

Fig. 2.4 Scaling relationship of rupture area with respect to the moment magnitude. Solid line is the fitting curve (Eq. 4) and dotted line is updated fitting curve in this study (Eq. 5). Blue dashed lines show upper and lower bounds by multiplying Eq. 4 by 2.0 and 0.5, respectively. Red dots present the data from Murotani et al. (2008), and cross symbols are data from Murotani et al. (2013). Asterisk symbols present the data by authors from Table 2.2, and black solid circle indicates the maximum rupture area at the CSZ (1,000 km × 120 km).

Table 2.2 Summary of recent events to update work of Murotani et al. (2013).

Event	M_0 [10^{21} Nm]	M_W [-]	S [10^3 km^2]	Reference
2003 Hokkaido	1.7	8.0	35.2	Yagi, 2004
2004 India Ocean	76.0	9.2	142.4	Grilli et al., 2007
2006 Kuril Island	5.0	8.3	56.0	Baba et al., 2009
2007 Kuril Island	2.6	8.2	22.4	Lay et al., 2009

2007 Solomon Island	2.3	8.2	30.0	Baba et al., 2008
2007 Southern Sumatra	4.2	8.4	70.0	Lorito et al., 2008
2007 Southern Sumatra	4.3	8.4	76.6	Ji, 2015b
2010 Chile	24.0	8.8	120.0	Shao et al., 2015
2011 Tohoku	49.0	9.0	156.0	Hayes, 2011
2011 Tohoku	57.5	9.1	125.9	Shao et al., 2011
2011 Tohoku	39.0	9.0	100.0	Ammon et al., 2011

2.3.3 Development of a new fault slip method

Our fault slip model for tsunami generation is parameterized by the moment magnitude of earthquake, M_W, the peak slip location, α', and the slip shape, β'. To generate possible near-field tsunami scenarios at the CSZ, we assume a full-rupture event with the moment magnitude in the range $8.6 < M_W < 9.3$. Although there are more frequent smaller intensity earthquakes at the CSZ ($M_W < 8.6$), especially near southern portion of the CSZ (Nelson et al., 2006), these slip distributions are concentrated on the southern portion and induce a relatively weaker impact on study area. Furthermore, we assume that the slip distributions will follow the Gaussian shape given in Eq. 1. We discuss the effect of the locations of peak slip and shape of slip for intensity of tsunami on Seaside in Subsection 2.4.3.

After determining the specific moment magnitude, (e.g. $M_W = 9.0$), we determine three slip shape (β') for each M_W scenarios. We calculate seismic moment (M_0) from Eq. 3, the potential rupture area (S) of the seismic moment from Eq. 4, and the mean slip ($\bar{D}$) from Eq. 2. To determine the slip shape (β') of the given rupture area limit (S), we set $\alpha' = 0$, and pick a reasonable β' as an initial trial. With both slip distribution parameters (α' and β') known and with fixed width ($W = 120$ km) for the CSZ, we can generate a single slip distribution along Y' at the peak slip transect. To generate a 3-dimension slip distribution, we extend the profile shape at the peak slip to other cross-profiles by scaling down the slip using an average decay rate of slip (solid line, Fig. 2.3b). The generated 3-dimension slip distribution has a dimensional rupture length and has non-dimension slip (D'). We multiply the mean slip ($\bar{D}$) to all slip conditions and calculate the seismic moment (M_0) of 3-dimension slip over the rupture area. We iterate this procedure until we find the desired seismic moment (e.g. $M_W = 9.0$) and determine the final β'. In this procedure, we use a constant shear modulus, $\mu = 4\times10^{10}\ N/m^2$. We also perform the same procedure to determine β' for both the upper and lower limit of S which ($2S$ and $S/2$, respectively) to obtain three possible slip shape parameters (β') for each moment magnitude.

2.3.4 Tsunami scenarios at the CSZ

We constrain the earthquake intensity in the range 8.6 < M_W < 9.3 from the relation between the maximum rupture area and moment magnitude shown in Section 2.2. This range of moment magnitude agrees with the range of CSZ events which occurred with a full-length rupture condition during the past 10,000 year (Goldfinger et al., 2012). To discretize the possible M_W conditions in this range, we consider three moment magnitudes M_W = 8.8, 9.0, and 9.2. Following the tsunami generation model procedure mentioned at Section 2.3, we calculate the three slip shape parameters (β') for each moment magnitude. We use eight possible locations for the peak slip (α' = 0.15, 0.25, 0.35, 0.45, 0.55, 0.65, 0.75, and 0.85). The full-length rupture length, L, is 1,000 km, and we exclude both the north and south boundary limits (α' = 0.05 and 0.95) as peak slip locations. A total of 72 scenarios (three moment magnitudes times three slip shapes times eight locations) are proposed here for the full-length rupture CSZ event. Fig. 2.5 shows the logic tree for a full-rupture CSZ event, and Table 2.3 lists the details of the model parameters.

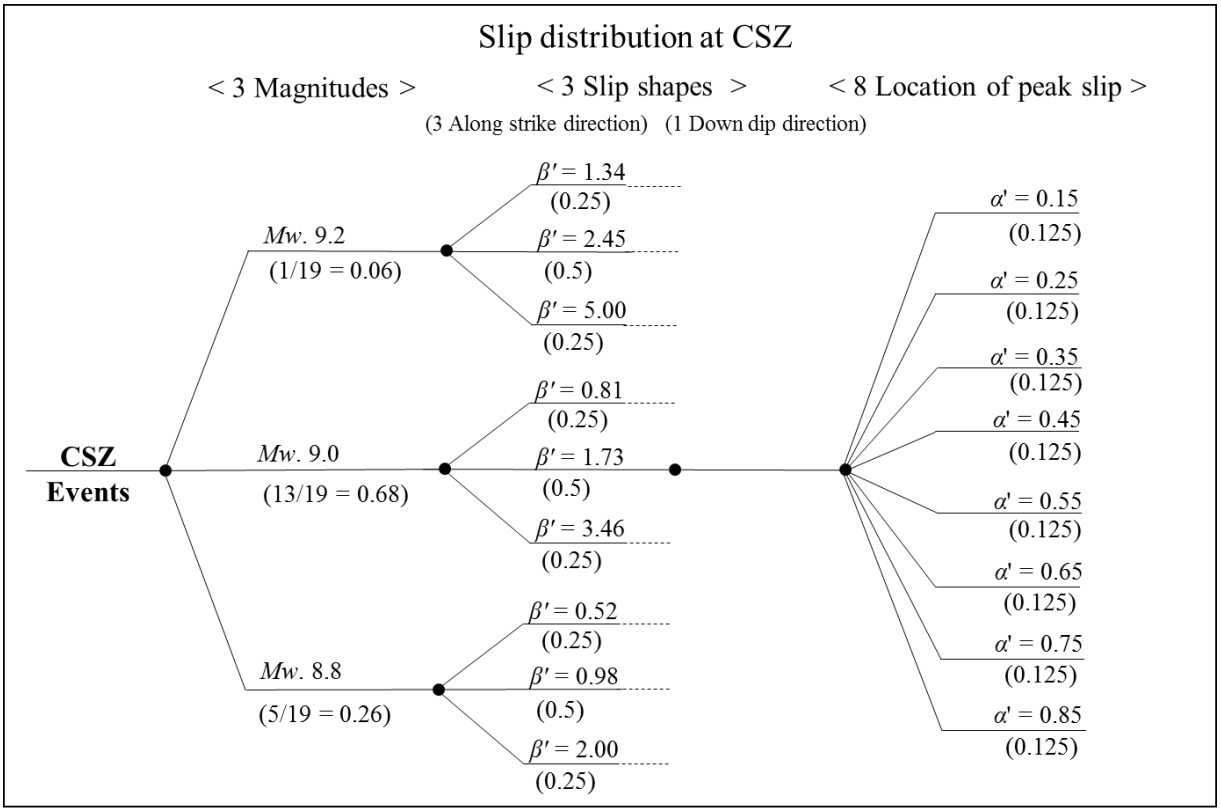

Fig. 2.5 Logic tree of the CSZ event at Seaside, OR.

Table 2.3 Summary of slip distribution parameters and weighting factors

M_W (P_W)	β' (P_W)	α' (P_W)	N_S

9.2 (0.06)	1.34 (0.25), 2.45 (0.5), 5.00 (0.25)	0.15 – 0.85 (0.125)	24
9.0 (0.68)	0.81 (0.25), 1.73 (0.5), 3.46 (0.25)	0.15 – 0.85 (0.125)	24
8.8 (0.26)	0.52 (0.25), 0.98 (0.5), 2.00 (0.25)	0.15 – 0.85 (0.125)	24

[a)] α' = 0.15, 0.25, 0.35, 0.45, 0.55, 0.65, 0.75, and 0.85

Since each of the 72 scenarios does not have an equal probability of occurrence, it is necessary to provide a weighting factor (P_W) for each scenario. During the past 10,000 years, a total of 19 full-length rupture CSZ events are considered to have occurred based on turbidite data (Goldfinger et al., 2012). The intensity of each of the 19 events was estimated from the density of turbidite (Priest et al., 2010; Goldfinger et al., 2012; Witter et al., 2103). Witter et al. (2013) suggested five sizes of earthquake intensity and an associated time interval: Small (300 years), Medium (425 − 525 years), Large (650 − 800 years), Extra-large (1,050 − 1,200 years), and Extra Extra-large (1,200 years). Of the 19 events, only one event is classified as Extra extra-large and Extra-large, and we relate this to a M_W 9.2 scenario. Thirteen events are classified as Medium and Large, and we relate these to M_W 9.0. The last five events are classified as Small, and we relate these to M_W 8.8. We applied weighting factors (P_W) based on these estimated occurrence rates, so the M_W 9.2, 9.0 and 8.8 scenarios has a weighting factor of 0.06 (1/19), 0.68 (13/19), and 0.26 (5/19), respectively.

In case of the weighting factors of slip shapes, we set 0.5 for the middle steepness shape which is estimated from the S (Eq. 4), and applied 0.25 for other two which are estimated from the upper and lower limits (2S, and S/2). In case of weighting factors for the peak slip location, we set an equal weighting factor (0.125) for all. These default weighting factors, particularly for slip shape and location are subjective and based on the opinions of the authors. The methodology can be re-weighted if sufficient data become available to determine the specific weighting factors for each scenario.

Fig. 2.6a, b, c shows examples of full-rupture scenarios at the CSZ for M_W 8.8, 9.0, and 9.2, respectively, for three slip shapes (β') at a given peak slip (α' = 0.35). The solid line represents the smallest β' which generates the narrowest slip shape per each M_W scenario. Blue dash and red dot line presents the middle and largest values of β'. As β' increases, the rupture length increases and correspondingly the peak slip decreases. This is significant, for example, because for a given moment magnitude as β' decreases, the resulting tsunami energy will be concentrated at a particular location along the CSZ. The range of peak slip among three slip

shapes were 10 − 40 m (M_W = 8.8), 15 − 54 m (M_W = 9.0), and 22 − 59 m (M_W = 9.2). Overall, the displacement of slip over the rupture area increases as the moment magnitude increases. Note that in implementing this methodology in the next section, the continuous curves shown in Fig 2.6 are discretized at each sub-fault, resulting in a stair-step distribution, similar to what is shown in Fig 2.2a, c, e.

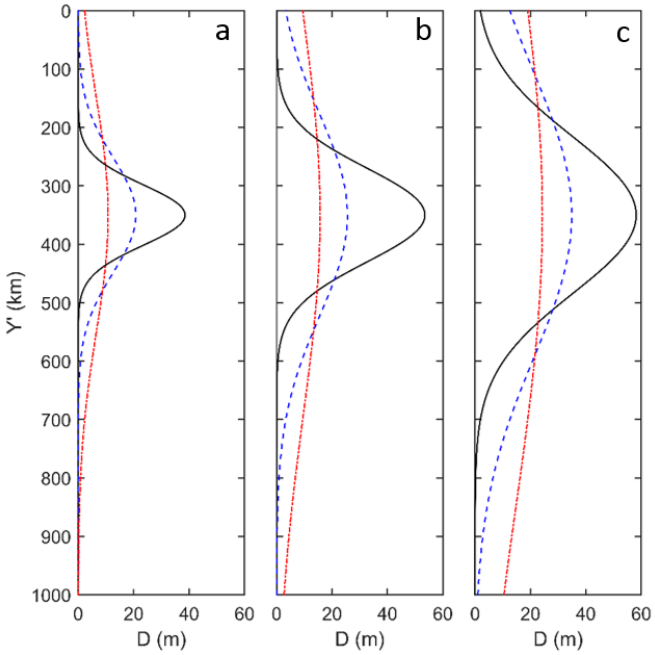

Fig. 2.6. Examples of the slip shapes at peak slip transect for (a) M_W 8.8, (b) M_W 9.0, and (c) M_W 9.2 with α'=0.35. Solid line presents the smallest β' among three β' per each M_W scenarios. Blue dash and red dot line presents the middle and largest β', respectively.

2.4 Numerical model setup for tsunami generation, propagation, and inundation

2.4.1 Numerical models

In this study, we use the ComMIT/MOST model for the tsunami generation and propagation analysis (Titov et al., 2011), and utilized COULWAVE (Lynett et al., 2002) for the inundation analysis. Fig. 2.7 shows the numerical model bathymetries and grid maps applied for this study. The ComMIT/MOST model is based on the non-linear shallow water equations implemented with a finite difference scheme. The tsunami generation model is embedded using the Okada (1985) elastic dislocation model. The ComMIT/MOST model has been verified with benchmark tests based on field observations and laboratory experiments (Synolakis et al., 2008). The model is maintained by the NOAA Center for Tsunami Research (NCTR) is used for

tsunami forecasting and mapping due to its accuracy and high calculation speed (Titov et al., 2011). It also has been applied for the PTHA study in Seaside, Oregon, by González et al. (2009) and for the damage estimation of building at Seaside for a set of hypothetical tsunamis M_W. 8.8 − 9.2 with a uniform distribution by Wiebe and Cox (2014).

COULWAVE solves a set of Boussinesq equations and includes bottom friction effects with a high-order finite-volume method. It has been validated with fundamental benchmark problems for the run-up and inundation problem using both field and experimental data including velocity and momentum flux on inundation zone (Lynett et al., 2002; Lynett and Liu, 2005) and to investigate the inundation through macro-roughness due to the built environment (Park et al., 2013, see Appendix A).

2.4.2 Model setup

We employ our new method of determining the spatially varying slip conditions (Fig. 2.5, 2.6 & Table 2.3) and apply these as a discretized slip fault as an input to the ComMIT/MOST model. Fig 2.7a shows the unit sub-fault utilized in ComMIT/MOST along the CSZ. A total of 27 sub-faults are arranged along the CSZ in ComMIT/MOST, each with 100 km unit length and 50 km unit width. Each sub-fault has a constant but spatially varying strike, dip and depth conditions. The rake is fixed as 90º for all sub-faults. The detailed parameters for each sub-fault are provided in Section 2.8 (Appendix). The tsunami generation and propagation analysis have performed by ComMIT/MOST model and it consists of three nested grids: A-Grid, B-Grid, and C-Grid (Fig. 2.7a, b, and c). The ComMIT/MOST model output from the C-Grid is not used and is replaced by the COULWAVE results.

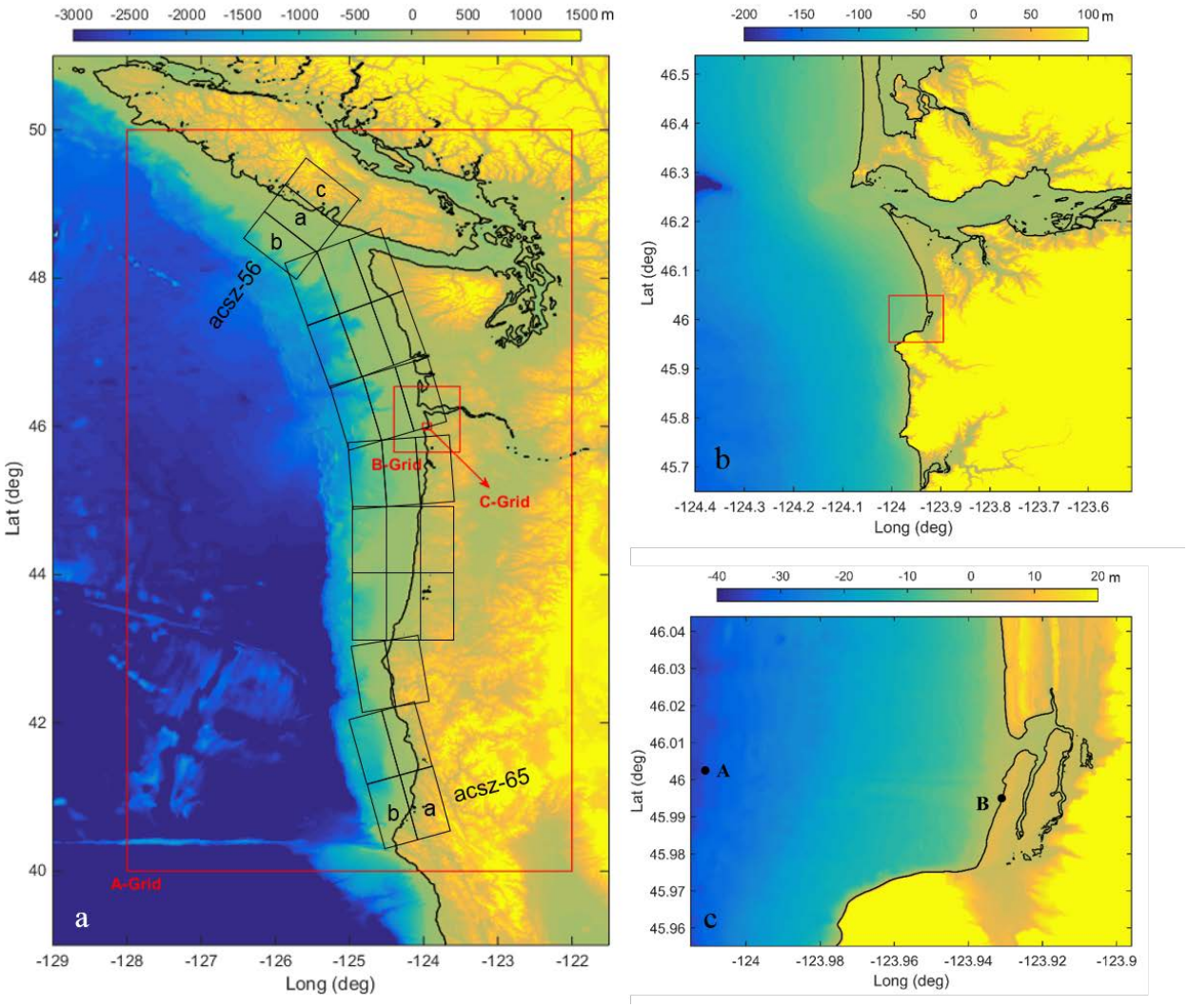

Fig. 2.7 Numerical model bathymetry and grid map for (a) A-Grid, (b) B-Grid, and (c) C-Grid.

For the inundation analysis, we utilized the ComMIT/MOST model output of the B-Grid for the input seaward boundary condition for COULWAVE using the C-Grid for the final inundation. The bathymetry data were obtained from NOAA's National Geophysical Data Center (NGDC). The Coastal Relief Model from the NGDC was used to construct the A-Grid and B-Grid. The Digital Elevation Model for the Seaside area was used for the C-Grid. The size and dimension of each A, B, and C-Grids were 1 min (400 × 400), 3sec (800 × 800), and 24 m (416 × 390), respectively. There are two observation points A and B identified in the C-Grid in Fig. 2.7c. Point A is located near the seaward boundary of the C-Grid where the water depth was z = -35 m, and Point B was located at the shoreline z = 0 m at Seaside.

The tide condition at the time of tsunami event is the one of aleatory uncertainties for the tsunami hazard assessment (Geist and Parsons, 2006; González et al., 2009). However, we only

focus on the aleatory uncertainty due to the slip distributions, so the DEMs are referenced to mean high water (MHW) to provide a conservative estimate of tsunami hazards (e.g., Wiebe and Cox, 2014).

Fig. 2.8a shows a satellite image of the Seaside study area. The flow (free surface and velocity) is computed everywhere in the domain, but we indicated Point B from Fig. 2.7c and nine representative inland observation points to be presented in detail in this study. Fig 2.8a (inset) lists the ground level of the observation points referenced to MHW. Points 1 − 3 are aligned parallel to the shoreline and are located west of the Necanicum River, Points 4 − 6 are also shore parallel and located between the Necanicum River and Neawanna Creek, and Points 7 − 9 are shore parallel and located east of the Neawanna Creek. The urban center of the city is located near the Points 2 and 5. Fig. 2.8b shows the detail bathymetry at the same region as Fig 2.8a. The black contour lines show the zero elevation referenced to MHW, and red dot lines show the contours 3 m above MHW. The bathymetric and topographic conditions of Seaside make it particularly vulnerable to tsunami inundation due to low elevations and due to the two streams crossing the town (Tsunami Pilot Study Working Group, 2006).

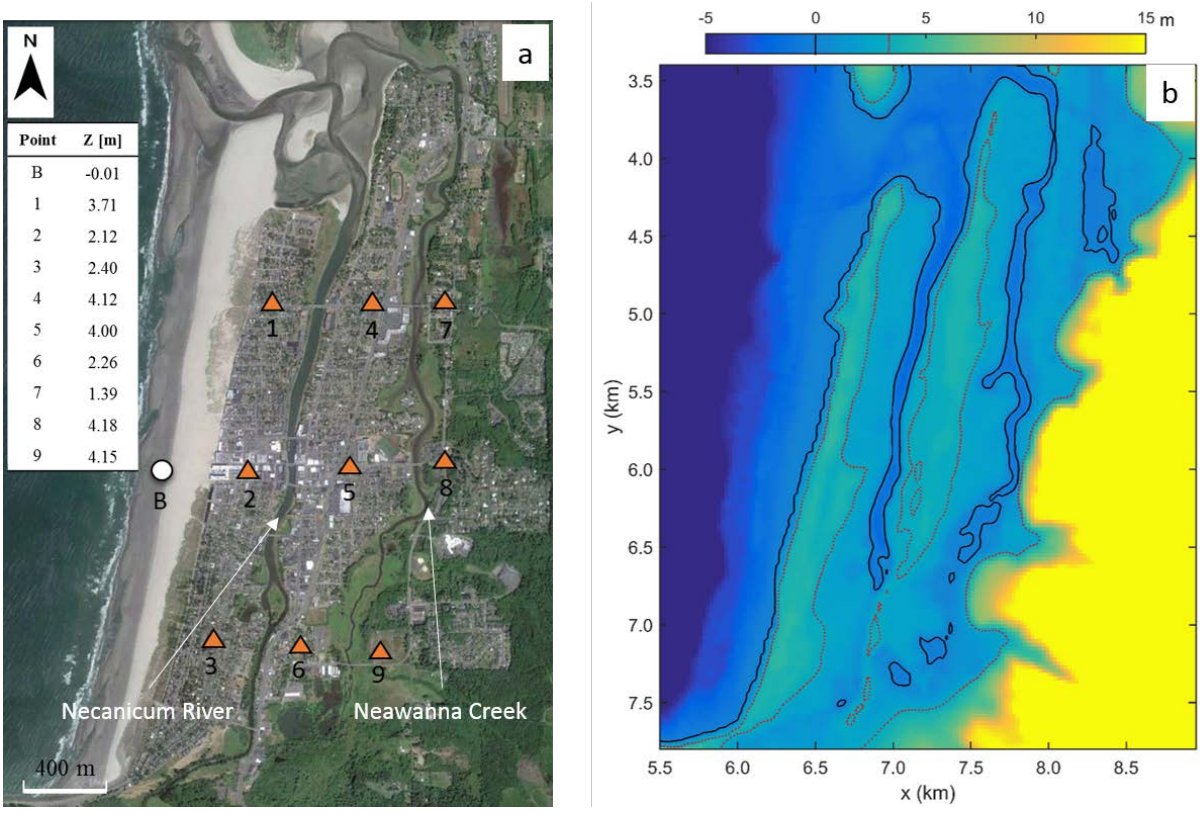

Fig. 2.8 (a) Satellite image of Seaside, OR with representative observation points and (b) detail bathymetry applied in COULWAVE. Dotted lines in Fig. 2.8b present 3 m contours above the MHW.

2.4.3 Example of model output time series at Points A and B.

Figure 2.9 shows inundation time series for the three scenarios presented in Fig. 2.6b. The scenarios are for the same intensity (M_W 9.0) and peak slip location (α'=0.35), but three different slip shapes, β' = 0.81 (black solid), 1.73 (blue dash) and 3.46 (red dash-dot). Fig. 2.9 shows time series of (a) the free surface elevation (η) at Point A, (b) the inundation depth, h, at B, (c) velocity, V, at B and (d) the momentum flux, $M = hV^2$, at B. Here, the inundation depth (h) is the net elevation of the free surface elevation (η) above the local land elevation (z) over the inundation area. In regions submerged below the MHW, the inundation depth h is defined to be the water level η above MHW. In other words, $h = \eta - z$ at overland and $h = d$ at sea.

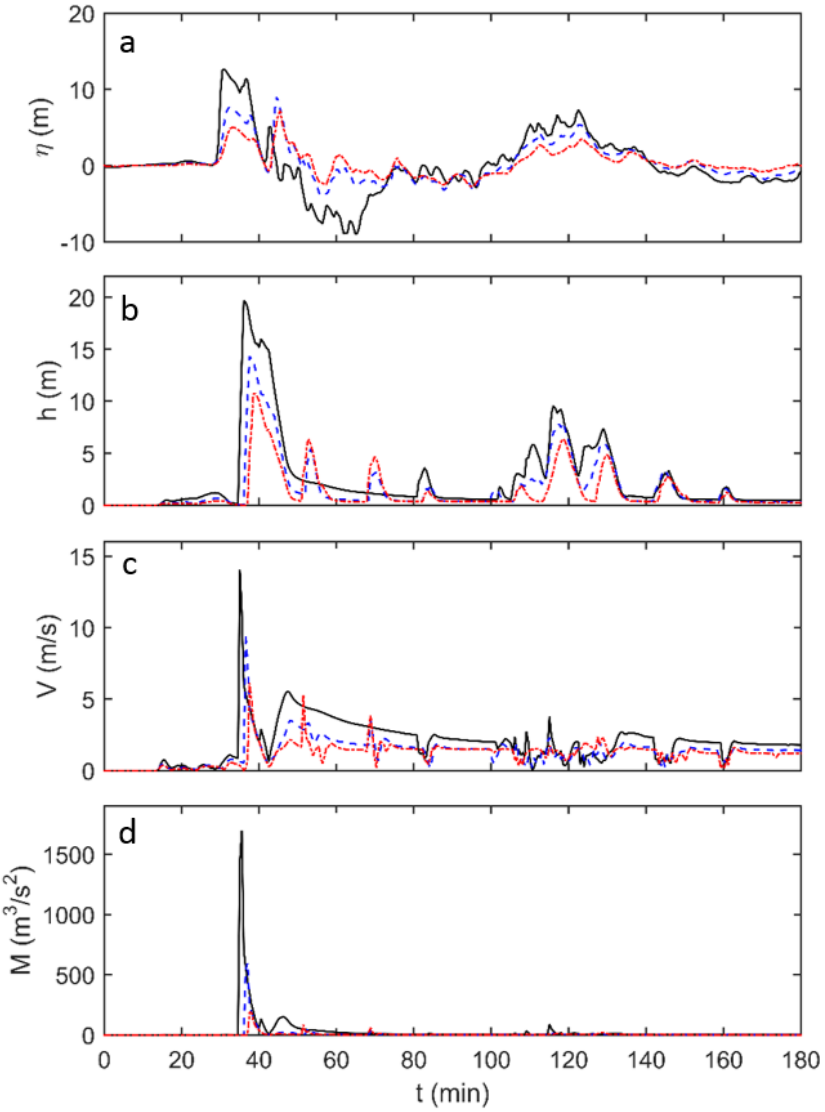

Fig. 2.9 Time series of (a) free surface elevation, η, at point A, (b) inundation depth, h, (c) velocity, V, and (d) momentum flux, M each at Point B. Scenarios are for β' = 0.81 (black solid), 1.73 (blue dash) and 3.46 (red dash-dot) with M_W 9.0 and α'=0.35.

The first peak of the free surface elevation at Point A is observed at 30 min after the initial surface deformation, and a second peak of the free surface elevation is observed at 120 min (Fig. 2.9a). The intensity of the peak is sensitive to β' and the arrival times are not. A short time later, the peak of the free surface elevation arrives at Point B (Fig 2.9b) and the corresponding maximum velocity and momentum flux are found during this first peak (Fig 2.9c, d). Although each scenario has the same moment magnitude and peak slip location, the largest intensity is found for β' = 0.81 (black solid line) correspond to the narrowest shape condition with the highest peak slip (54 m). The smallest intensity is found for β' = 3.46 (red dash dot line) which corresponds to the widest shape with the lowest peak slip (15 m). This highlights how slip shape affects the tsunami hazard intensity. It is noted that the arrival time of the peak is relatively insensitive to β' compared to the magnitude of the peak. Moreover, the maximum of the momentum flux varies by an order of magnitude for the scenarios shown.

To evaluate the sensitivity of hazards due to the moment magnitude of earthquake, slip shapes, and locations of the peak slip, the characteristics of surface elevation at Point A are shown in Fig. 2.10. Fig. 2.10 shows (a) the maximum surface elevation η_{Max} (b) representative period of tsunami, T_R, and (c) Iribarren number ξ at Point A. Fig. 2.10d shows the regional map of Seaside, OR with the latitude position of the peak slip from the north to south (α' = 0.15 – 0.85). Each triangle, square, and circle presents the three slip shape parameter (β') for each M_W scenario from the narrow (the smallest β') to wide (the largest β') slip shape, and each black, yellow, and white color presents three moment magnitudes such as M_W 8.8, 9.0 and 9.2. Note that the lower panel (Fig 2.10d) shows the origin (latitude) of the peak slip, not the location of the inundation. All values in Fig 2.10a, b and c are computed at Point A in the C-Grid for Seaside, Oregon.

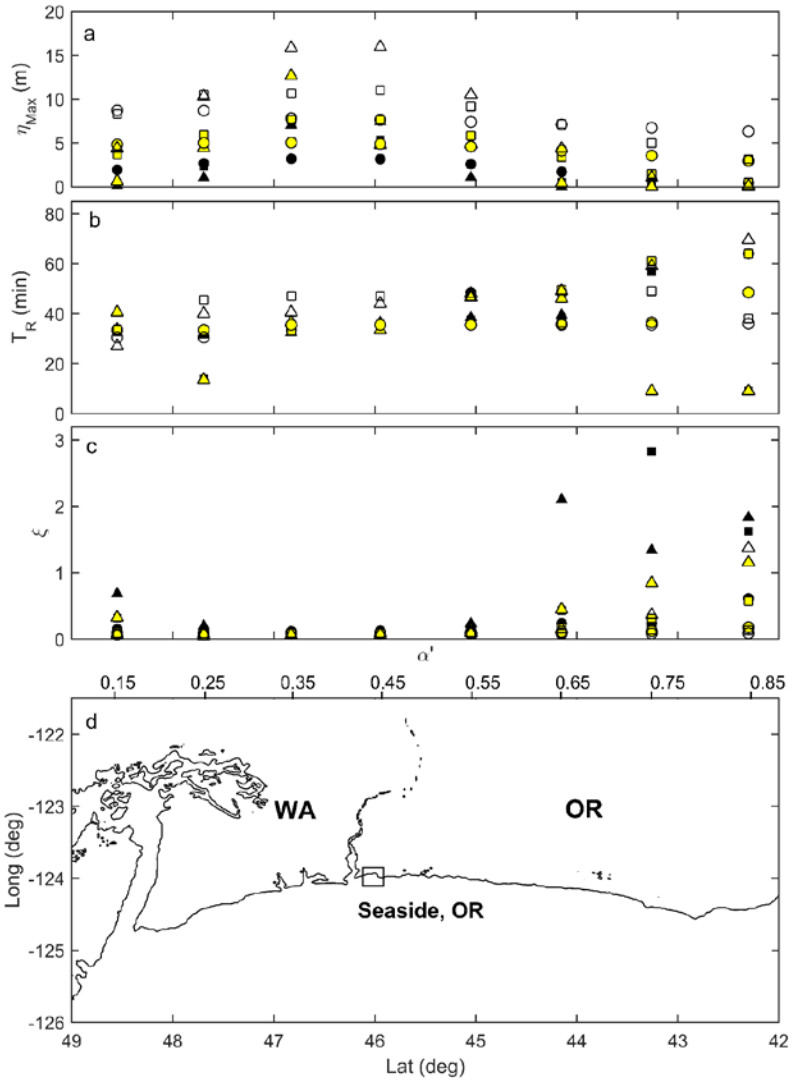

Fig. 2.10 Initial tsunami wave conditions at the COULWAVE model boundary (Point A, in Fig. 2.7) for the CSZ tsunami scenarios against the latitude positions of peak slip. Panel a, b, and c shows the maximum surface elevation (η_{Max}), representative period of tsunami (T_R), and Iribarren number (ξ) of 72 scenarios. Panel d shows the regional map of Seaside, OR. Top x-axis of panel d shows the eight peak slip location in terms of α'. Symbols represents a different β' as triangle (smallest β'), square, and circle (largest), and color presents a different M_W 8.8 (white), 9.0 (yellow), and 9.2 (black).

Fig. 2.10a shows η_{Max} along the eight peak slip locations. Generally the higher η_{Max} is observed at the highest moment magnitude conditions (M_W 9.2) and narrowest slip shape (triangles). The maximum η_{Max} is found at α' = 0.35 for M_W 9.2 and β' = 1.34. The overall range of η_{Max} for all 72 scenarios is 0.2 to 18 m. Among the same peak locations, the largest deviation of η_{Max} is found at α' = 0.35, while the smallest deviations are found at α' = 0.85, which means that the sensitivity of M_W and slip shape are significant as the peak slip is located near the target

area and vise-versa. As it was referred earlier, we observe that η increases as the shape of slip becomes narrower at $\alpha' = 0.35$ (Fig. 2.9a). We also find a similar pattern at $\alpha' = 0.45$ and 0.55 in Fig. 2.10a where the study area (Seaside, OR) is closest to the peak slip. However, this pattern is reversed when the location of the peak slip is far from the target area. We find that the widest shape condition (circle) among three shapes results in the highest η_{Max} at the study area when the peak slip locations are further from the study area at $\alpha' = 0.15$, 0.75 and 0.85.

Fig. 2.10b shows the variations of representative tsunami period, T_R, where T_R is the duration of the surface elevation exceeding 1% of the peak amplitude (e.g. Park et al., 2015). The overall range of T_R is 10 to 70 min, and T_R changes due to the different slip distributions. T_R shows small deviation when the peak slip is closest to the target area (at $\alpha' = 0.35$, and 0.45).

Fig. 2.10c shows the Iribarren number (ξ) which is a function of slop, η_{Max} and T_R. The Iribarren number relates to the type of tsunami waves (breaking or non-breaking) and can be used to estimate the tsunami run-up (Fuhrman and Madsen, 2008; Madsen and Schaffer, 2010; Park et al., 2015). Here we evaluate ξ following the notation of Park et al. (2015, Appendix B) which is

$$\xi = \frac{\gamma}{\sqrt{2\eta_{\mathrm{Max}} / \left(g T_R^{\,2} / 2\pi \right)}} \tag{6}$$

where g is gravity acceleration, and γ is the slope from shoreline to 100 m water depth (approximately 1/170 for Seaside). Overall, ξ is less than 0.5 for most scenarios and it is classified as a breaking tsunami wave condition. Fig 2.10c shows that ξ is an uniformly small when the location of peak slip is near the study area, and that there is large deviation in ξ as the peak slip location is further from the study area, particularly to the south.

Fig. 2.11 shows the five intensity measures (IMs) at Point B for the 72 scenarios plotted against the latitude of the peak slip using the similar format with Fig. 2.10. Fig 2.11a – e shows the maximum inundation depth (h_{Max}), velocity (V_{Max}), momentum flux (M_{Max}), the first arrival time of exceeding a 1 m inundation depth (T_A), and the total duration exceeding 1 m inundation depth (T_h), respectively. Generally, each IM shows a large deviation depending on the scenario. The largest deviations are found for M_{Max}, especially when the location of peak slip is close to target area ($\alpha' = 0.35$, and 0.45). Deviations for M_{Max} decrease as the location of peak slip is far from the target area ($\alpha' = 0.75$, and 0.85), consistent with our observation of η_{Max} in Fig. 2.10. Observations for T_A show the opposite trend, where the smallest deviations in T_A are observed

when the location of slip is close to the target area and the deviations in T_A increase as the peak slip is further away the target area. The minimum arrival time is T_A = 20 min, and most values of T_A are less than 50 min with the exception of a few scenarios whose peak slip located at the south (e.g. α' = 0.75, and 0.85). Overall, the IMs are sensitive to moment magnitude, slip shape and peak location. These variations in the IMs represent the aleatory uncertainty involved in the tsunami generation process. This work highlights the necessity to consider various slip shapes and locations of the peak slip for probabilistic tsunami hazard assessment.

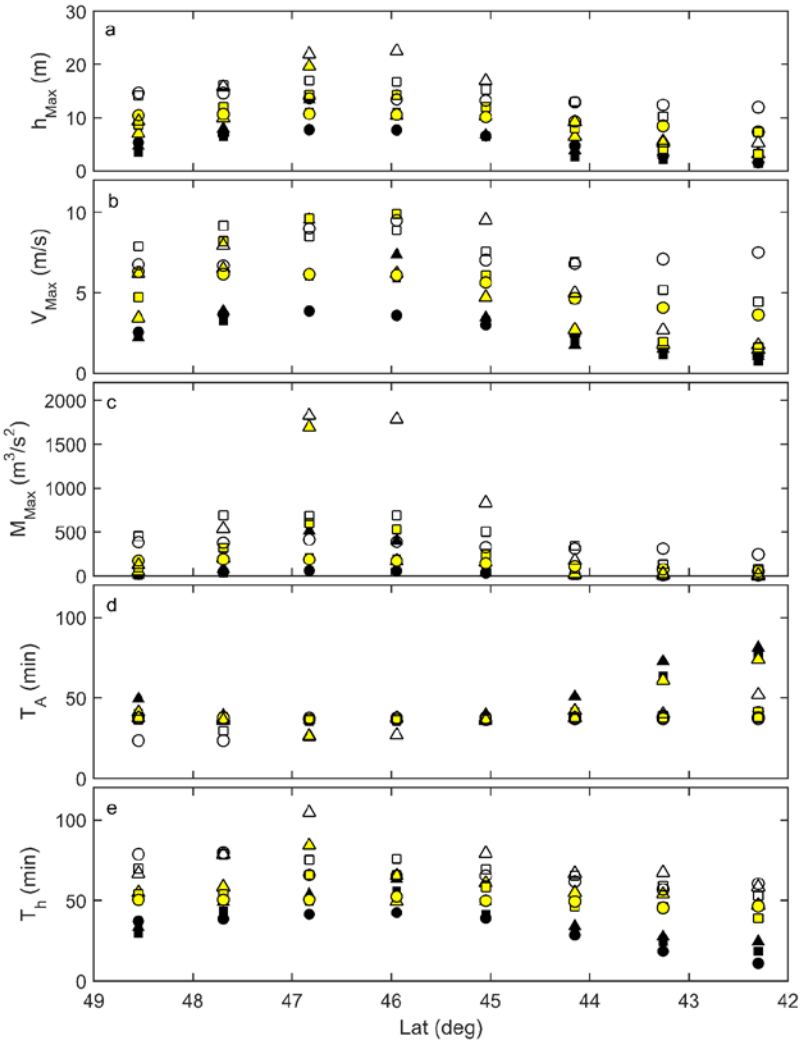

Fig. 2.11 Tsunami IMs at the shoreline of Seaside, OR (Point B) for all scenarios against the latitude positions of peak slip for (a) inundation depth (h_{Max}), (b) velocity (V_{Max}), (c) momentum flux (M_{Max}), (d) arrival time exceeding 1 m inundation depth (T_A), and (e) total duration exceeding 1 m inundation depth (T_h). Symbols are the same as Fig 2.10.

2.5 Probabilistic near-field tsunami hazard assessment (PNTHA)

2.5.1 Methodology of PNTHA

We assume that the occurrence rate, *v*, of the tsunami hazard follows the Poisson arrival process (Cornell, 1964). Admittedly, this is a somewhat crude assumption and neglects the complex subduction zone processes. Nevertheless, this assumption is consistent with what is considered in seismic engineering (McGuire, R.K., 2004) and provides a reasonable starting point for this study. The probability, *P*, of a number of events, *N*, in a fixed time, *t*, can be given as

$$P\left[N=n\right]=\frac{e^{-\nu t}\left(\nu t\right)^{n}}{n!},\quad n=0,1,2\cdots \tag{7}$$

when those events occur *n* times with a known average occurrence rate (ν) and independently of the time since the last event. The probability of the maximum hazard exceeding a certain level of that hazard is equal to the probability of at least one event occurring during *t*, and can be expressed as

$$P\left[Hazard > hazard_i\right]=1-e^{-\nu t} \tag{8}$$

where the subscript *i* describes the specific level of hazard or particular hazard bin used for the analysis. In case of the maximum inundation depth (h_{Max}), the exceedance probability of the specific inundation depth (h_i) during the time, *t* is

$$\mathrm{P}\left[h_{Max} > h_i\right]=1-\mathrm{e}^{-\nu t} \tag{9}$$

The mean occurrence rate is

$$\nu=-\ln\left(\mathrm{P}\left[h_{Max}\le h_i\right]\right)/t \tag{10}$$

where P [$h_{Max} \le h_i$] is the non-exceedance probability of the maximum inundation depth over a specific inundation depth (h_i) and *v* denotes the mean occurrence rate of the tsunami hazard.

To find the mean occurrence rate (ν) of a tsunami conditioned on a full-rupture CSZ event, we can estimate t = 526 year since there were 19 full-rupture events identified in the past 10,000 years (Witter et al., 2013). Using the discretized form of Eq. 10 for each moment magnitude scenario (M_W 8.8, 9.0, and 9.2), the sum of each mean occurrence rate (ν) in Eq. 10 are

$$\nu_{Mw=8.8}=-\ln\left(\mathrm{P}\left[h_{Max}\le h_i\right]\,|\,M_W=8.8\right)/t \tag{11}$$

$$\nu_{Mw=9.0} = -\ln\left(\mathrm{P}\left[h_{Max} \le h_i\right] | M_W = 9.0\right) / t \quad (12)$$

$$\nu_{Mw=9.2} = -\ln\left(\mathrm{P}\left[h_{Max} \le h_i\right] | M_W = 9.2\right) / t \quad (13)$$

Here, we set the unit bin of the inundation depth (h_i) equal to 0.2 m. Total sum of each mean occurrence rate (ν) is calculated by the sum of each discretized mean occurrence rate with a weighting factor and is given by.

$$\nu = \sum \nu_{M_w} \cdot P\left[M_W\right] \quad (14)$$

where P [M_W] is the weighting factor. For this analysis, the weighting factors for each moment magnitude are shown in Fig. 2.5 and Table 2.3 and are 0.06 for M_W 8.8, 0.68 for M_W 9.0, and 0.28 for M_W 9.2.

Fig. 2.12 shows an example of the non-exceedance probability of the maximum inundation depth at Point B for M_W 8.8 (green circle), 9.0 (blue square), and 9.2 (red triangle). Each discrete point shows the non-exceedance probability for a given scenario reflecting variations in slip distribution weighting factors described in Fig. 2.5 and Table 2.3.

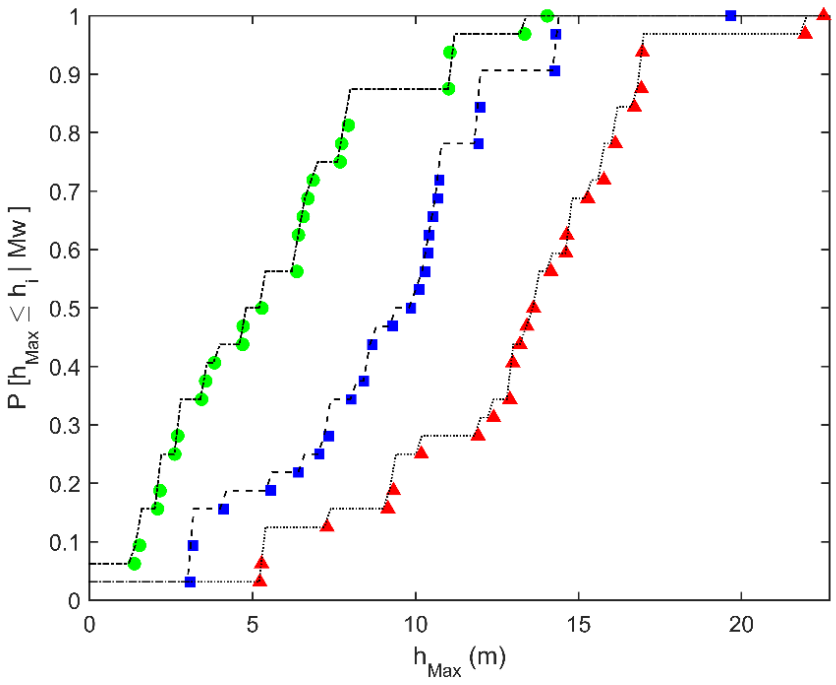

Fig. 2.12 Non-exceedance probability of the maximum inundation depth at Point B with the given three moment magnitudes. Each symbol presents the scenarios with M_W 8.8 (green circle), 9.0 (blue square), and 9.2 (red triangle).

As an intermediate step, Fig. 2.13 presents the mean occurrence rate (ν) of the maximum inundation depth at Point B corresponding to Figure 2.12. The dash-dot, dash, and dot lines represent mean occurrence rate of M_W 8.8, 9.0, and 9.2, and the solid black line shows the total mean occurrence rate (ν) from Eq. 14 with the correct weighting factors.

Fig. 2.14 shows the annual exceedance probability of the maximum inundation depth at Point B using Eq. 9 with the total mean occurrence rate ν from Eq. 14 shown as the solid black line in Fig 2.13. In Fig. 2.14, the x-axis is the maximum inundation depth and the y-axis is the probability that an inundation depth will exceed h_{Max} in a given year at Point B conditioned on the CSZ event of M_W 8.8 to 9.2. For example, there is a 0.001 annual probability of exceeding a 9.2 m inundation depth at Point B (nominally called the "1,000-year event"), and 0.002 annual probability of exceeding a 6.4 m inundation depth at point B ("500-year event"). It is worth noting that for this work, the probability is conditioned on the CSZ event with the full-length rupture area, and if additional tsunami sources were considered (including other near-field and all far-field sources), the exceedance probability curve would be different.

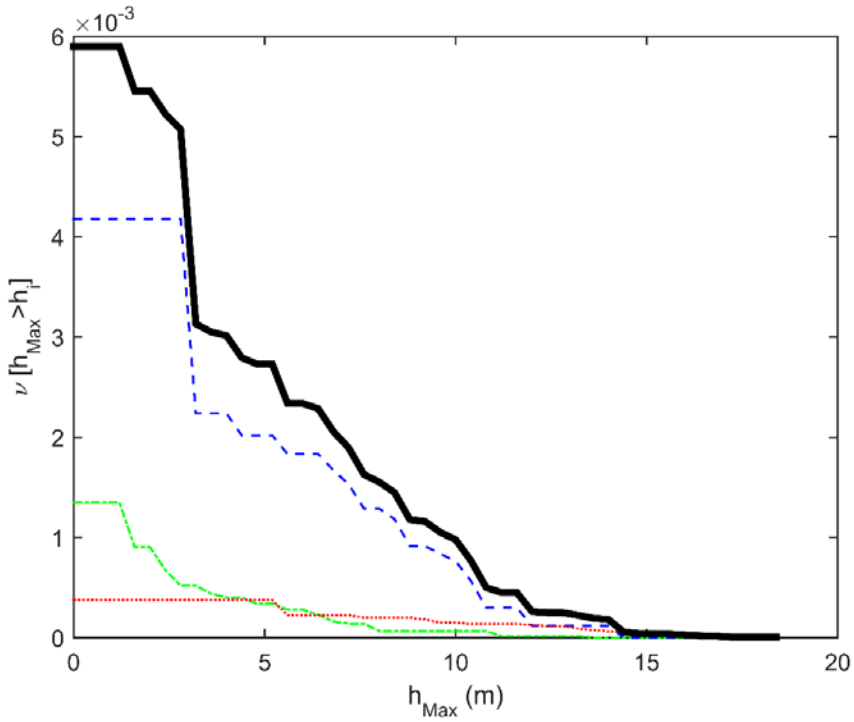

Fig. 2.13 Total mean occurrence rate of the max inundation depth at Point B (thick solid line). Three thin lines present the mean occurrence rate of the scenarios with M_W 8.8 (green dash-dot), 9.0 (blue dash), and 9.2 (red dot).

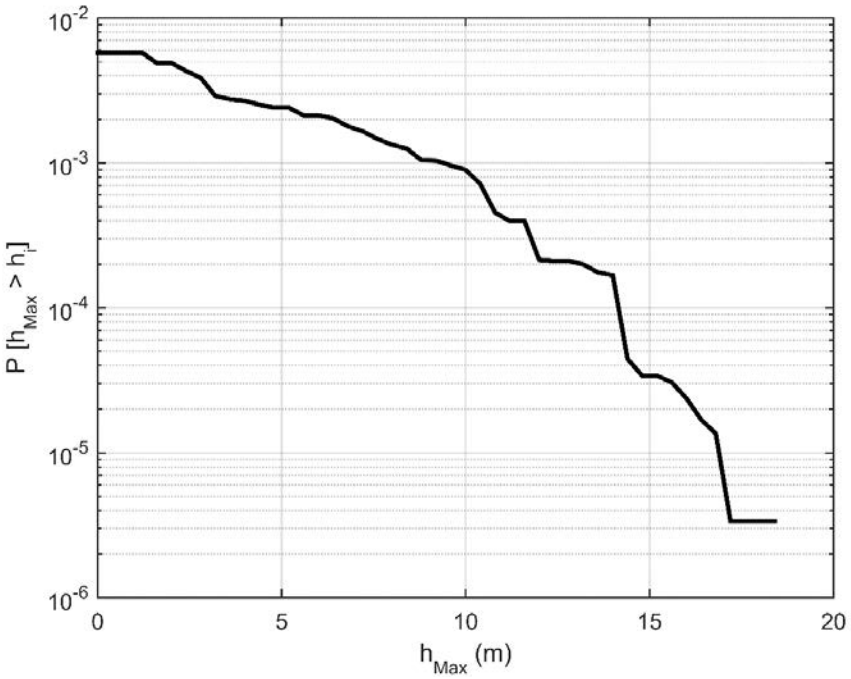

Fig. 2.14 Annual exceedance probability of the maximum inundation depth at Point B.

The same procedure from Eq. 9 to 14 can be performed for all IMs throughout the inundation area. For illustration, we will present the annual exceedance probability at Points 1 through 9 (Fig. 2.8a) using the following unit bin for each IM: h_{Max} (0.2 m), V_{Max} (0.1 m/s), M_{Max} (1.0 m^3/s^2), T_A (0.5 min), and T_h (0.5 min). In addition, we consider the Froude number, F, at the time of the maximum momentum flux to examine the relation among inundation depth, flow velocity, and exceedance probability. For this study, the Froude number is defined as

$$F = \frac{V_m}{\sqrt{g h_m}} \tag{15}$$

where subscription, m denotes the value at the time of the maximum momentum flux. The unit bin of F is 0.1 for these examples.

2.5.2 PNTHA results at observation points

Fig. 2.15 shows the annual exceedance probability (P) of the five IMs and the Froude number at Point 1 (black solid), Point 2 (red dash), and Point 3 (blue dash-dot). These observation points are oriented parallel to the shoreline and located between the shoreline and the Necanicum River. The elevations are 3.71, 2.12, and 2.40 m above MHW for Points 1 to 3, respectively (Fig. 2.8). The figure shows the annual exceedance probability for (a) the maximum

inundation depth, (b) velocity, (c) momentum flux, (d) duration, (e) arrival time, and (f) Froude number.

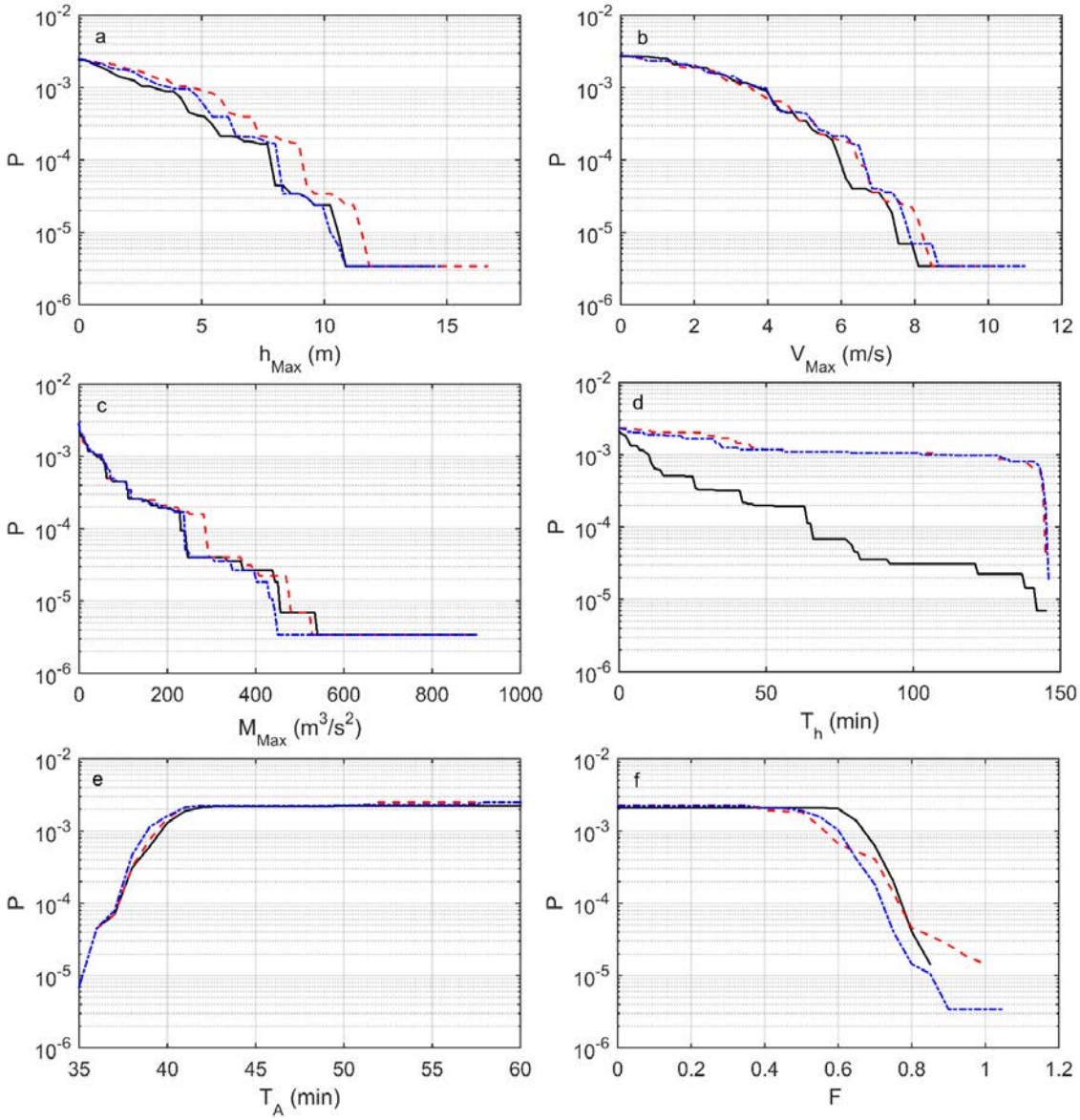

Fig. 2.15 Annual exceedance probability of (a) h_{Max}, (b) V_{Max} , (c) M_{Max}, (d) T_h , (e) T_A , (f) Froude number, F at Points 1 (black solid), 2 (red dash), and 3 (blue dash-dot).

The IMs generally increase as the annual exceedance probability decreases, and the figure shows a qualitatively similar pattern of distribution among the three observation points because of the similar bathymetric conditions and distance from the shoreline. The arrival time (T_A), however, shown in Fig 2.15e shows a different distribution compared to the others, and the arrival time is less sensitive to the exceedance probability, and the maximum momentum flux

(M_{Max}) is the most sensitive. For example at Point 2, h_{Max} changes from 1.7 m for P = 0.002 to 4.8 m for P = 0.001, an increase of about a factor of three, while M_{Max} changes from 4.5 m^3/s^2 for P = 0.002 to 49.2 m^3/s^2 for P = 0.001, an increase of order of magnitude. However, the arrival time decreases from T_A = 41 min to T_A = 39 min, or a decrease of about 5% over the same range of exceedance probabilities. Another notable observation of Fig 2.15 is that the duration (T_h) at Point 1 is significantly less compared with the other two points (2.15d). For example, for P = 0.001 at Point 1, T_h is approximately 10 min, while Point 2 and Point 3, T_h is more than 60 min. This difference occurs because Point 1 is approximately 1.5 m higher than other two observation points. Thus, Points 2 and 3 are more likely to be submerged due to their low elevation conditions. This information may be relevant, for example, for search and rescue operations and highlights that while the initial tsunami intensity may be similar in some cases (2.15a, b, c), the system may have different responses. Fig. 2.15f shows the Froude number at the time of maximum momentum flux. For most of the conditions, F is less than 1.0 with the lowest limit of 0.4 at three observation points. This suggests that the flow is subcritical at the time of the maximum momentum flux, and these values are generally consistent with the observation from 2011 Tohoku tsunami (Fritz et al., 2012).

Fig. 2.16 provides the annual exceedance probability (P) of the five IMs and the Froude number at Point 2 (black solid), 5 (red dash), and 8 (blue dash-dot). These points are aligned shore-normal along the urban center of Seaside from the shoreline to the inland (Fig. 2.8). Point 2 is located between the shoreline and the Necanicum River, Point 5 is located between the Necanicum River and Neawanna Creek, and Point 8 is located between Neawanna Creek, and the edge of inundation zone. Each panel has the same format as Fig. 2.15. Generally, the largest hazard intensity is found at Point 2 (closest to the shoreline) and decreases landward toward the edge of the inundation zone. For the maximum inundation depth in Fig 2.16a, the three observation points show different trends for more frequent events (e.g., P = 0.0005) with small inundation depths (h_{Max} < 4 m). However, for lower probability events with larger inundation depths in the range 5 < h_{Max} < 10 m, Points 5 and 8 have nearly the same exceedance probability for a given inundation depth in this range. This is due to local bathymetric effects, including effects of the river and creek effects at Points 5 and 8. On the other hand, the velocity (2.16b) does not show a similar trend: the three curves are distinct for each location. Similarly, the momentum flux (2.16c) also shows three distinct curves. We also found a similar and more

distinct pattern between Point 4 (z = 4.12 m) and 7 (z = 1.39 m) where Point 7 has a much lower elevation and is close to the Neawanna creek. This observation underscores the importance of understanding more than just the inundation depth during the tsunami inundation. For example, when trying to estimate damage to the built environment within this zone, the sharp gradation in momentum flux for a given value of P shown in 2.16c suggests that there should be a corresponding gradation of damage (assuming a constant building type, for example) if the damage is related to the momentum flux. Figure 2.16a, on the other hand, suggests that there would be little difference in observed damages between Point 5 and 8 (4 and 7) because the inundation depths are similar for a given value of P.

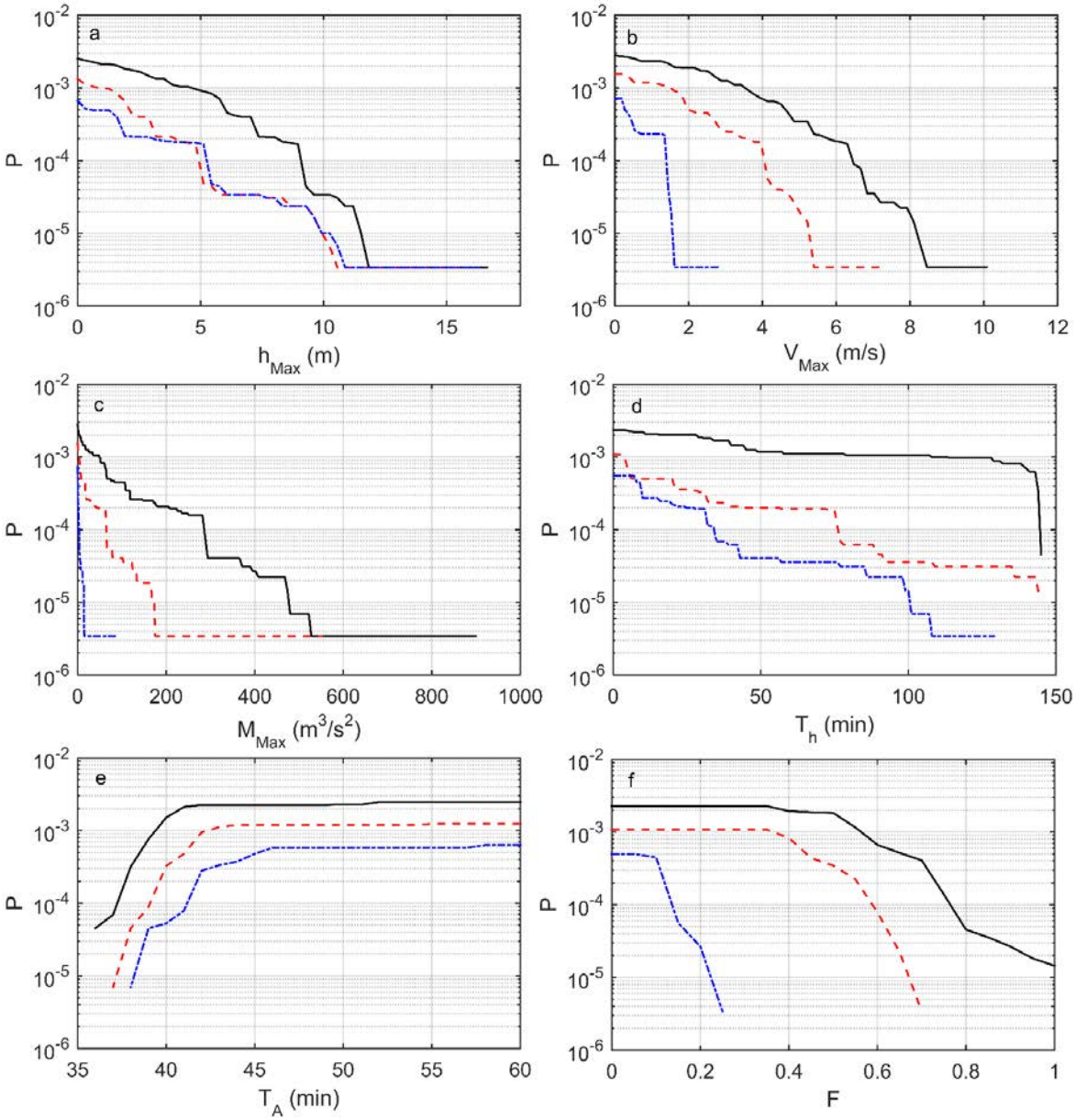

Fig. 2.16 Annual exceedance probability of the h_{Max} (panel a), V_{Max} (panel b), M_{Max} (panel c), T_h (panel d), T_A (panel e) and Froude number, F (panel f) at Points 2 (black solid line), 5(red dash line), and 8(blue dash-dot line).

Fig 2.16d show significant variations in the duration of inundation T_h. For P = 0.0001, for example, T_h = 140, 70, and 35 min along Point 2, 5, and 8, respectively. In other words, there is about a factor 2 difference in the inundation duration between Point 5 and 8 even though the maximum inundation level is about the same (2.16a). Fig 2.16e shows that the arrival time T_A increases from Point 2 to 8. In other words it takes longer for the tsunami to reach further inland. Although this result is somewhat expected, it shows that the presence of the Necanicum River

and Neawanna Creek does not have a significant effect on the tsunami arrival time. This is because the river and creek are shallow and do not allow the bore to propagate upstream quickly. Instead, the main bore exceeding 1 m depth is due to the inundation from the shoreline. Fig. 2.16f shows that the Froude number decreases from the shoreline landward for a given value of P. The Froude number is generally in the range $0.1 < F < 1.0$ and is subcritical at the time of maximum momentum flux.

2.5.3 Spatial distributions of IMs for Seaside, OR

Fig. 2.17a, b shows the spatial distributions of the maximum inundation depth at Seaside, Oregon, based on the $P = 0.002$ ("500-year") and 0.001 ("1,000-year") exceedance probabilities, respectively. The solid line shows the MHW. The dotted line in each panel shows the maximum inundation limit, defined here as the contour line for which is $h_{Max} = 0.3$ m. In both cases, h_{Max} is largest at the shoreline and decreases as it inundates across the shoreline, particularly of the first 100 m of shoreline. It is noted that h_{Max} is larger near the Necanicum River and reaches a value of 6 m for $P = 0.001$. In general, though, the maximum inundation depth is somewhat uniform at about 5 m for much of the inundation zone, consistent with Fig. 2.16a.

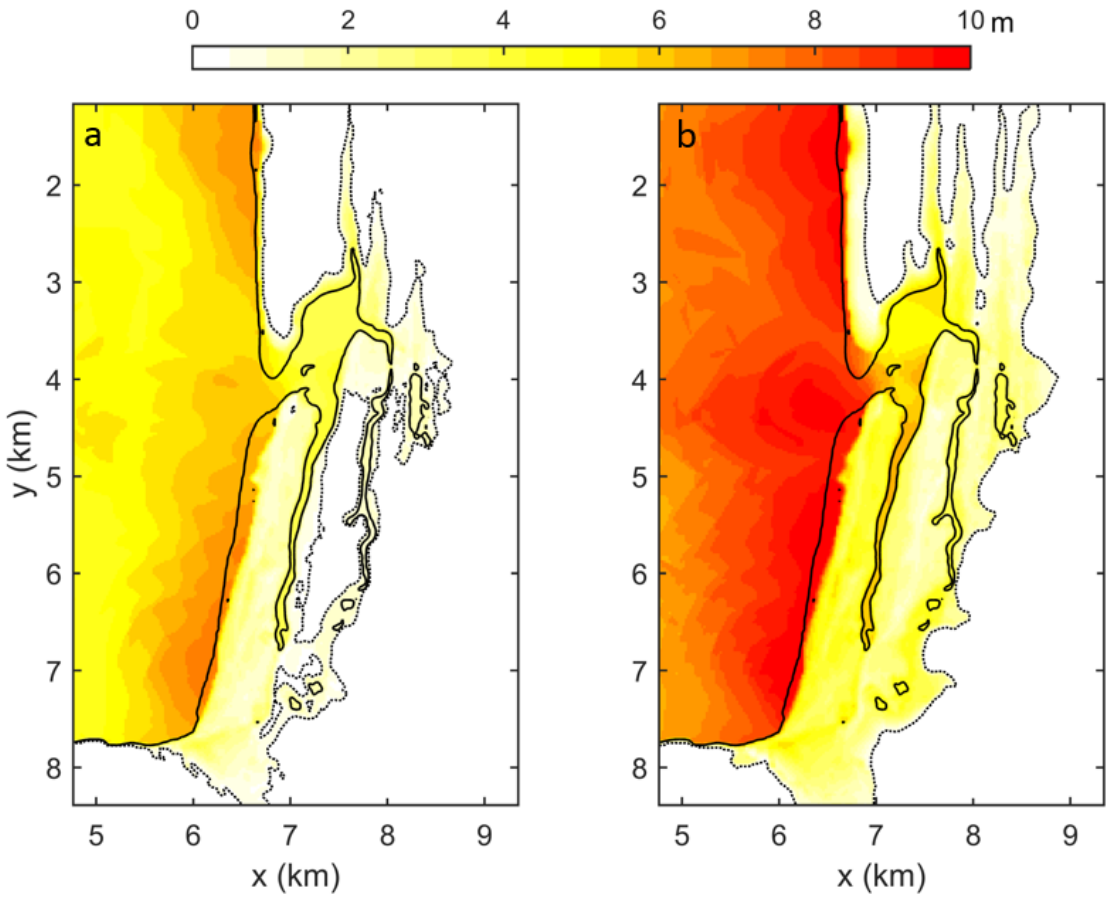

Fig. 2.17 Spatial distributions of h_{Max} for (a) P = 0.002 and (b) P = 0.0001.

Fig. 2.18a, b shows the spatial distributions of the maximum velocity for P = 0.002 and 0.001, respectively. The dotted line contour is set for V_{Max} = 0.3 m/s. Similar to Fig 2.17, the velocity is strongest at the shoreline. There is also large velocity in the center of peninsula between the shoreline and the Necanicum River. The velocity within the river running parallel to the shoreline, however, is not strong. The maximum velocity in the mouth of river is strong, and large scour would likely develop here.

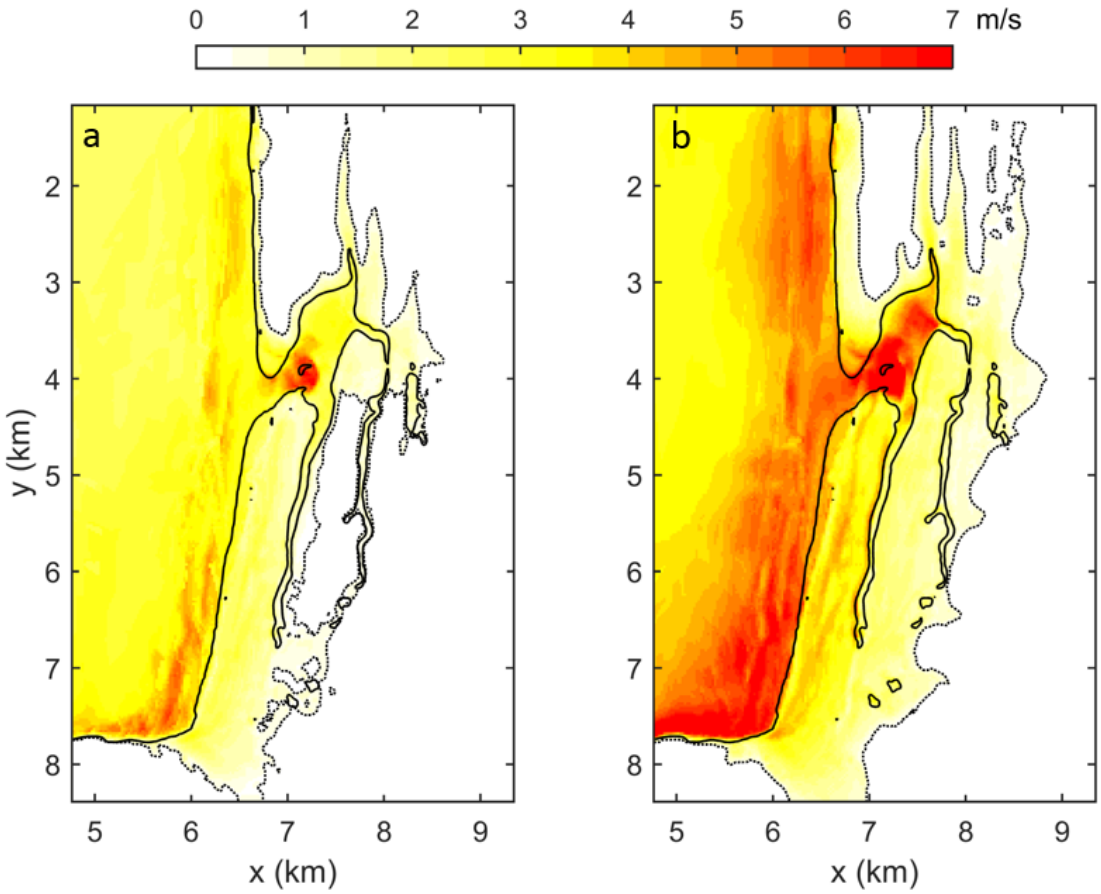

Fig. 2.18 Spatial distribution of V_{Max} for (a) P = 0.002 and (b) P = 0.001.

Fig. 2.19a, b shows the spatial distributions of the maximum momentum flux for the two cases. The dotted contour line is M_{Max} = 1 m^3/s^2. Similar to the maximum velocity in Fig 2.18, the momentum flux is strongest at the shoreline and decreases as the tsunami reaches the Necanicum River (Fig. 2.19b). The maximum momentum flux abruptly decreases near the river and shows a larger deviation over the inundation region compared to the inundation depth or velocity.

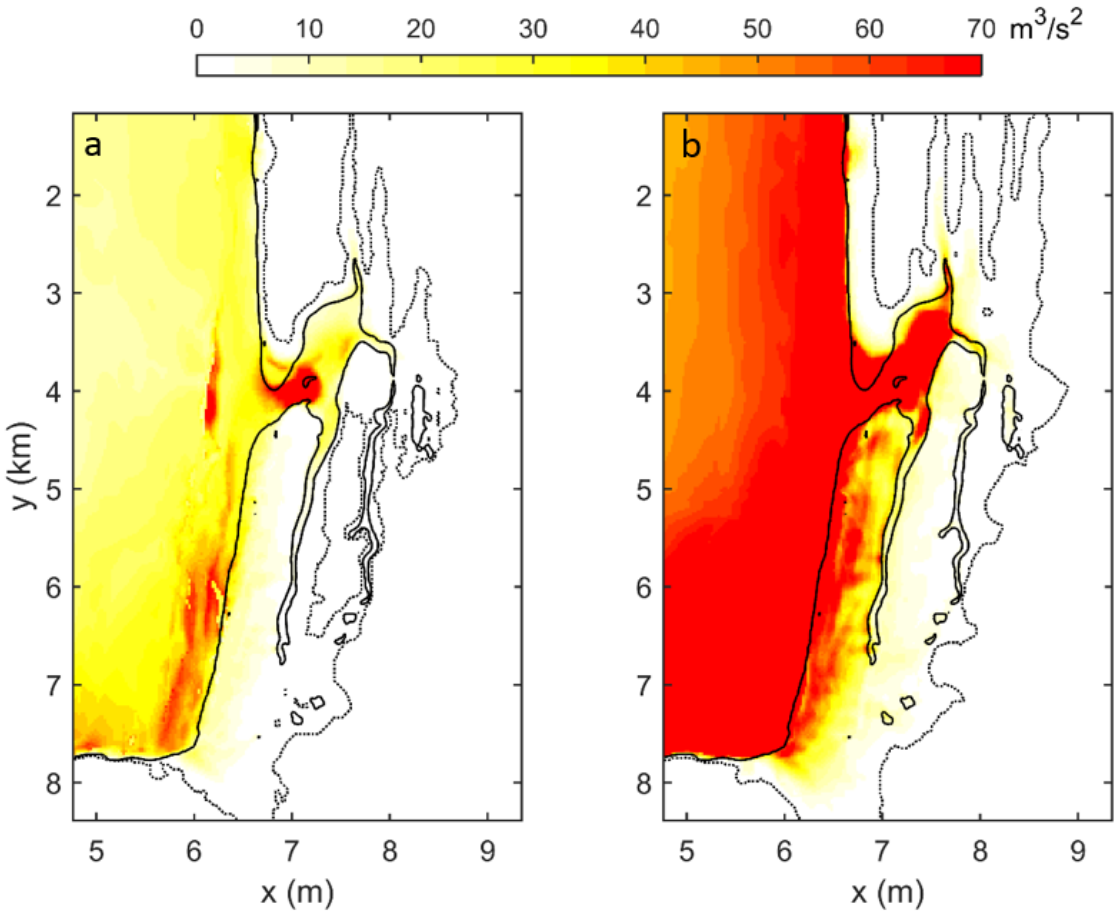

Fig. 2.19 Spatial distribution of M_{Max} for (a) P = 0.002 and (b) P = 0.001.

Fig. 2.20a, b shows the spatial distribution of the total duration exceeding a 1 m inundation depth (T_h) for the two cases. The dotted line is set with the duration limit of T_h = 0.5 min. Fig 2.20b, in particular, shows the effect of the low elevation near Necanicum River and Neawanna creek. Here, the inundation duration exceeds more than 100 min and can have significant implications for the immediate response after the event. Moreover, Fig. 2.20b clearly shows an isolated region (white region) between the Necanicum River and Neawanna creek which would presumably impede immediate response to this area.

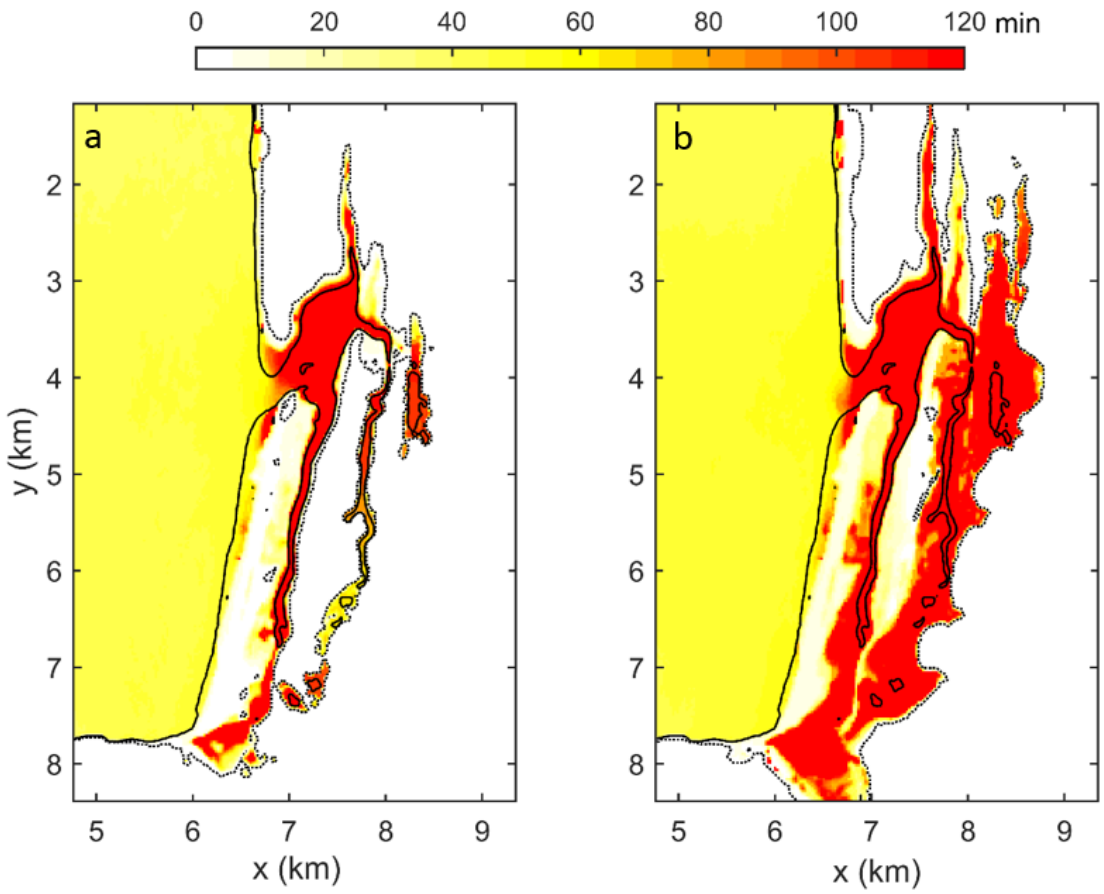

Fig. 2.20 Spatial distribution of T_h for (a) P = 0.002 and (b) P = 0.001.

2.6 Discussion

2.6.1 Uncertainties on the input slip conditions

Our new method to determine the fault slip distribution at the CSZ is developed by utilizing the inversion model results from different study groups, thus the inversion model results may contain epistemic uncertainties from their own inversion process. Some of inversion models utilized finer resolution of unit sub-faults than our model setup (100 km length, and 50 km width). In this study, we do not attempt to find the certain type of slip distribution which matches with observation data. Instead, we focus on characterizing possible tsunami scenarios at the CSZ considering the effects of varying M_W, location of peak slip, and slip shape. For this study, we used the default setup for sub-faults provided in ComMIT/MOST. Moreover, we considered instantaneous fault rupture along the entire length of the CSZ. For future work, it would be interesting to evaluate the effect of sub-faults size and a time-dependent rupture scenario.

In addition, there are possible uncertainties resulting from the sub-fault information such as strike, dip, rake and depth (Goda et al., 2014). In our study, we did not account for the effect of variations of the sub-fault information as a possible epistemic uncertainty. We used the constant but spatially varying sub-fault condition, following the embedded tsunami generation model in ComMIT/MOST for the CSZ (Section 2.8, Appendix). The accuracy of sub-fault information could be further investigated in future studies.

2.6.2 Uncertainties on the weighting factors

We perform a total of 72 scenarios with the weighting factors for each scenario based on the occurrence rate of the three moment magnitudes of earthquake, eight possible peak slip locations and three slip shapes. The weighting of the moment magnitude was consistent with earlier work (e.g., Witter et al., 2013) and the weighting of the slip shape and location was based on the authors' judgement. Although these are somewhat crude assumptions, we note that a previous PTHA study at Seaside, OR by González et al. (2009) utilized only 12 scenarios with M_W = 9.1 conditions for the CSZ without attention to weighting factors. In future studies, the uncertainties involved in the weighting factors may be decreased by modifying or updating the weighting factor based on the relevant studies without the need to re-run the inundation models.

2.6.3 Uncertainties on the initial conditions of numerical models

We do not include the aleatory uncertainties due to the tide condition. As mentioned earlier, our study assumes a constant mean high water level (MHW) resulting in conservative estimates of the inundation. However, the real tide level may change significantly during the inundation process depending on the bathymetry condition. It may locally accelerate or decelerate IMs, thus the detail interaction of tide and tsunami wave is complex to be modeled exactly.

We applied ComMIT/MOST model for the tsunami generation and propagation analysis, and COULWAVE for the tsunami inundation analysis. Both numerical models may contain uncertainties generated from the computation process due to the input and default model setup. We used a bare-earth bathymetry condition for each model, which means that models do not reflect any structures or vegetation which create complex flows, sheltering, concentrating or dissipations during real tsunami inundation. In addition, we setup the default friction term as a Manning number, n = 0.03 for all models (ComMIT/MOST and COULWAVE). This value may

reasonable for the sea bottom, but it is a relatively small value for the inundation over the urban area (Koshimura et al., 2009; Bricker et al., 2015). There are two possible ways to improve the model results. The first one would be to apply a spatial varying Manning number depending on land conditions, and the other is to use a refined mesh to include the structures in the inundation modelling (Park et al., 2013). The fact that the structures are damaged and can be washed away during the inundation event would result in a temporally varying friction factor or grid, adding further complexity to the problem. For simplicity in this study, we utilized a constant Manning number.

2.7 Conclusions

This study highlights the significance of the uncertainty on tsunami hazards analysis regarding the randomness of the tsunami generation (aleatory uncertainty). We introduce a new method to determine the initial fault slip to simplify the randomness of tsunami slip condition. We determine range of moment magnitudes of earthquakes at the CSZ using the relation between the rupture area and seismic moment of historic tsunami events. We characterize the peak slip location and slip shapes from inversion model results. We utilize 72 scenarios as tsunami sources with different weighting factors assigned based on the occurrence rate of historic events at the CSZ and slip distributions based on expert opinion of the authors. We estimate the exceedance probability for 5 intensity measures, assuming a Poisson arrival process. The main conclusions of this work are:

1. The new method for the fault slip distributions accounts for some of the aleatory uncertainty in tsunami generation. Using published slip models of recent earthquakes, we characterize the fault slip distribution as a Gaussian distribution with moment magnitude (M_W), and two slip distribution parameters, α' and β'.
2. We perform a probabilistic near-field tsunami hazards assessment (PNTHA) at Seaside, Oregon, to illustrate our general methodology and examine five tsunami intensity measures (IMs): the maximum inundation depth (h_{Max}), the maximum velocity (V_{Max}), the maximum momentum flux (M_{Max}), the arrival time exceeding a 1 m inundation depth (T_A), and total duration exceeding a 1 m inundation depth (T_h).

3. The intensity of IMs are observed to increase as the moment magnitude (M_W) increase, as the peak slip location becomes closer to the study area, and as the slip shape becomes narrower.
4. Among the IMs, the arrival time (T_A) shows relatively weak sensitivity to the aleatory uncertainty, while other IMs shows significant sensitivity, especially momentum flux (M_{Max}). We observed that M_{Max} increases by an order of magnitude from the 500-year to 1,000-year event, while h_{Max} increases by a factor of 3 and T_A decreases by a factor of 0.05.
5. The inundation duration T_h can vary due to the local bathymetric conditions and can range a relatively short duration (< 10 min) to a relatively longer duration (~100 min) observed near the river and creek where the elevation is closed to the sea-level.

This study provides the probabilistic spatial distributions of each IM at Seaside, Oregon, and can be utilized for damage or loss estimation. In particular, the maximum inundation depth, velocity, or momentum flux are applicable for tsunami building damage estimation at a community scale. Arrival time and duration are utilized for the evacuation planning. Future work may consider a more refined model for tsunami generation, including a refined sub-fault model and a time-varying rupture. Future work for the tsunami inundation model should consider the effects of macro-roughness and a time-varying roughness due to damage during the inundation process.

2.8 Appendix

The following table provides the geologic information on sub-faults used in the ComMIT/MOST model v. 1.7.0. Each sub-fault is 100 km length and 50 km width. Rake is 90º for all sub-faults. Here each coordinate indicates the left top corner of each sub-fault.

Table 2.4. Sub-fault information for Aleutian–Alaska–Cascadia Subduction Zone (ACSZ).

Sub-faults	Longitude (°*E*)	Latitude (°*N*)	Strike (°)	Dip (°)	Depth (*m*)
acsz-56a	234.0588	49.1702	315	11	12.82
acsz-56b	233.5849	48.8584	315	9	5.00

acsz-56z	234.5230	49.4727	315	18	22.36
acsz-57a	234.9041	48.2596	341	11	12.82
acsz-57b	234.2797	48.1161	341	9	5.00
acsz-57z	235.5249	48.4018	341	14	22.36
acsz-58a	235.3021	47.3812	344	11	12.82
acsz-58b	234.6776	47.2597	344	9	5.00
acsz-58z	235.9298	47.5029	344	11	22.36
acsz-59a	235.6432	46.5082	345	11	12.82
acsz-59b	235.0257	46.3941	345	9	5.00
acsz-59z	236.2591	46.6216	345	13	22.36
acsz-60a	235.8640	45.5429	356	11	12.82
acsz-60b	235.2363	45.5121	356	9	5.00
acsz-60z	236.4860	45.5734	356	14	22.36
acsz-61a	235.9106	44.6227	359	11	12.82
acsz-61b	235.2913	44.6150	359	9	5.00
acsz-61z	236.5211	44.6303	359	15	22.36
acsz-62a	235.9229	43.7245	359	11	12.82
acsz-62b	235.3130	43.7168	359	9	5.00
acsz-62z	236.5213	43.7321	359	16	22.36
acsz-63a	236.0220	42.9020	350	11	12.82
acsz-63b	235.4300	42.8254	350	9	5.00
acsz-64a	235.9638	41.9818	345	11	12.82
acsz-64b	235.3919	41.8677	345	9	5.00
acsz-65a	236.2643	41.1141	345	11	12.82
acsz-65b	235.7000	41.0000	345	9	5.00

2.9 References

Baba, T., Cummins, P. R., Thio, H. K., and Tsushima, H. (2009) Validation and joint inversion of teleseismic waveforms for earthquake source models using deep ocean bottom pressure records: A case study of the 2006 Kuril megathrust earthquake. *Pure and Applied Geophysics*, 166(1-2), 55-76.

Bricker, J.D., Gibson, S., Takagi, H. and Imamura, F. (2015) On the Need for Larger Manning's Roughness Coefficients in Depth-Integrated Tsunami Inundation Models. *Coastal Engineering Journal*, 57(02), 1550005.

Bruneau, M., Chang, S.E., Eguchi, R.T., Lee, G.C., O'Rourke, T.D., Reinhorn, A.M., Shinozuka, M., Tierney, K., Wallace, W.A. and von Winterfeldt, D. (2003) A framework to quantitatively assess and enhance the seismic resilience of communities. *Earthquake Spectra*, 19(4), 733-752.

Cornell, C.A. (1968) Engineering seismic risk analysis. *Bulletin of the Seismological Society of America*, 58(5), 1583-1606.

Dominey-Howes, D., Dunbar, P., Varner, J., and Papathoma-Köhle, M. (2010) Estimating probable maximum loss from a Cascadia tsunami. *Natural Hazards*, 53(1), 43-61.

FEMA P-646 (2012) *Guidelines for Design of Structures for Vertical Evacuation from Tsunamis* (2nd Ed.), Federal Emergency Management Agency, Washington, D.C.

Fritz, H.M., Phillips, D.A., Okayasu, A., Shimozono, T., Liu, H., Mohammed, F., Skanavis, V., Synolakis, C.E. and Takahashi, T. (2012) The 2011 Japan tsunami current velocity measurements from survivor videos at Kesennuma Bay using LiDAR. *Geophysical Research Letters*, 39(7).

Fuhrman, D. R., and Madsen, P. A. (2008) Simulation of nonlinear wave run-up with a high-order Boussinesq model. *Coastal Engineering*, 55(2), 139-154.

Fujii, Y., and Satake, K. (2007) Tsunami source of the 2004 Sumatra–Andaman earthquake inferred from tide gauge and satellite data. *Bulletin of the Seismological Society of America*, 97(1A), S192-S207.

Geist, E. L. (2005) *Local tsunami hazards in the Pacific Northwest from Cascadia subduction zone earthquakes*. US Dept. of the Interior, US Geological Survey.

Geist, E. L., and Parsons, T. (2006) Probabilistic Analysis of Tsunami Hazards. *Natural Hazards*, 37(3), 277-314.

Goda, K., Mai, P. M., Yasuda, T., and Mori, N. (2014) Sensitivity of tsunami wave profiles and inundation simulations to earthquake slip and fault geometry for the 2011 Tohoku earthquake. *Earth, Planets and Space*, 66(1), 1-20.

Goldfinger C, Nelson CH, Morey AE, Johnson JE, Patton JR, Karabanov E., Patton, J., Gracia, E., Enkin, R., Dallimore, A., Dunhill, G., and Vallier, T. (2012) *Turbidite Event History: Methods and Implications for Holocene Paleoseismicity of the Cascadia Subduction Zone* U.S. Geological Survey Professional Paper 1661-F, 178 p.

González, F.I., Geist, E.L., Jaffe, B., Kânoğlu, U., Mofjeld, H., Synolakis, C.E., Titov, V.V., Arcas, D., Bellomo, D., Carlton, D. and Horning, T. (2009) Probabilistic tsunami hazard assessment at seaside, Oregon, for near-and far-field seismic sources. *Journal of Geophysical Research: Oceans*, 114(C11).

Grilli, S. T., Ioualalen, M., Asavanant, J., Shi, F., Kirby, J. T., and Watts, P. (2007) Source constraints and model simulation of the December 26, 2004, Indian Ocean tsunami. *Journal of Waterway, Port, Coastal, and Ocean Engineering*, 133(6), 414-428.

Hanks, T. C., and Kanamori H. (1979) Moment magnitude scale. *Journal of Geophysical, Research*, 84, 2348–2350.

Hayes, P. (2011) Rapid source characterization of the 2011 M w 9.0 off the Pacific coast of Tohoku Earthquake. *Earth, Planets and Space*, 63(7), 529-534.

Heaton, T. H., and Hartzell, S. H. (1987) Earthquake hazards on the Cascadia subduction zone. *Science*, 236(4798), 162-168.

Jaffe, B.E., Borrero, J.C., Prasetya, G.S., Peters, R., McAdoo, B., Gelfenbaum, G., Morton, R., Ruggiero, P., Higman, B., Dengler, L. and Hidayat, R. (2006) Northwest Sumatra and offshore islands field survey after the December 2004 Indian Ocean tsunami. *Earthquake Spectra*, 22(S3), 105-135.

Ji, C. (2015a) Rupture process of the 2007 Jan 13 Mw 8.1 - KURIL Island Earthquake, Publishing USGSWeb.
http://earthquake.usgs.gov/earthquakes/eqinthenews/2007/us2007xmae/figures/static_out
Accessed 02 June 2015.

Ji, C. (2015b) Preliminary Result of the Sep 12, 2007 Sumatra Earthquake, Publishing USGSWeb.
http://earthquake.usgs.gov/earthquakes/eqinthenews/2007/us2007hear/results/static_out.
Accessed 02 June 2015.

Koketsu, K., Yokota, Y., Nishimura, N., Yagi, Y., Miyazaki, S.I., Satake, K., Fujii, Y., Miyake, H., Sakai, S.I., Yamanaka, Y. and Okada, T. (2011) A unified source model for the 2011 Tohoku earthquake. *Earth and Planetary Science Letters*, 310(3), 480-487.

Koshimura, S., Oie, T., Yanagisawa, H., and Imamura, F. (2009) Developing fragility functions for tsunami damage estimation using numerical model and post-tsunami data from Banda Aceh, Indonesia. *Coastal Engineering Journal*, 51(03), 243-273.

Kulkarni, R., Wong, I., Zachariasen, J., Goldfinger, C., and Lawrence, M. (2013) Statistical analyses of great earthquake recurrence along the Cascadia subduction zone. *Bulletin of the Seismological Society of America*, 103(6), 3205-3221.

Lay, T., Kanamori, H., Ammon, C. J., Hutko, A. R., Furlong, K., and Rivera, L. (2009) The 2006–2007 Kuril Islands great earthquake sequence. *Journal of Geophysical Research*: Solid Earth (1978–2012), 114(B11).

Lorito, S., Romano, F., Piatanesi, A., and Boschi, E. (2008) Source process of the September 12, 2007, Mw 8.4 southern Sumatra earthquake from tsunami tide gauge record inversion. *Geophysical Research Letters*, 35(2).

Lynett, P., and Liu, P. L. F. (2005) A numerical study of the run-up generated by three-dimensional landslides. *Journal of Geophysical Research: Oceans*, 110(C3).

Lynett, P., Wu, T., and Liu, P. (2002) Modeling wave runup with depth-integrated equations. *Coastal Engineering* 46: 89-107.

McGuire, R. K. (2004) *Seismic hazard and risk analysis*. Earthquake Engineering Research Institute.

Mikami, T., Shibayama, T., Esteban, M. and Matsumaru, R. (2012) Field survey of the 2011 Tohoku earthquake and tsunami in Miyagi and Fukushima prefectures. *Coastal Engineering* Journal, 54(01), p.1250011.

Mofjeld, H. O., González, F. I., Titov, V. V., Venturato, A. J., and Newman, J. C. (2007) Effects of Tides on Maximum Tsunami Wave Heights: Probability Distributions*. *Journal of Atmospheric and Oceanic Technology*, 24(1), 117-123.

Mori, N., Takahashi, T., Yasuda, T. and Yanagisawa, H. (2011) Survey of 2011 Tohoku earthquake tsunami inundation and run-up. *Geophysical Research Letters*, 38(7).

Murotani, S., Miyake, H., and Koketsu, K. (2008) Scaling of characterized slip models for plate-boundary earthquakes. *Earth, Planets and Space*, 60(9), 987-991.

Murotani, S., Satake, K., and Fujii, Y. (2013) Scaling relations of seismic moment, rupture area, average slip, and asperity size for M~ 9 subduction-zone earthquakes. *Geophysical Research Letters*, 40(19), 5070-5074.

Nelson, A. R., Kelsey, H. M., and Witter, R. C. (2006) Great earthquakes of variable magnitude at the Cascadia subduction zone. *Quaternary Research*, 65(3), 354-365.

Okada, Y. (1985) Surface deformation due to shear and tensile faults in a half-space. *Bulletin of the Seismological Society of America*, 75(4), 1135-1154.

Park, H., Cox, D. T., Lynett, P. J., Wiebe, D. M., and Shin, S. (2013) Tsunami inundation modeling in constructed environments: A physical and numerical comparison of free-surface elevation, velocity, and momentum flux. *Coastal Engineering*, 79, 9-21.

Park, H., Cox, D. T., and Petroff, C. M. (2015). An empirical solution for tsunami run-up on compound slopes. *Natural Hazards*, 76 (3), 1727-1743.

Priest, G. R., Goldfinger, C., Wang, K., Witter, R. C., Zhang, Y., and Baptista, A. M. (2010) Confidence levels for tsunami-inundation limits in northern Oregon inferred from a 10,000-year history of great earthquakes at the Cascadia subduction zone. *Natural Hazards*, 54(1), 27-73.

Rossetto, T., Peiris, N., Pomonis, A., Wilkinson, S.M., Del Re, D., Koo, R. and Gallocher, S. (2007) The Indian Ocean tsunami of December 26, 2004: observations in Sri Lanka and Thailand. *Natural Hazards*, 42(1), 105-124.

Satake, K., Wang, K., and Atwater, B. F. (2003) Fault slip and seismic moment of the 1700 Cascadia earthquake inferred from Japanese tsunami descriptions. *Journal of Geophysical Research: Solid Earth* (1978–2012), 108(B11).

Satake, K., Fujii, Y., Harada, T., and Namegaya, Y. (2013) Time and space distribution of coseismic slip of the 2011 Tohoku earthquake as inferred from tsunami waveform data. *Bulletin of the Seismological Society of America*, 103(2B), 1473-1492.

Shao, G., Li, X., Ji, C., and Maeda, T. (2011) Focal mechanism and slip history of the 2011 M w 9.1 off the Pacific coast of Tohoku Earthquake, constrained with teleseismic body and surface waves. *Earth, Planets and Space*, 63(7), 559-564.

Shao et al. (2015) Preliminary slip model of the Feb 27, 2010 Mw 8.9 Maule, Chile Earthquake, Publishing USGSWeb.
http://www.geol.ucsb.edu/faculty/ji/big_earthquakes/2010/02/27/result/static out Accessed 02 June 2015.

Suppasri, A., Mas, E., Koshimura, S., Imai, K., Harada, K., and Imamura, F. (2012) Developing tsunami fragility curves from the surveyed data of the 2011 Great East Japan tsunami in Sendai and Ishinomaki Plains. *Coastal Engineering Journal*, 54(01), 1250008.

Synolakis, C. E., Bernard, E. N., Titov, V. V., Kânoğlu, U., and González, F. I. (2008) Validation and verification of tsunami numerical models. *Pure and Applied Geophysics*, 165(11-12), 2197-2228.

Titov, V.V., Gonzalez, F.I., Bernard, E.N., Eble, M.C., Mofjeld, H.O., Newman, J.C. and Venturato, A.J. (2005) Real-time tsunami forecasting: Challenges and solutions. In *Developing Tsunami-resilient Communities* (41-58). Springer Netherlands.

Titov, V. V., Moore, C. W., Greenslade, D. J. M., Pattiaratchi, C., Badal, R., Synolakis, C. E., and Kânoğlu, U. (2011) A new tool for inundation modeling: Community Modeling Interface for Tsunamis (ComMIT). *Pure and Applied Geophysics*, 168(11), 2121-2131.

Tsunami Pilot Study Working Group (2006) Seaside, Oregon, *Tsunami Pilot Study-Modernization of FEMA Flood Hazard Maps*. Joint NOAA/USGS/FEMA Special Report 94.

Wang, H., Mostafizi, A., Cramer, L., Cox, D., and Park. H. (2015) An agent-based model of a multimodal near-field tsunami evacuation: Decision-making and life safety. *Transportation Research Part C: Emerging Technologies*, http://dx.doi.org/10.1016/j.trc.2015.11.010.

Wang, K., Wells, R., Mazzotti, S., Hyndman, R. D., and Sagiya, T. (2003) A revised dislocation model of interseismic deformation of the Cascadia subduction zone. *Journal of Geophysical Research: Solid Earth* (1978–2012), 108(B1).

Wiebe, D. M., and Cox, D. T. (2014) Application of fragility curves to estimate building damage and economic loss at a community scale: a case study of Seaside, Oregon. *Natural Hazards*, 71(3), 2043-2061.

Witter, R.C., Zhang, Y.J., Wang, K., Priest, G.R., Goldfinger, C., Stimely, L., English, J.T. and Ferro, P.A. (2013) Simulated tsunami inundation for a range of Cascadia megathrust earthquake scenarios at Bandon, Oregon, USA. *Geosphere*, 9(6), 1783-1803.

Yagi, Y. (2004) Source rupture process of the 2003 Tokachi-oki earthquake determined by joint inversion of teleseismic body wave and strong ground motion data. *Earth, Planets and Space*, 56(3), 311-316.

Zhang, Y. and Baptista, A.M. (2008) SELFE: a semi-implicit Eulerian–Lagrangian finite-element model for cross-scale ocean circulation. *Ocean Modelling*, 21(3), pp.71-96.

2.10 Nomenclature

Symbol	Descriptions	Unit
D	Fault slip displacement	L
D'	Normalized D by D_P	-
D_P	Peak fault slip displacement	L
dL	Unit rupture length	L
dW	Unit rupture width	L
h	Inundation depth	L
L	Rupture length	L
Lat	Latitude	L
$Long$	Longitude	L
M	Momentum flux	L^3T^{-2}
M_W	Moment magnitude	ML^2T^{-2}
M_0	Seismic moment	ML^2T^{-2}
min	Minute	T
N	Number of occurrence	-
N_s	Numbers of scenarios	-
P	Probability	-
P_W	Weighting factor	-
S	Rupture area	L^2
s	Second	T
T_A	The first arrival time of exceeding 1 m inundation	T
T_h	Duration of exceeding 1 m of inundation depth	T
T_R	Representative tsunami period	
V	Velocity	LT^{-1}
W	Rupture width	L
X'	Dip direction	L
Y'	Strike direction	L
z	Ground elevation from referenced level	L
α	Mean of Gaussian distribution	L
α'	Peak slip location parameter, normalized α	-
β	Standard deviation of Gaussian distribution	L
β'	Slip shape parameter	-
ξ	Iribarren number	-
η	Surface elevation	L
μ	Shear modulus of the rock	$ML^{-1}T^{-2}$
ν	Mean occurrence rate	-
$(\bar{\ })$	Mean of ( )	-
$(\ )_{Max}$	Maximum value of ( )	-

3. Probabilistic Tsunami Damage Estimation on Built Environments and Sensitivity Applied at Seaside, Oregon.[2]

3.1 Abstract

Annual exceedance probabilities of flow depth, h_{Max} and momentum flux, M_{Max} for a tsunami conditioned on a full-rupture of the Cascadia Subduction Zone are used to estimate building damage using a fragility curve analysis. Tax lot data, Google Street View, and field reconnaissance surveys are used to classify the buildings at a community scale and match with existing fragility curves according to construction material, floor level and build year. The fragility analysis is used to estimate the damage probability of buildings for a 1,000-year event conditioned on a full-rupture CSZ event. The sensitivity of building damage to the both the aleatory and epistemic uncertainty involved in the process of damage estimation are presented. Fragility curves based on depth and based on momentum flux both generally show higher damage probability for structures that are wooden and closer to the shoreline than those that are reinforced concreted (RC) and landward of the shoreline. However, a relatively high damage probability was found at the river and creek region from the fragility curve analysis using h_{Max}. Within 500 m from the shoreline, wood structure damage shows a significant sensitivity to the aleatory uncertainty of the tsunami generation from the CSZ event. On the other hand, RC structure damage showed equal sensitivity to the aleatory uncertainty of the tsunami generation as well as the epistemic uncertainties due to the numerical modelling of the tsunami inundation (friction), the building classification (material and build year), and the type of fragility curves (depth or momentum type curves). Further from the shoreline, the wood structures showed similar uncertainties to the aleatory and epistemic uncertainties.

3.2 Introduction

Over the past two decades, megathrust earthquakes and resulting tsunamis, such as the 2004 Indian Ocean tsunami, the 2010 Chile tsunami, and the 2011 Tohoku tsunami have generated catastrophic casualties and damage to the built and natural environments. Post-disaster surveys provide records of tsunami damage to the built environment (Jaffe et al., 2006; Rosetto

[2] Hyoungsu Park, Daniel T. Cox, and Andre Barbosa. “Probabilistic Tsunami Damage Estimation on Built Environments and Sensitivity Applied at Seaside, Oregon,” in preparation for *Natural Hazard*.

et al., 2007; Mikami et al., 2012). These studies highlight the need for strategies to increase the resilience of communities to prepare and minimize damages and losses from future tsunami events. For the study of tsunami resilience, it is necessary to understand the hazard, to estimate how the systems in the built environment will respond, and to predict the recovery processes of these systems. The five most critical civil infrastructure systems are buildings, transportation networks (bridges and roads, harbors, railways, and airports), water and wastewater networks, energy networks (electric power and fuel) and communication networks (radio, landlines and wireless). To mitigate or minimize the damage and improve the resilience against to future tsunami events at coastal regions, it is important to evaluate both the future tsunami hazards and corresponding damage and loss to each engineered systems.

Considering the response of buildings from tsunami inundation, several attempts have been made to estimate the direct tsunami induced forces on buildings utilizing the components of tsunami inundation depth, velocity, and also shape of buildings (e.g. Yeh 2007; Nistor et al., 2009). FEMA P-646 (2012) conveniently classifies seven tsunami induced forces on a building during tsunami inundation process as the hydrostatic force, buoyancy force, hydrodynamic force, impulsive force, debris impact force, debris damming force and uplift force. Although it might be possible to estimate these forces for an individual building to determine the design considerations to enable it to withstand the tsunami inundation, it is difficult to apply these forces on the scale of an entire city comprised of thousands of buildings. Moreover, there are a wide range of possibilities for failure include foundation failure, structural failure of columns or beams, failure of infilled walls, or the displacement, rotating, and overturning of buildings (Ruangrassamee et al., 2006; Reese et al. (2007), Valencia et al. (2011), Mori et al., 2013; Yeh et al., 2013).

A fragility curve analysis is a widely utilized probabilistic methods to estimate the building and other infrastructure damage from diverse hazards such as earthquake, flood, hurricane, and tsunami. The fragility curve describes the probability of reaching or exceeding damage levels for a given intensity measure. The damage levels are often described as minor, moderate, major, complete, and collapse damage. Minor damage is considered as easily reparable and often does not affect the functionality of the building. Complete or collapse damage, on the other hand, can be considered as a failure of building and can be a threat to life safety for building occupants. For tsunamis, a higher damage state “washed away” can also be

considered (Suppasri et al., 2013). The intensity measures (IMs) parameterize the hazard and can include peak ground acceleration (PGA) for earthquakes (MRl, HAZUS-MH, 2003), flood depth for floods (Scawthorn et al., 2006), maximum wind speed for hurricanes (Ellingwood, et al., 2004; van de Lint and Dao, 2009), and the maximum inundation depth, velocity or momentum flux for tsunami (Koshimura et al., 2009; Suppasri et al., 2013; FEMA 2013). A fragility curve must be constructed for different building types. For example, construction material (wood versus reinforce concrete), the number of floors, the age of construction all affect the ability of the structure to withstand the environmental forces. Therefore, it is necessary to construct a large number of fragility curves to apply this type of analysis to a community with possibly hundreds of different types of structures.

In this study, we provide a general framework for the probabilistic damage assessment on buildings from future tsunami events with a community scale utilizing existing diverse fragility curves, utilized the tsunami hazard assessment from Chapter 2. Here are the four major objectives of this study for Chapter 3:

1) Provide a framework of the probabilistic tsunami damage estimation on buildings with a community scale.
2) Compare the fragility curves developed by other authors from two types of intensity measures (inundation depth and momentum flux)
3) Provide the method to determine for building classification, introducing three tools (a tax lot database, Google Street View, and field reconnaissance (Rapid Visual Screening)).
4) Estimate the building damage probability at Seaside, Oregon, conditioned on a full-rupture CSZ event.
5) Evaluate the sensitivity of building damage from the uncertainties (aleatory and epistemic) on the damage assessment process such as tsunami generation (different scenarios), numerical modelling (friction), building information (floors and build year), and fragility curve types (inundation depth or momentum flux).

These objectives are achieved in the following sections. Section 3.3 introduces the study area, Seaside, Oregon, and the methodology utilized in this study with a review of previous work. Section 3.4 introduces the existing fragility curves utilized in this study. Section 3.5 introduces

the tools for the collecting building information to apply for the fragility curve analysis and shows the building classification results. Section 3.6 shows the probabilistic tsunami damage estimation on buildings at Seaside, Oregon. Section 3.7 introduces the sensitivity of damage probability due to the uncertainties involved in the damage estimation process, and quantitatively compares five uncertainties. Section 3.8 discusses about the limits of the current work and possible future works. Finally, Section 3.9 provide the conclusions of this study.

3.3 Study Area and Methodology

3.3.1 Study area

Seaside, Oregon, is used as the study area. Seaside has been described as the most vulnerable coastal city in Oregon from Cascadia Subduction Zone (CSZ) events (Wood, 2007). Fig 3.1a shows a regional map of the CSZ and our study area. The CSZ is located at the converging area between Juan de Fuca Plate and North American Plate from Vancouver Island (Canada) to northern California. Fig. 3.1a also shows three Grid maps (Grid-A, B, and C) of numerical models ComMIT/MOST (Titov et al., 2011) and COULWAVE (Lynett et al., 2002) using in this study. The detail bathymetry information of C-Grid is presented in Fig. 3.1b. The elevations of most entire city are less than 5 m (dashed lines) above the mean high water level (MHW), and the elevations are close to MHW near the region of the river and creek which penetrate the city. The detail information of numerical modelling and boundary conditions are summarized at Subsection 3.3.3.

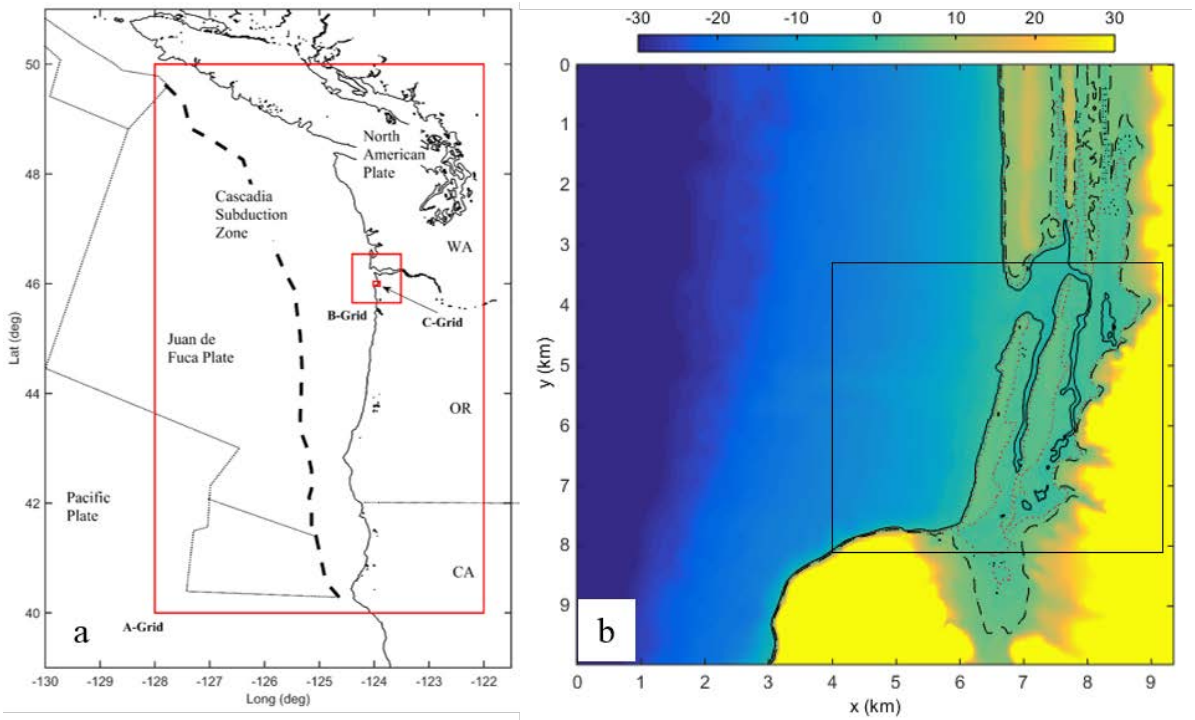

Fig. 3.1 (a) Regional map of Cascadia Subduction Zone with numerical model grids and (b) C-Grid bathymetry. Dotted and dashed lines in are 3 m and 5 m elevation contours from the MHW. Inner box shows the region of aerial view will be shown at Fig. 3.2a.

The vulnerability of this city to possible tsunami hazards, including estimates of damage and life safety, have been widely studied by various research groups (Tsunami Pilot Study Working Group, 2006; González et al., 2009; Dominey-Howes et al., 2010; Wiebe and Cox, 2012; Wang et al., 2015; Chapter 2). In recent studies on life safety and evacuation from tsunami event at Seaside by Wang et al. (2015) and Priest et al. (2016) indicated the problems of existing evacuation routes and the necessity of evacuation shelters to minimize the casualties in the city. Alternatively, the high floors of existing or proposed buildings may serve as a potential heaven for evacuees, but the damage estimation of buildings is a priority task for this option.

Fig. 3.2a shows the aerial view of Seaside, with a detailed view of the central area shown in Fig. 3.2b. The Necanicum River and Neawanna Creek penetrate the city from the south to north and flow out to the ocean at the northern edge of city. The city is vulnerable from future tsunami event at the CSZ due to the shallow and flat ground elevations. The extent of the tsunami inundation for most full-rupture CSZ scenarios covers approximately 90% of the town area. The arrival time of initial tsunami wave is only 35 – 40 minutes at Point 1 as shown in

Chapter 2. Point 1 (formerly Point B in Chapter 2) indicates a representative observation location at the shoreline, the center of Seaside.

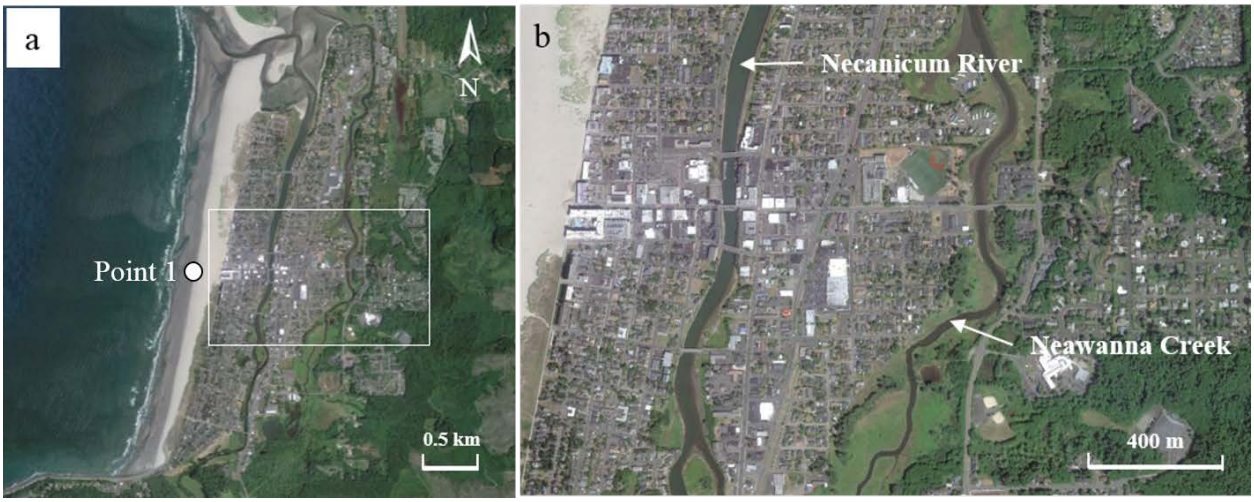

Fig. 3.2 Aerial photos of Seaside, Oregon (images modified from Google Earth).

3.3.2 Methodology

Fig. 3.3 shows the framework of the probabilistic tsunami damage assessment on buildings at a community scale. The flow chart is separated into 2 parts and was described in Chapter 1 (Introduction). For completeness, each of the seven steps is discussed briefly.

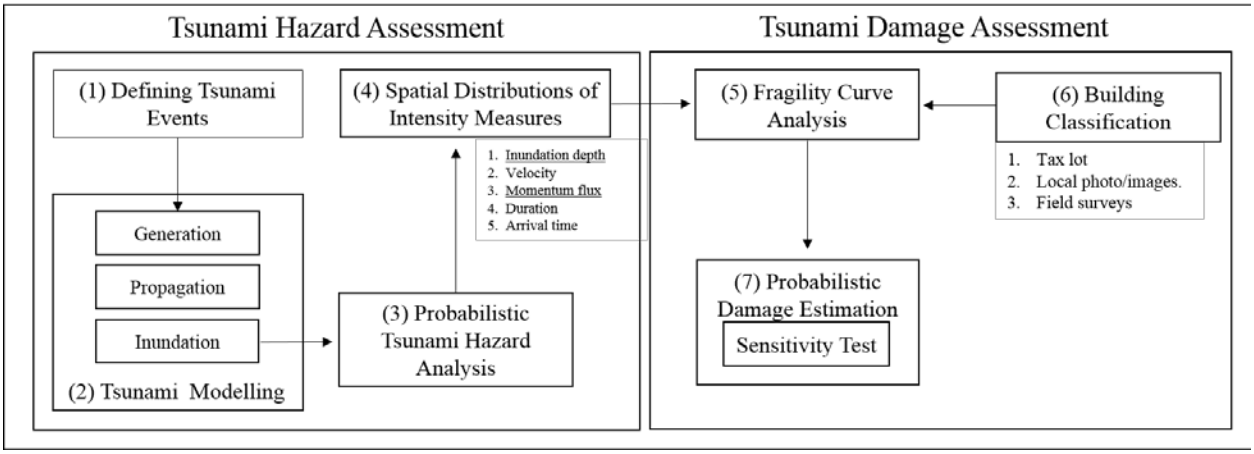

Fig. 3.3 Flow chart of the probabilistic tsunami damage estimation process.

1) Defining Tsunami Events: We determine the seismic conditions conditioned on a full-rupture CSZ event. Parameters include moment magnitude, peak slip location, and slip distribution (Chapter 2).

2) Tsunami Modelling: We calculate the tsunami generation, propagation, and inundation process. For this study, we utilized ComMIT/MOST model for tsunami generation and propagation, and COULWAVE for tsunami inundation. The COULWAVE model provides the time series of surface elevation and velocity over the entire inundation area.
3) Probabilistic Tsunami Hazard Analysis: We integrate the numerical results and utilized a Poisson arrival process to estimate the annual exceedance probability of five intensity measures (IMs) conditioned on a full-rupture CSZ event.
4) Spatial Distribution of Intensity Measures: We provide the spatial distributions of IMs at for a P = 0.002 and P=0.001 annual exceedance probability ("500-year" and "1,000-year events) for both maximum inundation depth and maximum momentum flux.
5) Fragility Curves Analysis: We estimate the building damage using existing fragility curves developed for a set of building characteristics (material, floors, or build year), and different types of IMs (maximum inundation depth and momentum flux).
6) Building Classification: We collect building information at Seaside, Oregon, classifying each building to match with fragility curves.
7) Probabilistic Damage Estimation and Sensitivity Test: We provide the building damage probabilities with sensitivity tests to quantify the aleatory and epistemic uncertainties involved in this frame work.

3.3.3 Review of probabilistic tsunami hazards assessment at Seaside, OR.

Probabilistic tsunami hazard assessments (PTHA) at Seaside have been performed by several research groups. González et al. (2009) suggested the integration of numerical tsunami inundation modeling and with the methodology used for probabilistic seismic hazard assessment (PSHA). They developed a maximum tsunami wave amplitude map for a given annual probability of exceedance, such as 100 or 500-year event using Seaside as an example case. However, they only examined 12 scenarios for the CSZ and provided the maximum inundation depth only. Recently, Park and Cox (2016, Chapter 2) performed probabilistic near-field tsunami hazard assessment (PNTHA) at the CSZ utilizing the similar probabilistic approaches. They implemented the new method to define a fault rupture of earthquake for tsunami generation modelling reflecting the randomness of nature on tsunami generation, and they characterized the randomness of the fault slip distribution at rupture area as a Gaussian distribution with three

parameters, which are moment magnitude of earthquake, location of peak slip, and shape of faults slip along the strike direction. They also adapted the weighting factors for each scenario, and provide five tsunami hazard metrics including the maximum inundation depth velocity, and momentum flux, which are the possible IMs for the tsunami fragility curve analysis. In this study, we utilized the work at Chapter 2 for the tsunami hazard assessment process, which are steps (1) through (4) in the flow chart (Fig. 3.3). The remainder of this work focuses on the remaining steps (5) to (7) to estimate buildings damage.

Fig. 3.4 shows an example of Step (3) which is the annual exceedance of the maximum inundation depth (Fig. 3.4a) and momentum flux (Fig. 3.4b) at Point 1 from the CSZ event. Fig. 3.4a shows that there is 0.001 annual probability of exceeding a 9.2 m inundation depth and a 0.0001 annual probability exceeding 14 m inundation depth at Point 1 conditioned on a full-rupture CSZ event. In the same manner, Fig. 3.4b shows that there is 0.001 annual probability exceeding 150 m^3/s^2 momentum flux and 0.0001 annual probability exceeding 530 m^3/s^2 momentum flux at Point 1.

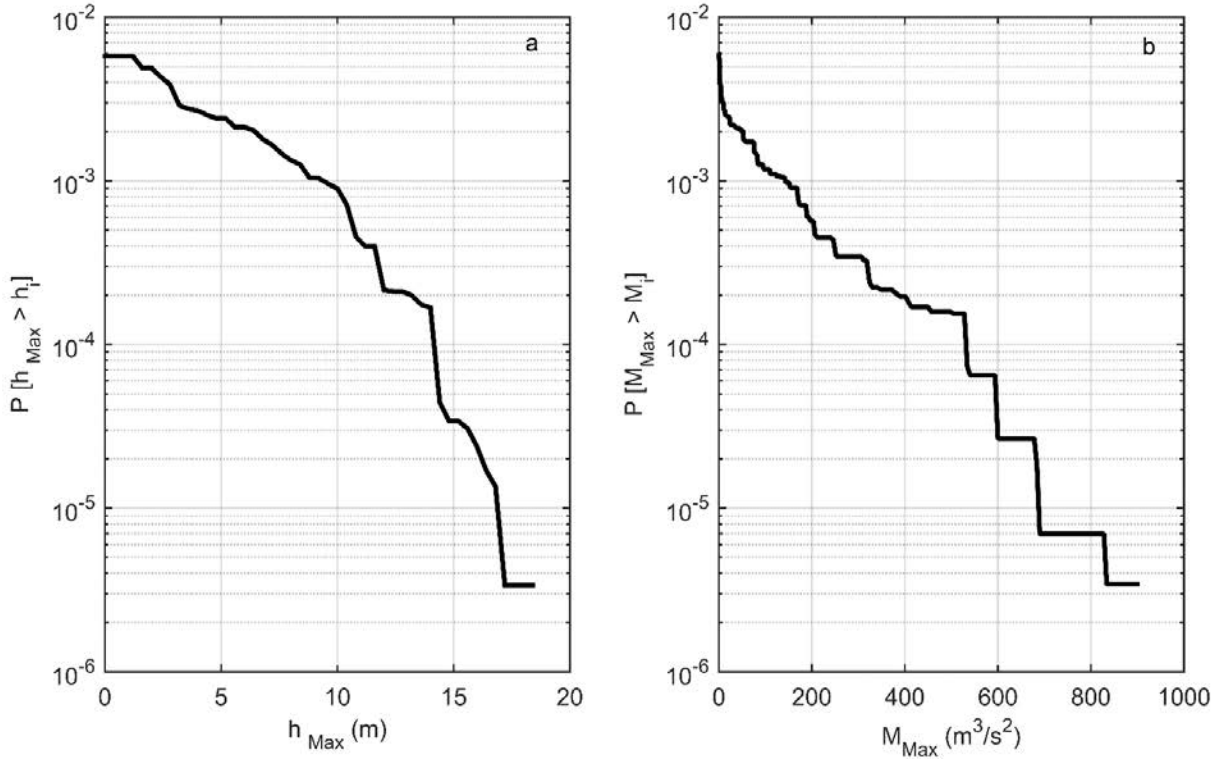

Fig. 3.4 Example of the annual exceedance of the maximum inundation depth and momentum flux at Point 1.

Fig. 3.5 shows the result of Step (4) to quantify the spatial distribution of the intensity measures (IMs). Fig 3.5 shows the 1,000-year event at CSZ over the tax lot parcel grid for the maximum inundation depth (h_{Max}) and the maximum momentum flux (M_{Max}). The tax lot data are described in Section 3.5. For clarity in the discussions and descriptions of the results we separate the detailed area into three regions: Region A from the shoreline to the Necanicum River where the most significant hazards and damages are predicted, Region B from the Necanicum River to the Neawanna Creek, and Region C from the Neawanna Creek to the inland inundation limit which is about 2 km from the shoreline.

Fig. 3.5 Spatial distributions of h_{Max} (top panels), and M_{Max} (bottom panels) from 1,000-year event at CSZ over the tax lot shapefile format at Seaside, OR.

The both spatial distribution show that the intensity of h_{Max} and M_{Max} generally decrease from the shoreline to inland (from Region A to C). The range of the maximum inundation depth and momentum flux at the Region A is $4.0 < h_{Max} < 10.0$ m and $20 < M_{Max} < 150$ m^3/s^2, while in Region B it is $1.0 < h_{Max} < 5$ m and $0 < M_{Max} < 10$ m^3/s^2 at, and in Region C it is only $0 < h_{Max} <$

1 m and $0 < M_{Max} < 5$ m^3/s^2 at Region C. There are two distinct differences between the spatial distributions of h_{Max} and M_{Max}. First, a relatively higher h_{Max} is found near the Necanicum River (6 to 7 m) and also the Neawanna Creek (3 to 5 m), while there is no amplification of M_{Max} at the same regions. The increase of h_{Max} at the river and creek is caused from the overlapping of two inundation flows such as shore-normal and following up the river and creek. The similar phenomenon had been observed during 2011 Tohoku tsunami in Japan (Mimura et al., 2011; Suppasri et al., 2012) Second, the intensity of M_{Max} decreases significantly across Region A, and decrease slowly and more uniform across Region B.

3.4 Fragility curves analysis

A tsunami fragility curve provides a quantitative estimate of the damage probability exceeding a given damage state on a building as a function of the tsunami intensity measure (IM) such as the maximum inundation depth, velocity, or momentum flux. Tsunami fragilities have developed only relatively recently since the 2004 Indian Ocean tsunami (Koshimura et al., 2009). There are four types of methods to develop the tsunami fragility curves, such as a satellite image, numerical simulation, field survey, and experiment or theory. In addition, more than two methods are utilized together as a hybrid method (Koshimura et al., 2009; Valencia et al. (2011); Suppasri et al., 2011; Gokon et al., 2014). They utilized the both satellite image inspection or field survey to determine the damage state of building and also utilized numerical simulation to estimate other types of IMs such as the maximum velocity or hydrodynamic force beside the inundation depth. The 2011 Tohoku tsunami provides a large number of observations of buildings damage states, building materials, and number of floors by The Ministry of Land, Infrastructure, and Transportation (MLIT) with corresponding measured of the maximum inundation depth by the Tohoku Earthquake Tsunami Joint Survey Group (2011). Correspondingly, a number fragility curves relating the damage states and building characteristics were developed utilizing the surveyed maximum inundation depth as an IM for the fragility curve (Suppasri et al., 2013; Charvet et al., 2014; Suppasri et al., 2015). Table 3.1 summarizes previously developed fragility curves which utilized relatively large numbers (> 900) of building samples to develop tsunami fragility curves empirically after the 2004 Indian Ocean, 2009 American Samoa, 2010 Chilean tsunami, and 2011 Tohoku tsunami.

Table 3.1 Summary of developed fragility curve since 2004 Indian Ocean tsunami

Source	Country/Location	Sample	Method	IM	Reference
2004 Indian Ocean	Indonesia/ Banda Aceh	48,910	SI, NS	h_{Max}, V_{Max}, F_{Max}	Koshimura et al. (2009)
	Indonesia/ Banda Aceh	2,576	SI, FS	h_{Max}	Valencia et al. (2011)
	Thailand/ Phang Nga, Phuket	4,596	FS, NS	h_{Max}, V_{Max}, F_{Max}	Suppasri et al. (2011)
	Sri Lanka/SW coast	1,535	FS	h_{Max}	Murao & Nakazato (2010)
2009 American Samoa	American Samoa/ 4 Sites	6,239	SI, NS	h_{Max}, V_{Max}, F_{Max}	Gokon et al. (2014)
2010 Chile	Chile/Dichato	915	SI, FS	h_{Max}	Mas et al. (2012)
2011 Tohoku	Japan/ Miyagi Prefecture	157,640	SI, FS	h_{Max}	Koshimura & Gokon (2014)
	Japan/East coast	251,301	FS	h_{Max}	Suppasri et al. (2013)
	Japan/Ishinomaki	63,605	FS	h_{Max}	Suppasri et al. (2015)
Hazus-EQ	United States	-	ET	M_{Max}	FEMA (2013)

Method: SI (Satellite images) NS (Numerical simulation), FS (Field survey), ET (Experiment or Theory)
IM: h_{Max} (The maximum inundation depth), V_{Max} (The maximum velocity), F_{Max} (The maximum hydrodynamic force) and M_{Max} (The maximum momentum flux)

The basic functional form of a tsunami fragility curve can be given by (e.g., Koshimura et al., 2009) as

$$P(X) = \Phi\left[(X-\mu)/\sigma\right] \tag{16}$$

$$P(X) = \Phi\left[(\ln(X)-\mu')/\sigma'\right] \tag{17}$$

where P is the cumulative probability of damage, Φ is the standardized normal (lognormal) distribution function, X is the intensity measure and μ and σ (μ' and σ') are the mean and standard deviation of X (ln (X)), determined by least-square fitting. The intensity measures considered by Koshimura et al. (2009) include the maximum inundation depth (h_{Max}), velocity (V_{Max}) and hydrodynamics force (F_{Max}) and were used to develop fragility curves from 2004 Indian Ocean tsunami at Banda Aceh. They calculated the maximum inundation depth and

velocity at the site numerically, and they evaluated the corresponding damage level using before and after satellite images. They developed a fragility curves for wood and reinforced concrete building and the three IMs (h_{Max}, V_{Max}, and F_{Max}) through the regression analysis using a standardized normal (log normal) function. A similar approach was adapted in different sites in Thailand based on the surveyed damage levels and numerical model results by Suppasri et al. (2011). Similarly, other research groups utilized building survey damage and the observed inundation depth as the IM (Murao and Nakazato, 2010; Valencia et al., 2011; Reese et al., 2011) to develop fragility curves. After 2011 Tohoku tsunami, a total of 251,301 damaged buildings were surveyed in Japan. A series of fragility curves were developed using the surveyed maximum inundation depth for six building materials, six damage states (e.g. minor, moderate, major, complete, collapse, and wash away), and three building floor levels, or topography conditions (Suppasri et al., 2013). Recently, the Federal Emergency Management Agency (FEMA) suggested using a momentum flux based fragility curve for tsunamis in their unpublished *Tsunami Methodology Technical Manual* (FEMA, 2013). Fragility curves from FEMA (2013) assume that the lateral force plays significant role in determining the damage condition during the tsunami inundation, and utilizes the maximum momentum flux (M_{Max}) as an IM for the new fragility curve for building damages. More details are discussed in Subsection 3.4.2.

However, it is noted that significant variations were found for fragility curves of the same building type and damage state. These variations could be due to local variations in the different sites where the building damage were observed because of unconsolidated methodology for typology of building and damage state and limited sources for fragility curve development (Tarbotton et al., 2015). More detail history of development of tsunami fragility curves and limits of current applications were summarized in Leelawat et al. (2014) and Suppasri et al. (2015).

3.4.1 Tsunami fragility curves with the maximum inundation depth

The maximum inundation depth is widely utilized as a preferable IM to develop tsunami fragility curve because it is measurable during a post-tsunami survey from indicators such as water marks and debris. The inundation velocity is difficult to measure and are extremely rare (Fritz et al., 2012). Moreover, the inundation depth can be predicted numerically with less variation compared to velocity. For example, the maximum inundation depth is less sensitive to

bottom roughness compared to maximum velocity (e.g. Park et al., 2013, Appendix A). Therefore, most recent fragility curves use the maximum inundation depth as the representative IM. However, the maximum inundation depth does not represent the complex hydrodynamics and interactions between water and structure during tsunami inundation (Valencia et al., 2011; Mas et al., 2012; Koshimura and Gokon, 2012; Suppasri et al., 2013; Charvet et al., 2014). Recently, comparisons of two different sites from 2011 Tohoku tsunami induced from the different velocity fields and it highlighted the necessity of an additional tsunami parameter such as the maximum velocity, momentum flux, hydrodynamic force, or debris concentration (Suppasri et al., 2015).

3.4.2 Tsunami fragility curves with the maximum momentum flux

The momentum flux, which is proportional to the inundation depth times of the square of velocity, is can be used to represent the hydrodynamic forces (lateral force) or debris damming force on structures (Yeh, 2007; Koshimura et al., 2009). FEMA (2013) introduces new sets of tsunami fragility curves for building damage, which comprises of 36 building types (materials, types and floor level) with three damage states and seven seismic building codes. The new damage fragility curves utilizes the maximum momentum flux (M_{Max}) to represent the lateral force induced from the inundation flow which induces the damage on the structures. The new approach assumes that the building damage is caused from mostly hydrodynamic and debris impact forces among the seven conceptual tsunami induced forces. The lateral tsunami flow force (F_{TS}) on an idealized building is

$$F_{TS} = K_d \left(0.5 \rho_s C_d B\left(M'\right)\right) \tag{18}$$

where K_d is coefficient related to the shielding or debris impact which has a default value of K_d =1.0, ρ_s is the fluid density, C_d is the drag coefficient which has a default value as C_d = 2.0 from FEMA P-646 (2012) for a rectangular building shape, B is building width normal to flow direction, and M' is median maximum momentum flux. B is representative width for each 36 building types, and M' characterizes the lateral tsunami force on the building accounting for hydrodynamic and debris damming forces. The format of damage fragility curve is

$$P\left(M\right) = \Phi\left[\ln\left(M_{Max} / M'\right) / \beta_M\right] \tag{19}$$

where M_{Max} is the given input maximum momentum flux from tsunami analysis modelling at a specific building, M' is the median value of the maximum momentum flux associated with

building types and damage state, which is determined by the assumption that the estimated tsunami lateral force from Eq. 18 is equal to the lateral capacity force of each building estimated from the Earthquake Model Technical Manual (FEMA, 2011). β_M is the logarithmic standard deviation describing the total uncertainty of the damage associated with debris (K_d), dimension of the building (B), and the earthquake lateral force estimation.

3.4.3 Comparison of two types of fragility curves

We select both sets of fragility curves developed using h_{Max} and M_{Max} for the building damage estimation, and we compare the damage probability from each types of fragility curve quantitatively at Seaside. As a representative fragility curves using h_{Max}, we utilized the work of Suppasri et al. (2013) whose fragility curves were developed from 2011 Tohoku tsunami, referred to hereafter as the "S2013 model"). For the momentum flux, we use the set of fragility curve from FEMA (2013) which were described in Section 3.2, referred to hereafter as the "FEMA model").

The S2013 and FEMA models used different methodology to classify the building damage states (DS), building types, and floor levels. The S2013 model followed the format of MLIT survey results, but the FEMA model followed the format of a previous hazard model developed by FEMA for flood, earthquake and hurricane damage estimation, referred to as the "HAZUS-MH" model. The differences between the two models are summarized in Table 3.2.

Table 3.2 Summary of the comparison of two types of fragility curves

IM	Model/Sources	DS	Material	N_{SF}[(1)]	Stories	Seismic code
h_{Max}	S2013 model / 2011 Tohoku Tsunami	Minor Moderate Major Complete Collapse Washed away	W Ma RC S B Mix	1	1[(2)] 2 ≥ 3	None
M_{Max}	FEMA model / Hazus-MH model	Moderate Extensive Complete	W S C PC RM UM MH	2 5 3 2 2 1 1	1 – 3 (Low) 4 – 7 (Mid) ≥ 8 (High)	Pre Low Moderate High Special-High Special-Moderate Special-Low

[(1)]: Number of structure frames applied in building typology; [(2)]: Stories information is only applicable for wood and RC structures in S2013 model.

The S2013 model utilized more detail damage states (DS), such as minor, moderate, major, complete, collapse, and washed away following the post tsunami survey results. On the other hand, the FEMA model only used three damage states, such as moderate, extensive and complete following the Hazus-MH model conventions (FEMA 2002). The detail descriptions of each DS are listed in Table 3.3.

Table 3.3 Damage state (DS) comparisons

Models	DS	Description
S2013 model	Minor	No significant structural or nonstructural damage, possibly only minor flooding
	Moderate	Slight damage to nonstructural components
	Major	Heavy damage to some walls but no damages in columns
	Complete	Heavy damage to several walls and some columns
	Collapse	Destructive damage to walls and several columns
	Washed away	Washed away, only foundation remained, totally overturned
FEMA model	Moderate	Less than 25% economic loss but no long-term building closure and collapse probability
	Extensive	25 – 100% economic loss, 50% of long-term building closure and local collapse of building.
	Complete	100% economic loss, long-term building closure or more than partial or full collapse including washed away.

In case of building materials, the S2013 model provides six classes for building material [wood (W), masonry (Ma), steel (S), reinforced concrete (RC), and Brick (B) and one mixed building material condition (Mix)], while the FEMA model provides seven classes [wood (W), steel (S), concrete (C), precast concrete (PC), reinforced masonry (RM), unreinforced masonry (UM), and mobile homes (MH)]. Each type of building material can be comprised of different building frames in the FEMA model. For example, a wood building can be classified as two types of building frames depending on its size (e.g. smaller or greater than 5,000 ft^2). Each steel and concrete buildings separated into 5 and 3 frame conditions, respectively as listed in Table 3.2. Both steel and RC utilized 3 classifications of building stories. The S2013 model classifies the number of stories as one, two and more than 3 stories. On the other hand, the FEMA model classifies the stories as ‘Low-Rise’ (1 – 3 stories), ‘Mid-Rise’ (4 – 7 stories) and ‘High-Rise’ (≥ 8 stories).

One of the significant differences between the two models is that the FEMA model provides a different classification for the year of construction (building year). The FEMA model classifies seven seismic design categories (SDCs) depending on the usage and age of the building (for example, a ‘4’ for ‘common’ building, and a ‘3’ for ‘special’ buildings such as hospitals and emergency centers, FEMA 2013). These building parameters are utilized to determine M' in Eq. 18 and 19, and show significant deviation depending on the SDCs. Generally, higher SDCs have a better capacity to withstand the tsunami induced lateral force. Suppasri et al. (2015) could not found any correlation between build year and intensity of building damage based on their study of 526 residential wooden houses surveyed in Japan after 2011 Tohoku tsunami.

Fig. 3.6 shows example fragility curves utilized in this study to estimate building damage. Fig. 3.6a shows four fragility curves of complete damage level from the S2013 model. Each thin solid and dashed line shows the fragility curve for a one story wood structure (W1) and a two story wood structure (W2). Thick solid and dashed lines show the fragility curve for a two story RC structure and an RC structure of more than 3 stories, respectively. W1 and W2 show only a small sensitivity to the number of stories, while RC building show much higher sensitivity to floor level conditions in the S2013 model.

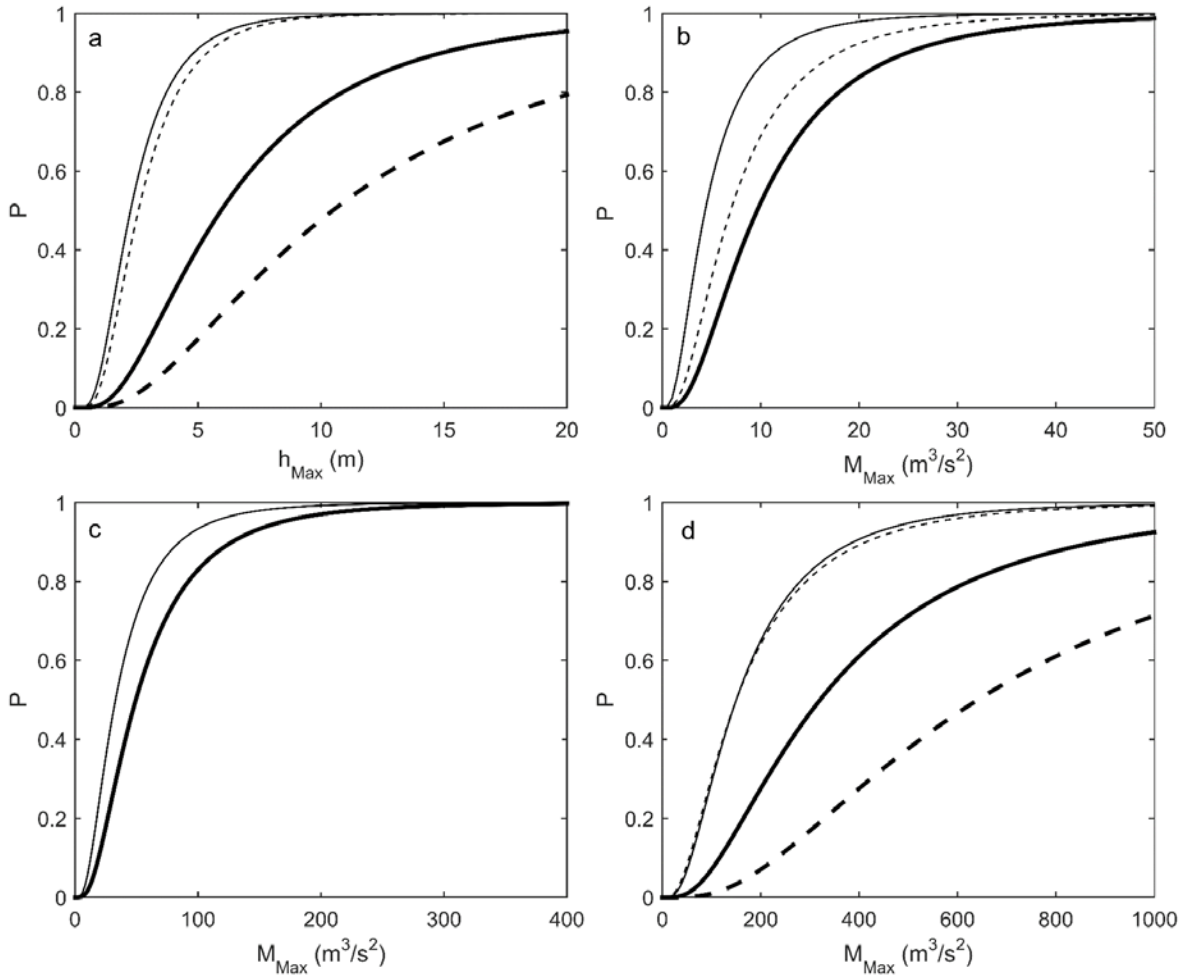

Fig. 3.6 Examples and comparisons of two types of tsunami fragility curves using h_{Max} or M_{Max} as IMs. (a) Fragility curve for 1 story wood structure (thin solid), 2 stories wood (thin dash line), 2 stories RC structure (thick solid), and RC structure more than 3 stories (thick dash) from S2013 model. (b) Wood structure fragility curves developed with momentum flux. Thin solid line presents the wood structure fragility curve from Koshimura et al. (2009) which is converted to momentum flux, and each thin dash and think solid line presents the wood structure less than 5,000 ft^2 and greater than 5,000 ft^2 from FEMA model. (c) The fragility curve of the RC building with a moment frame and 1 – 3 floors level. Thin solid line present the both 'Moderate' and 'Extensive' damage state fragility curves, and the thick solid line presents the 'Complete' damage state fragility curve of FEMA model. (d) the fragility curve of RC building with a moment frame, 'Complete' damage state and 4 – 6 stories, but having four different Seismic Design Categories, Pre (solid, light), Low (dash, light), Moderate (solid, heavy), and High (dash, heavy).

We cannot directly compare S2013 and FEMA model since they utilized different IMs and damage states. Instead, we can compare the fragility curve sets which utilized hydrodynamic force as an IM to FEMA model. Fig. 3.6b compares the fragility curves for wood structures based on the hydrodynamic force developed by Koshimura et al. (2009) and the FEMA model in term of a momentum flux. The thin solid line presents the fragility curve from Koshimura et al.

(2009) and each thin dashed and thick solid line presents two types of wood structure fragility curves with complete damage level for the FEMA model. The FEMA model shows a more conservative wood structure fragility curve than that from Koshimura et al. (2009).

Fig. 3.6c shows the fragility curves for three DS of Low-Rise (1 – 3 stories) RC buildings with a moment frame at Low Seismic Design Categories (SDCs) from the FEMA model. Since moderate and extensive fragility curves are same in this condition, there are only two curves in Fig. 3.6c, which are thin solid (moderate and extensive DS) and thick solid line (Complete DS). Fig. 3.6d shows the difference of four Seismic Design Categories (SDCs), such as Pre, Low, Moderate, High codes for the Mid-Rise (4 – 7 stories) and a moment frame RC building of complete damage state. Each thin solid and dashed line shows the fragility curve for Pre and Low SDCs, and each thick solid and dashed line shows the fragility curve for Moderate and High SDCs. Pre and Low SDCs cases are similar, but the Moderate and High SDCs show increasingly conservative fragility curves. In other words, the improved seismic design standards would also enable the building to withstand greater tsunami forces. Whether or not that is indeed the case is open to future research. The detail information of each fragility curve in Fig. 3.6 is summarized in Table 3.4.

Table 3.4 Detail information of fragility curves

Fig. 3.6	Eq.	*IM*	μ (μ') [-]	σ (σ') [-]	M' [ft^3/s^2]	β_M [-]	*DS*	*SDCs*	Descriptions	Ref.
(a)	17	h_{Max}	0.81	0.59			Collapse	None	Wood, 1 story	(1)
	17	h_{Max}	0.95	0.57			Collapse	None	Wood, 2 stories	(1)
	17	h_{Max}	1.78	0.72			Collapse	None	RC, 2 stories	(1)
	17	h_{Max}	2.35	0.79			Collapse	None	RC, > 3 stories	(1)
(b)	16	M_{Max}	1.47	0.75			Complete	None	Wood	(2)
	19	M_{Max}			247	0.74	Complete	None	Wood, Less than 5,000 ft^2.	(3)
	19	M_{Max}			343	0.73	Complete	None	Wood, Greater than 5,000 ft^2	(3)
(c)	19	M_{Max}			1,170	0.74	Moderate	Low	RC, 1 – 3 stories, Moment Frame	(3)
	19	M_{Max}			1,170	0.74	Extensive	Low	RC, 1 – 3 stories, Moment Frame	(3)
	19	M_{Max}			1,758	0.74	Complete	Low	RC, 1 – 3 stories, Moment Frame	(3)

(d)	19	M_{Max}	5,347	0.74	Complete	Pre	RC, 4 – 7 stories, Moment Frame	(3)
	19	M_{Max}	5,347	0.79	Complete	Low	RC, 4 – 7 stories, Moment Frame	(3)
	19	M_{Max}	11,407	0.79	Complete	Mod.	RC, 4 – 7 stories, Moment Frame	(3)
	19	M_{Max}	22,813	0.79	Complete	High	RC, 4 – 7 stories, Moment Frame	(3)

IM: Intensity Measure; DS: Damage State; SDCs: Seismic Design Categories of ASCE 7. (1) Suppasri et al. (2013); (2) Koshimura et al. (2009); (3) FEMA (2013).

3.5 Building Classification (Typology)

As shown in the previous section, the classification of buildings is an essential component to the fragility analysis. The next step in the process is to develop a system to classify buildings at a community scale, which is to classify several thousand buildings for a community (Step 3 discussed in Section 3.2).

The most credible method to obtain the correct building information is based on field survey combined the obtaining the engineering drawings for a particular buildings. However, field survey are labor intensive and are feasible for only a small number of buildings. Moreover, engineering drawings may not be easily available, particularly for older buildings that were designed before the advent of computer aided drawing (CAD), and building owners may be unwilling to provide this information. Alternatively, we propose three sources to collect the building information for this study: 1) Tax lot data, 2) Images from Google Street View, and 3) a field survey using Rapid Visual Screening (RVS).

Tax lot data is advantageous because, in general, tax data is in the public domain and are typically updated on an annual basis. For this project, the 2012 tax lot data was obtained for Clatsop County and was the same data sets used by Wiebe and Cox (2014). The data base is conveniently accessible using geographic information system (GIS) software with shape file format. The data base is composed of individual parcels for tax lots (shown in Fig. 3.7). Tax lot data provides general features of each parcel such as the centroid coordinates, size (ft^2), address, date of construction, owner, real market value, and land value. It also the data base contains building information in the form of a three-digit, ‘stat class’. The first digit identifies whether the land use is zoned as residential, commercial, or industrial structure. The second digit provides

addition information regarding the building occupancy or use. The third digit provides additional information such as the number of floors (Dominey-Howes et al., 2010; Wiebe and Cox, 2014). The methodology to utilize the 'stat class' summarized in Table 3.5. In this way, tax lot information provides us the general features of building uses, floor levels or building types, size of parcels, and build years, therefore it allows us to classify the building class quickly over a large region. However, the tax lot data does not the exact details of the building materials, floor levels for all (only some of floor levels for some building types are provided), and building frame types. Moreover, the tax lot data may be outdated due to re-modeling or changes in building use.

As a way to cross-check the tax lot data and to make up for some its inherent limitations, we utilized Google Street View (GSV) to validate and modify some of our classified data. With only an image of a store front, for example, GSV allows us to quickly evaluate the features such as number of floors and possible construction type and general age based on architectural detail. It is possible that GSV can be used to obtain the number of windows or other openings that would affect the tsunami forces. GSV could be combined with satellite imagery to estimate building width and proximity to other buildings and to debris hazards. These are left for future research works. In addition to GSV, we performed a short field survey for Rapid Visual Screening (RVS) suggested by FEMA P-154 (2002), with six people (led by the third author of this chapter) at Seaside on July 4, 2015. The RVS is typically used to identify the building seismic vulnerability depends on building structure and foundation soil types. We used RVS to verify that the tax lot data and GSV methods for 10 buildings.

Table 3.5 Applied building classification standard using the 'stat class' in tax lot data of Seaside, OR.

Class		Description	Material	Floors	Classification
< 400 Residential Buildings	< 200 [(a)] 'c' ≥ 6	1 stories	Wood	1	W1
		≥ 2 stories		2	W2
	≥ 200	Multiple family ≥ 2 stories		2	W2
≥ 400 Commercial Buildings	410 – 414	Motel & Hotel	RC	4	C1
	420, 421	Apartment (Low)	Wood	2	W2
	422, 423	Apartment (Mid, High)		4	
	446, 447	Large market, Merchandising store	Wood	2	W2
	485	Parking structure, Garage	RC	4	C1
	498, 511	Parking lots	None	-	None
	563	Church	Wood	2	W2

900	Condominium	RC	7	C1
Others	Other commercials	RC	1	C1

[(a)] 'c' indicates the third digit of 'stat class' ('a-b-c')

Fig. 3.7 shows the spatial distribution of the building classification of the details area at Seaside. Fig. 3.7a, b, and c show the building classification map for building types (W1, W2, and C1), building stories (1 to ≥ 6), and building seismic codes based on the date of construction for Oregon as listed in Table 3.6. To account for the realistic between the adoption and implementation of each new seismic code update, we added five years for the each SDC interval.

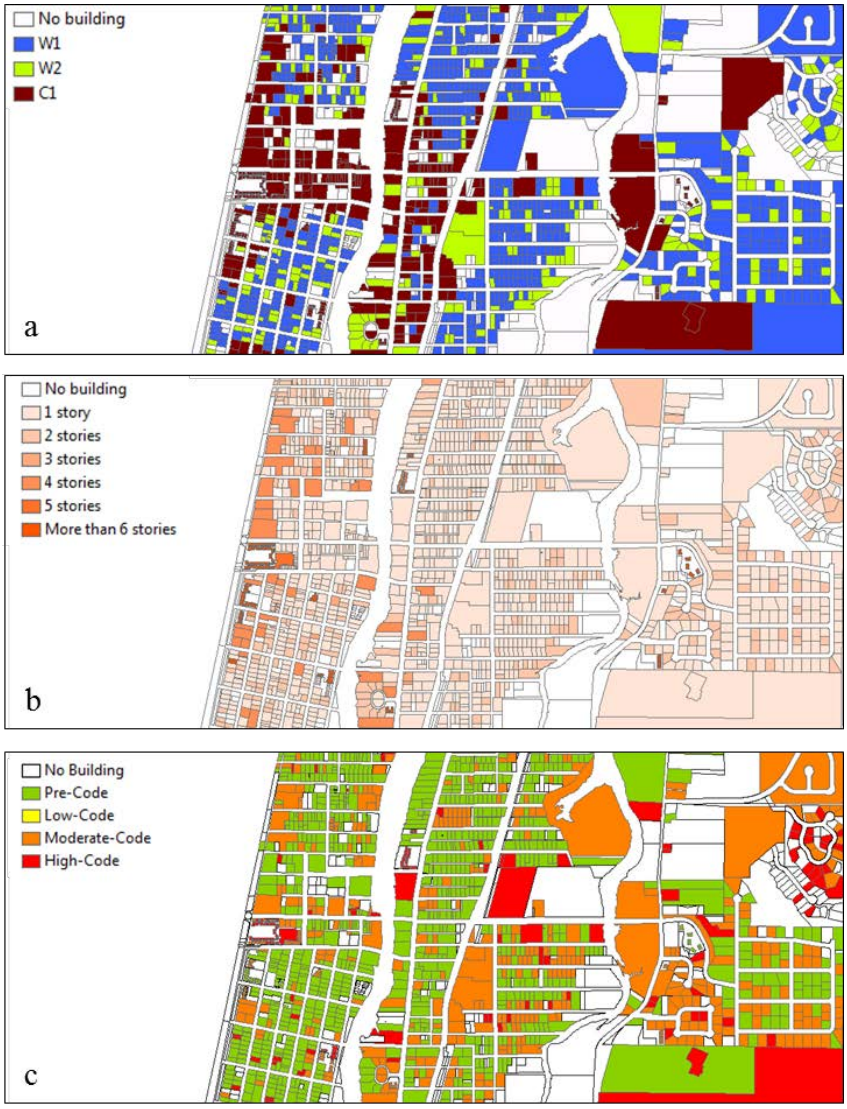

Fig. 3.7 Building classification map for (a) building type, (b) building stories, and (c) building Seismic Design Code for detail portion of Seaside.

Table 3.6 Seismic Design Codes applied for the buildings in Oregon.

Seismic Design Level	Year Adopted	Year Applied
Pre-Code	Before 1974	Before 1979
Low-Code	1974 – 1990	1979 – 1995
Moderate-Code	1990 – 1998	1995 – 2003
High-Code	After 1998	After 2003

Table 3.7 lists the general number of buildings information of each building's material shown in Fig. 3.7a. Total 1,098 parcels of tax lot data are found at region A and among them, 36% of parcels are wood structures and 54% are RC structures. The remaining proportion (10%) indicates the blank parcel, which does not have any structure on it. Each region B and C composes of 855 and 403 parcels, and the proportions of wood structure in both regions (62 and 68%) are higher than RC structures (23 and 10%). The downtown of Seaside (Region A) has relatively more commercial buildings (RC structures).

Table 3.7 General number of buildings by type and region in detail area of Seaside (Fig 3.7a).

Region	N_{Wood} (%)	N_{RC} (%)	N_{Total}
A	394 (35.9)	592 (53.9)	1098
B	530 (62.0)	193 (22.6)	855
C	274 (68.0)	41 (10.2)	403

Region A: Shoreline to Necanicum River; Region B: Necanicum River to Neawanna Creek, Region C: Neawanna Creek to the inland inundation limit.

The detail information of floor levels and SDCs in Fig 3.7b and c are summarized at Table 3.8. It is noted here that no differences are found between different SDCs for wood structures in FEMA model and that the three special SDCs referred at Table 3.1 are not included in this study.

Table 3.8 Detailed number of buildings by type and region in detail area of Seaside (Fig 3.7a).

Region	N_{Wood} (%)		N_{RC} (%)						
			Stories			Seismic Design Codes[(a)]			
	W1	W2	1 – 3 Low	4 – 7 Mid	≥ 8 High	Pre < 1979	Low 1979 – 1995	Moderate 1995 – 2003	High ≥ 2003
A	284	110	116	464	12	151	67	331	43
B	426	104	101	92	0	65	35	10	83
C	221	53	9	32	0	21	16	1	3

[(a)] Seismic Design Codes classification adapted for Oregon State policy.

3.6 Probabilistic damage estimation.

The 1,000-year event of the maximum inundation depth and momentum flux (Fig. 3.5) used as representative conditions to demonstrate the method of probabilistic damage estimation of buildings at Seaside for the S2013 and FEMA models. For the quantitative comparison of damage state from two fragility curve models, we utilize the similar DS conditions for each model based on Table 3.4, collapse for the S2013 model and complete damage for the FEMA model. We apply the detail typology of buildings in Section 3.4 based on number of floors, seismic codes, materials, and building frames.

Fig. 3.8 shows the spatial distributions of building damage probability of Seaside due to the 1,000-year event at the CSZ. Fig. 3.8a and 3.8c shows the collapse damage probability of building from S2013 model (h_{Max}) and the complete damage probability of building from FEMA model (M_{Max}). Fig. 3.8b and 3.8d are details of each of these distributions. Overall, both model results show a similar distribution of probable damage. In general, the probability of damage decreases from the shoreline toward inland, following the pattern of decreasing intensity of h_{Max} and M_{Max} shown in Fig. 3.5. Relatively smaller damage probability is found at the center of downtown (middle of Region A) where the most commercial buildings are located. Most residential buildings (classified as wood buildings) to the north and south of the downtown area have more than 80% probability of complete damage at Region A in the both models. There are some distinct difference between two models. The S2013 model shows a relatively higher damage at the Necanicum River and Neawanna Creek, and relatively higher damages on Region B than FEMA model. This is related to the higher flood levels near the river and creek, and it is possible these would overestimate the damage in these regions. On the other hand, the FEMA model shows higher damage levels to several of the RC building in the center of downtown.

Fig. 3.8 Spatial distribution of probability of complete damage from 1,000-year event using two types of fragility curves. (a) S2013 model, (b) detail, (c) FEMA model, and (d) detail.

3.7 Sensitivity tests

One of the main research topic is to understand the relative importance of the uncertainties in the damage estimation process. For this purpose, we performed a series of sensitivity tests to investigate the aleatory uncertainty of the tsunami generation process and the epistemic uncertainties related to the hydrodynamic model (frictions), floor levels information, build year information (seismic codes categories), and fragility curve types (different IMs). We utilized the FEMA model results for a majority of the sensitivity tests, and we utilized both the S2013 and FEMA models for the fragility curve sensitivity test.

We conduct the sensitivity test on the detail portion of Seaside shown in the previous figures. Fig. 3.9 shows the centroid points of tax lot parcels applied in this detail area. It is noted that a few buildings are composed of several tax lot parcels as shown by the cluster of dots in some areas. The coordinates are rotated to the shore normal direction (x'), and the shore parallel

direction (y'). Because the tsunami intensity is fairly uniform in the shore parallel direction, the study region is divided into a sub units with a 50 m interval (dashed lines) from the shoreline (x' = 0 m) to the inland limit (x' = 1,500 m). To evaluate the change of damage probability as move to the inland, we take averages of damage probability for all parcels per each sub-unit width (50 m). We separate into wood and RC building cases because of the significant difference in the damage probability.

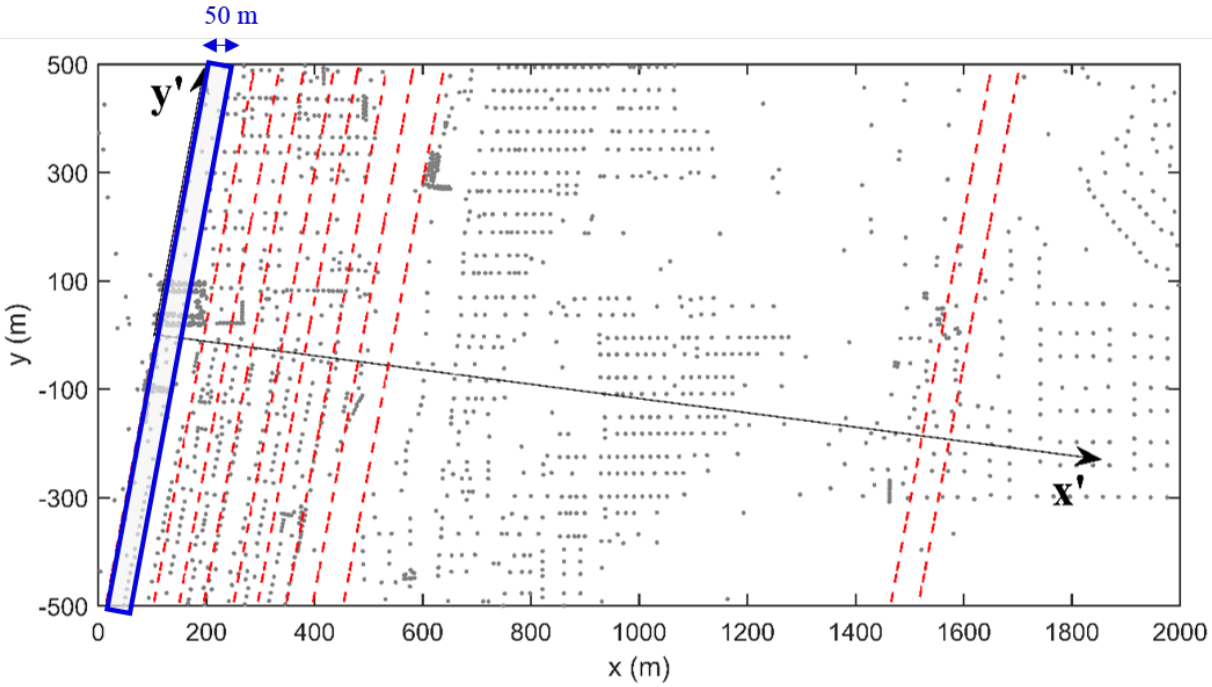

Fig. 3.9 The map of tax lot parcels applied in the sensitivity test. Each dot presents the centroid of tax lot. Box indicates the unit width (50 m).

3.7.1 Tsunami intensity (Tsunami generation)

Fig. 3.10 shows the average damage probabilities in each 50 m bin from the shoreline to the inland limits for the 500, 1,000 and 2,000-year events. Because we set 1,000-year event as the representative tsunami for the damage estimation, we choose 500 year and 2,000-year event as the possible deviated scenarios to represent the aleatory uncertainty of the tsunami generation. Each Fig. 3.10a and b shows the mean probability of wood buildings and RC buildings, respectively, for 500-year (blue circle), 1,000-year (black triangle) and 2,000-year (red square) events using the FEMA model for complete damage. Fig. 3.10c shows total number of wood (circle) and RC (triangle) buildings parcels in each bin.

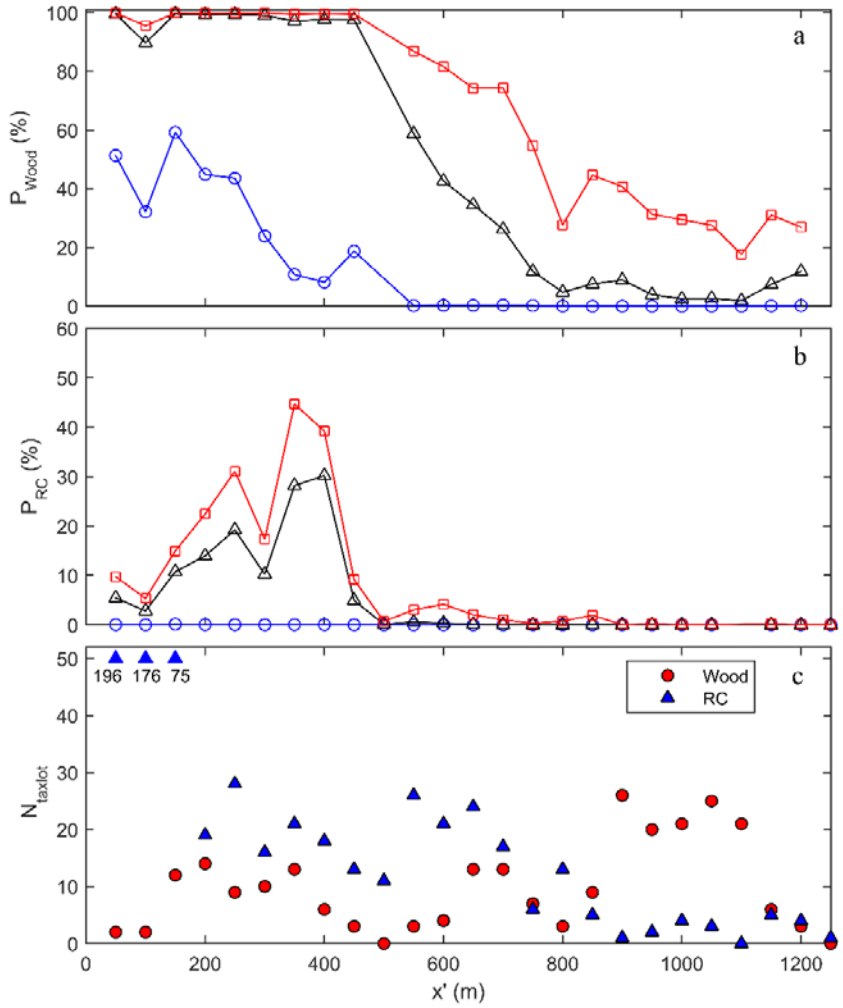

Fig. 3.10 Average probability of complete damage for (a) wood and (b) RC buildings with different tsunami events, 2,000-year (red square), 1,000-year (black triangle), and 500-year event (blue circle). (c) Total number of wood (circle) and RC (triangle) buildings parcels in each bin.

In case of wood structures, Fig. 3.10a shows that both the 1,000 and 2,000-year events result in high probability of complete damage (> 95%) at Region A ($x' \leq 500$ m), while 500-year event generates relatively low probabilities of complete damage (< 60%). At Region B (500 < x' < 1,200 m), the both 1,000 and 2,000-year events show a nearly linear decreases of damage probabilities. This is somewhat surprising since the IM for maximum momentum flux appeared to be uniform in this area. The probability of complete damage is very low for the 500-year event.

For the case of RC structures (Fig. 3.10b), there is a near zero probability of complete damage for RC buildings for the 500-year event for the all three regions. Both the 1,000 and 2,000-year events generate the similar pattern of damage probability at Region A for RC buildings. Interestingly, the peak damage probability for these events are located not at the

shoreline but at approximately 400 m from the shoreline just before reaching the Necanicum River. After the Necanicum River (x' > 500), the probability of complete damage to RC buildings decreases significantly and show an almost zero probability at Region B.

Overall, the relatively large deviation of probabilities for complete damage is found between the 500-year and 1,000-year events at Region A for both wood and RC structures. A relatively small deviation is found between the 1,000 and 2,000-year events for wood structures at Region A because the most wood structures at Region A are essentially destroyed for anything exceeding the 1,000-year event.

3.7.2 Frictions (Manning, n=0.04, 0.03, and 0.02)

Friction terms are included in the inundation models to present the dissipation effects from uneven bottom conditions during the propagation and inundation of tsunami. It is well known that friction from large macro-roughness in the built and natural environment such as building structures and vegetation can significantly change the hydrodynamic fields (Koshimura et al., 2009; Bricker et al., 2015). It is important to determine reasonable friction terms for more precise numerical inundation modelling because velocity and momentum flux are significantly affected by the friction value used to model the inundation process (Park et al., 2013). In this study, we used a constant Manning number (n = 0.03) as a default for all scenarios. For the sensitivity test, we choose a single scenario which intensity of tsunami is equivalent to the 1,000-year event among 72 scenarios presented in Chapter 2 and repeat the inundation with two other Manning friction values, n = 0.04 and 0.02.

Fig. 3.11 shows the average probability of complete damage at each bin for the three different friction values. Fig. 3.11a and b show the mean probabilities of wood buildings and RC buildings, respectively, for the three Manning numbers, n = 0.04 (blue circle), n = 0.03 (black triangle), and n = 0.02 (red square) for complete damage states with the FEMA model. The same number of wood and RC parcels applied in this comparison as in Fig. 3.10c.

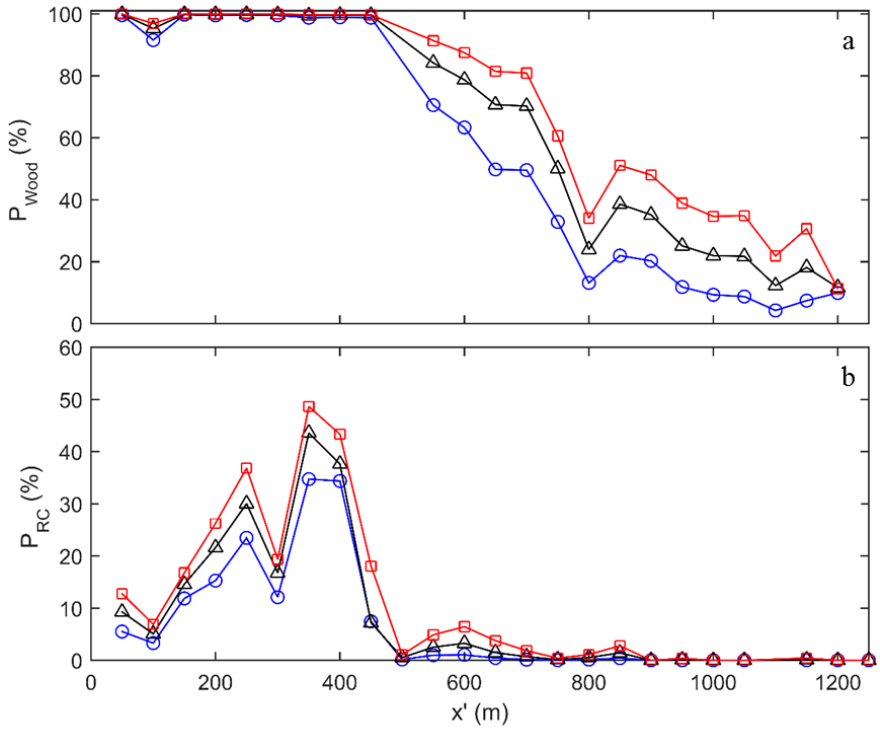

Fig. 3.11 Average probability of complete damage for (a) wood and (b) RC buildings with different friction terms, n=0.02 (red square), 0.03 (black triangle), and 0.04 (blue circle).

In case of wood structures (Fig. 3.11a) at Region A ($x' \leq 500$ m), all model results show the almost a high probability of complete damage. For Region B, It decreases approximately linearly shoreward as x' increases. A smaller Manning number (n = 0.02) results in a higher probability of complete damage because there is less dissipation and therefore a larger peak velocity. In the case of RC structures (Fig. 3.11b), all friction cases show a similar pattern of damage probabilities, with a somewhat larger variation for 300 < x' < 400 where the average probability is largest.

3.7.3 Floor levels (Low, Mid, and High-Rise)

Fig. 3.12 shows the average probability of complete damage in each with different floor levels assumed in FEMA model (Low, Mid, and High-Rise) for the 1,000-year tsunami event. To evaluate the sensitivity of floor levels, we assume that all RC buildings in each scenario have a fixed floor level condition such as Low-Rise (1 – 3), Mid-Rise (4 – 7), or High-Rise floors (≥ 8) for all buildings. Fig. 3.12a shows the estimated average damage probabilities of RC buildings using the fixed floor level assumptions, such as Low (blue circle), Mid (red triangle), and High-

Rise (green square) floor levels for all RC building in Region A. The solid line represents the estimate using the correct floor levels based on the building classification in Section 3.5. We excluded the wood buildings cases in this test because the FEMA model does not include effects of floor levels for wood buildings. The number of RC parcels per each floor levels used in the bin averaging are shown in Fig. 3.12b. Overall, higher damage probabilities are observed at lower floor conditions. In particular, High and Mid-Rise floor scenarios show similarly low (less than 5%) damage probability at Region A, but the Low–Rise floor scenario shows significant deviation (up to 25%) to other floor conditions at x' = 400 m.

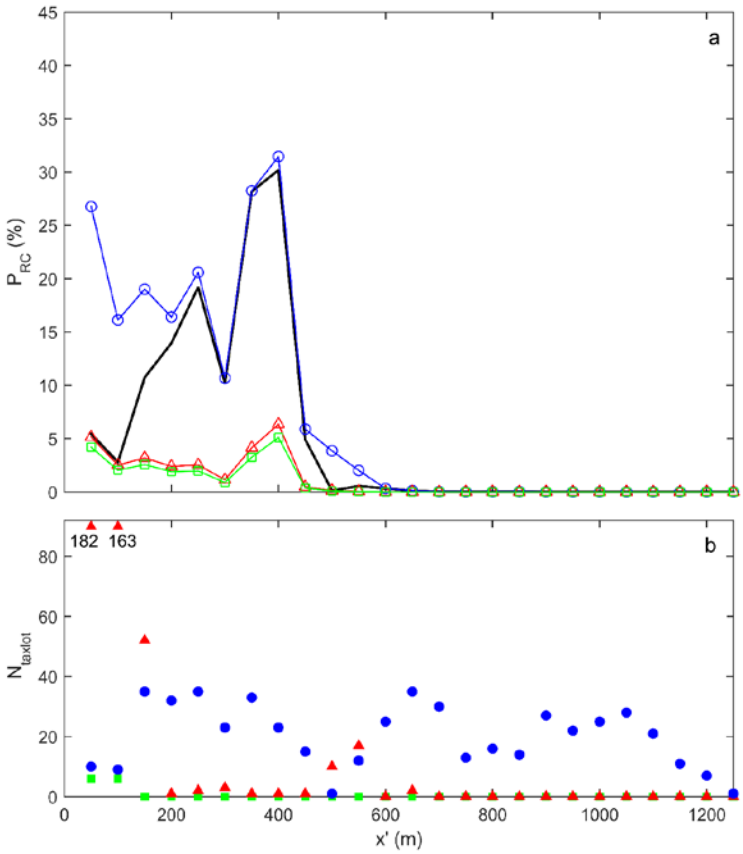

Fig. 3.12 (a) Building damage sensitivity to the building floor level information such as Low-Rise (blue circle), Mid-Rise (red triangle), and High-Rise (green square). Solid line presents the results from the correct floor level information. (b) The number of tax lot cells of different floor levels used for averaging in each bin.

3.7.4 Seismic Design Categories (Pre, Moderate, and High)

Fig. 3.13 shows the average probability of complete damage with different Seismic Design Categories (SDCs) in the FEMA model (Pre & Low, Moderate, and High) for the 1,000-year event. Similar to the previous sensitivity test for the floor levels, we assume that all RC

buildings in each scenario have a fixed SDC condition such as Pre, Moderate, or High codes. We treat Low SDC as a Pre SDC because of the minor differences between Pre and Low SDCs (e.g. Fig. 3.6d). Fig. 3.13a shows the average probabilities for complete damage of RC buildings for the different SDCs assumptions: Pre (blue circle), Moderate (red triangle), and High SDCs (green square) for all RC buildings. The solid line represents the scenario using the correct SDCs from tax lot data. There are no provisions for wood structures in the FEMA model, thus we also exclude them for this section. The numbers of RC parcels for bin averaging presented in Fig. 3.13b. Overall the higher damage probabilities are observed at lower SDCs conditions. The peak damage probability of the Pre & Low SDCs (circle) is 42% at x' = 200 m. The solid line, which utilizes the correct building build year information from tax lot, shows only a 13% probability of complete damage at the same location, indicating that the results would be sensitive to the uncertainties of the code level.

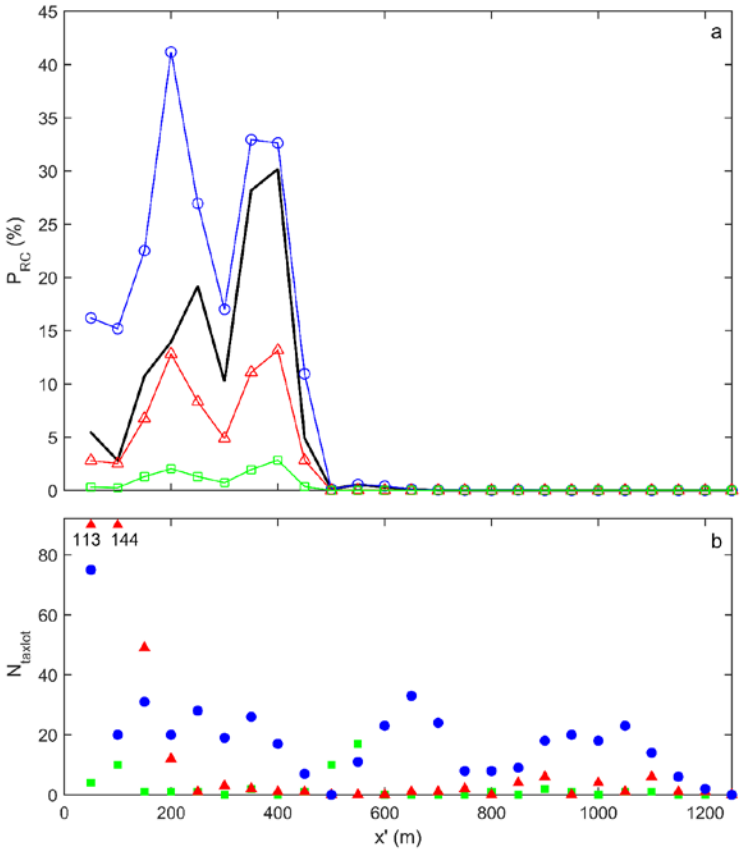

Fig. 3.13 (a) Building damage sensitivity to the building floor level information with different SDCs assumptions: Pre and Low (blue circle), Moderate (red triangle), and High code (green square). Solid line presents the results from the correct SDC information. (b) The number of parcels use for bin averaging.

3.7.5 Fragility curve types

Fig. 3.14 shows the average probability for complete damage probabilities considering the two different fragility models. Each Fig. 3.14a and 3.14b shows the mean probability of wood and RC buildings against to the 1,000-year (solid line) and 500-year (dashed line) events. Each damage estimation is performed based on either the S2013 model (black triangle & inverse triangle) or the FEMA model (red circle and square). The number of wood and RC parcels applied for the bin averaging are shown Fig. 3.10c.

In case of the damages on wood buildings against to 1,000-year event (Fig. 3.14a, solid lines), both the S2013 and FEMA model show the high probability of complete damage at Region A , but they show quite a deviation from each other at Region B ($500 \leq x' < 1200$ m). The FEMA model results show that the linear decrease of damage probability as x' increases, while the S2013 model shows that the average damage probability decreases until x'= 900 and it increases again as x' approaches the Neawanna creek (x' = 1,200 m), consistent with the high flood levels in the area. In case of the 500-year event (Fig. 3.14a dashed lines), the overall damage probabilities of both models are similar in Region A. However, the S2013 model shows an increase in the probability of complete damage by a factor of 3 at x' = 450 m, adjacent to the Necanicum River. In Region B, both model shows distinct differences.

For the case of a RC structures, the average probability of complete damage from the 1,000-year event (Fig. 3.14b, solid lines) are less than 40% for both models in Region A. But, the location of the peak from the FEMA model is at x' = 400 m while S2013 model is at x' = 200 m. In the case of the 500-year event, the range of probability of complete damage for FEMA model is approximately 5 to 10% in Region A. On the other hand, the probability of complete damage is near zero for the S2013 model. Overall, the both 500 and 1,000-year event result in quite different damage probability distributions depends on fragility model types (S2013 or FEMA model). The main deviations of each model result from the different IMs (inundation depth or momentum flux), as we found relatively higher inundation depth at the Necanicum River and the Neawanna Creek.

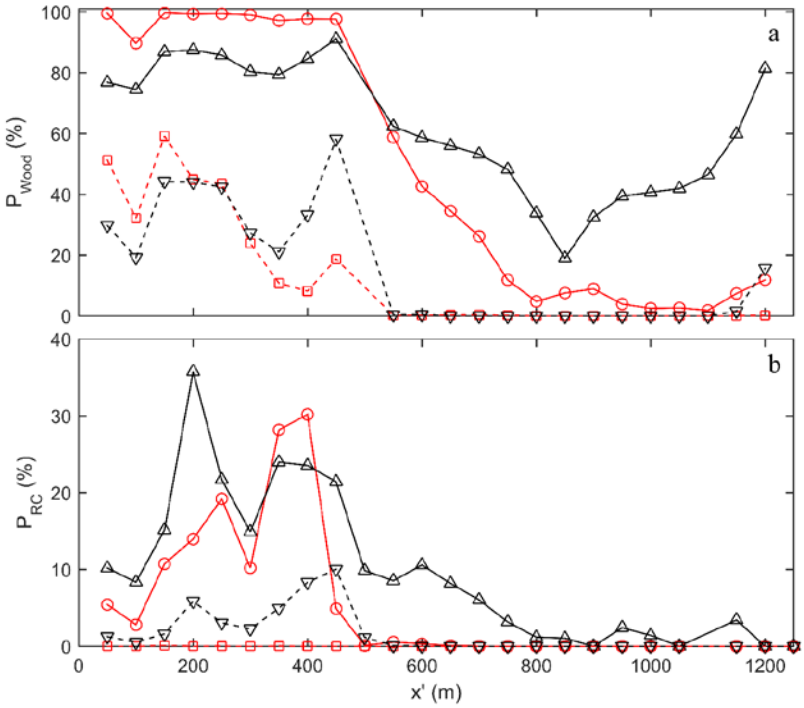

Fig. 3.14 Building damage sensitivity to fragility curve types for (a) wood and (b) RC structures. Symbols: the 1,000-year (solid) and 500-year event (dashed); S2013 model (black) and FEMA model (red).

3.7.6 Summary of sensitivity tests

In this subsection, we summarize the five sensitivity test results. Figure 3.15 summarizes the results in (a) Region A for wood and RC structures and (b) Region B for wood structures only. Fig 3.15a shows the average probability of complete damage and the error bars indicate the standard error with a 50% confidence interval in indicates the uncertainties in the generation (Aleatory uncertainty) represented by the 500, 1,000, and 2,000 year events; the friction term in the inundation modeling with n = 0.02, 0.03, and 0.04; the floor level information; the date of construction related to the seismic code, and the two different fragility curve types. These last four represent the epistemic modeling uncertainties. Note that Fig 3.15a is for both wood and RC structures, although floor level and date of construction (seismic code) are not included for wood buildings as discussed earlier. We repeat the analysis for Region B as shown in Fig 3.15b for wood buildings only because there were few RC buildings in that region.

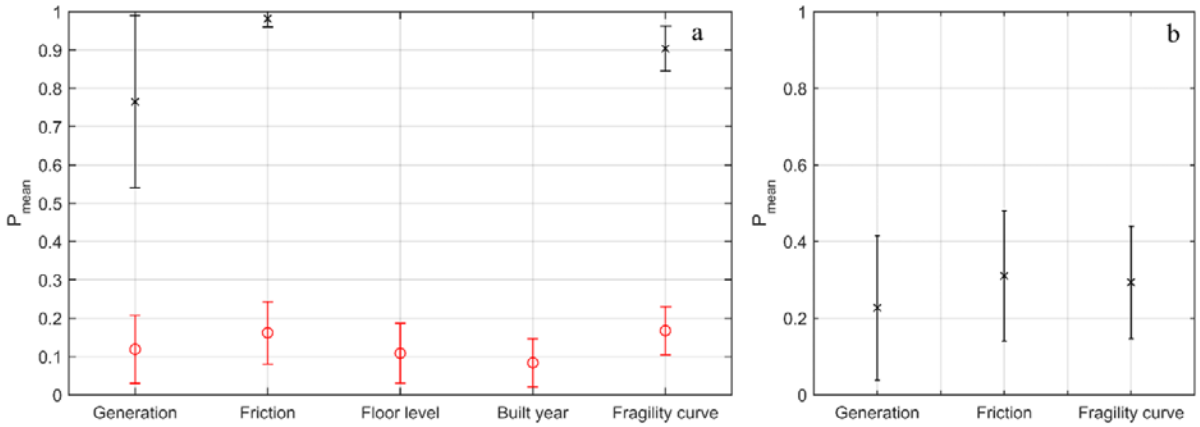

Fig. 3.15 Summary of building damage sensitivity tests with standard error for 50% confidence interval for (a) Region A with wood (black lines, star symbols) and RC (red lines, circles) and (b) Region B for wood only (black lines, star symbols).

Figure 3.15a shows that in Region A the largest sensitivity for wood structures is related to the uncertainty of the tsunami generation. The probability of complete damage does not appear to be sensitive to the modeling of bottom friction in this case and the fragility model shows a small sensitivity relative to the tsunami generation. On the other hand, Fig 3.15a shows that in Region A, for RC structures, all factors show relatively the same level of sensitivity. This is a major finding of this thesis: it appears that the aleatory uncertainty in the tsunami generation is of equal importance to the epistemic uncertainties in the inundation modeling, fragility modeling, and building classification. Similarly, Fig 3.15b shows that in Region B for the case of wood structures there is an equal importance in the epistemic and aleatory uncertainties

3.8 Discussions

3.8.1 Limits of the fragility curves used in this study

Several types of fragility curves were developed by different research groups. Each fragility curve generally follow the same mathematical formulation, but there are differences in the curves as shown in this dissertation. The differences exist for several reasons: 1) Each fragility curve set is developed for a different building classification and damage state description, 2) the building classifications and damage states do not enough to represent all of the building cases, 3) the techniques for tsunami hazard assessment and statistical methods to develop fragility curves are also different each other (Tarbotton et al., 2015). In this study, we

use the S2013 model as a representative fragility curves using maximum inundation depth as an IM and also compared with FEMA model using maximum momentum flux as an IM.

3.8.2 Limits of intensity measures from numerical modelling

When we evaluated the maximum inundation depth and momentum flux for the fragility curve analysis, the inundation model (e.g. COULWAVE) utilized on bare-earth bathymetry and topography, which means that it could not incorporate structures or vegetation effects which create complex flows or dissipations during tsunami inundation. In particular, the maximum momentum flux can vary significantly, depends on the details of the built environment such as the layout of buildings and streets. In the future, it is necessary to quantify the effects of bare earth models on estimating the tsunami intensity measures.

3.8.3 Limited building information for the fragility analysis.

We used tax lot data, Google Street View, and Rapid Visual Screening (RVS) as three sources to obtain building information for the fragility curve analysis. Because of the large number of buildings, this study relied primarily on the typology from tax lot data, and some of building information may not be correct. Perhaps more important, each tax lot parcel presents a single business unit rather than a particular structure. For example, several business may occupy a single building. Moreover, on large lots, our method assumes that the building is in the center of the lot. For some cases where the spatial variation of the IM is low, this may not be an issue. However, there can be large spatial variations in momentum flux as shown in this work.

3.8.4 Multi-hazard (Earthquake) and other factor beyond current fragility curves

Before the inundation damage from the tsunami, the shaking and ground deformation from the earthquake will likely create building damage, particularly for RC buildings. Fragility curves developed from field survey data (e.g. S2013 model) may include some earthquake damage aspects. In the future, it is necessary to include a multi-hazard analysis that combines the earthquake and tsunami damage.

3.9 Conclusions

This study provides a framework for a probabilistic tsunami damage assessment of buildings at the scale of a small coastal city. We applied this framework to Seaside, Oregon, where it is exposed to the threat of a future CSZ event. Our framework is composed of two main

parts: (a) the tsunami hazard assessment, and (b) the tsunami damage assessment. The main conclusions of this work are:

1. The tax lot data enables classification of buildings quickly at a community scale. Google Street View and RVS can be used to verify and to update the building classification.
2. In Region A closest to the shoreline, the wood structures have a high probability of complete damage (> 80%) from 1,000-year CSZ tsunami. RC structures have a lower probability of complete damage (< 40%) due to the conservative building characteristics.
3. The S2013 model predicted a higher probability of complete damage for buildings near the Necanicum River and the Neawanna Creek while the FEMA model results showed a sharp decrease the probability of complete damage in Region B between the Necanicum River and the Neawanna Creek.
4. For the case of wood buildings in Region A, the damage assessment was most sensitive to the aleatory uncertainty of the tsunami generation and was least sensitive to variation of bottom friction in the numerical modelling.
5. For the case of RC buildings at Region A, all uncertainty factors such as tsunami generation, numerical modelling, building information (floors and build year) and fragility curve types show the similar sensitivity on the damage estimation. Similarly, for the case of wood buildings in Region B, the tsunami generation, numerical modelling and fragility curve types were equally important for the damage assessment sensitivity.

3.10 Reference

Bricker, J.D., Gibson, S., Takagi, H. and Imamura, F. (2015) On the Need for Larger Manning's Roughness Coefficients in Depth-Integrated Tsunami Inundation Models. *Coastal Engineering Journal*, 57(02), 1550005.

Charvet, I., Suppasri, A. and Imamura, F. (2014) Empirical fragility analysis of building damage caused by the 2011 Great East Japan Tsunami in Ishinomaki City using ordinal regression, and influence of key geographical features. *Stochastic Environmental Research and Risk Assessment*, 28(7), 1853-1867.

Dominey-Howes, D., Dunbar, P., Varner, J., and Papathoma-Köhle, M. (2010) Estimating probable maximum loss from a Cascadia tsunami. *Natural Hazards*, 53(1), 43-61.

Ellingwood, B.R., Rosowsky, D.V., Li, Y. and Kim, J.H. (2004) Fragility assessment of light-frame wood construction subjected to wind and earthquake hazards. *Journal of Structural Engineering*, 130(12), 1921-1930.

FEMA (2002) *Earthquake Loss Estimation Methodology*, HAZUS99-MR1, Advanced Engineering Building Module, Technical and User's Manual, prepared by National Institute of Building Sciences (NIBS) for the Federal Emergency Management Agency. (Washington, D.C.: NIBS).

FEMA P-154 (2002) *Rapid Visual Screening of Buildings for Potential Seismic Hazards* (2nd Ed.), Federal Emergency Management Agency, Washington, D.C.

FEMA (2011) *Multi-hazard Loss Estimation Methodology: Earthquake Model*, HAZUS-MH MR4 Technical Manual, prepared by the National Institute of Building Sciences (NIBS) for the Federal Emergency Management Agency. (Washington, D.C.: NIBS).

FEMA P-646 (2012) *Guidelines for Design of Structures for Vertical Evacuation from Tsunamis (2nd Ed.)*, Federal Emergency Management Agency, Washington, D.C.

FEMA (2013) *Tsunami Methodology Technical Manual*, prepared by the National Institute of Building Sciences (NIBS) for the Federal Emergency Management Agency. (Washington, D.C.: NIBS).

Fritz, H.M., Phillips, D.A., Okayasu, A., Shimozono, T., Liu, H., Mohammed, F., Skanavis, V., Synolakis, C.E. and Takahashi, T. (2012) The 2011 Japan tsunami current velocity measurements from survivor videos at Kesennuma Bay using LiDAR. *Geophysical Research Letters*, 39(7).

Geist, E. L., and Parsons, T. (2006) Probabilistic Analysis of Tsunami Hazards. *Natural Hazards*, 37(3), 277-314.

Goda, K., Yasuda, T., Mori, N., and Mai, P. M. (2015) Variability of tsunami inundation footprints considering stochastic scenarios based on a single rupture model: Application to the 2011 Tohoku earthquake. *Journal of Geophysical Research: Oceans*, 120(6), 4552-4575.

Goldfinger C, Nelson CH, Morey AE, Johnson JE, Patton JR, Karabanov E., Patton, J., Gracia, E., Enkin, R., Dallimore, A., Dunhill, G., and Vallier, T. (2012) *Turbidite Event History: Methods and Implications for Holocene Paleoseismicity of the Cascadia Subduction Zone* U.S. Geological Survey Professional Paper 1661-F, 178 p.

González, F.I., Geist, E.L., Jaffe, B., Kânoğlu, U., Mofjeld, H., Synolakis, C.E., Titov, V.V., Arcas, D., Bellomo, D., Carlton, D. and Horning, T. (2009) Probabilistic tsunami hazard assessment at seaside, Oregon, for near-and far-field seismic sources. *Journal of Geophysical Research: Oceans*, 114(C11).

Jaffe, B.E., Borrero, J.C., Prasetya, G.S., Peters, R., McAdoo, B., Gelfenbaum, G., Morton, R., Ruggiero, P., Higman, B., Dengler, L. and Hidayat, R. (2006) Northwest Sumatra and offshore islands field survey after the December 2004 Indian Ocean tsunami. *Earthquake Spectra*, 22(S3), 105-135.

Koshimura, S., Oie, T., Yanagisawa, H., and Imamura, F. (2009) Developing fragility functions for tsunami damage estimation using numerical model and post-tsunami data from Banda Aceh, Indonesia. *Coastal Engineering Journal*, 51(03), 243-273.

Leelawat, N., Suppasri, A., Charvet, I. and Imamura, F. (2014) Building damage from the 2011 Great East Japan tsunami: quantitative assessment of influential factors. *Natural Hazards*, 73(2), 449-471.

Lynett, P., Wu, T., and Liu, P. (2002) Modeling wave runup with depth-integrated equations. *Coastal Engineering* 46: 89-107.

Mas, E., Koshimura, S., Suppasri, A., Matsuoka, M., Matsuyama, M., Yoshii, T., ... and Imamura, F. (2012) Developing Tsunami fragility curves using remote sensing and survey data of the 2010 Chilean Tsunami in Dichato. *Natural Hazards and Earth System Science*, 12(8), 2689-2697.

Mikami, T., Shibayama, T., Esteban, M. and Matsumaru, R. (2012) Field survey of the 2011 Tohoku earthquake and tsunami in Miyagi and Fukushima prefectures. *Coastal Engineering* Journal, 54(01), p.1250011.

Mimura, N., Yasuhara, K., Kawagoe, S., Yokoki, H. and Kazama, S. (2011) Damage from the Great East Japan Earthquake and Tsunami-a quick report. *Mitigation and Adaptation Strategies for Global Change*, 16(7), 803-818.

Mori, N., Cox, D.T., Yasuda, T. and Mase, H. (2013) Overview of the 2011 Tohoku earthquake tsunami damage and its relation to coastal protection along the Sanriku Coast. *Earthquake Spectra*, 29(s1), S127-S143.

MRl, HAZUS-MH (2003) *Multi-Hazard Loss Estimation Methodology: Earthquake Model.* Department of Homeland Security, FEMA, Washington, DC.

Murao, O., and Nakazato, H. (2010) Vulnerability functions for buildings based on damage survey data in Sri Lanka after the 2004 Indian Ocean tsunami, *in Proceedings of the 7th*

International Conference on Sustainable Built Environment, 13–14 December 2010, Kandy, Sri Lanka.

Park, H., Cox, D. T., Lynett, P. J., Wiebe, D. M., and Shin, S. (2013) Tsunami inundation modeling in constructed environments: A physical and numerical comparison of free-surface elevation, velocity, and momentum flux. *Coastal Engineering*, 79, 9-21.

Park, H and Cox, D. T. (expect in 2016) Probabilistic Assessment of Near-field Tsunami Arrival Time, Inundation depth, Velocity, Momentum Flux, and Duration Applied to Seaside, Oregon. On preparing for the *Coastal Engineering*.

Priest, G. R., Goldfinger, C., Wang, K., Witter, R. C., Zhang, Y., and Baptista, A. M. (2010) Confidence levels for tsunami-inundation limits in northern Oregon inferred from a 10,000-year history of great earthquakes at the Cascadia subduction zone. *Natural Hazards*, 54(1), 27-73.

Priest, G.R., Stimely, L.L., Wood, N.J., Madin, I.P. and Watzig, R.J. (2016) Beat-the-wave evacuation mapping for tsunami hazards in Seaside, Oregon, USA. *Natural Hazards*, 80(2), 1031-1056.

Reese, S., Cousins, W. J., Power, W. L., Palmer, N. G., Tejakusuma, I. G., and Nugrahadi, S. (2007) Tsunami vulnerability of buildings and people in South Java–field observations after the July 2006 Java tsunami. *Natural Hazards and Earth System Science*, 7(5), 573-589.

Rossetto, T., Peiris, N., Pomonis, A., Wilkinson, S.M., Del Re, D., Koo, R. and Gallocher, S. (2007) The Indian Ocean tsunami of December 26, 2004: observations in Sri Lanka and Thailand. *Natural Hazards*, 42(1), 105-124.

Scawthorn, C., Flores, P., Blais, N., Seligson, H., Tate, E., Chang, S., Mifflin, E., Thomas, W., Murphy, J., Jones, C. and Lawrence, M. (2006) HAZUS-MH flood loss estimation methodology. II. Damage and loss assessment. *Natural Hazards Review*, 7(2), pp.72-81.

Suppasri, A., Koshimura, S., and Imamura, F. (2011) Developing tsunami fragility curves based on the satellite remote sensing and the numerical modeling of the 2004 Indian Ocean tsunami in Thailand. *Natural Hazards and Earth System Science*, 11(1), 173-189.

Suppasri, A., Mas, E., Koshimura, S., Imai, K., Harada, K. and Imamura, F. (2012) Developing tsunami fragility curves from the surveyed data of the 2011 Great East Japan tsunami in Sendai and Ishinomaki plains. *Coastal Engineering Journal*, 54(01), p.1250008.

Suppasri, A., Mas, E., Charvet, I., Gunasekera, R., Imai, K., Fukutani, Y., Abe, Y., Imamura, F. (2013) Building damage characteristics based on surveyed data and fragility curves of the 2011 Great East Japan tsunami. *Natural Hazards*, 66(2), 319-341.

Suppasri, A., Charvet, I., Imai, K. and Imamura, F. (2015) Fragility Curves Based on Data from the 2011 Tohoku-Oki Tsunami in Ishinomaki City, with Discussion of Parameters Influencing Building Damage. *Earthquake Spectra*, 31(2), 841-868.

Tarbotton, C., Dall'Osso, F., Dominey-Howes, D. and Goff, J. (2015) The use of empirical vulnerability functions to assess the response of buildings to tsunami impact: Comparative review and summary of best practice. *Earth-Science Reviews*, 142, 120-134.

Titov, V. V., Moore, C. W., Greenslade, D. J. M., Pattiaratchi, C., Badal, R., Synolakis, C. E., and Kânoğlu, U. (2011) A new tool for inundation modeling: Community Modeling Interface for Tsunamis (ComMIT). *Pure and Applied Geophysics*, 168(11), 2121-2131.

Tsunami Pilot Study Working Group (2006) Seaside, Oregon, *Tsunami Pilot Study-Modernization of FEMA Flood Hazard Maps*. Joint NOAA/USGS/FEMA Special Report 94.

Valencia, N., Gardi, A., Gauraz, A., Leone, F., and Guillande, R. (2011) New tsunami damage functions developed in the framework of SCHEMA project: application to European-Mediterranean coasts. *Natural Hazards and Earth System Science*, 11(10), 2835-2846.

van de Lindt, J.W. and Dao, T.N. (2009) Performance-based wind engineering for wood-frame buildings. *Journal of Structural Engineering*, 135(2), 169-177.

Wang, H., Mostafizi, A., Cramer, L., Cox, D., and Park. H. (2015) An agent-based model of a multimodal near-field tsunami evacuation: Decision-making and life safety. *Transportation Research Part C: Emerging Technologies*, http://dx.doi.org/10.1016/j.trc.2015.11.010.

Wiebe, D. M., and Cox, D. T. (2014) Application of fragility curves to estimate building damage and economic loss at a community scale: a case study of Seaside, Oregon. *Natural Hazards*, 71(3), 2043-2061.

Witter, R. C., Zhang, Y. J., Wang, K., Priest, G. R., Goldfinger, C., Stimely, L., ... and Ferro, P. A. (2013) Simulated tsunami inundation for a range of Cascadia megathrust earthquake scenarios at Bandon, Oregon, USA. *Geosphere*, 9(6), 1783-1803.

Wood, N. (2007) *Variations in city exposure and sensitivity to tsunami hazards in Oregon* (No. 2007-5283). Geological Survey (US).

Yeh, H. (2007) Design tsunami forces for onshore structures. *Journal of Disaster Research*, 2(6), 531-536.

Yeh, H., Sato, S., & Tajima, Y. (2013) The 11 March 2011 East Japan earthquake and tsunami: tsunami effects on coastal infrastructure and buildings. *Pure and Applied Geophysics*, 170(6-8), 1019-1031.

3.11 Nomenclature

Symbol	Descriptions	Unit
B	Width of a building	L
C_d	Drag coefficient	-
F_{TS}	Lateral tsunami flow force	MLT^{-2}
h	Inundation depth	L
K_d	Coefficient for the shielding or debris impact	-
M	Momentum flux	L^3T^{-2}
M'	Mean momentum flux	L^3T^{-2}
n	Manning number	$TL^{-1/3}$
P	Cumulative probability of damage	-
P_{mean}	Mean probability damage	-
P_{RC}	Probability damage of RC buildings	-
P_{Wood}	Probability damage of wood buildings	-
x'	Distance to shore-normal direction	L
y'	Distance to shore-parallel direction	L
z	Ground elevation from referenced level	L
β_M	Total logarithmic standard deviation	-
μ	Mean	L
μ'	Lognormal mean	L
ρ_s	Density of water	ML^{-3}
σ	Standard deviation	L
σ'	Lognormal standard deviation	L
Φ	Standardized normal distribution function	-
( )	Maximum value of ( )	-

4. General conclusions

A framework for probabilistic tsunami damage assessment for the built environment at a community scale was develop and applied to the city of Seaside, Oregon, for a nearfield CSZ event. In Chapter 2, we perform a probabilistic near-field tsunami hazards assessment (PNTHA) and introduced five tsunami intensity measurements (IMs): 1) the maximum inundation depth, h_{Max}, 2) the maximum velocity, V_{Max}, 3) the maximum momentum flux, M_{Max}, 4) the arrival time exceeding a 1 m inundation depth, T_A, and 5) the total duration exceeding a 1 m inundation depth, T_h. We introduce a new method to determine the initial fault slip condition of the tsunami generation model. The new model characterizes the randomness of fault slip in terms of the moment magnitude (M_W), peak slip location, and slip shape parameterized as a Gaussian distribution. A total of 72 CSZ scenarios were utilized as input, and each scenario was assigned different weighting factors originating from the occurrence rate of historic tsunami moment magnitude at the CSZ and based on the expert judgment. Finally, we evaluate annual exceedance of the IMs by assuming a Poisson arrival process for the 72 tsunami modeling results.

In Chapter 3, we utilize the hazard assessment results of Chapter 2 (specifically, the annual exceedance probabilities of h_{Max} and M_{Max}) and perform a damage estimation utilizing the fragility curve analysis. We implement a new tool for building classification utilizing tax lot data, Google Street View, and Rapid Visual Screening (RVS) to characterize the building information and to match the building classifications to the different fragility curves. To demonstrate of methodology, we estimated the probability of complete damage using the 1,000-year CSZ event. We quantified the assessment sensitivity to five uncertainty factors on the damage probabilities. The main conclusions of the dissertation are

1. The new method for the fault slip distributions accounts for some of the aleatory uncertainty in tsunami generation. Using published slip models of recent earthquakes, we characterize the fault slip distribution as a Gaussian distribution with moment magnitude (M_W), and two slip distribution parameters, α' and β'.
2. We perform a probabilistic near-field tsunami hazards assessment (PNTHA) at Seaside, Oregon, to illustrate our general methodology and examine five tsunami intensity measures (IMs): the maximum inundation depth (h_{Max}), the maximum velocity (V_{Max}), the

maximum momentum flux (M_{Max}), the arrival time exceeding a 1 m inundation depth (T_A), and total duration exceeding a 1 m inundation depth (T_h).

3. The intensity of IMs are observed to increase as the moment magnitude (M_W) increase, as the peak slip location becomes closer to the study area, and as the slip shape becomes narrower.
4. Among the IMs, the arrival time (T_A) shows relatively weak sensitivity to the aleatory uncertainty, while other IMs shows significant sensitivity, especially momentum flux (M_{Max}). We observed that M_{Max} increases by an order of magnitude from the 500-year to 1,000-year event, while h_{Max} increases by a factor of 3 and T_A decreases by a factor of 0.05.
5. The inundation duration T_h can vary due to the local bathymetric conditions and can range a relatively short duration (< 10 min) to a relatively longer duration (~100 min) observed near the river and creek where the elevation is closed to the sea-level.
6. The tax lot data enables classification of buildings quickly at a community scale. Google Street View and RVS can be used to verify and to update the building classification.
7. In Region A closest to the shoreline, the wood structures have a high probability of complete damage (> 80%) from 1,000-year event at the CSZ. RC structures have a lower probability of complete damage (< 40%) due to the conservative building characteristics.
8. The S2013 model predicted a higher probability of complete damage for buildings near the Necanicum River and the Neawanna Creek while the FEMA model results showed a sharp decrease the probability of complete damage in Region B between the Necanicum River and the Neawanna Creek.
9. For the case of wood buildings in Region A, the damage assessment was most sensitive to the aleatory uncertainty of the tsunami generation and was least sensitive to variation of bottom friction in the numerical modelling.
10. For the case of RC buildings at Region A, all uncertainty factors such as tsunami generation, numerical modelling, building information (floors and build year) and fragility curve types show the similar sensitivity on the damage estimation. Similarly, for the case of wood buildings in Region B, the tsunami generation, numerical modelling and fragility curve types were equally important for the damage assessment sensitivity.

Bibliography

Baba, T., Cummins, P. R., Thio, H. K., and Tsushima, H. (2009) Validation and joint inversion of teleseismic waveforms for earthquake source models using deep ocean bottom pressure records: A case study of the 2006 Kuril megathrust earthquake. *Pure and Applied Geophysics*, 166(1-2), 55-76.

Bricker, J.D., Gibson, S., Takagi, H. and Imamura, F. (2015) On the Need for Larger Manning's Roughness Coefficients in Depth-Integrated Tsunami Inundation Models. *Coastal Engineering Journal*, 57(02), 1550005.

Bruneau, M., Chang, S.E., Eguchi, R.T., Lee, G.C., O'Rourke, T.D., Reinhorn, A.M., Shinozuka, M., Tierney, K., Wallace, W.A. and von Winterfeldt, D. (2003) A framework to quantitatively assess and enhance the seismic resilience of communities. *Earthquake Spectra*, 19(4), 733-752.

Charvet, I., Suppasri, A. and Imamura, F. (2014) Empirical fragility analysis of building damage caused by the 2011 Great East Japan Tsunami in Ishinomaki City using ordinal regression, and influence of key geographical features. *Stochastic Environmental Research and Risk Assessment*, 28(7), 1853-1867.

Cornell, C.A. (1968) Engineering seismic risk analysis. *Bulletin of the Seismological Society of America*, 58(5), 1583-1606.

Dominey-Howes, D., Dunbar, P., Varner, J., and Papathoma-Köhle, M. (2010) Estimating probable maximum loss from a Cascadia tsunami. *Natural Hazards*, 53(1), 43-61.

FEMA (2002) *Earthquake Loss Estimation Methodology*, HAZUS99-MR1, Advanced Engineering Building Module, Technical and User's Manual, prepared by National Institute of Building Sciences (NIBS) for the Federal Emergency Management Agency. (Washington, D.C.: NIBS).

FEMA P-154 (2002) *Rapid Visual Screening of Buildings for Potential Seismic Hazards* (2nd Ed.), Federal Emergency Management Agency, Washington, D.C., 140 pp

FEMA (2011) *Multi-hazard Loss Estimation Methodology: Earthquake Model*, HAZUS-MH MR4 Technical Manual, prepared by the National Institute of Building Sciences (NIBS) for the Federal Emergency Management Agency. (Washington, D.C.: NIBS).

FEMA P-646 (2012) *Guidelines for Design of Structures for Vertical Evacuation from Tsunamis (2nd Ed.)*, Federal Emergency Management Agency, Washington, D.C., 174 pp

FEMA (2013) *Tsunami Methodology Technical Manual*, prepared by the National Institute of Building Sciences (NIBS) for the Federal Emergency Management Agency. (Washington, D.C.: NIBS).

Fritz, H.M., Phillips, D.A., Okayasu, A., Shimozono, T., Liu, H., Mohammed, F., Skanavis, V., Synolakis, C.E. and Takahashi, T. (2012) The 2011 Japan tsunami current velocity

measurements from survivor videos at Kesennuma Bay using LiDAR. *Geophysical Research Letters*, 39(7).

Fuhrman, D. R., and Madsen, P. A. (2008) Simulation of nonlinear wave run-up with a high-order Boussinesq model. *Coastal Engineering*, 55(2), 139-154.

Fujii, Y., and Satake, K. (2007) Tsunami source of the 2004 Sumatra–Andaman earthquake inferred from tide gauge and satellite data. *Bulletin of the Seismological Society of America*, 97(1A), S192-S207.

Geist, E. L. (2005) *Local tsunami hazards in the Pacific Northwest from Cascadia subduction zone earthquakes.* US Dept. of the Interior, US Geological Survey.

Geist, E. L., and Parsons, T. (2006) Probabilistic Analysis of Tsunami Hazards. *Natural Hazards*, 37(3), 277-314.

Goda, K., Mai, P. M., Yasuda, T., and Mori, N. (2014) Sensitivity of tsunami wave profiles and inundation simulations to earthquake slip and fault geometry for the 2011 Tohoku earthquake. *Earth, Planets and Space*, 66(1), 1-20.

Goda, K., Yasuda, T., Mori, N., and Mai, P. M. (2015) Variability of tsunami inundation footprints considering stochastic scenarios based on a single rupture model: Application to the 2011 Tohoku earthquake. *Journal of Geophysical Research: Oceans*, 120(6), 4552-4575.

Goldfinger C, Nelson CH, Morey AE, Johnson JE, Patton JR, Karabanov E., Patton, J., Gracia, E., Enkin, R., Dallimore, A., Dunhill, G., and Vallier, T. (2012) *Turbidite Event History: Methods and Implications for Holocene Paleoseismicity of the Cascadia Subduction Zone* U.S. Geological Survey Professional Paper 1661-F, 178 p.

González, F.I., Geist, E.L., Jaffe, B., Kânoğlu, U., Mofjeld, H., Synolakis, C.E., Titov, V.V., Arcas, D., Bellomo, D., Carlton, D. and Horning, T. (2009) Probabilistic tsunami hazard assessment at seaside, Oregon, for near-and far-field seismic sources. *Journal of Geophysical Research: Oceans*, 114(C11).

Grilli, S. T., Ioualalen, M., Asavanant, J., Shi, F., Kirby, J. T., and Watts, P. (2007) Source constraints and model simulation of the December 26, 2004, Indian Ocean tsunami. *Journal of Waterway, Port, Coastal, and Ocean Engineering*, 133(6), 414-428.

Hanks, T. C., and Kanamori, H. (1979) Moment magnitude scale. *Journal of Geophysical, Research*, 84, 2348–2350.

Hayes, P. (2011) Rapid source characterization of the 2011 M w 9.0 off the Pacific coast of Tohoku Earthquake. *Earth, Planets and Space*, 63(7), 529-534.

Heaton, T. H., and Hartzell, S. H. (1987) Earthquake hazards on the Cascadia subduction zone. *Science*, 236(4798), 162-168.

Jaffe, B.E., Borrero, J.C., Prasetya, G.S., Peters, R., McAdoo, B., Gelfenbaum, G., Morton, R., Ruggiero, P., Higman, B., Dengler, L. and Hidayat, R. (2006) Northwest Sumatra and offshore islands field survey after the December 2004 Indian Ocean tsunami. *Earthquake Spectra*, 22(S3), 105-135.

Ji, C. (2015a) Rupture process of the 2007 Jan 13 Mw 8.1 - KURIL Island Earthquake. Publishing USGSWeb. http://earthquake.usgs.gov/earthquakes/eqinthenews/2007/us2007xmae/figures/static_out Accessed 02 June 2015.

Ji, C. (2015b) Preliminary Result of the Sep 12, 2007 Sumatra Earthquake, Publishing USGSWeb. http://earthquake.usgs.gov/earthquakes/eqinthenews/2007/us2007hear/results/static_out. Accessed 02 June 2015.

Koketsu, K., Yokota, Y., Nishimura, N., Yagi, Y., Miyazaki, S.I., Satake, K., Fujii, Y., Miyake, H., Sakai, S.I., Yamanaka, Y. and Okada, T. (2011) A unified source model for the 2011 Tohoku earthquake. *Earth and Planetary Science Letters*, 310(3), 480-487.

Koshimura, S., Oie, T., Yanagisawa, H., and Imamura, F. (2009) Developing fragility functions for tsunami damage estimation using numerical model and post-tsunami data from Banda Aceh, Indonesia. *Coastal Engineering Journal*, 51(03), 243-273.

Kulkarni, R., Wong, I., Zachariasen, J., Goldfinger, C., and Lawrence, M. (2013) Statistical analyses of great earthquake recurrence along the Cascadia subduction zone. *Bulletin of the Seismological Society of America*, 103(6), 3205-3221.

Lay, T., Kanamori, H., Ammon, C. J., Hutko, A. R., Furlong, K., and Rivera, L. (2009) The 2006–2007 Kuril Islands great earthquake sequence. *Journal of Geophysical Research*: Solid Earth (1978–2012), 114(B11).

Leelawat, N., Suppasri, A., Charvet, I. and Imamura, F. (2014) Building damage from the 2011 Great East Japan tsunami: quantitative assessment of influential factors. *Natural Hazards*, 73(2), 449-471.

Lorito, S., Romano, F., Piatanesi, A., and Boschi, E. (2008) Source process of the September 12, 2007, Mw 8.4 southern Sumatra earthquake from tsunami tide gauge record inversion. *Geophysical Research Letters*, 35(2).

Lynett, P., and Liu, P. L. F. (2005) A numerical study of the run-up generated by three-dimensional landslides. *Journal of Geophysical Research: Oceans*, 110(C3).

Lynett, P., Wu, T., and Liu, P. (2002) Modeling wave runup with depth-integrated equations. *Coastal Engineering* 46: 89-107.

Mas, E., Koshimura, S., Suppasri, A., Matsuoka, M., Matsuyama, M., Yoshii, T., ... and Imamura, F. (2012) Developing Tsunami fragility curves using remote sensing and survey data

of the 2010 Chilean Tsunami in Dichato. *Natural Hazards and Earth System Science*, 12(8), 2689-2697.

McGuire, R. K. (2004) *Seismic hazard and risk analysis*. Earthquake Engineering Research Institute.

Mikami, T., Shibayama, T., Esteban, M. and Matsumaru, R. (2012) Field survey of the 2011 Tohoku earthquake and tsunami in Miyagi and Fukushima prefectures. *Coastal Engineering* Journal, 54(01), p.1250011.

Mimura, N., Yasuhara, K., Kawagoe, S., Yokoki, H. and Kazama, S. (2011) Damage from the Great East Japan Earthquake and Tsunami-a quick report. *Mitigation and Adaptation Strategies for Global Change*, 16(7), 803-818.

Mofjeld, H. O., González, F. I., Titov, V. V., Venturato, A. J., and Newman, J. C. (2007) Effects of Tides on Maximum Tsunami Wave Heights: Probability Distributions*. *Journal of Atmospheric and Oceanic Technology*, 24(1), 117-123.

Mori, N., Takahashi, T., Yasuda, T. and Yanagisawa, H. (2011) Survey of 2011 Tohoku earthquake tsunami inundation and run-up. *Geophysical Research Letters*, 38(7).

Mori, N., Cox, D.T., Yasuda, T. and Mase, H. (2013) Overview of the 2011 Tohoku earthquake tsunami damage and its relation to coastal protection along the Sanriku Coast. *Earthquake Spectra*, 29(s1), S127-S143.

Murao, O., and Nakazato, H. (2010) Vulnerability functions for buildings based on damage survey data in Sri Lanka after the 2004 Indian Ocean tsunami, *in Proceedings of the 7th International Conference on Sustainable Built Environment*, 13–14 December 2010, Kandy, Sri Lanka.

Murotani, S., Miyake, H., and Koketsu, K. (2008) Scaling of characterized slip models for plate-boundary earthquakes. *Earth, Planets and Space*, 60(9), 987-991.

Murotani, S., Satake, K., and Fujii, Y. (2013) Scaling relations of seismic moment, rupture area, average slip, and asperity size for M~ 9 subduction-zone earthquakes. *Geophysical Research Letters*, 40(19), 5070-5074.

MRl, HAZUS-MH (2003) *Multi-Hazard Loss Estimation Methodology: Earthquake Model*. Department of Homeland Security, FEMA, Washington, DC.

Nelson, A. R., Kelsey, H. M., and Witter, R. C. (2006) Great earthquakes of variable magnitude at the Cascadia subduction zone. *Quaternary Research*, 65(3), 354-365.

Okada, Y. (1985) Surface deformation due to shear and tensile faults in a half-space. *Bulletin of the Seismological Society of America*, 75(4), 1135-1154.

Park, H., Cox, D. T., Lynett, P. J., Wiebe, D. M., and Shin, S. (2013) Tsunami inundation modeling in constructed environments: A physical and numerical comparison of free-surface elevation, velocity, and momentum flux. *Coastal Engineering*, 79, 9-21.

Park, H., Cox, D. T., and Petroff, C. M. (2015). An empirical solution for tsunami run-up on compound slopes. *Natural Hazards*, 76 (3), 1727-1743.

Priest, G. R., Goldfinger, C., Wang, K., Witter, R. C., Zhang, Y., and Baptista, A. M. (2010) Confidence levels for tsunami-inundation limits in northern Oregon inferred from a 10,000-year history of great earthquakes at the Cascadia subduction zone. *Natural Hazards*, 54(1), 27-73.

Reese, S., Cousins, W. J., Power, W. L., Palmer, N. G., Tejakusuma, I. G., and Nugrahadi, S. (2007) Tsunami vulnerability of buildings and people in South Java–field observations after the July 2006 Java tsunami. *Natural Hazards and Earth System Science*, 7(5), 573-589.

Rossetto, T., Peiris, N., Pomonis, A., Wilkinson, S.M., Del Re, D., Koo, R. and Gallocher, S. (2007) The Indian Ocean tsunami of December 26, 2004: observations in Sri Lanka and Thailand. *Natural Hazards*, 42(1), 105-124.

Satake, K., Wang, K., and Atwater, B. F. (2003) Fault slip and seismic moment of the 1700 Cascadia earthquake inferred from Japanese tsunami descriptions. *Journal of Geophysical Research: Solid Earth* (1978–2012), 108(B11).

Satake, K., Fujii, Y., Harada, T., and Namegaya, Y. (2013) Time and space distribution of coseismic slip of the 2011 Tohoku earthquake as inferred from tsunami waveform data. *Bulletin of the Seismological Society of America*, 103(2B), 1473-1492.

Scawthorn, C., Flores, P., Blais, N., Seligson, H., Tate, E., Chang, S., Mifflin, E., Thomas, W., Murphy, J., Jones, C. and Lawrence, M. (2006) HAZUS-MH flood loss estimation methodology. II. Damage and loss assessment. *Natural Hazards Review*, 7(2), 72-81.

Shao, G., Li, X., Ji, C., and Maeda, T. (2011) Focal mechanism and slip history of the 2011 M w 9.1 off the Pacific coast of Tohoku Earthquake, constrained with teleseismic body and surface waves. *Earth, Planets and Space*, 63(7), 559-564.

Shao et al. (2015) Preliminary slip model of the Feb 27, 2010 Mw 8.9 Maule, Chile Earthquake, Publishing USGSWeb.
http://www.geol.ucsb.edu/faculty/ji/big_earthquakes/2010/02/27/result/static out Accessed 02 June 2015.

Suppasri, A., Mas, E., Koshimura, S., Imai, K., Harada, K. and Imamura, F. (2012) Developing tsunami fragility curves from the surveyed data of the 2011 Great East Japan tsunami in Sendai and Ishinomaki plains. *Coastal Engineering Journal*, 54(01), 1250008.

Suppasri, A., Mas, E., Charvet, I., Gunasekera, R., Imai, K., Fukutani, Y., Abe, Y., Imamura, F. (2013) Building damage characteristics based on surveyed data and fragility curves of the 2011 Great East Japan tsunami. *Natural Hazards*, 66(2), 319-341.

Suppasri, A., Charvet, I., Imai, K. and Imamura, F. (2015) Fragility Curves Based on Data from the 2011 Tohoku-Oki Tsunami in Ishinomaki City, with Discussion of Parameters Influencing Building Damage. *Earthquake Spectra*, 31(2), 841-868.

Tarbotton, C., Dall'Osso, F., Dominey-Howes, D. and Goff, J. (2015) The use of empirical vulnerability functions to assess the response of buildings to tsunami impact: Comparative review and summary of best practice. *Earth-Science Reviews*, 142, 120-134.

Titov, V.V., Gonzalez, F.I., Bernard, E.N., Eble, M.C., Mofjeld, H.O., Newman, J.C. and Venturato, A.J. (2005) Real-time tsunami forecasting: Challenges and solutions. In *Developing Tsunami-resilient Communities* (41-58). Springer Netherlands.

Titov, V. V., Moore, C. W., Greenslade, D. J. M., Pattiaratchi, C., Badal, R., Synolakis, C. E., and Kânoğlu, U. (2011) A new tool for inundation modeling: Community Modeling Interface for Tsunamis (ComMIT). *Pure and Applied Geophysics*, 168(11), 2121-2131.

Tsunami Pilot Study Working Group (2006) Seaside, Oregon, *Tsunami Pilot Study-Modernization of FEMA Flood Hazard Maps*. Joint NOAA/USGS/FEMA Special Report 94.

Valencia, N., Gardi, A., Gauraz, A., Leone, F., and Guillande, R. (2011) New tsunami damage functions developed in the framework of SCHEMA project: application to European-Mediterranean coasts. *Natural Hazards and Earth System Science*, 11(10), 2835-2846.

van de Lindt, J.W. and Dao, T.N. (2009) Performance-based wind engineering for wood-frame buildings. *Journal of Structural Engineering*, 135(2), 169-177.

Wang, H., Mostafizi, A., Cramer, L., Cox, D., and Park. H. (2015) An agent-based model of a multimodal near-field tsunami evacuation: Decision-making and life safety. *Transportation Research Part C: Emerging Technologies*, http://dx.doi.org/10.1016/j.trc.2015.11.010.

Wang, K., Wells, R., Mazzotti, S., Hyndman, R. D., and Sagiya, T. (2003) A revised dislocation model of interseismic deformation of the Cascadia subduction zone. *Journal of Geophysical Research: Solid Earth* (1978–2012), 108(B1).

Wiebe, D. M., and Cox, D. T. (2014) Application of fragility curves to estimate building damage and economic loss at a community scale: a case study of Seaside, Oregon. *Natural Hazards*, 71(3), 2043-2061.

Witter, R.C., Zhang, Y.J., Wang, K., Priest, G.R., Goldfinger, C., Stimely, L., English, J.T. and Ferro, P.A. (2013) Simulated tsunami inundation for a range of Cascadia megathrust earthquake scenarios at Bandon, Oregon, USA. *Geosphere*, 9(6), 1783-1803.

Wood, N. (2007) *Variations in city exposure and sensitivity to tsunami hazards in Oregon* (No. 2007-5283). Geological Survey (US).

Yagi, Y. (2004) Source rupture process of the 2003 Tokachi-oki earthquake determined by joint inversion of teleseismic body wave and strong ground motion data. *Earth, Planets and Space*, 56(3), 311-316.

Yeh, H. (2007) Design tsunami forces for onshore structures. *Journal of Disaster Research*, 2(6), 531-536.

Yeh, H., Sato, S., & Tajima, Y. (2013) The 11 March 2011 East Japan earthquake and tsunami: tsunami effects on coastal infrastructure and buildings. *Pure and Applied Geophysics*, 170(6-8), 1019-1031.

Zhang, Y. and Baptista, A.M. (2008) SELFE: a semi-implicit Eulerian–Lagrangian finite-element model for cross-scale ocean circulation. *Ocean Modelling*, 21(3), pp.71-96.

5. Appendix

Here attached two additional manuscripts which are related with the thesis work.

5.1 Appendix A

1. Park, H., Cox, D. T., Lynett, P. J., Wiebe, D. M., and Shin, S. (2013) Tsunami inundation modeling in constructed environments: A physical and numerical comparison of free-surface elevation, velocity, and momentum flux. Coastal Engineering, 79, 9-21.

Tsunami Inundation Modeling in Constructed Environments: A Physical and Numerical Comparison of Free-Surface Elevation, Velocity, and Momentum Flux.

Hyoungsu Park*
Graduate Research Assistant, School of Civil and Construction Engineering, Oregon State University, Corvallis, OR 97331-2302, USA, Email: Hyoungsu.park@gmail.com, Tel: 1-541-602-8618, Fax: 541-737-3052

Daniel T. Cox
Professor, School of Civil and Construction Engineering, Oregon State University, Corvallis, OR 97331-2302, USA, Email: dan.cox@oregonstate.edu

Patrick J. Lynett
Associate Professor, Dept. of Civil and Environmental Engineering, University of Southern California, Los Angeles, CA 90089-2531, USA, Email: plynett@usc.edu

Dane M. Wiebe
Graduate Research Assistant, School of Civil and Construction Engineering, Oregon State University, Corvallis, OR 97331-2302, USA, Email: wiebed@onid.orst.edu

Sungwon Shin
Assistant Professor, Waterfront and Coastal Research Center, Kwandong University, 522 Naegok-dong Universtel #731, Gangneung, Gangwon-do, 210-701, South Korea, Email: sungwshin@gmail.com

* Corresponding Author

Abstract

A laboratory benchmark test for tsunami inundation through an urban waterfront including free surface elevation, velocity, and momentum flux is presented and compared with a numerical model (COULWAVE). The physical model was a 1:50 scale idealization of the town Seaside, Oregon, designed to observe the complex tsunami flow around the macro-roughness such as buildings idealized as impermeable, rectangular blocks. Free surface elevation and velocity time series were measured and analyzed at 31 points along 4 transects. Optical measurements of the leading bore front were used in conjunction with the in-situ velocity and free surface measurements to estimate the time-dependent momentum flux at each location. The maximum free surface elevation and momentum flux sharply decreased from the shoreline as measurement location moves landward, while the cross-shore velocity slowly decreased linearly. The experimental results show that the maximum momentum flux is overestimated by 60 to 260%, if it is calculated using the each maximum values of the free surface elevation and cross-

shore velocity. Comparisons show that the numerical model is in good agreement with the physical model at most locations when tuned to a friction factor of 0.005. When the friction factor decreased by a factor of 10 (from 0.01 to 0.001), the average maximum free surface elevation increased 15%, and the average cross-shore velocity and momentum flux increased 95 and 208%, respectively. This highlights the importance of comparing velocity in the validation and verification process of numerical models of tsunami inundation.
Keywords: Tsunami, Inundation, Macro-roughness, Benchmark, COULWAVE, Friction factor.

1.1 Introduction

Tsunamis are unpredictable natural events which are most commonly associated with large magnitude earthquakes along coastal plate boundaries. For near field events, the first waves often arrive in the tens of minutes, leaving little time for preparation or evacuation, and can inundate several kilometers inland. Tsunamis, such as the 2004 Indian Ocean event, delivered widespread damage to coastal communities both near and far from the epicenter, and caused casualties in the hundreds of thousands, which is devastating both locally and regionally (Imamura *et al.*, 2006). The most recent tsunami occurred on March 11th, 2011 in the north-western Pacific Ocean 72 km east of the Oshika Peninsula of Tōhoku, Japan. This event resulted in 15,844 fatalities 3,394 missing peoples and damaged 128,530 houses, 230,332 buildings and 78 bridges (Mori *et al.*, 2011).

To minimize casualties and damage from future events, a deeper understanding of tsunamis is required, particularly for the complex flows associated with the tsunami inundation and the return flow over complex bathymetry and around structures. Due to the increasing computational power and maturation of numerical schemes, the numerical modeling of tsunami inundation is becoming increasingly important for tsunami mitigation (e.g., Lynett, 2007). However, some simplifications of the numerical schemes are required, particularly with respect to the problem of turbulence closure, and to extend the model over a sufficiently large domain (e.g., several km to encompass a coastal community).

To model the tsunamis hazard for coastal communities accurately, the constructed environment must be incorporated into the numerical model as it strongly influences the hydrodynamics. The 2004 Indian Ocean Tsunami field survey highlighted the importance of coastal structures in mitigating tsunami damage (Darlymple and Kriebel, 2005; Tomita *et al.*,

2006). After the 2011 Great East Japan Tsunami, the field survey also highlighted that tsunami damage is strongly dependent on location and environment (Yeh *et. al*., 2012). Yeh (2006) showed that the hydrodynamic force of the tsunami on structures in the inundation zone is proportional to the momentum flux, which is the inundation depth multiplied by the squared velocity, and can be related to the probability of damage (*e.g*., Koshimura *et al*. 2009a; Koshimura *et al*. 2009b; FEMA, 2008).

It is also necessary to benchmark these models performance in terms of predicting the free surface and velocity as well as their sensitivity to tuning parameters. Several benchmark tests are prevailing as standard verification methods for the numerical modeling of tsunamis (Yeh *et al.*, 1996; Synolakis *et al.*, 2007; Liu *et al.*, 2008) such as exact solutions and physical model data of solitary waves on simple sloped beaches (Synolakis, 1987) and on compound sloped beaches (Kânoğlu and Synolakis, 1998), large scale conical island physical model (Briggs *et al.*, 1995), and runup on a complex three-dimensional coast (Hokkaido Tsunami Survey Group, 1993). In addition, landslide tsunamis generated by submarine mass failure received much attention after the 1998 Papua New Guinea tsunami, and a three dimensional landslides experiment (Synolakis, 2003) was performed as a benchmark test. Even though most casualties and damage from tsunamis are related to the complex inundation flow, which includes wave breaking at the shoreline and interaction with coastal structures, the most advanced numerical models and benchmark tests only provide the maximum run-up heights or a time series of free surface elevation. Complex flows are difficult to both estimate due to the required computing power and validate due to the absence of proper benchmark tests. As a result, most numerical models focused on the estimation of tsunami propagation, and calculation of arrival times and maximum runup heights.

Several studies related to macro-roughness and tsunami velocity variation have been performed. Cox *et al.* (2008) performed physical model tests of Seaside, Oregon, which showed that the macro-roughness reduced the tsunami inundation velocity by 40% (Rueben *et al.*, 2010). The reduction in runup elevations and maximum overland velocities due to obstructions have been studied numerically (Lynett, 2007) and Tomita and Honda (2007) highlighted that the resulting inundation area and depth from the numerical model with macro-roughness was in good agreement with the actual inundation observed in Galle city, Sri Lanka from the 2004 Indian Ocean Tsunami. Other studies on the influence of macro-roughness element arrays

compared the free surface elevation of numerical and physical model results (Goseberg and Schlurmann, 2010), and the effect of bed slope and bottom friction on maximum tsunami runup height and velocity using numerical models (Apotsos *et al.*, 2011). More recently, the importance of artificial and natural structures on tsunami mitigation was studied through a numerical and field study (Nandasena *et al*., 2012).

In this project, we present a model study of tsunami flow over and around macro-roughness in the idealized physical model of Seaside, Oregon, and provide a new data set of free surface elevation, velocity, and momentum to be used as a benchmark test. This data set was used to validate the numerical model results from COULWAVE (Lynett *et al.,* 2002). This paper is outlined as follows. Section 2 presents the large-scale physical model basin, measurement devices and their locations, describes the model data analysis, and shows the results of the experiment. Section 3 presents the numerical model setup. Section 4 presents a comparison between the physical and numerical model. Section 5 concludes the paper with summary findings and ideas for future work.

2.1 Model Design Setup

The physical model was an idealized representation of Seaside, Oregon, located in the Pacific Northwest, United States constructed at 1:50 scale. There are several reasons why this site was chosen for study. One, the proximity to the Cascadia Subduction Zone (CSZ) which generates tsunamis in excess of 10 m with a recurrence interval of 500 years (Tsunami Pilot Study Working Group, 2006). Two, the simple bathymetry of shore parallel contours and a large onshore spit. And three, the high concentration of residential and commercial buildings concentrated near the water front and located well within the expected tsunami inundation zone. Fig. 1 shows the expected extent of inundation from the CSZ event tsunami (solid line) (DOGAMI, 2001), the dimensions of the physical model basin (dash-dot line), and the dimensions of the physical model with macro-roughness (dashed line). The inset map within Fig. 1 shows the location of Seaside, Oregon, on a region scale, the proximity to the CSZ, and the location of the Deep-ocean Assessment and Reporting of Tsunamis (DART) buoys (NOAA, 2012).

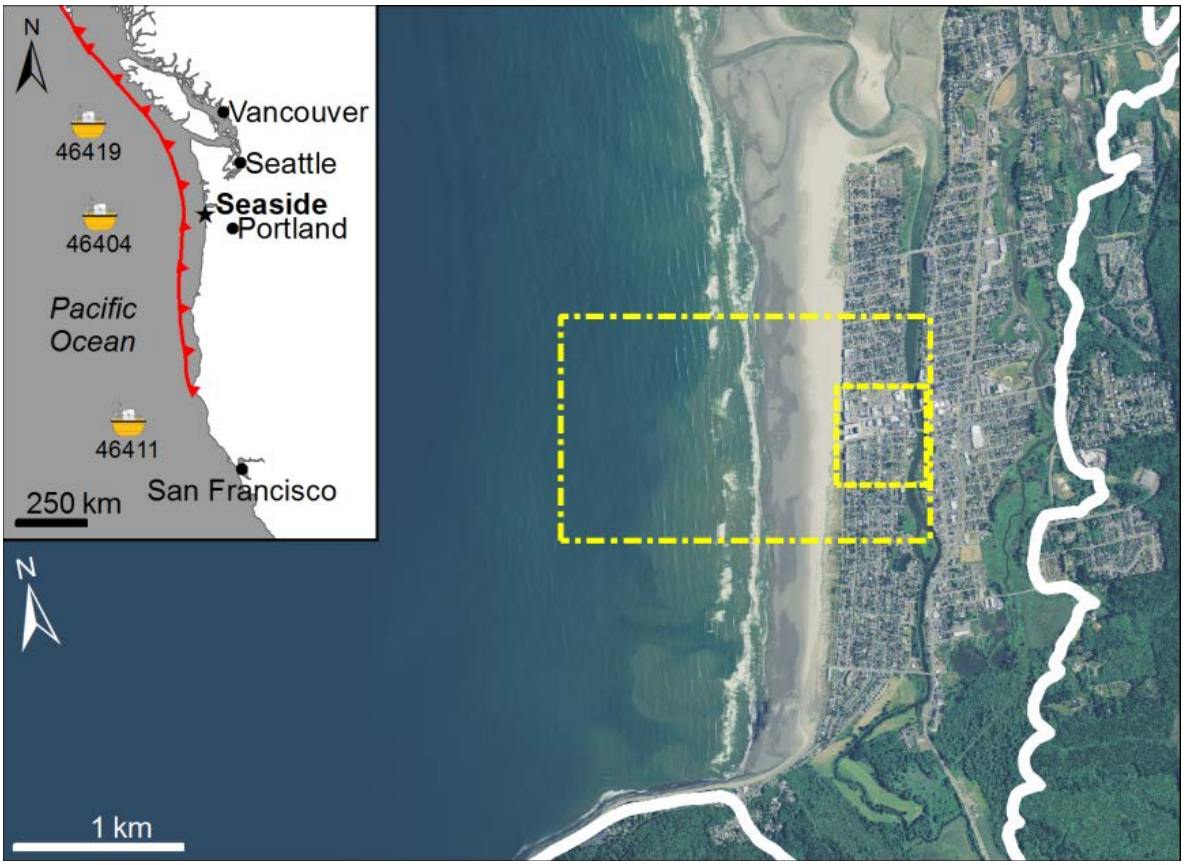

Fig. 1. Seaside, Oregon. Main map shows the 1:50 physical model region (dash-dot), macro-roughness region (dash), and tsunami inundation line (solid). Inset map shows regional location of Seaside, location of offshore DART buoys, and proximity to the Cascadia Subduction Zone.

Plan and elevation views of the physical model in the Tsunami Wave Basin at O.H. Hinsdale Wave Research Laboratory, Oregon State University, are shown in Fig. 2. The background images are satellite imagery of Seaside and a photo of the top view of the physical model (Rueben *et al.*, 2010). The origin of the *x* and *y* axes was centered on the wavemaker, with *x* positive onshore and *y* positive to the north. The rectangular basin was 48.8 m long, 26.5 m wide, and 2.1 m deep, and was equipped with a segmented, piston-type wavemaker with a maximum stroke of 2.1 m and maximum velocity of 2.0 m/s (Cox *et al.*, 2008). The idealized bathymetry for Seaside was constructed of smooth concrete with a flat finish, and an estimated roughness height of 0.1-0.3 mm (Rueben *et al.*, 2010). The profile consisted of a 10 m horizontal section near the wavemaker with a depth of 0.97 m, an 8 m section at a 1:15 slope, a 15 m section at a 1:30 slope, on which the SWL intersected, and another horizontal section 11 m in length which extended to the back wall. The idealized buildings which created the macro-roughness elements were fixed in place on the upper horizontal section to provide repeatability

between tests. Four surface piercing wire resistance wave gages (WG1-WG4) were fixed in the basin at the following locations: WG1 (2.086 m, -0.515 m), WG2 (2.068 m, 4.065 m), WG3 (18.618 m, 0.000 m), and WG4 (18.618, 2.860 m).

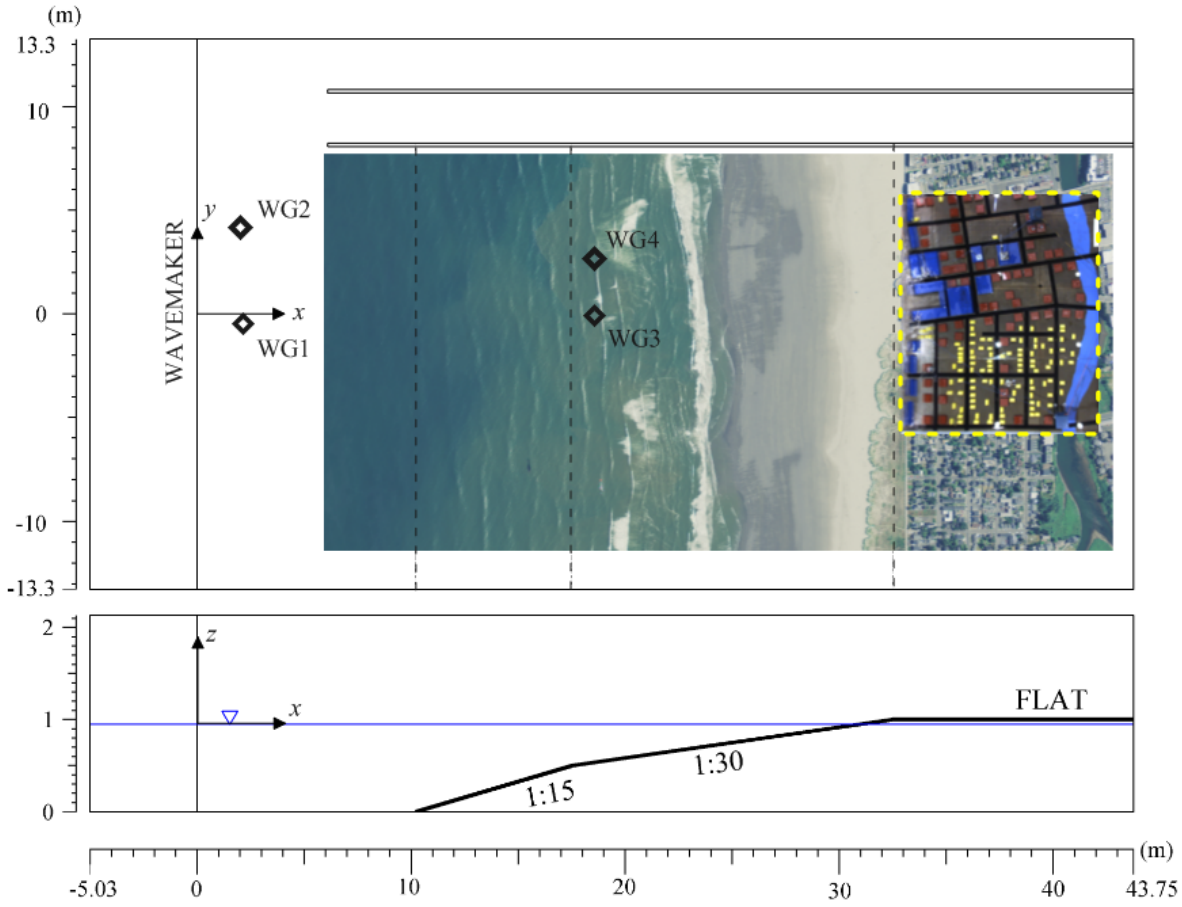

Fig. 2. Plan and elevation view of the physical model in the Tsunami Wave basin. Satellite imagery and a laboratory photo provide the scale of the Seaside, OR, model.

A detailed plan view of the macro-roughness elements is shown in Fig. 3 in the same orientation as Fig. 1 and Fig. 2, with the Pacific Ocean to the left. In the model, the town is fronted by a 2 m (prototype scale) seawall. The blocks represent large hotels or commercial buildings, light commercial buildings, and residential houses, and the thick solid black lines between the blocks represent city streets. The buildings were positioned on the flat ground using aerial imagery and field survey data. The Necanicum River which flows through the center of Seaside (x = 42 m), was not included in the model, and is only referenced with blue paint. Other parameters not taken into account by the physical model include vegetation, debris, sediment, and other small-scale roughness effects. The white boxes labeled A to D and 1 through 9,

represent measurement locations of free surface elevation and velocity. Measurement locations are divided into 4 lines; A to D. Line A is located on a city street parallel to the primary inundation flow direction and numbered sequential 1 to 9, as the measurement locations move inland. Lines B and C are on streets inclined approximately 10° to the flow direction, are flanked by hotels or commercial buildings, and numbered the same as Line A. Line D is located mostly behind buildings and only had 4 measurement locations. In total there were 31 measurement locations.

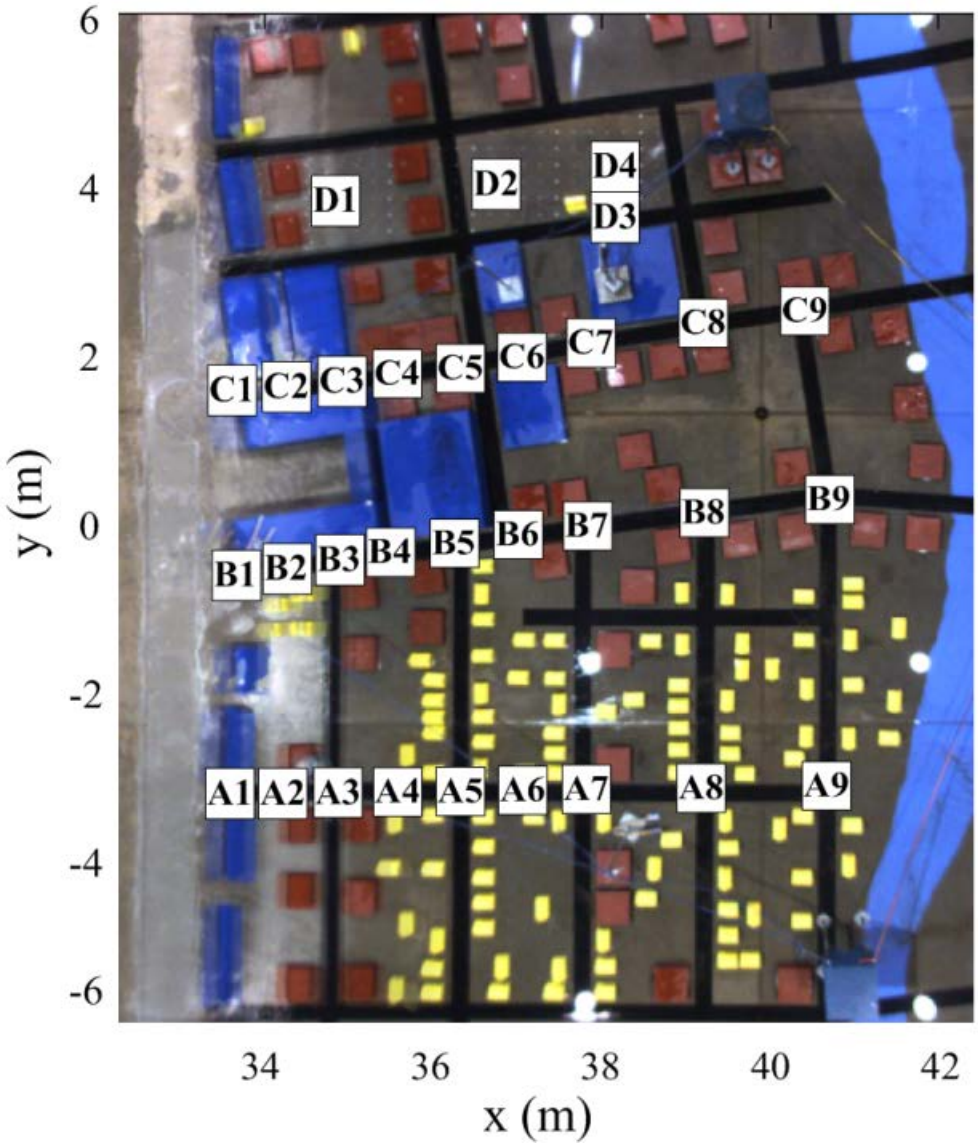

Fig. 3. Detailed plan view of macro-roughness elements of the physical model, annotated with measurement locations.

Four pairs of co-located ultra-sonic surface wave gages (USWG, Senix Corporation TS-30S1-IV) and acoustic-Doppler velocimeters (ADV, Nortec Vectrino) sensors were used to measure the free surface and flow velocity in Lines A, B, C, and D, simultaneously. Through the experiment, the sensors in lines A, B, and C moved in unison from Positions 1 through 9, while the sensors in Line D moved somewhat independently. For the single tsunami wave condition, the total number of trials, N_T, was 136, of which the total number of acceptable trials, N_V, which were suitable for analysis was 99. The majority of trials (N_T = 53) were performed with all the sensors located at Position 1 to collect statistics of turbulence due to the wave breaking. Because of time constraints, the number of trials performed at the remaining locations decreased; however, an adequate number of trials were still performed to provide reliable ensemble averages. Table 1 lists the coordinates of each measurement location and the total number of trials performed and available. Again, the origin of the coordinates is the center of the wave maker (Fig. 2).

Table 5**.** Measurement locations and numbers of total and available trials, N_T and N_V, respectively.

Num.	**Line A**		**Line B**		**Line C**		**A, B, & C**		**Num.**	**Line D**			
	x (m)	y (m)	x (m)	y (m)	x (m)	y (m)	N_T	N_V		x (m)	y (m)	N_T	N_V
1	33.61	-3.19	33.72	-0.59	33.81	1.51	53	48	1	35.12	3.71	53	48[i]
2	34.10	-3.19	34.22	-0.53	34.55	1.60	11	10	2	36.68	3.89	33	26[ii]
3	34.53	-3.18	34.68	-0,47	35.05	1.69	12	12					
4	35.04	-3.18	35.18	-0.41	35.56	1.77	12	4					
5	35.54	-3.19	35.75	-0.32	36.05	1.85	18	5	3	38.09	4.07	18	5[iii]
6	36.35	-3.20	36.64	-0.23	37.05	1.99	7	6	4	38.14	3.59	28	20[iv]
7	37.76	-3.20	37.77	-0.07	38.24	2.19	6	3					
8	39.22	-3.20	39.22	0.14	39.21	2.34	8	7					
9	40.67	-3.23	40.67	0.27	40.40	2.58	9	4					
Total							136	99				136	99

*i) Corresponds to line A to C Num. 1; ii) Corresponds to lines A to C Num. 2, 3 and 4; iii) Corresponds to lines A to C Num. 5; iv) Corresponds to lines A to C Num. 6, 7, 8 and 9

** Ensemble averaged data at all 31 measurement locations are available by contacting the first author.

The design tsunami condition produced by the wavemaker used an error function to maximize the full 2.0 m stroke, and had a duration of 10.0 s. The wave height measured at WG1, over the horizontal section of the basin, was approximately 0.20 m. At prototype scale, this wave height is 10 m, which corresponds to the estimated tsunami wave height for the "500-yr" CSZ tsunami for this region (Tsunami Pilot Study Working Group, 2006).

2.2 Model Results

This section presents the measured time dependent and cross-shore variability of maximum free surface displacement, velocity, and momentum flux. Fig. 4a shows the wave-maker paddle displacement, *S* (solid line), as a function of time and the free surface elevation on the paddle (dashed line) for Trial 51. Fig. 4b shows the measured time series of free surface elevation at WG1 (solid line) and WG3 (dashed line) for Trial 51. WG 1 and 3 were located 2.0 m and 18.6 m from the wavemaker, and had peak elevations of 0.17 and 0.20 m, respectively. The shape of wave at WG3 was asymmetric and pitched forward as it passed the change in bathymetry. At t = 35 s, reflected waves were detected at WG3 due to wave interaction on the shoreline and front row of buildings. Fig. 4c and 4d show the time series of free surface elevation and cross-shore velocity for Trial 51 at A1 (solid line) and C1 (dash line). The maximum free surface elevation, $(\eta)_m$, and maximum cross-shore velocity, $(u)_m$, were 0.25 and 0.18 m and 1.45 and 1.85 m/s at A1 and C1, respectively. The USWG and ADV sensors were intended to measure the instantaneous velocity over land; however, the ADV sensor only detected velocities after t = 26.4 s, which was 1.3 s after the USWG sensor recorded the changes in the free surface elevation. The leading edge velocity was determined using optical measurements (Reuben et al., 2010) and an interpolation was used to replace the missing velocity data as explained in the next paragraph.

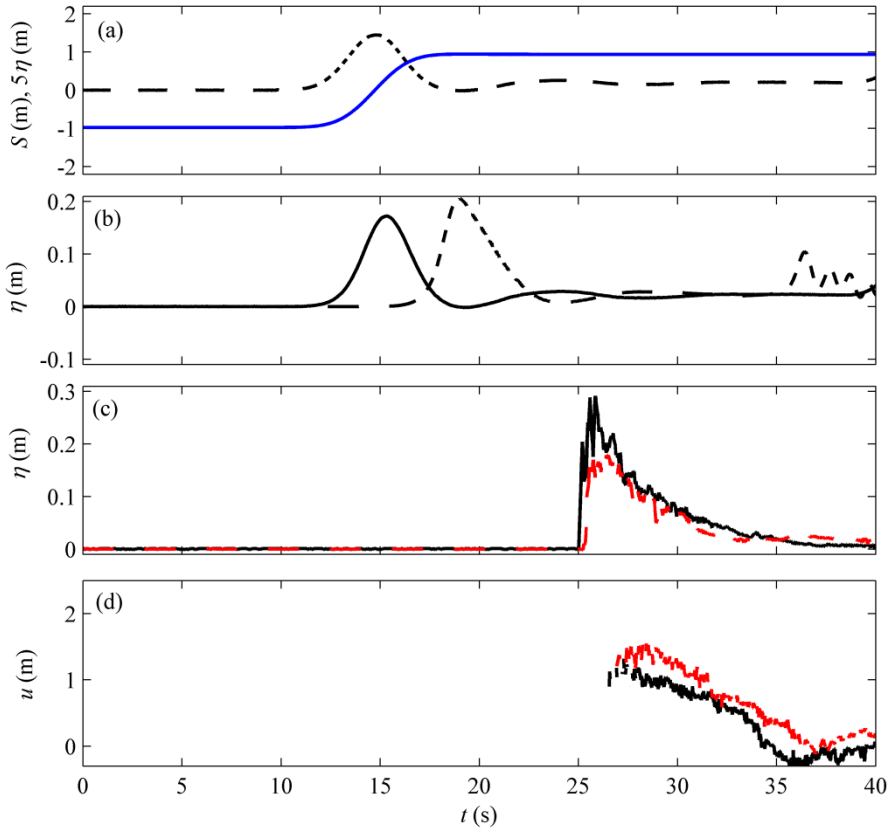

Fig. 4. Time series plots for Trial #51. (a) Wave-maker paddle displacement, S, (solid line) and free surface elevation on paddle multiplied by a factor of 5, 5η (dashed line. (b) η, at WG1 (solid line) and at WG3 (dashed line).(c) η at A1 (solid line) and at C1 (dashed line). (d) u at A1 (solid line, down) and at C1 (dashed line, upper).

Fig. 5a shows the time series of ensemble averaged free surface elevation, $<\eta>$, ensemble averaged cross-shore velocity, $<u>$, and ensemble averaged momentum flux, $<M>$ at A1. The momentum flux per unit mass is generally calculated as Hu^2, where H is the total water depth, calculated by subtraction of vertical datum, h, from free surface elevation. Fig. 5b shows the number of recorded data for free surface elevation, N_η and cross-shore velocity, N_u, at each time step for location A1. The total number of available trials, N_V, at A1 was 48 (Table 1). For the USWG, there were some dropouts in the free surface measurements before the arrival of the bore ($t < 25.1$ s) and the number of available measurements was approximately $N_\eta = 40$. After arrival of the bore, the sensor accurately captured the free surface elevation and $N_\eta = N_V = 48$. For the ADV, due to air entrainment in the leading edge of the bore, no data were collected for $25.1 < t < 26.4$ s. After 26.4 s, the number of trials for which data were available increased as shown in Fig 5b (open circles) with $N_u > 40$ at around $t = 28.5$ s, leading to a stable estimate of the velocity as

can be seen in Fig 5a. To obtain an estimate of the missing data, the leading wave velocities were analyzed by tracking the leading edge trajectory of each time step using two high resolution video cameras mounted on the ceiling of the wave basin (Rueben *et al.*, 2010). A second order polynomial curve (slender lines) was fit from the leading velocity (filled circle) to the ensemble averaged ADV data at t = 28.5 s. The velocity was assumed to increase linearly from zero (recorded by the USGW) to the leading edge velocity. The ensemble averaged momentum flux $\langle M \rangle$ was estimated from the ensemble estimates of the total water depth and the measured and interpolated velocity,

$$\langle M \rangle = \langle \eta \rangle \cdot \langle H \rangle^2$$

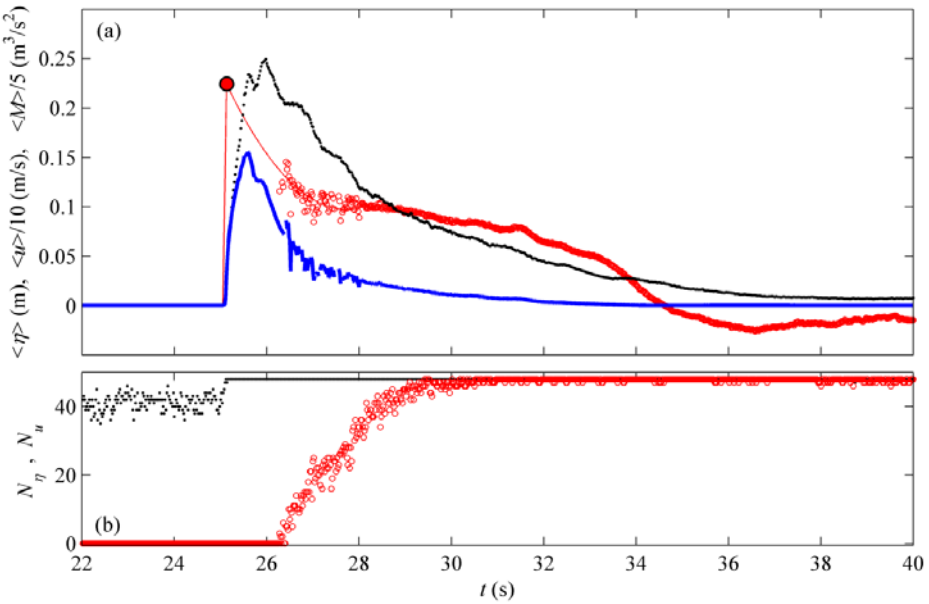

Fig. 5. Measured and calculated inundation flow data at A1. (a): Ensemble averaged free surface elevation, $\langle \eta \rangle$ (dot), ensemble averaged velocity, $\langle u \rangle$ (circle), ensemble averaged momentum flux, $\langle M \rangle$ (thick line), leading wave velocity from optical measurement, u_L (filled circle), fitted curve for $\langle u \rangle$ (slender line). (b): Number of recorded free surface elevation at each time step, N_η (dot) and number of recorded cross-shore velocity at each time step, N_u (circle).Number of data recorded at each time step from USWG (dot) and ADV (circle).

The same procedure was performed at each measurement location, and the results at A8 are shown in Fig. 6. For A8, the ADV was able to capture more of the leading wave velocity because there was less air entrainment at A8. However, there was still some missing velocity data, and the same curve fitting procedure was used. The optical measurement at A8 was located within the scatter of the measured $\langle u \rangle$ and gives confidence that the procedure was reasonable.

As the wave propagated around the macro-roughness, properties such as wave shape and the location of maximum free surface elevation, cross-shore velocity, and momentum flux, changed (Fig. 5 and Fig. 6). The maximum free surface elevation and cross-shore velocity decreased from A1 to A8 from 0.25 to 0.06 m and 2.3 to 1.6 m/s, respectively. As the wave inundated the land, the location of maximum free surface elevation occurred later in time, but the location of maximum velocity remained at the front part of the wave. The maximum momentum flux decreased from A1 to A8 from 0.82 to 0.05 m^2/s^3, and the locations did not coincide with either the maximum velocity or free surface elevation. Similar to the maximum free surface elevation, the location of the maximum momentum flux also transitioned from the front to the rear of wave as it propagated over the land.

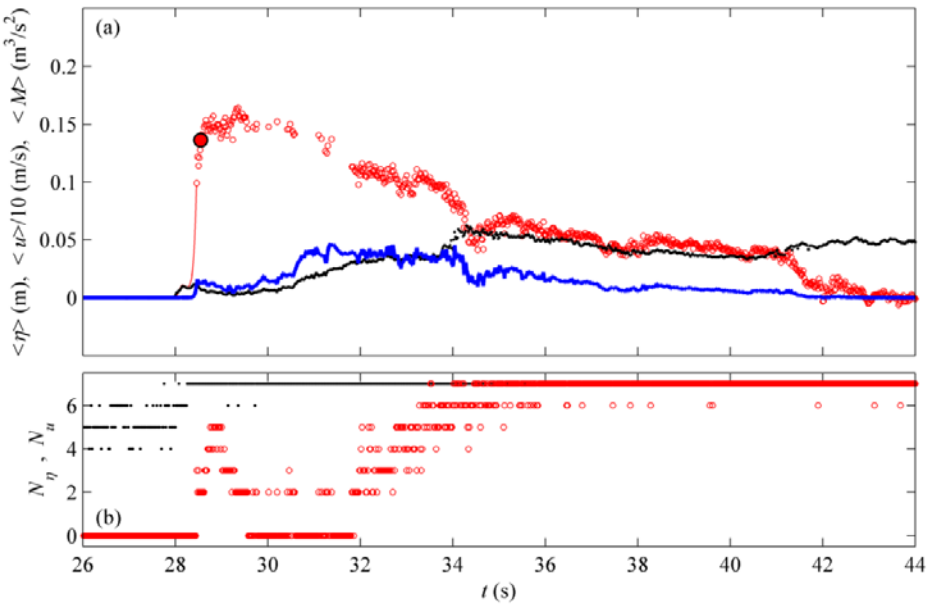

Fig. 6. Measured and calculated inundation flow data at A8. (a): Ensemble averaged free surface elevation, <η> (dot), ensemble averaged velocity, <u> (circle), ensemble averaged momentum flux, <M> (thick line), leading wave velocity from optical measurement, u_L (filled circle), and interpolated velocity (slender line). (b): Number of recorded free surface elevation at each time step, N_η (dot) and number of recorded cross-shore velocity at each time step, N_u (circle).Number of data recorded at each time step from USWG (dot) and ADV (circle).

Note that the momentum flux, M, are calculated by multiplying each time series of H by u^2, and the maximum momentum flux, $(M)_m$, taken as the maximum value over the time series. However, if $(M)_m$ were to be calculated by multiplying the maximum value of H and, u then $(M)_m$ would be overestimated by approximately 60% at A1 and 260% at A8. The importance of

correctly estimating the maximum momentum flux as it relates to hydrodynamic force on infrastructure has been discussed by FEMA (2008).

3.1 Numerical Model

There is a wide range of numerical models that could be used to simulate the Seaside experiments. Depth-integrated models, such as those based on the nonlinear shallow water (e.g. Titov and Synolakis, 1995) or Boussinesq-type (e.g. Shi *et al*., 2012) equations are commonly used to simulate overland tsunami flow. Here, we use the model COULWAVE which solves a Boussinesq set of equations and approximately includes the effects of bottom-stress-driven turbulence with the associated vorticity (Kim *et al*., 2009) and small-scale turbulent mixing (Kim and Lynett, 2011). The governing equations are tedious and will not be repeated here, but can be found with details in the above references. A high-order finite-volume numerical solution scheme is employed to solve the conservative-form equations, and the model has been validated for wave overtopping of structures and interaction with steep slopes (Lynett *et al*., 2010).

For the simulations presented in this paper, the wave basin is discretized with a constant and uniform grid of 5 cm. The wave is generated along the offshore boundary by implementing a wavemaker-type condition (horizontally moving vertical wall) and is forced with the wavemaker trajectory measured during the experiment. The bathymetry and topography grid employs the lidar-surveyed data taken during the experiment, spatially averaged to fit the coarser numerical grid. It is important to note here that the individual structures and buildings in the town are approximated as steep-sided topography; while in reality the sides of these buildings are vertical they are not numerically modeled as such. Many of the buildings are overtopped by the wave, and it is very difficult to numerically implement a vertical wall boundary condition and simultaneously allow dynamic overtopping. Therefore, the maximum bottom slope found in the domain can be controlled by the grid resolution, and here any side slope that exceeds 2:1 (~63 degrees) is smoothed until no longer this steep. Results have been checked for grid-length-dependent numerical convergence.

The breaking model used is that described in Lynett (2006), which is very similar to the scheme given in Kennedy *et al*. (2000). Bottom stress is calculated with the common quadratic friction law, *i.e.* $\frac{\partial u}{\partial t} + \cdots + \frac{fu|u|}{H} = 0$, where the dimensionless friction factor, *f*, is given as an input value, constant in both space and time throughout the simulation. The stochastic backscatter model presented in Kim and Lynett (2011) is not used in the simulations presented

here. The full Boussinesq-type set of equations are solved at all points in the domain; there is no switch-off of high-order terms over initially dry grid points.

4.1 Comparison of Results and Discussions

The majority of previous benchmark tests for inundation models typically compare a time series of free surface elevation or maximum run-up height, but in this study, the time series and maximum values of free surface elevation, cross-shoreline velocity, and momentum flux are extracted from the numerical model and directly compared with the physical model results for model verification.

A time series comparison of $<\eta>$, $<u>$ and $<M>$ between the physical model (dotted line) and numerical model (COULWAVE) (solid line) at B1, B4, B6, and B9 (Line B is parallel to the flow direction and flanked by hotels and commercial buildings) are shown in Fig. 7, Fig. 8, and Fig. 9, respectively. There are local disagreements in free surface elevation and momentum flux comparison, but general tendencies and magnitudes were well matched with physical model results. Specifically, COULWAVE underestimates the free surface elevation at B1 and B4, whereas at B9 it overestimates the value. However, for momentum flux, COULWAVE underestimates the value at B1, and overestimates at B6 and B9.

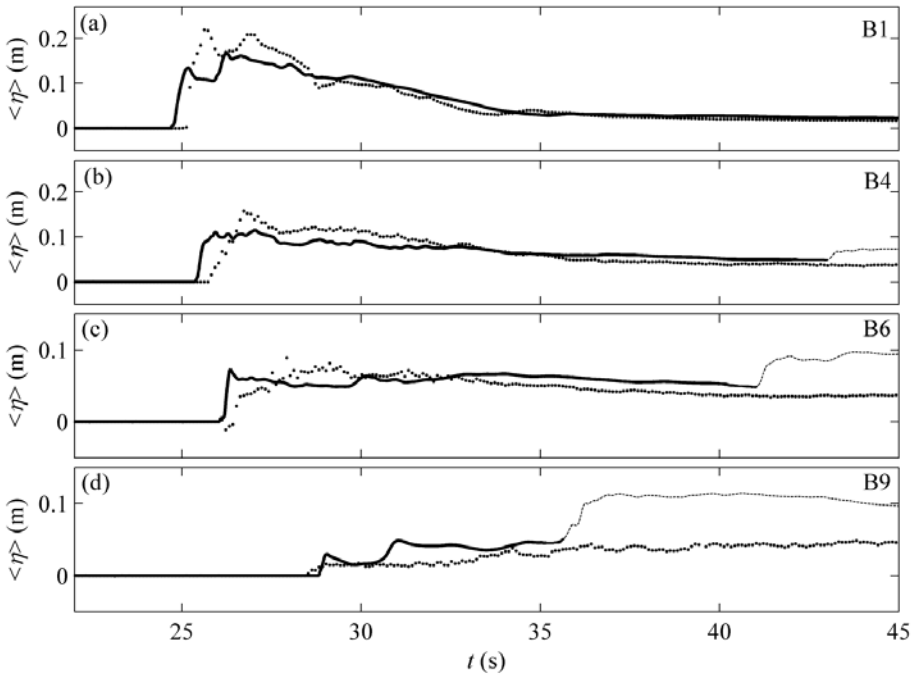

Fig. 7. Comparison of <η> between physical model (dot) and numerical model (solid line) at B1, B4, B6 and B9. Where wave reflection is present in the numerical model, the solid line switches to a dashed line.

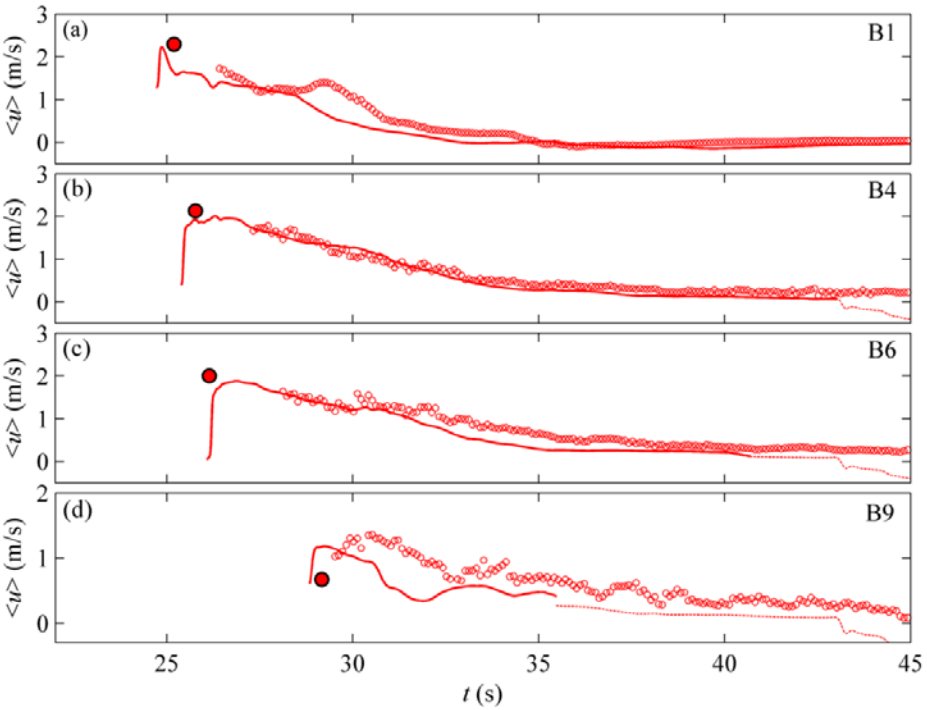

Fig. 8. Comparison of <u> between physical model (circle) and numerical model (solid line) at B1, B4, B6 and B9 with the leading velocity from optical measurement (filled circle). Where wave reflection is present in the numerical model, the solid line switches to a dashed line.

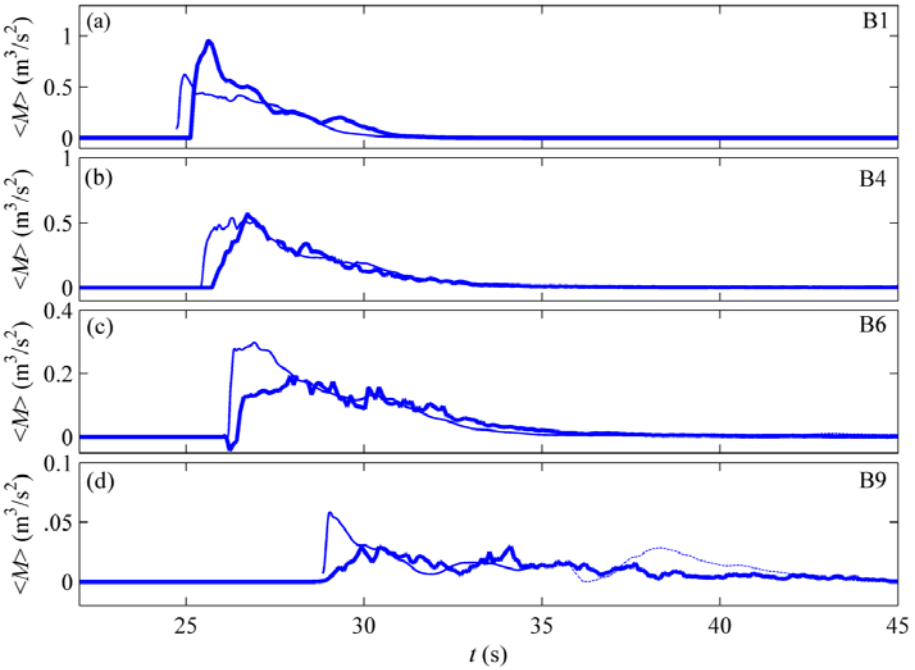

Fig. 9. Comparison of <*M*>between physical model (thick solid line) and numerical model (solid) at B1, B4, B6 and B9. Where wave reflection is present in the numerical model, the solid line switches to a dashed line.

To calibrate COULWAVE for these comparisons, three different friction factors, f = 0.001, 0.005, and 0.01 were tested. A friction factor of f = 0.005 was found to produce results most similar to the physical model and was used for all subsequent analysis. The expected differences due to friction factors will be discussion in more detail in section 4.1.

Reflection from the model boundaries was simulated by COULWAVE. The back end of the tank in the numerical model is at a different x location than in the physical model study, and the reflection off this back wall arrives at the measurement locations earlier. Therefore, reflection effects produced by COULWAVE resulted in some erroneous data when compared to the physical model which is shown in Fig. 7, Fig. 8, and Fig. 9 (dotted lines). For example, in Fig. 7d, the magnitude of free surface elevation from COULWAVE was nearly twice as large as the physical model values due to reflection. Reflection wave effects are also observed in cross-shore velocity and momentum flux in Fig. 8 and Fig. 9.

Fig. 10 compares the maximum free surface elevation, cross-shore velocity and momentum flux between the numerical and physical model from B1 to B9. The x-axis represents the distance to each measurement location (B1 to B9) in the x-direction from the origin, B1. The maximum values of <η>, <u> and <M> were extracted at each location, and therefore, do not

necessarily correspond to the same instant in time. Reflection effects present in the numerical model were excluded in the maximum value comparison. Within the first 1.5 m, there are minor disagreements in the $<\eta>$ and $<M>$, however the numerical model values of $<M>$ shows the same abrupt decrease and increase pattern between 0 and 1 m as the physical model. Overall the physical and numerical model show good agreement. In both models, it is observed that the maximum free surface elevation and momentum flux sharply decrease from the shoreline as the measurement location moves landward, while the cross-shore velocity slowly decreases linearly. Specifically, from B1 to B9, the maximum free surface elevation, $(\eta)_m$ decreases 72%, the maximum momentum flux, $(M)_m$ decreases 96% and the maximum cross-shore velocity, $(u)_m$ decreases 41% in physical model.

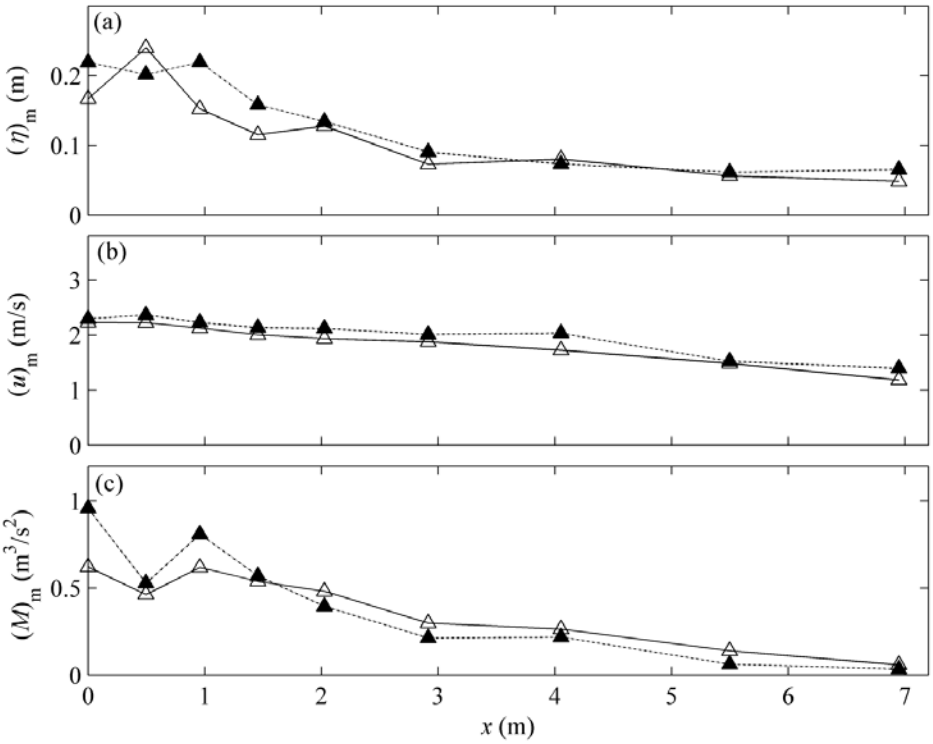

Fig. 10. Comparison of the maximum values between physical model (filled triangle) and numerical model (unfilled triangle) for line B. (a): Maximum free surface elevation, $(\eta)_m$. (b): Maximum cross-shore velocity, $(u)_m$. (c): Maximum momentum flux, $(M)_m$.

Fig. 11 shows the normalized root mean square errors of the numerical model compared to the physical model at each measurement location for η, u, and M, respectively. The normalized root mean square errors are evaluated as:

$$NRMSE\ (\phi) = \frac{\sqrt{\frac{\sum_{i=1}^{r}\left(\hat{\phi}_i - \phi_i\right)^2}{r}}}{\phi_{max} - \phi_{min}}$$

where $\hat{\phi}_i$ is the numerical model value, ϕ_i is the physical model value, ϕ_{max} and ϕ_{min} are the maximum and minimum from the physical model, r is the time step number which is less than 1% of the maximum free surface elevation or the time step number when reflection effects first appear, and the i is the time step for each value of η, u, and M. The normalized root mean square errors for the free surface elevation at lines A, B, and C are within 0.1, except at C1 where it increased to 0.2, and for line D where the numerical model results overestimated the values and are approximately 0.3 to 0.4 (Fig. 11a). Most of the normalized root mean square errors of cross-shore velocity for lines A and D were less than 0.4, and for lines B and C less than 0.2 (Fig. 11b). In the case of momentum flux, with the exception of line D which measured around 0.8, most values are less than 0.2. Overall, with the exception of line D, and line A for velocity, the normalized root mean square errors are less than 0.2.

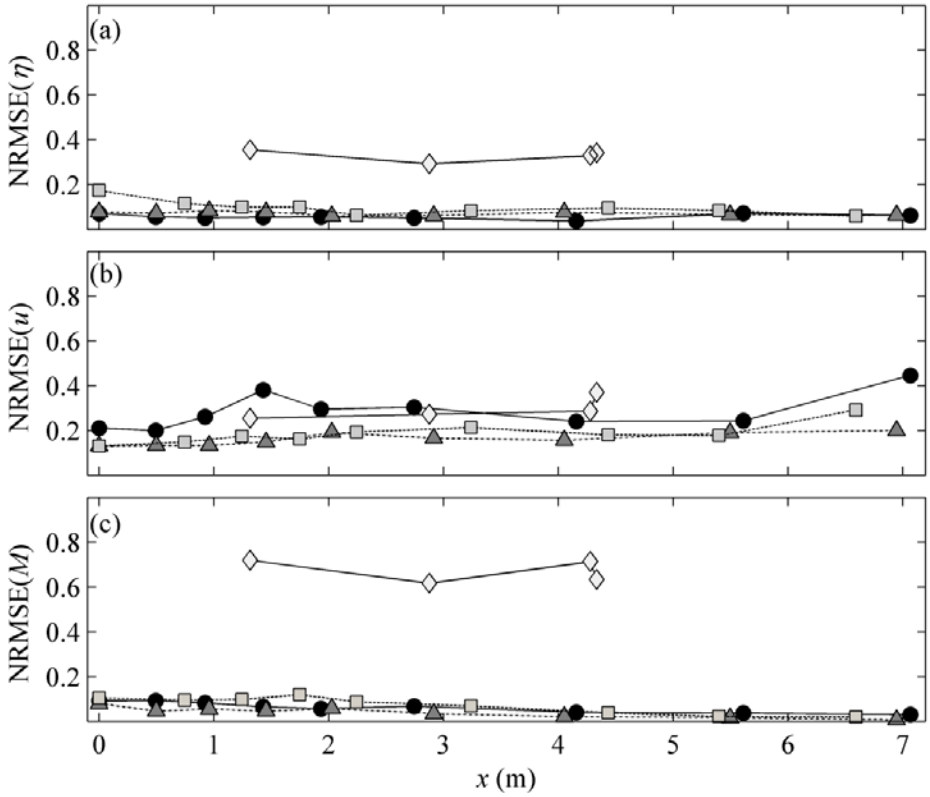

Fig. 11. Normalized root mean square errors (NRMSE) of numerical results at lines A, B, C, and D (circle, triangle, square, and diamond). (a): Free surface elevation, η. (b): Cross-shore velocity, u (c): Momentum flux, M.

The normalized root mean square errors for line D are relatively large, and in excess of four times that measured in the other three lines. This anomaly may be attributed to the difference of measurement location. Lines A, B, and C were located on the road, with no obstructions between the locations and the ocean, while line D was located mostly behind buildings. The discrepancy between lines A, B and C and line D may arise from the inherent difficulty of generating an energy dissipation process which includes turbulence in the numerical model, as the broken wave passes around the buildings.

4.2 Model sensitivity for friction factors.

To test the numerical model sensitivity, three different friction factors, f = 0.001, 0.005 and 0.01, were modeled, and the maximum values of free surface elevation, $(\eta)_m$, velocity, $(u)_m$, and momentum flux, $(M)_m$, compared to the physical model data as a time series. Fig. 12 shows the comparison between the physical model and numerical model for these friction factors using the maximum values at B1 to B9. The x-axis represents the distance to each measurement location (B1 to B9) in the x-direction from B1. Fig. 12a shows the change in $(\eta)_m$, Fig. 12b shows the change in $(u)_m$, and Fig. 12c shows the change in $(M)_m$ Smaller friction factor values represent less bottom friction; therefore, increased wave magnitude and phase speed are expected as the friction factor decreases. In the numerical model, as f was decreased, the tendencies of $(\eta)_m$, $(u)_m$, and $(M)_m$ remained constant and overall the values increased. The values of $(\eta)_m$ remained relatively unchanged until x = 4 m (B1 to B7), after which the fiction factor exhibited a greater influence. As the friction factor decreased by a factor of 10 (from 0.01 to 0.001), the maximum free surface elevation increased an average of 15%, but the cross-shore velocity and momentum flux increased 95 and 208%. This fact reveals that the numerical model's velocity and flux terms are highly sensitive to the bottom friction factor, and there is a potential hazard to verify results with bench mark tests which only compare the maximum free surface elevation. Overall, a friction factor of f = 0.005 (triangle) was found to provide results which best matched the physical model.

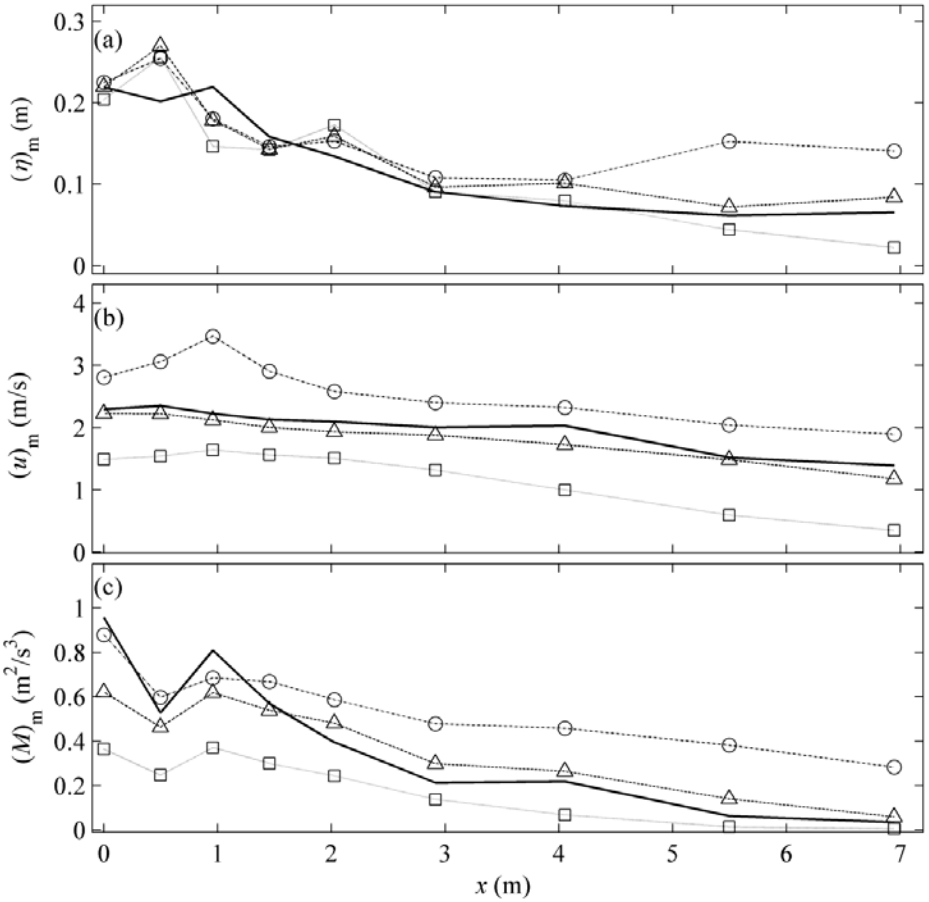

Fig. 12. Numerical model sensitivity test of three friction factors, f = 0.001, 0.005, and 0.01 (circle, triangle, and square), compared to the physical model (solid line) showing maximum values for line B. (a): $(\eta)_m$. (b): $(u)_m$. (c): $(M)_m$.

Fig. 13a, b, and c shows the numerical model sensitivity of η, u, and M, respectively, to the three different friction factors at location B1. When the friction factor was 0.001 (circle), the smallest value, the arrival time of wave was faster than the other two conditions. As the friction factor was increased, the initial magnitude of η, u, and M decreased before t = 25.3 s, but after which all only show small changes. It appears that only the leading velocity part was dominated by the friction factors. These results could not be corroborated by the physical model data as only one friction factor was tested.

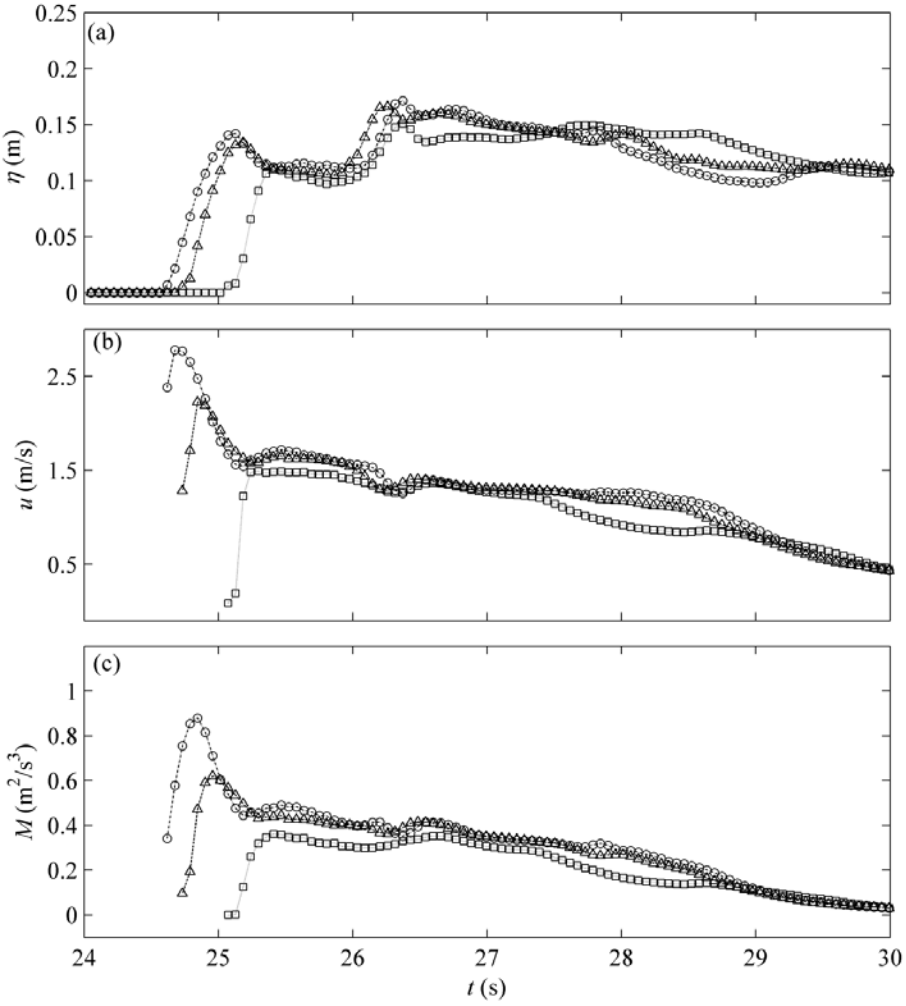

Fig. 13. Numerical model time series sensitivity test of three friction factors, f = 0.001, 0.005, and 0.01 (circle, triangle, and square) for location B1. . (a): $(\eta)_m$. (b): $(u)_m$. (c): $(M)_m$.

Fig. 14 shows the same sensitivity test as Fig. 13, but for location B4. Similar to Fig. 13, the arrival time of the inundation wave was earlier and the leading velocity larger as the friction factor decreased. Unlike at location B1, the cross-shore velocity at B4 after t = 25.3 s for f = 0.01 was noticeably smaller than for the other two friction factors. However, there were still no discernible changes to the free surface elevation due to the various friction factors. The maximum momentum flux increased by more than a factor of two as the friction factor decreased from 0.01 to 0.001. This fact highlights the importance of comparing velocity terms in the validation and verification process of numerical models of tsunami inundation when evaluating velocity or force on the structures.

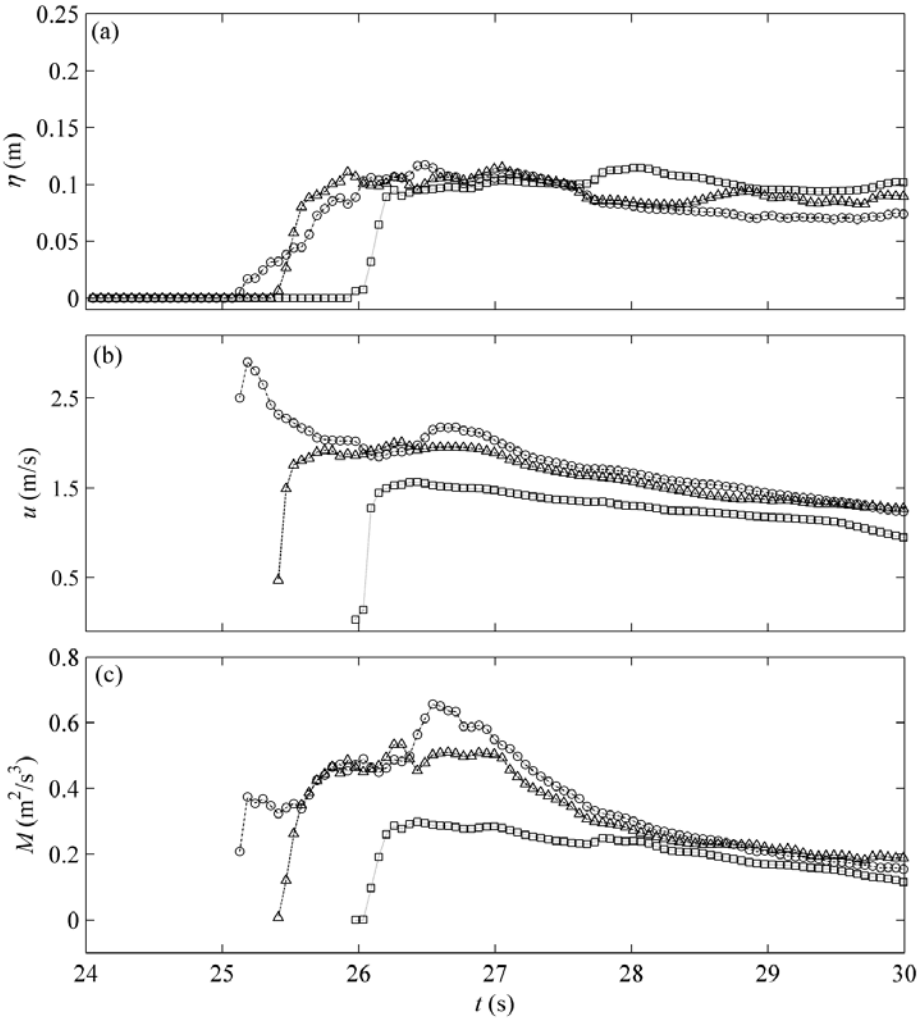

Fig. 14. Numerical model time series sensitivity test of three friction factors, f = 0.001, 0.005, and 0.01 (circle, triangle, and square) for location B4. (a): $(\eta)_m$. (b): $(u)_m$. (c): $(M)_m$.

5.1 Conclusion

This paper presents a comparison of free surface elevation, velocity, and momentum flux for tsunami inundation over and around the macro-roughness of a constructed environment between a physical and numerical model (COULWAVE). The physical model was a 1:50 scale idealization of Seaside, Oregon designed to observe the effects of building array and density on tsunami inundation (Fig. 2). In total the free surface elevation and velocity of the inundation flow was measured at 31 locations (Fig. 3). The design wave height was approximately 20 cm, which corresponds to the prototype scale wave height of 10 m (Fig. 4). Measured velocities at the leading edge of the wave were not recorded by the ADV, so leading velocities were determined

from optical measurements (Rueben *et al.*, 2010) and interpolated velocity fitting curves applied to calculate the momentum flux (Fig. 5 and Fig. 6). Primary conclusions are:

1. As the inundating wave propagated around the macro-roughness, the wave shape and location of maximum values of free surface, velocity, and momentum flux changed. If the ensemble average momentum flux is calculated using the maximum values of $<\eta>$ and$<u>$, it will be overestimated by approximately 60% at A1 and 260% at A8 (Fig. 5 and Fig. 6).
2. In general, the time series and maximum values of free surface elevation, velocity, and momentum flux from the numerical model show good agreement with the physical model results (Fig. 7, Fig. 8, Fig. 9, and Fig. 10) except behind the macro-roughness units (Fig. 11, line D).
3. Different friction factors (f = 0.01, 0.005 and 0.001) were applied to test the model sensitivity. Result showed that the velocity and flux terms in the numerical model are highly sensitive to the bottom friction factor, while the free surface elevations are only slightly effected. When the friction factor decreased by a factor of 10 (from 0.01 to 0.001), the average maximum free surface elevation only increased 15%, but the average maximum cross-shore velocity and momentum flux increased 95 and 208%, respectively (Fig. 12).

This research highlights the importance of comparing velocity terms in the validation and verification process of numerical models of tsunami inundation when evaluating velocity or force on structure. Future research in this area should focus on measuring pressure and force on structures to validate and improve numerical results; model the tsunami return flow, as it is known to induce scour and cause soil instability; and model complex bathymetry and topography.

Acknowledgement

This material is based upon work partially supported by the National Science Foundation under Grant No. 0830378 and Oregon Sea Grant under Award No. NB223X. Any opinion, findings, and conclusions or recommendations expressed in this material are those of the authors and do not necessarily reflect the views of the National Science Foundation or Oregon Sea Grant.

6.1 References

Apotsos, A., Jaffe, B, and Gelfenbaum, G. (2011). "Wave Characteristic and Morphologic Effects on the Onshore Hydrodynamic Response of Tsunamis." Coastal Engineering 58: 1034-1048.

Briggs, M., Synolakis, C., Harkins, G., and Green, D. (1995). "Laboratory experiments of tsunami runup on Circular Island." Pure and Applied Geophysics 144(3/4): 569-593.

Cox, D., Tomita, T., Lynett, P., and Holman, R. (2008). "Tsunami inundation with macro-roughness in the constructed environment." Proc. 31st International Conference on Coastal Engineering: 1421–1432.

Dalrymple, R., A., Kribel, D., L. (2005). "The Bridge – Linking Engineering and Society: Lessons in Engineering from the Tsunami in Thailand." National Academy of Engineering 35(2):4-14.

DOGAMI (Oregon Department of Geology and Mineral Industries), (2001). "Senate Bill 379." Portland, OR. Retrieved from: Oregon Geospatial Enterprise Office (GEO). http://cms.oregon.gov/DAS/CIO/GEO/Pages/index.aspx

FEMA (Federal Emergency Management Agency) (2008). "Guidelines for Design of Structures for Vertical Evacuation from Tsunamis - FEMA P646 Report." Prepared by the Applied Technology Council for the Federal Emergency Management Agency, Redwood City, C.A..

Goseberg, N., and Schlurmann, T. (2010). "Numerical and experimental study on tsunami run-up and inundation influenced by macro roughness elements." Proceedings of the International Conference on Coastal Engineering, 32.

HOKKAIDO TSUNAMI SURVEY GROUP (1993), Tsunami devastates Japanese coastal region, EOS Trans. Amer. Geophys. Un. 74(37), 417 and 432.

Imamura, F., Koshimura, S., Goto, K., Yanagisawa, H., and Iwabuchi, Y. (2006). "Global disaster due to the 2004 Indian Ocean tsunami." Journal of Disaster Research 1(1): 131-135.

Jaffe, B., and Gelfenbuam, G. (2007). "A simple model for calculating tsunmai flow speed from tsunami deposits." Sedimentary Geology 200: 347-361.

Kânoğlu, U., and Synolakis, C., E.(1998). "Long wave runup on piecewise linear topographies." Journal of Fluid Mechanics 374: 1-28.

Kennedy, A. B., Chen, Q., Kirby, J. T., and Dalrymple, R. A. 2000. "Boussinesq modeling of wave transformation, breaking and runup. I: 1D." J. Waterw., Port, Coastal, Ocean Eng., 1261, 39–47.

Kim, D.-H., Lynett, P., and Socolofsky, S. "A Depth-Integrated Model for Weakly Dispersive, Turbulent, and Rotational Fluid Flows." Ocean Modeling, v. 27 (3-4), p. 198-214, 2009.

Kim, D.-H. and Lynett, P., "Turbulent Mixing and Scalar Transport in Shallow and Wavy Flows," Physics of Fluids, v. 23 (1), doi:10.1063/1.3531716, 2011.

Koshimura, S., Oie, T., Yanagisawa, H., Imamura, F. (2009)a. "Developing fragility functions for tsunami damage estimation using numerical model and post-tsunami data from banda aceh, Indonesia." Coastal Engineering Journal 51(3): 243-273.

Koshimura, S., Namegaya, Y., Yanagisawa, H. (2009)b. "Tsunami fragility: A new measure to identify tsunami damage." Journal of Disaster Research 4(6): 479-488.

Liu, P., Yeh, H., and Synolakis, C. (2008). "Advanced numerical models for simulation tsunami and runup." Singapore, World Scientific Publishing Co. Pte. Ltd.

Lynett, P., “Nearshore Modeling Using High-Order Boussinesq Equations,” Journal of Waterway, Port, Coastal, and Ocean Engineering (ASCE), v. 132(5), p. 348-357, 2006.

Lynett, P. (2007). "Effect of a shallow water obstruction on long wave runup and overland flow velocity." Journal of Waterway, Port, Coastal, and Ocean Engineering 133(6): 455-462.

Lynett, P., Wu, T., and Liu, P. (2002). "Modeling wave runup with depth-integrated equations." Coastal Engineering 46: 89-107.

Lynett, P., Melby, J., and Kim, D.-H. “An Application of Boussinesq Modeling to Hurricane Wave Overtopping and Inundation,” Ocean Engineering. v. 37, p. 135-153. 2010.

Matstomi, H., and Okamoto, K. (2010). "Inundation flow velocity of tsunami on land." Island Arc 19: 443-457.

Moore, A., McAdoo, B., and Ruffman, A. (2007). "Landward fining from multiple sources in a sand sheet deposited by the 1929 Grand Banks tsunami, Newfoundland." Sedimentary Geology 200: 336-346.

Mori, N., Takahashi, T., Yasuda, T., and Yanagisawa, H. (2011). “Survey of 2011 Tohoku earthquake tsunami inundation and run-up.” Geophysical Research Letters, 38.

Nandasena, N., A., K., Sasaki, Y., Tanaka, N. (2012). “Modeling field observations of the 2011 Great East Japan tsunami: Efficacy of artificial and natural structures on tsunami mitigation.” Coastal Engineering 67: 1-13.

National Oceanic and Atmospheric Administration (NOAA), (2012). “National Data Buoy Center.” Stennis Space Center, Mississippi. Retrieved from: National Data Buoy Center. http://www.ndbc.noaa.gov/

Rueben, M., Holman, R., Cox, D., Shin, S., Killian, J., and Stanley, J. (2010). "Optical measurements of tsunami inundation through an urban waterfront modeled in a large-scale laboratory basin." Coastal Engineering 58(3): 229-238.

Shi, Fengyan, Kirby, T., James, Harris, C., Jeffrey, Geiman, D., Joseph, Grilli, T., Stephan (2012). "A high-order adaptive time-stepping TVD solver for Boussinesq modeling of breaking waves and coastal inundation." Ocean Modelling 43-44: 36-51.

Synolakis, C., Bernard, E., Titov, V., Kânoğlu, U., and Gonzalez, F. (2007). “Standards, criteria, and procedures for NOAA evaluation of tsunami numerical models.” Commerce, NOAA Tech. OAR PMEL-135.

Synolakis, C. a. R., F. (2003). "Waves and Run-Up Generated By a Three-Dimensional Sliding Mass." Advances in Natural and Technological Hazards Research 19(1): 113-119.

Synolakis, C. E. (1987). "The runup of solitary waves." Journal of Fluid Mechanics 185: 523-545.

Titov, V.V., Synolakis, C.E., 1995. Modeling of breaking and non-breaking long wave evolution and runup using VTCS-2. J. Waterw. Port Coast. Ocean Eng. 121, 308– 316.

Tomita, T., and Honda, K. (2007). "Tsunami estimation including effect of coastal structures and buildings by 3D model." Coastal Structures 2007: 681-692.

Tomita, T., Honda, K.,and Kakinuma, T. (2006). "Application of storm surge and tsunami simulator in ocean and coastal areas (STOC) to tsunami analysis." Technical Memorandum of Public Works Research Institute 4022.

Tsunami Pilot Study Working Group (2006). “Seaside, Oregon Tsunami Pilot Study—Modernization of FEMA Flood Hazard Maps.” NOAA OAR Special Report, NOAA/OAR/PMEL, Tsunami Pilot Study Working Group

Yeh, H., Sato, S., Tajima, Y. (2012). “The 11 March 2011 East Japan Earthquake and Tsunami: Tsunami Effects on Coastal Infrastructure and Buildings”. Pure and Applied Geophysics.

Yeh, H. (2006). "Maximum fluid forces in the tsuami runup zone." Journal of Wateray, Port, Coastal, and Ocean Engineering 132(6): 496-500.

Yeh, H., Liu, P., and Synolakis, C. (1996). Long-wave runup models. Singapore, World Scientific.

Nomenclature

Symbol	Description	Units
F	Friction factor	-
H	Total water depth	L
h	Vertical datum	L
M	Momentum flux	L^3T^{-2}
N_T	Number of experiment trials for each measuring location	L
N_V	Available number of measurement data for each measuring location	L
N_η	Recorded number of free surface elevation at each time step.	L
N_u	Recorded number of cross-shore velocity at each time step.	L
$NRMSE$	Normalized root mean square error value	-
S	Wave maker displacement	L
u	Cross-shore (x-axis) velocity	LT^{-1}
u_L	Leading wave velocity	LT^{-1}
v	Along-shore (y-axis) velocity	LT^{-1}
w	Vertical (z-axis) velocity	LT^{-1}
x	x-coordinate in the experiment	L
y	y-coordinate in the experiment	L
η	Free surface elevation	L
η_w	Free surface elevation at wavemaker	L
$< >$	Ensemble averaged value	-
$( )\_$	Maximum value of ( )	-

5.2 Appendix B

Park, H., Cox, D. T., and Petroff, C. M. (2015). An empirical solution for tsunami run-up on compound slopes. Natural Hazards, 76 (3), 1727-1743.

An empirical solution for tsunami runup on compound slopes

Hyoungsu Park*
Graduate Research Assistant, School of Civil and Construction Engineering, Oregon State University, Corvallis, OR 97331-2302, USA, Email: Hyoungsu.park@gmail.com, Tel: 1-541-602-8618, Fax: 541-737-3052

Daniel T. Cox
Professor, School of Civil and Construction Engineering, Oregon State University, Corvallis, OR 97331-2302, USA, Email: dan.cox@oregonstate.edu

Catherine M. Petroff, Ph.D., P.E.Principal, LP4 Associates LLCAffiliate Faculty, Professional Staff, Dept. of Civil and Env. Engineering, University of Washington

* Corresponding Author

Abstract

An empirical solution for tsunami runup is developed based on an analytic solution and calibrated using a Boussinesq wave model for plane-sloped and compound-sloped cases, including the effects of bottom friction, wave breaking, and the slope of the inundated land area. The new relation is a function of the tsunami wave amplitude at a specific water depth (100 m) to provide clear guidance for practical application, and of two values of the surf similarity parameter to account for a compound slope. The model comprises three equations for three regions: breaking, transition and non-breaking. The model predictions are compared with survey data from the 2011 Tohoku tsunami in Japan without recalibration, and the new equation provides reasonable estimates of runup height and is generally conservative.

Keywords: Tsunami, Runup, analytic solution, empirical solution, compound slope, surf similarity

1. Introduction

Since the 2004 Indian Ocean tsunami, there has been a renewed interest in developing numerical models to estimate tsunami behavior (i.e. generation, propagation and inundation process) including the maximum runup to define the tsunami hazard zone. However, although there has been rapid improvement in reducing the errors associated with the tsunami propagation and, to a lesser extent, tsunami inundation, there are still significant uncertainties at the generation process to estimate the effects of future tsunamis. Those uncertainties generated from

the randomness of nature are often referred to as an aleatory uncertainties (Beven, 2013), and these may be more significant in comparison with epistemic uncertainties which come from the lack of our knowledge (model limitations or limited input).

Generally, numerical models of tsunami runup are based on depth integrated 2-D (horizontal) or, in limited cases, 3-D models and incorporate horizontal 2-D effects such as diffraction, refraction, reflection and dispersion during the propagation to the near shore, accounting for the complex bathymetry, bottom friction, wave breaking, dissipation, and turbulence during inundation. Even though there are uncertainties due to the gaps between real physics and the existing state-of-art-numerical models, particularly with respect to modeling energy losses during the inundation phase, it is generally true that numerical models provide more accurate results compared to simple analytical or empirical expressions.

However, deterministic numerical models have some limitations with regard to assessing the risk from the tsunami hazard, particularly with respect the aleatory uncertainty at the point of the tsunami generation. This is because deterministic numerical models generally require long computation times, skilled modelers, and detailed input information. For example, when using a statistical approach to estimate the probable extent of the inundation area, it is necessary to simulate hundreds of scenarios given the uncertainty in predicting the tsunami source, resulting in increased costs and time using numerical models. In addition, the specification of other inputs, including empirical constants to account for surface roughness and other sources of energy loss as well as variations in the tide level, will add to uncertainties of the runup estimates.

As an alternative to time-dependent tsunami inundation models, analytical or semi-empirical models can provide runup predictions, and while less precise than time-dependent models for a given scenario, semi-empirical models have an advantage of being computed quickly. Therefore, they can be used in combination with Monte Carlo-type simulations to provide a runup probability conjoined with the probability of the tsunami source. The basic study of tsunamis started with solving the run-up problem on a beach slope. Carrier & Greenspan (1958) investigated the explicit solution of the non-linear, inviscid shallow water equation on a sloping beach, and Keller & Keller (1964) showed the linear solution of the canonical tsunami run-up problem, that is, a simple uniformly sloped beach with constant depth. Synolakis (1987) used a solitary wave as the tsunami like wave form and provided an analytic solution of a non-linear shallow water wave equation with the simple uniform beach slope condition. Synolakis

(1987) noted the importance of classifying the breaking and non-breaking regimes in the experiment data and suggested an empirical run-up solution in the breaking regime based on laboratory experiment data.

Using a wave form composed of a positive solitary wave crest and a negative solitary wave trough, Tadepalli & Synolakis (1994) introduced an analytic solution of positive and negative N-waves which more closely resembles tsunami waves. Kanoğlu & Synolakis (1998) provided an analytic solution on the piecewise linear topographies, and Li & Raichlen (2001) provided an empirically derived correction to Synolakis' analytic solution of the non-linear shallow water problem in the non-breaking regime. Li & Raichlen (2003) also derived a semi-analytical solution for the breaking regime through an energy balance model. Besides the solitary wave, Carrier, Wu & Yeh (2003) solved a fully nonlinear shallow water equation with Gaussian-type single and N-waves as input conditions, and provided run-up and draw-down motions in physical time and space domain by numerical integration.

Hunt (1959) provided a simple run-up equation for breaking regular waves, where the Irribaren number (surf-similarity parameter) is equal to the ratio of run-up height to deep water wave height (Battjes, 1974). Ahrens & Titus (1985) introduced empirical runup equations as a function of surf-similarity for regular waves depending on the wave conditions (nonbreaking, plunging, and transitional) and concluded that the regular wave runup on smooth slopes is largely controlled by surf conditions, slope, and nonlinear effects. Kobayashi & Karjadi (1994) combined numerical model results with laboratory experiments to develop an empirical formula to predict the runup height normalized by the incident solitary wave amplitude as a function of surf-similarity. More recently, Lo, Park & Liu (2013) provided empirical run-up formulae with modified forms of the surf-similarity parameter for single and double solitary waves based on experimental data. As an alternative to the surf similarity parameter, Hughes (2004) suggested the use of a momentum flux parameter to estimate the run-up height for the canonical solitary runup problem.

Madsen, Fuhrman & Schaffer (2008) questioned using a solitary wave as an initial condition for a tsunami runup problem since the solitary wave cannot appropriately define the relevant length and time-scales of observed tsunamis. Madsen & Fuhrman (2008) provided maximum runup and velocity in terms of surf-similarity and amplitude to depth ratio from the analytic solution of a non-linear shallow water problem at the non-breaking regime. Based on

this work, Madsen & Schaffer (2010) provided analytic tsunami runup solutions in terms of the surf-similarity parameter for sinusoidal waves, a single positive wave, N-waves and shoaled linear transient waves in both breaking and non-breaking regimes.

Although the analytical and empirical solutions described above have significantly improved our understanding of tsunami runup, it can be challenging to apply these formulations in practice. First, there is an ambiguity in input parameters. Several of the previous solutions are based on hydraulic laboratory studies in a wave flume and require knowledge of water depth and wave height at the base of the offshore slope. However, the location of a constant offshore starting depth is uncertain in real applications, and some choices could include the point of wave generation, the edge of a continental shelf, or an arbitrary location that depends on the modeler. Second, existing solutions do not consider compound slopes in part because laboratory studies were often conducted using a plane slope for simplicity and because the analytical treatment of a compound slope is more difficult. In reality, though, the offshore slope (defined here as the slope from the seaward boundary to the shoreline) is often different from the onshore slope (defined here as the slope from the shoreline to the maximum extent of runup). In general, for the same offshore slope, a milder onshore slope will have a lower runup than a steeper onshore slope because bottom friction acts over a longer distance for the milder slope and because of the time-dependent nature of the inundation process itself. Finally, previous analytic studies do not include the effects of both wave breaking and bottom friction on the run-up process, factors that cannot be ignored in real tsunami inundation problems.

The purpose of this paper is to provide a new empirical tsunami runup equation for practical applications. A new set of equations is presented to account for the three factors described above: well-defined input boundary conditions, compound slopes, and energy loss due to bottom friction and wave breaking. In Section 2, we present the model definitions and a brief review of the analytic solution of Madsen & Schaffer (2010; denoted MS10 hereafter) on which our solution is based. We also apply the Boussinesq model COULWAVE (Lynett et. al., 2002) which we use for model calibration. In Section 3, we present the numerical model estimates of runup for uniform plane slope and compound slope case studies. First, we test both friction and frictionless conditions with various plane beach slopes and prototype scale tsunami wave input conditions. Second, we test the compound slope (offshore slope and onshore slope) using various wave conditions and describe the slope effects in terms of the surf-similarity parameter. In

Section 4, we introduce a new empirical tsunami runup equation, and review its general characteristics. In Section 5, we present a comparison between the new equation to survey data from the 2011 Tohoku tsunami. In Section 6, we conclude the paper with summary findings, limitations, and recommendations for future work.

2. Definition of parameters

Fig. 1 shows the definition sketch of the one-dimensional tsunami run-up model for this study. Essentially, we use the same canonical 2D runup problem (Carrier and Greenspan, 1958; Synolakis, 1987; Li and Raichlen, 2001; Carrier et. al., 2003; Madsen and Fuhrman, 2008), but include an additional slope after the shoreline for a compound slope case. The variable h_0 is the flat bottom water depth, and β_1 and β_2 are the offshore slope and onshore slope. When the offshore slope (β_1) and onshore slope (β_2) are equal, the problem reduces to the standard plane slope (β) problem used in MS10 and others. We apply a "single" wave form as defined in MS10 as a tsunami source input time series η given as

$$\eta = A_0 \, \mathrm{sech}^2 (2\pi/T) (t) \qquad \text{Eq. 1}$$

where A_0 is positive tsunami amplitude and T is the representative wave period.

The MS10 study provides analytic runup solutions for the canonical run-up problem in the non-breaking and breaking regimes. The solutions are

$$R/A_0 = C_1 \, \xi_1^{\,2.0} \qquad \text{Eq. 2}$$

$$R/A_0 = C_2 \, \alpha \, \xi_1^{\,-0.5} \qquad \text{Eq. 3}$$

where R/A_0 is the relative run-up height, and α is $(A_0/h_0)^{-0.25}$. The final relative runup height is the smaller value between Eq. 2 and Eq. 3. C_1 and C_2 are analytical constants depending on input wave types such as single, N-type, or transient waves. For single wave, $C_1 = 0.1512$ and $C_2 = 4.0513$. Both breaking (Eq.2) and non-breaking (Eq. 3) runup solutions are functions of the surf-similarity parameter, ξ_1, which is defined as

$$\xi_1 = \tan\beta \, / \, (2A_0 \, / \, (g \, T^2 / \, 2\pi))^{\,0.5} \qquad \text{Eq. 4}$$

where g is the gravitational acceleration, noting that this is the same as the conventional surf-similarity parameter (Battjes, 1974) when $H_0 = 2A_0$. For this paper, we retain the same definition of surf similarity ξ_1 in Eq. 4 for the offshore slope (β_1) and introduce ξ_2 as the surf-similarity for the onshore slope (β_2) as

$$\xi_2 = \tan\beta_2 \, / \, (2A_0 \, / \, (g \, T^2 / \, 2\pi))^{\,0.5} \qquad \text{Eq. 5}$$

when discussing the compound slope case.

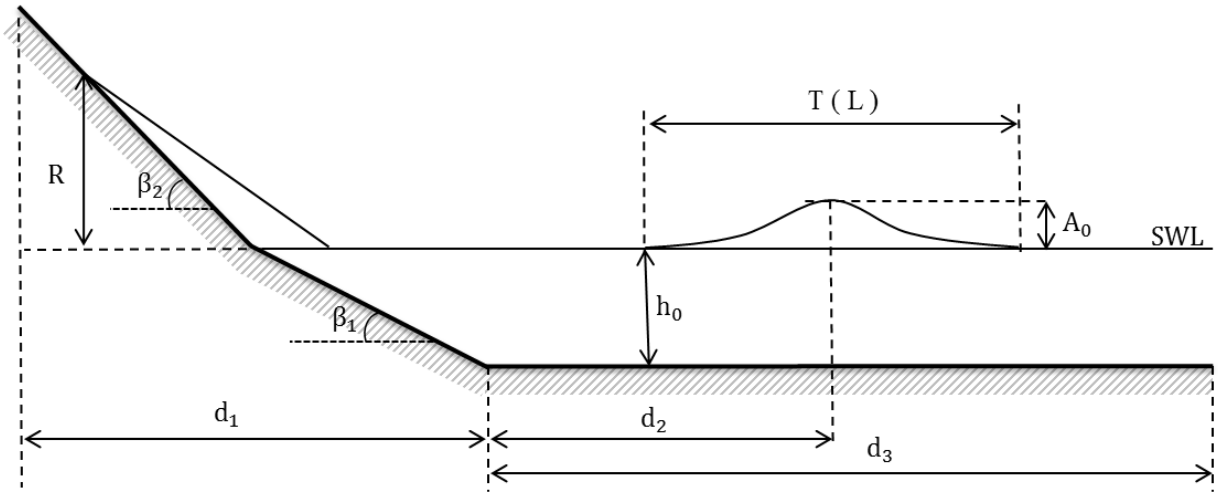

Fig. 1: Sketch of the tsunami run-up height model bathymetry and setup for the compound slope condition. Offshore slope is β_1 and onshore slope is β_2.

We use the model COULWAVE (Lynett et. al., 2002) as a numerical run-up model. COULWAVE solves a set of Boussinesq equations and includes the effects of bottom friction. A high-order finite-volume numerical solution scheme is employed to solve the conservative-form equations, and the model has been validated through fundamental bench mark problems for the runup including field data and experiment data (Lynett el. al, 2002; Lynett el. al, 2003; Lynett & Liu, 2005; Park et al, 2013). As a breaking model, COULWAVE applies the eddy viscosity model which is described in Lynett (2006). A common quadratic friction law is applied for the bottom stress term, and the dimensionless friction factor, F, is given as an input value that is constant in both space and time throughout the simulation.

3. 1 Run-up height for a plane slope condition

To verify our numerical model setup, we initially compare with the analytic solution of MS10 on a plane slope. For a plane slope comparison, we set $\beta_1 = \beta_2$, and we investigate cases with and without friction. Parameters are selected from the following sets: tan (β) = 1/15, 1/25, 1/50, 1/75, 1/100, 1/150, 1/200, and 1/250; A_0 = 1, 2, and 4 m; and T = 300, 480, 600, and 900 s. To avoid possible ambiguity in the A_0/h_0 term and to provide some guidance for practical applications, we use a fixed water depth of h_0 = 100 m as this was thought to be a reasonable offshore depth prior to any effects of wave breaking and close enough to the shore to account for effects of refraction and shoaling from the source. In other words, we assume that there is less uncertainty in the tsunami propagation phase from the source to the 100 m depth contour. We calculated a total of 96 combinations with plane slope, amplitude (A_0), and representative period

(T), and bottom friction was set to zero (F=0) to allow direct comparison with the work of MS10. To investigate the effect of bottom friction on the solution, we ran an additional 96 cases with F = 0.005, 0.01, and 0.015 using $A_0 = 4$ m, and the same values tan (β) and T listed above.

The resolution of the model grid was 5 or 10 m, depending on the plane slope (5 m resolution for 1/15, 1/25, and 1/50; 10 m resolution for milder slopes). The length of the numerical wave flume was 90 km and included a sponge layer on the seaward side to eliminate the wave reflections from the open boundary. The projected length of the compound slopes d_1 was 10 km, the length from the slope to the crest of a single wave d_2 was 40 km, and the length of constant depth d_3 was 80 km.

Fig. 2 compares the analytic solution of MS10 and numerical simulation as a function of ξ_1 when $A_0/h_0 = 0.01$ and no friction. The dotted line (from Eq. 3) and cross marked line (from Eq. 2) show R/A_0 at the non-breaking regime and breaking regime, respectively, and the final analytic solution (solid line) is the smaller value of R/A_0 from the two equations. The numerical model results are plotted with different tsunami periods as follows: T = 300 s (circle), 480 s (triangle), 600 s (square), and 900 s (reverse triangle) corresponding to a range of $1.2 < \xi_1 < 42$. According to the analytic solution in Fig. 2 (solid line), the peak point ($\xi_1 \approx 6.0$) is a breaking limit criterion. The relative run-up height (R/A_0) follows the non-breaking run-up solution (Eq. 3) for $\xi_1 > 6.0$, and follows the breaking run-up solution (Eq. 2) for $\xi_1 < 6.0$. In the non-breaking region ($\xi_1 > 6.0$), the numerical results agree well with the analytic solutions (as was demonstrated by MS10) using four different wave periods when $A_0/h_0 = 0.01$, providing confidence in our numerical model setup. However, for $\xi_1 < 6.0$, the results diverge, and the breaking limit criterion of numerical results is closer to $\xi_1 = 2.5$ and not $\xi_1 = 6.0$.

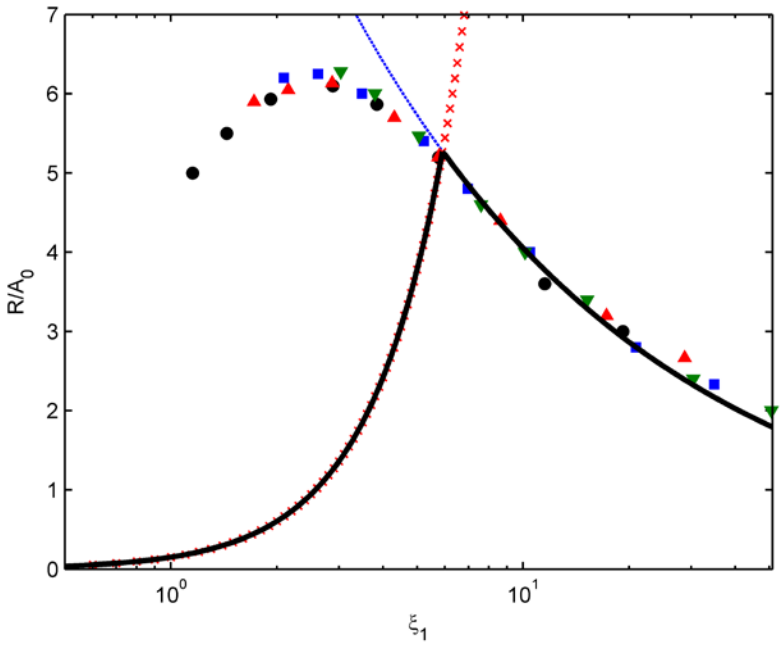

Fig. 2: Comparison between the dimensionless maximum run-up height for single wave, A_0/h_0 = 0.01, of Madsen and Schaffer (2010) analytic solution (thick black solid line) and numerical model (COULWAVE) results (solid symbols) as a function of the surf-similarity defined by Madsen and Schaffer (2010). The dotted line is an analytic solution of Madsen and Schaffer (2010) at the non-breaking regime and x marked line is at the breaking regime. Each symbol represents different tsunami periods; T=300 s (circle), T=480 s (triangle), T=600 s (square), and T=900 s (inverse triangle).

This disagreement for $\xi_1 < 6.0$ originates from a difference between the theoretical breaking criterion and the parameterized breaking in the numerical model. The theoretical breaking criterion is the moment when the Jacobian collapses in the analytic solution; it cannot be utilized to calibrate the numerical model quantitatively at the breaking region (Synolakis, 1987; Madsen and Fuhrman, 2008). Synolakis (1987) suggested an empirical run-up solution based on his laboratory data, but it was limited to a single slope of 1:19.85 and the solitary wave condition. Kobayashi & Karjadi (1994) used numerical solutions to the nonlinear shallow water wave equations to analyze the run-up problem in the breaking regime and suggested an empirical run-up solution as a function of surf-similarity. However, the solution is only validated from the small range of surf similarity ($\xi_1 < 2$) with limited steep plane slope conditions.

Fig. 3 compares the MS10 analytic solution and numerical model results with friction and without friction where A_0/h_0 is increased to 0.04 (A_0 = 4 m at h_0 = 100 m). In comparing the analytic solution (solid line) to the numerical results with no friction (open symbols), the analytical solution shows a deviation even in the non-breaking region ($\xi_1 > 6$) for A_0/h_0 =0.04. This is likely because of the undulation induced from the sharp transition between the flat bottom

and the plane slope (Madsen & Furman, 2008). In comparing the no friction with the friction cases (closed symbols), Fig. 3 shows that without friction, the breaking limit criterion for the analytic solution is about ξ_1 = 6.0, and that for the numerical result was about ξ_1 = 2.5. With friction, the peak shifts to the right, and ξ_1 is almost 10.0. R/A_0 varies noticeably between cases with different friction values. For the breaking region (ξ_1 < 10) as the value of friction increases, the relative run-up decreases as expected. For the nonbreaking region (ξ_1 > 10), the frictional effects are less pronounced and the relative run-up is less sensitive to friction values. This implies that reasonable estimates for friction are required especially for the breaking region (mild slopes) rather than nonbreaking region (steep slopes) to estimate the run-up.

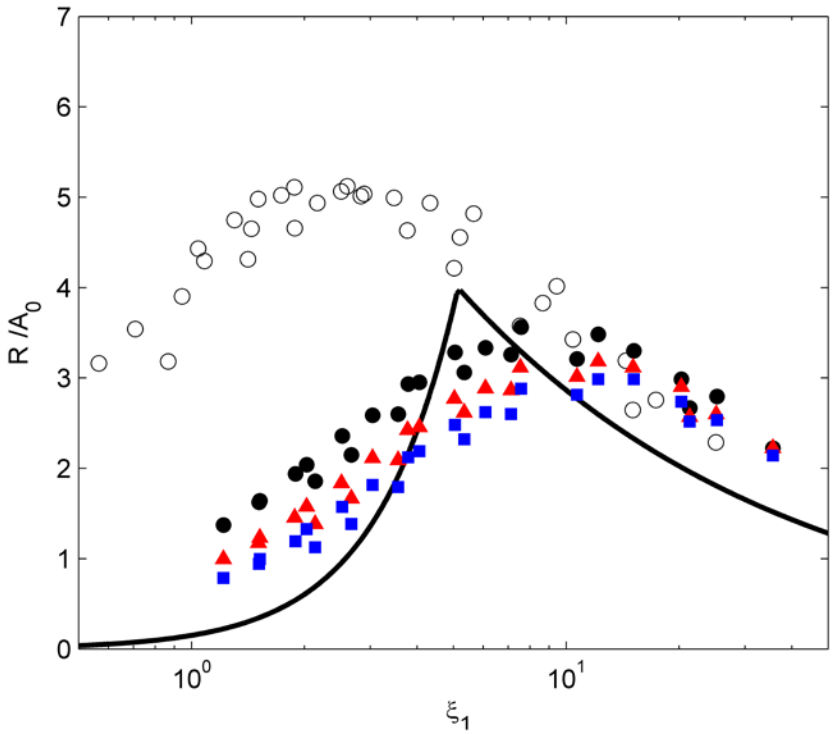

Fig. 3: Comparison between Madsen & Schaffer (2010) single wave analytic solution and Numerical model (COULWAVE) results with various friction values; F=0 (open circle), F=0.005 (solid circles), 0.01 (solid triangles) and 0.015 (solid squares). A_0/h_0 = 0.04.

3.2 Run-up height for a compound slope

We extend the work of the previous subsection considering a compound slope shown in Fig. 1, using a total of 288 combinations of slopes (β_1 and β_2), amplitude (A_0), and representative period (T). Parameters were selected from the following sets: tan (β_1) = 1/15, 1/50, 1/100, and 1/250; tan (β_2) = 1/15, 1/25, 1/50, 1/75, 1/100, 1/150, 1/200, and 1/250; A_0 = 1.0, 4.0, and 8.0 m; T = 480, 600, and 900 s. As before, the water depth was kept constant at h_0 = 100 m, and the

bottom friction was set as F = 0.01. The resolution of the model grid was 5 or 10 m, depending on β_1 and β_2 (5 m resolution for β_1=1/15 and 1/50 or β_2=1/15, 1/25 and 1/50; 10 m resolution for other cases).

Fig. 4 shows the relative runup height versus ξ_1 for three relative amplitudes: A_0/h_0 = 0.01 (circle), 0.04 (triangle), and 0.08 (square). The overall trends from plane slope cases with friction in Fig. 3 (solid symbols) are seen again in Fig. 4, and the peak value of R/A_0 occurs around ξ_1 = 8. Some trends can be seen relative to the input value, for example as A_0/h_0 decreases, the relative runup (R/A_0) generally increases for given ξ_1. However, there is still a large variation in R/A_0 for a given value of ξ_1 due to the compound slope as will be addressed in the next section.

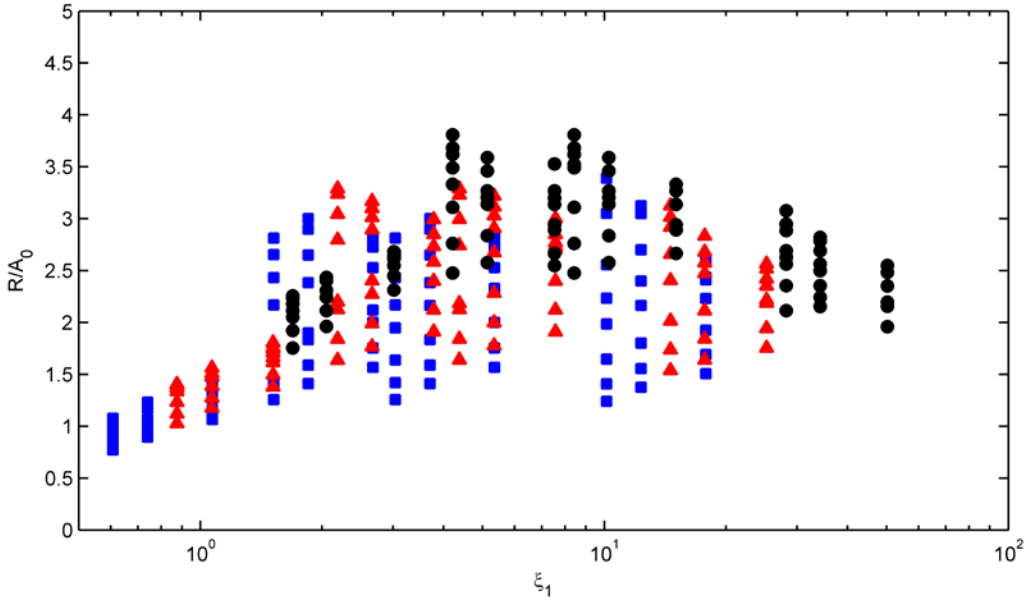

Fig. 4: Relative run-up height from compound slope numerical model results as a function of the surf-similarity parameter (ξ_1) with various amplitudes (A_0); A_0/h_0 = 0.01 (solid circles), A_0/h_0 = 0.04 (solid triangles), and A_0/h_0 = 0.08 (solid squares).

4. Developing a new empirical run-up equation.

To develop a new empirical equation, we started with the basic format of the MS10 analytic solutions that showed good agreement with plane slope numerical model results in the non-breaking regions. In the work of MS10, there was a clear delineation of two regions (breaking and non-breaking) based on ξ_1. For the present compound slope cases with friction and values of A_0/h_0 ranging from 0.01 to 0.08, there appears to be a broader distribution of R/A_0 values near the breaking criterion. Given this, we have designated this region located between

the breaking and non-breaking region a 'transition region', located approximately in the range 4 $< \xi_1 <$ 10. Furthermore, to reflect the effect of a compound slope, we introduce the dimensionless parameter ξ_2 (Eq. 6).

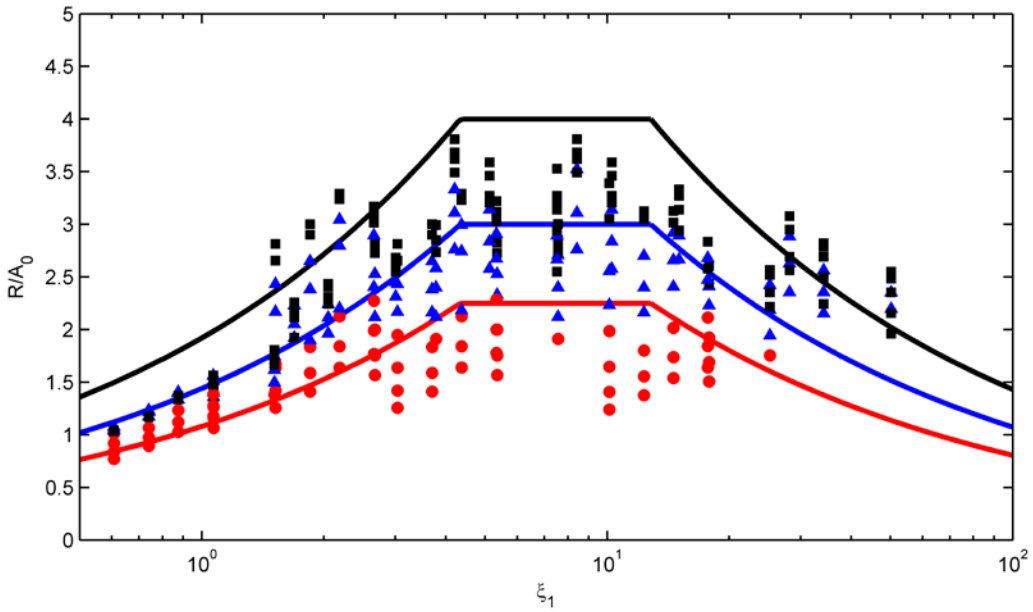

Fig. 5. Eq. 11 (solid lines) for $A_0/h_0 = 0.04$, and numerical model results (symbols) classified by onshore surf-similarity (ξ_2) as follows: $\xi_2 < 1.8$ (bottom line, circles), $1.8 \leq \xi_2 < 4.5$ (middle line, triangles), and $\xi_2 \geq 4.5$ (top line, squares).

Fig. 5 shows the data of Fig. 4 re-plotted with different symbols to differentiate the onshore conditions. When $\xi_2 < 1.8$ (circle), the corresponding R/A_0 values are roughly less than 2.0, and when ξ_2 is in the range of $1.8 \leq \xi_2 < 4.5$ (triangle), the corresponding R/A_0 values are less than 3.0. When $\xi_2 \geq 4.5$ (square), R/A_0 values are less than 4.0. Each range of ξ_2 exhibits a threshold value of relative runup height for each region, and these regions are represented by a single constant variable (γ) in the new empirical equations given by:

$$R/A_0 = C_3 \gamma \xi_1^{0.5} \quad \text{Eq. 6}$$

$$R/A_0 = C_4 \gamma \quad \text{Eq. 7}$$

$$R/A_0 = C_5 \alpha \gamma \xi_1^{-0.5} \quad \text{Eq. 8}$$

$$\gamma = [0.9, 1.2, 1.6] \text{ for } [\xi_2 < 1.8, 1.8 \leq \xi_2 < 4.5, \xi_2 \geq 4.5] \quad \text{Eq. 9}$$

Here, γ is a constant value that depends on the range of ξ_2, and C_3, C_4, and C_5 are empirical constants derived from the numerical results taken as 1.2, 2.5 and 4.0, respectively. The variable $\alpha = (A_0/h_0)^{-0.25}$ is the same as that used in MS10. Eqs. 6, 7, and 8 represent equations for breaking,

transition, and non-breaking regions. We did not use the least squares regression for our empirical constant. Instead, we opted for simple values to estimate conservative run-up heights for practical uses. The final form of the new empirical runup equation is

$$R/A_0 = \text{MIN}\left[(1.2\,\gamma\,\xi_1^{\,0.5}),\ (2.5\,\gamma),\ (4.0\alpha\,\gamma\,\xi_1^{\,-0.5})\right] \qquad \text{Eq. 10}$$

where MIN is the function selecting a minimum value between the three equations and γ is defined by Eq. 9. Fig. 5 shows these new empirical runup equations (solid lines, Eq. 10) plotted against the numerical model results as a function of surf-similarity parameter ξ_1 for $A_0/h_0 = 0.04$.

Generally, a weak positive correlation between run-up height and ξ_2 is observed: as ξ_2 is increased, R/A_0 also increases, but the value decreases or remains constant in several cases. Thus, we allow ξ_2 to vary as a stepped constant γ rather than a linear parameter in the new empirical runup equations. Fig. 6 shows the characteristics of the new empirical runup equation with A_0/h_0 = 0.01, 0.04, and 0.08. R/A_0 is a function of A_0/h_0 only at the non-breaking region. As A_0/h_0 increases, the range of the transition region, the region with constant R/A_0 also increases.

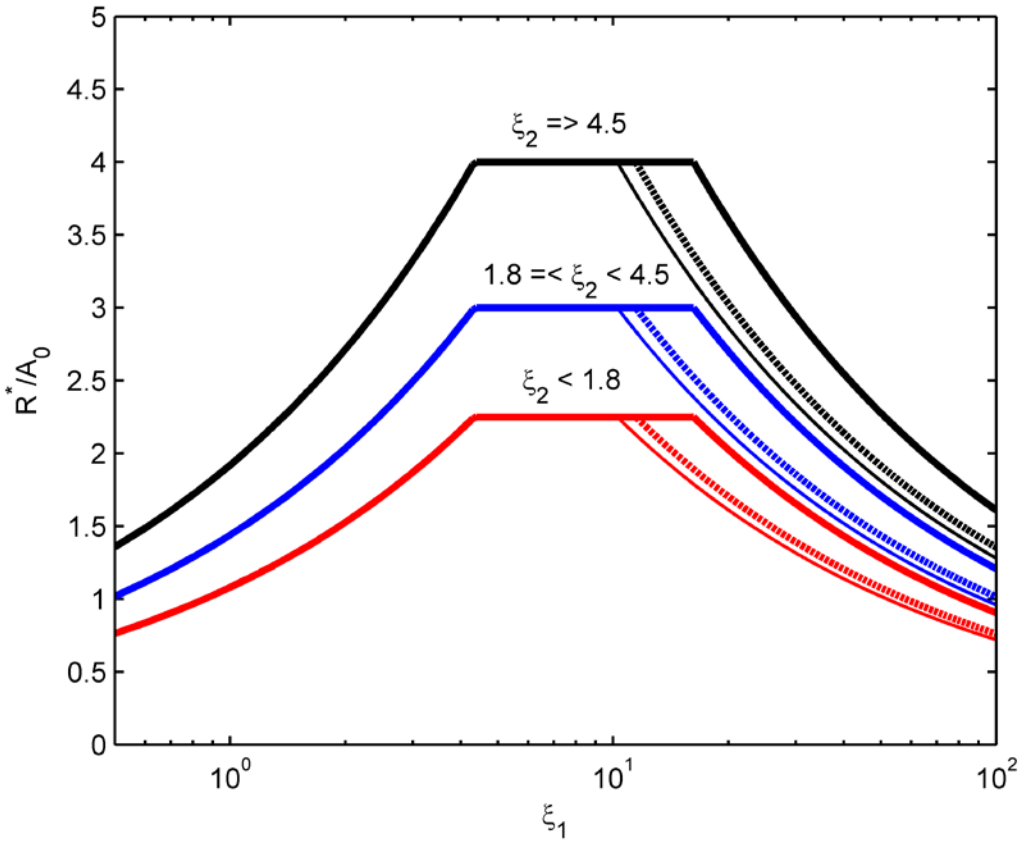

Fig. 6: Eq. 11 with A_0/h_0 of 0.01 (thick), 0.04 (dotted), and 0.08 (thin) for $\xi_2 < 1.8$ (bottom lines), $1.8 \leq \xi_2 < 4.5$ (middle lines), and $\xi_2 \geq 4.5$ (top lines).

5. Application

In this section, we apply Eqs. 9 and 10 to the 2011 Tohoku tsunami. We use the data from the Nationwide Ocean Wave Information Network for Ports and Harbors (NOWPHAS) GPS buoys as input data and compare calculated relative runup heights with a subset of the survey data collected from The 2011 Tohoku Earthquake Tsunami Joint Survey Group (TTJS).

The 6 GPS buoys were moored 10 to 20 km offshore and successfully recorded the sea surface elevations as summarized in Table 1 (Kawai et. al., 2012). The water depths at the buoys ranged from $125 < h_{buoy} < 204$ m, the amplitudes of maximum elevations were $2.6 < A_{buoy} < 6.5$ m, and the representative wave periods were between $1000 < T < 1510$ s depending on the buoy location. The representative tsunami period T was determined at each buoy from the elapsed time of a positive wave train exceeding 1% of the maximum amplitude. The corresponding A_{buoy}/h_{buoy} values ranged from 0.019 to 0.040, which is similar to the range of A_0/h_0 used in our new equation. We note that in MS10, A_0/h_0 ranged from 0.00015 to 0.01 which is more indicative of wave conditions in deeper water, such as near the wave source.

Table 1: Detail GPS Buoy Data in 2011 Tohoku Tsunami, Japan

Buoy	Location	Distance (km)	h_{buoy} (m)	A_{buoy} (m)	H_{buoy} (m)	T (s)	A_{buoy}/h_{buoy} (-)
GB807	40°07′00″ 142°04′00″	20.6	125	4.0	4.5	1100	0.032
GB804	39°37′38″ 142°11′12″	14.5	200	6.5	8.2	1200	0.033
GB802	39°15′31″ 142°05′49″	17.2	204	6.1	9.4	1510	0.030
GB803	38°51′28″ 141°53′40″	25.5	160	5.9	8.9	1000	0.037
GB801	38°13′57″ 141°41′01″	30.9	144	5.8	10.8	1400	0.040
GB806	36°58′17″ 141°11′08″	20.1	137	2.6	2.7	1250	0.019

Fig. 7 shows the geographic locations of the 6 GPS buoys (GB807, GB804, GB802, GB803, GB806, and GB801), the location of the $h_0 = 100$ m contour, the seven study sites located to the west of the buoys, and positions of the runup surveys. The runup data of 2011 Tohoku tsunami were conducted by joint research groups comprising 299 tsunami, coastal, seismology, and geology researchers from 64 universities and institutes throughout Japan (The 2011 Tohoku Earthquake Tsunami Joint Survey Group, 2011, Mori, et. al., 2011, Mori, Takahashi, and TTJS, 2012). The text file of surveyed data was available from the 2011 Tohoku Earthquake Tsunami Joint Survey Group, released 2012-03-30, at http://www.coastal.jp/ttjt/ and provided the location of the end of the runup points in terms of longitude and latitude, various runup heights depend on the filtering methods, and distances from shoreline to runup points. The provided runup distances and runup heights allow for calculated ξ_2 values using runup corrected

from the local MSL. In other words, we assume a plane slope from the shoreline to the runup point and ignore topographic features in between. Lastly, the survey runup height data are classified with four reliability levels, and we use only the higher ranked reliability data (2163 points from highly ranked two levels), and these data are presented in Fig. 7 as dots along the eastern coastline from 36.5°N to 40.5°N.

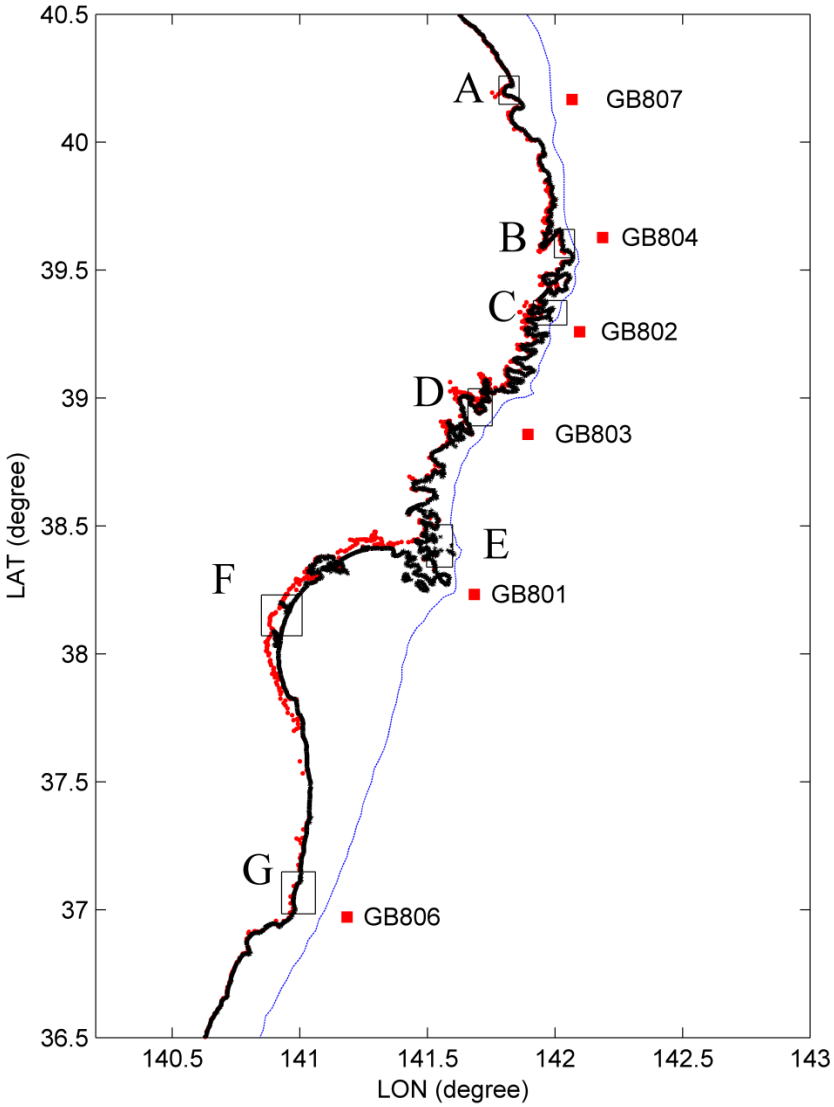

Fig. 7: The eastern Japan coastline with surveyed run-up points (dots) from 2011 Tohoku Earthquake Tsunami Joint Survey (TTJS) Group, location of GPS buoy data from NOWPHAS (squares), regions for the run-up height comparison (open rectangles), and a 100 m water depth contour from mean high water level (thin line).

In Fig. 7, we select seven comparison regions (A to G) based on the close proximity to the buoys. One exception is region F which was included because of the significant difference in

the onshore slopes relative to the other regions. Positive wave height for each region is calculated at the 100 m water contour line based on the GPS buoy data and linear shoaling excluding effects of wave refraction. Table 2 presents the detailed input information used in the comparisons. A_0 is the positive wave height at 100 m water depth, $Dist_1$ is the average horizontal distance from the 100 m depth point to the shoreline, and $Dist_2$ is the average horizontal distance from the shoreline to the end of the runup point. Note that we calculate $Dist_1$ and $Dist_2$ for each run-up point, and the average distances are not used in the comparison. A total of 233 run-up points are included in the seven delineated regions.

We present four representative regions (B, E, F, and G) in detail in Figs. 8, 9, 10, and 11. The mean values of ξ_1 for each region (B, E, F, and G) are 11, 3, 1, and 6 respectively (Table. 2), and these values correspond to the three new sub-equations we suggest for the non-breaking (B), breaking (E & F), and transition (G) region. For each of the figures, panel (a) shows a map of the coastline, area of detail, runup survey location, 100 m contour, and location of the seaward boundary (solid circle). Panel (b) shows the observed relative runup heights (solid) and predicted (open) versus latitude. Panel (c) plots the corresponding distributions of ξ_1 (square) and ξ_2 (triangle) versus latitude.

Table 2: Surveyed data for the model comparison.

SITE	A_0 (m)	$Dist_1$ (km)	$Dist_2$ (m)	T (s)	$Cot(\beta_1)$ MEAN (STD)	ξ_1 MEAN (STD)	$Cot(\beta_2)$ MEAN (STD)	ξ_2 MEAN (STD)
A	4.2	13.0	300	1100	130 (14.4)	4 (0.5)	46 (123.2)	132 (114.0)
B	7.7	3.7	160	1200	37 (1.2)	11 (0.3)	7 (4.7)	149 (154.3)
C	7.3	10.0	410	1510	100 (6.1)	5 (0.3)	28 (36.1)	161 (372.8)
D	6.6	8.4	210	1000	84 (11.7)	4 (0.7)	15 (14.3)	105 (140.0)
E	6.4	19.7	120	1400	197 (31.3)	3 (0.4)	8 (6.1)	142 (105.7)
F	4.6	44.3	2,200	1250	443 (12.0)	1 (0.0)	896 (723.2)	13 (35.9)
G	2.8	11.9	390	1100	112 (14.3)	6 (0.7)	96 (128.3)	42 (55.3)

Fig. 8 shows Region B, on the Omoe Peninsula, near Miyako, corresponding to GB804 which recorded A_{buoy} = 6.5 m and T = 1100 s in a depth of h_{buoy} = 200 m (Table 1). The corresponding shoaled amplitude at h_0 = 100 m water depth was A_0 = 7.7 m, which gives A_0/h_0 = 0.077. The observed runup varied $2.0 < R/A_0 < 3.7$, while calculated results were generally R/A_0 = 4.0, which would be conservative. Fig 8c shows that ξ_1 = 11 and controls the predicted runup value even though ξ_2 values vary from 40 to 300. This is due to the large value of A_0/h_0 = 0.077 (see Fig 6, thin lines for A_0/h_0 = 0.08).

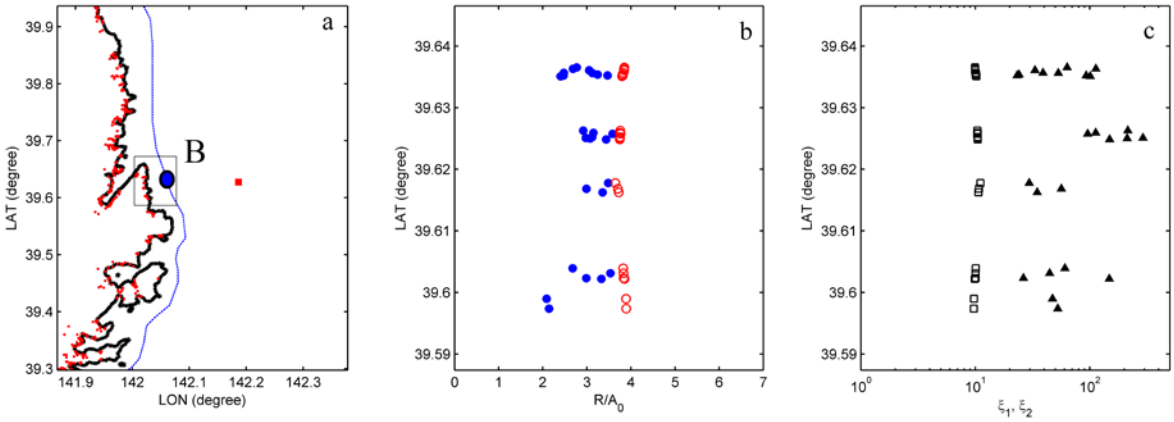

Fig. 8: Run-up height comparison results for Region B. (a) Coastline map with 100 m water contour (thin line), location of 100 m water depth for model input (solid circle), and GPS buoy location (solid square). (b) Comparison of the relative run-up heights from the survey (solid circle) and the new equation (open circle). (c) ξ_1 and ξ_2 values (open squares and solid triangles).

Fig. 9 evaluates the model performance in Region E which lies near Onagawa along the ria coast and has a complex shoreline, testing the 2D assumption used to derive and calibrate the equation. In this region, the buoy observed A_{buoy} = 5.8 m and T = 1400 s in a depth of h_{buoy} = 144 m. At the 100 m offshore boundary, A_0/h_0 = 0.064. Figure 9b shows that model is generally conservative with R/A_0 in the range $2.5 < R/A_0 < 3.4$ and the observations falling at or below these values in the range $1.0 < R/A_0 < 3.2$.

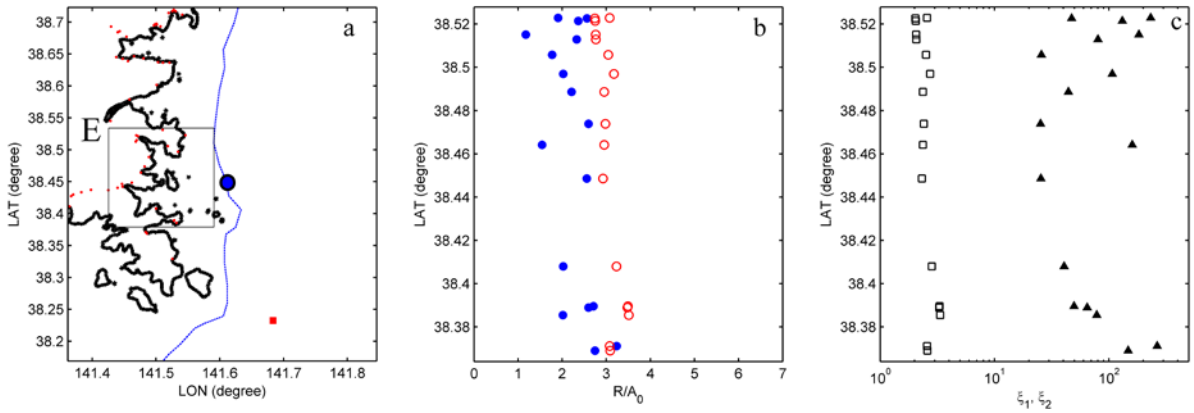

Fig. 9: Run-up height comparison results for Region E. Symbols are same as Fig. 8.

Fig. 10 evaluates the model for Region F along the Sendai plain which has a much flatter onshore slope and is markedly different from the other regions. We estimated that the amplitude at the h_0 = 100 m contour was A = 4.6 m based on the observations of GB801 and GB806. Fig 10b shows that the compound slope equations predict the runup reasonably well and are generally conservative. The predicted runup is generally R/A_0 = 1.1 except for some values in

the latitude ranging from 38.37 to 38.29 degrees. Here, the predicted values increase to R/A_0 = 2.2 consistent with several of the observations. Fig. 10c shows that the offshore value of ξ_1 remains nearly constant in this region, and the increases in R/A_0 are due to the variations in the onshore slope seen in the values of ξ_2 of Fig. 10c.

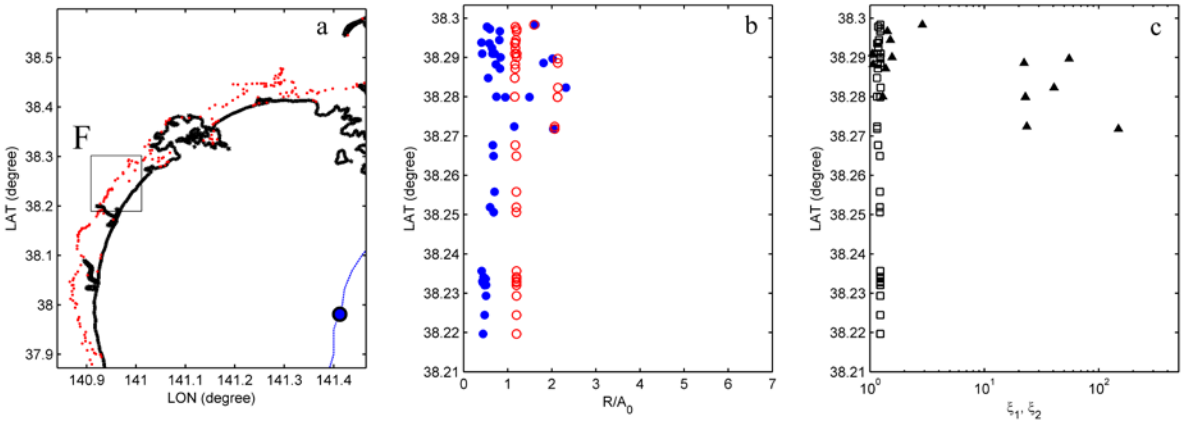

Fig. 10: Run-up height comparison results for Region F. Symbols are same as Fig. 8.

Fig. 11 evaluates the model performance in Region G which lies near Iwaki and represent the transition region of the model. In this region, the buoy observed A_{buoy} = 2.6 m, T = 1250 s in a depth of h_{buoy} = 137 m. At the 100 m offshore boundary, A_0/h_0 = 0.028 based on the observations of GB806. Fig. 11b shows that the model is generally conservative with R/A_0 in the range $2.3 < R/A_0 < 4.0$ while the observed R/A_0 is in the range $0.8 < R/A_0 < 3.5$. Fig 11c shows that ξ_1 remains mostly constant with a value of 8.0.

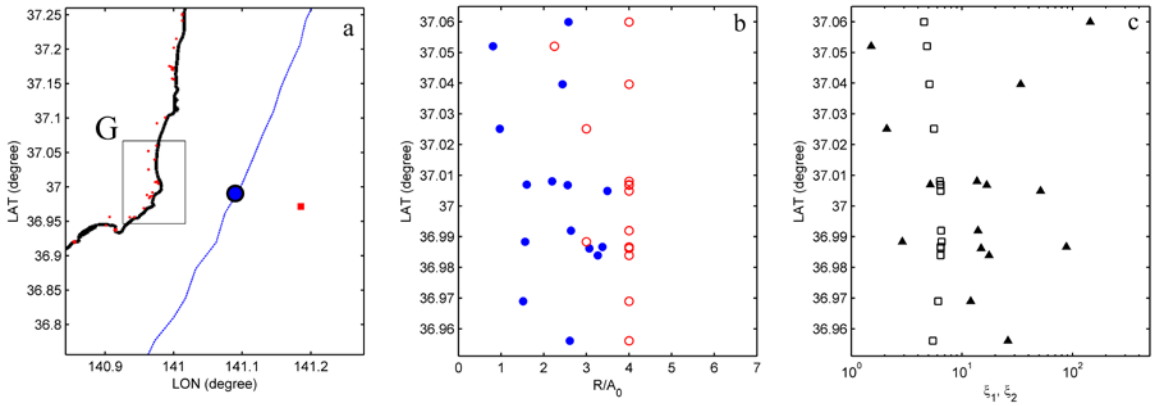

Fig. 11: Run-up height comparison results for Region G. Symbols are same as Fig. 8.

The measured and predicted runup heights are compared Fig. 12 for all 7 regions without normalization by the offshore amplitude. The dots comprise all of the surveyed runup height data from Fig. 7, and cross marks illustrate the data used in the comparison (i.e., locations A - G). The

open circles are the calculated results using the new equations estimates of the local tsunami and slope information (Table 1 and Table 2). The surveyed runup heights were scattered from almost zero to 40 m depending on the location. Note that in the area around 39.6 ˚N the survey data exhibits a large range of values. This wide variation may result from the complex local geophysical conditions or macro-roughness (i.e. vegetation, harbor infrastructures, or structures) effects which our model could not include at the inundation region.

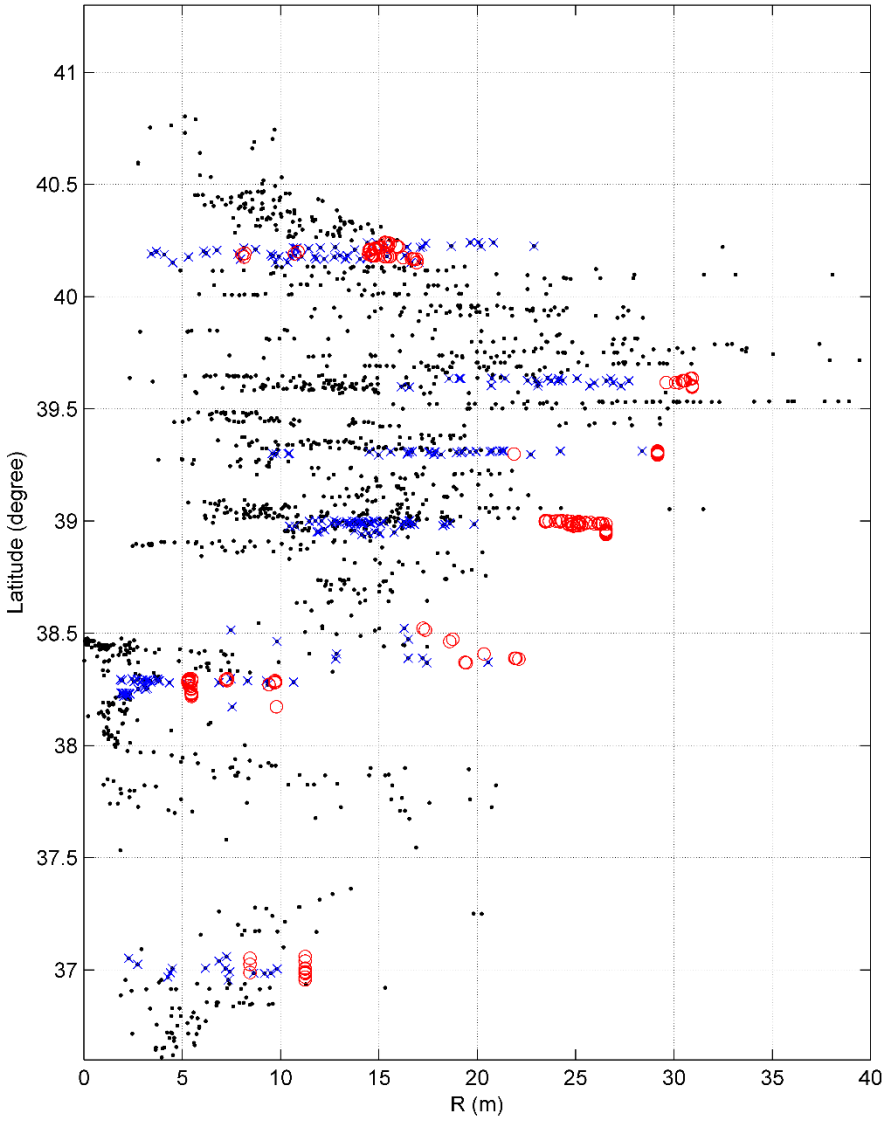

Fig. 12: Total surveyed run-up heights (dots) along the coastline from 36.5˚N to 41˚N, surveyed data used for comparison (cross marks), and corresponding Eq. 11 estimates (open circles).

6. Conclusion

This paper introduces an empirical tsunami run-up equation that includes the effects of bottom friction, wave breaking, and compound beach slopes. The new equation defines tsunami input wave conditions at the 100 m contour and employs a set of three equations that depend on the surf-similarity (Irribaren number). The format of the new equation originates from the runup solution of MS10, and it includes a parameterization to account for the onshore slope and for the transition between breaking and non-breaking regions. The equations were calibrated using a time-dependent numerical model including the effects of bottom friction. We compared our model without recalibration to the observed runup data from the 2011 Tohoku Tsunami using shoaled observed buoy data as input. Our model compares well to the observed data and is generally conservative.

The new empirical equation is not applicable for extremely small amplitude or large amplitude waves (much greater than 8 m or less than 1 m), and may not be suitable for complex geophysical conditions (e.g., around headlands, in narrow bays or with effects of coastal structures). For this study we used a single positive wave that follows a sech2 shape as in MS10 and a single general friction coefficient. Future research may include the effect of different types of wave or varying friction coefficients depending on the local inundation circumstances (vegetation or dense urban area). The new equation may be applicable to stochastic approaches for estimating the tsunami inundation hazard when the tsunami source is uncertain. This equation may also useful be for preliminary run-up height estimates without detailed geophysical information for practical engineering problems.

Acknowledgement

This research is based upon work partially supported by the National Science Foundation under Grant No. 0830378 and Oregon Sea Grant under Award No. NB223X. Any opinion, findings, and conclusions or recommendations expressed in this document are those of the authors and do not necessarily reflect the views of the National Science Foundation or Oregon Sea Grant.

6.1 References

Ahrens, J. P., & Titus, M. F. (1985) Wave runup formulas for smooth slopes. Journal of Waterway, Port, Coastal, and Ocean Engineering, 111(1), 128-133.

Battjes, J. A (1974) Surf similarity. In Proceedings of the Fourteenth International Coastal Engineering Conference, vol. 1, pp. 466–480. ASCE.

Beven, K (2013) So how much of your error is epistemic? Lessons from Japan and Italy. Hydrological Processes, 27(11), 1677-1680.

Carrier, G.F., Greenspan, H. P (1958) Water waves of finite amplitude on a sloping beach. Journal of Fluid Mechanics 17, 97–110.

Carrier, G. F., Wu, T. T. & Yeh, H (2003) Tsunami runup and drawdown on a plane beach, J. Fluid Mech. 475, 79–99.

Fuhrman, D. R. & Madsen, P. A (2008) Simulation of nonlinear wave runup with a high-order Boussinesq model. Coast. Eng. 55 (2), 139–154.

Hughes, A. S (2004) Estimation of wave run-up on smooth, impermeable slopes using the wave momentum flux parameter, Coast. Eng. 51, 1085-1104.

Hunt, I. A (1959) Design of Seawalls and Breakwaters, Journal of Waterway Harbors Division, ASCE, WW3, 123–152.

Kanoğlu, U (2004) Nonlinear evolution and runup-rundown of long waves over a sloping beach. J. Fluid Mech. 513, 363–372.

Kawai, H., Satoh, M., Kawaguchi, K., & Seki, K (2012) Recent Tsunamis observed by GPS buoys off the Pacific coast of Japan. Coastal Engineering Proceedings, 1(33), currents.1

Kobayashi, N. & Karjadi, E.A (1994) Surf-similarity parameter for breaking solitary wave run-up. Journal of Waterway, Port, Coastal, and Ocean Engineering 120, 645–650.

Li, Y. & Raichlen, F (2001) Solitary wave runup on plane slopes. J. Waterway Port Coast. Ocean Eng. 127 (1), 33–44.

Li, Y. & Raichlen, F (2003) Energy balance model for breaking solitary wave run-up. J. Waterway Port Coast. Ocean Eng. 47, 47–59.

Lo, H. Y., Park, Y. S., & Liu, P. L. F (2013) On the run-up and back-wash processes of single and double solitary waves-An experimental study. Coastal Engineering, 80, 1-14.

Lynett, P., Borrero, J., Liu, P. L.-F., and Synolakis, C.E (2003) Field Survey and Numerical Simulations: A Review of the 1998 Papua New Guinea Tsunami. Pure and Applied Geophysics, v.160, p. 2119-2146.

Lynett, P. and Liu, P. L.-F (2005) A Numerical Study of the Runup Generated by Three-Dimensional Landslides. JGR-Oceans, v. 110, C03006, doi:10.1029/2004JC002443.

Lynett, P., Wu, T., and Liu, P (2002) Modeling wave runup with depth-integrated equations. Coastal Engineering 46: 89-107.

Lynett, P (2006) Nearshore modeling high-order Boussinesq eqution, Journal of Waterway, Port, Coastal, and Ocean Engineering (ASCE), v. 132(5), 348-357.

Madsen, P. A. & Fuhrman, D. R (2008) Runup of tsunamis and long waves in terms of surf-similarity. Coast. Eng. 55 (3), 209–224.

Madsen, P. A., Fuhrman, D. R., Schaffer, H. A (2008) On the solitary wave paradigm for tsunamis. J. Geophys. Res. 113, C12012, 1–22.

Madsen, P. A. & Schaffer, H. A (2010) Analytical solutions for tsunami runup on a plane beach: single waves, N-waves and transient waves. J. Fluid Mech. 645, 27–57.

Mori, N., T.Takahashi, T.Yasuda and H.Yanagisawa (2011) Survey of 2011 Tohoku earthquake tsunami inundation and run-up, Geophysical Research Letters, 38, L00G14, doi:10.1029/2011 GL049210.

Nobuhito Mori, Tomoyuki Takahashi and The 2011 Tohoku Earthquake Tsunami Joint Survey Group (2012) Nationwide Post Event Survey and Analysis of the 2011 Tohoku Earthquake Tsunami, Coastal Engineering Journal, Vol.54, Issue 4, 1250001, 27p.

Park, H., Cox, D. T., Lynett, P. J., Wiebe, D. M., & Shin, S (2013) Tsunami inundation modeling in constructed environments: A physical and numerical comparison of free-surface elevation, velocity, and momentum flux. *Coastal Engineering*, *79*, 9-21.

Synolakis, C. E (1987) The runup of solitary waves. J. Fluid Mech. 185, 523–545.

Tadepalli, S. & Synolakis, C. E (1994) The run-up of N-waves on sloping beaches. Proc. R. Soc. Lond. A 445, 99–112.

The 2011 Tohoku Earthquake Tsunami Joint Survey Group (2011) Nationwide Field Survey of the 2011 Off the Pacific Coast of Tohoku Earthquake Tsunami, Journal of Japan Society of Civil Engineers, Series B, Vol. 67 (2011), 1, 63-66.

Nomenclature

Symbol	Descriptions	Unit
A_0	Tsunami wave amplitude	L
d_1	Distance from the slope to the end of the land	L
d_2	Distance from the slope to the center of the tsunami wave	L
d_3	Distance from the slope to the end of the model	L
$Dist_1$	Averaging distance from 100 m contour to shoreline	L
$Dist_2$	Averaging distance from shoreline to end of run-up point	L
F	Friction factor	-
g	Acceleration of gravity	L/T^2
H_0	Wave height	L
h_0	Water depth at the flat bottom	L
MIN	Minimum value	-
R	Tsunami runup height	L
STD	Standard deviation	-
T	Representative wave period	T
SWL	Still water level	-
β_1	Offshore slope	-
β_2	Onshore slope	-
γ	Empirical coefficient dependent on ξ_2	-
η	Surface elevation	L
ξ_1	Surf-similarity (Irribaren number) for offshore slope	-
ξ_2	Surf-similarity for onshore slope	-